

**INVESTIGATIONS OF OPEN-FRAMEWORK  
METAL SULFATES AND SUPERCAPACTIORS BASED  
ON VANADIUM CHALCOGENIDES-RGO/CNT HYBRIDS**

*BY*

**SUBBA REDDY MARRI  
CHEM07201004008**

**National Institute of Science Education and Research  
Jatni, Odisha-752050**

*A thesis submitted to the  
Board of Studies in Chemical Sciences  
In partial fulfillment of requirements  
For the degree of*

**DOCTOR OF PHILOSOPHY**

*of*

**HOMI BHABHA NATIONAL INSTITUTE**



**April-2016**



## **STATEMENT BY AUTHOR**

This dissertation has been submitted in partial fulfillment of requirements for an advanced degree at Homi Bhabha National Institute (HBNI) and is deposited in the Library to be made available to borrowers under rules of the HBNI.

Brief quotations from this dissertation are allowable without special permission, provided that accurate acknowledgement of source is made. Requests for permission for extended quotation from or reproduction of this manuscript in whole or in part may be granted by the Competent Authority of HBNI when in his or her judgment the proposed use of the material is in the interests of scholarship. In all other instances, however, permission must be obtained from the author.

**Subba Reddy Marri**

## **DECLARATION**

I, hereby declare that the investigation presented in the thesis has been carried out by me. The work is original and has not been submitted earlier as a whole or in part for a degree / diploma at this or any other Institution / University.

**Subba Reddy Marri**

## List of Publications

### a) Published

1. #**Subba R. Marri**, J. N. Behera, Synthesis, structure and photoluminescence properties of amine-templated open-framework bismuth sulfates. *J. Solid state Chem.*, **2014**, *1*, 15-21.
2. #J. N. Behera, J. Bhattacharjee, S. Horike, **Subba R. Marri**, P. P. Dahiya, Synthesis and characterization of robust three-dimensional chiral metal sulfates. *RSC Adv.*, **2014**, *4*, 50435-50442.
3. #S. Rath\*, **Subba R. Marri**\*, N. A. Lanzillo, S. Moshkalev, S. K. Nayak, J. N. Behera, Supercapacitors based on patronite–reduced graphene oxide hybrids: experimental and theoretical insights. *J. Mater. Chem.*, **2015**, *3*, 18874-18881. (\*contributed equally)
4. #S. Rath, **Subba R. Marri**, J. N. Behera, C. S. Rout, High-energy-density supercapacitors based on patronite/single-walled carbon nanotubes/reduced graphene oxide hybrids. *Eur. J. Inorg. Chem.*, **2016**, 259–265.
5. S. Bhowmick, S. Chakraborty, **Subba R. Marri**, J. N. Behera, N. Das, Pyrazine based donor tectons: synthesis, self-assembly and characterization. *RSC Adv.*, **2016**, *6*, 8992-9001.

### b) Communicated

6. **Subbba R. Marri**, N. Chauhan, J. Kumar, R. K. Tiwari, J. N. Behera, Hierarchical 3D assembly of a bio-friendly Ca(II) ion based MOF with tripodal ligand. *Manuscript submitted*.
7. #**Subbba R. Marri**, J. Kumar, J. N. Behera, Kagome-type isostructural 3D-transition metal fluorosulfates with spin 3/2 and 1: synthesis, characterization and magnetic properties. *Manuscript submitted*.

8. **#Subba R. Marri**, V. Chandra, S. Mahana, D. Topwal, J. N. Behera, Synthesis and characterization of layered metal sulfates containing  $M^{II}_3(\mu^3\text{-OH/F})_2$  (M = Mg, Co) diamond chains. *Manuscript submitted.*
9. **#Subba R. Marri**, J. N. Behera, Organically templated linear and layered Tin (II) sulfates. *Manuscript submitted.*

**c) Manuscript under preparation**

10. **Subba R. Marri**, S. Ratha, J. N. Behera, C. S. Rout, Facile synthesis and high performance supercapacitance of VSe<sub>2</sub>/RGO composite hybrid. *Manuscript under preparation*

#pertaining to thesis

## Conferences attended

1. Participated Symposium in chemistry, Chemical Research Society of India (CRSI-2011), Feb 4-6, 2011, conducted jointly by NISER and KIIT, Bhubaneswar, India.
2. Chemistry Research scholar's meet (CRSM-2011), July 14-15, held at IGCAR, Kalpakkam, Tamil Nadu, India. Presented a poster entitled "*Controlled synthesis of Hetero metallic  $\beta$ -Diketonates and their use as single source precursors*"
3. International workshop on functional materials (IWFM-2011), December 20-22, 2011 conducted by NIST, Berhampur, India. Presented a poster entitled "*Controlled synthesis of Hetero metallic  $\beta$ -Diketonates and their use as single source precursors*"
4. Recent development in chemical science and technology: Young Scientist Meet (RDCST-2014), March 15-16, 2014. Conducted by NIT-Rourkela, Odisha, India. Presented oral presentation entitled "*Porous materials: Synthesis and their applications*"
5. Participated in Indo-European symposium on frontiers of chemistry, November 10-12, 2011, conducted at School of Chemical Sciences, NISER, Bhubaneswar, India.
6. Indo-French Symposium on "Functional Metal-Organics: Applications in Materials and Catalysis", Feb 24 - 26, 2014 conducted at School of Chemical Sciences, NISER, Bhubaneswar, India. Presented a poster entitled "*Synthesis and characterization of robust three-dimensional chiral metal sulfates*"

**Subba Reddy Marri**

*Dedicated to*

*My parents*

## ACKNOWLEDGEMENTS

*I would like to express my gratitude to Dr. J. N. Behera, my guide, for continuous support, encouragement, patience exhibited and freedom provided for free thinking.*

*I am thankful to Prof. V. Chandrasekhar, Director-NISER for the laboratory facilities and financial support.*

*I thank my TMC members, Prof. A. Srinivasan and Dr. C. S. Purohit, chairperson-SCS, Dr. M. Sarkar, all other faculties in SCS. Also, I appreciate the help provided by Mr. Deepak Kumar Behera for collecting X-ray data, Mr. Sanjay during NMR analyses and Mr. Satyajit (IIT-BBS) for collecting supercapacitance data.*

*I remember our collaborators, Dr. C. S. Rout (IIT-BBS), Dr. Dinesh Topwal (IOP-BBS), Dr. Joydeep Bhattacharjee (NISER-SPS) and Dr. Sathoshi Horike (Kyoto University) immense pleasure for their valuable contributions.*

*I thank all my past lab members (under graduates) Prem, Archana, Vineet and Neha Chauhan, who have worked with me in different time period for their help and support.*

*I thank my present lab members Dr. Jitendra Kumar, Ranjay, jiban, Hinmanshu and Niharika for creating healthy atmosphere in lab and their fruitful discussions.*

*I remember all my friends in NISER with great gratitude, especially, Giri, Venkat, Thirupathi, Pedda, Pardhu, Manoj, Nayan, Mriganka, Ajesh, Adi, Antra, Woormi, Tapas, and balu.*

*Finally, above all I thank my teachers, brother (Srikanth), sister (Ramana) father (Thirupathi Reddy) and mother (Hanavayamma) for their unconditional love, care, affection and support.*

**Subba Reddy**

# CONTENTS

	<b>Page No.</b>
Thesis title	1
Recommendations of Viva Voce Board	2
Statement by the Author	3
Declaration	4
Publications List	5
Dedications	8
Acknowledgements	9
Contents	10
Synopsis	11
List of Figures	22
List of Tables	34
List of Abbreviations	35
Part-1	38
Chapter-1	39
Chapter-2	72
Chapter-3	117
Summary of part-1	161
Part-2	162
Chapter-1	163
Chapter-2	192
Chapter-3	221
Summary of part-2	246

## SYNOPSIS

The current thesis contains two parts and each part has three chapters. Part 1 details the synthesis of few novel open framework materials and their various applications. Part 2 deals about the development of hybrid materials based on transition metal chalcogenides (TMCs) and reduced graphene oxide (RGO) and carbon nanotubes.

### **Part-1** **Investigations of Open-Framework Metal Sulfates**

Open-framework inorganic and inorganic-organic hybrid materials constitute an important area of study in materials chemistry, because of their potential applications in areas such as sorption and catalysis. Besides aluminosilicate zeolites, the metal phosphates and carboxylates constitute large families of open-framework structures. The possibility of building open architectures with the sulfate anions as the basic building units has been explored in this thesis. Investigations of a variety of open-framework metal sulfates are presented.

Part one detail the synthesis of few novel open framework materials and their various applications. These materials have potential applications due to their unique pore size and topology. Last two decades have seen the development of such materials based on silicates, phosphates and carboxylates.<sup>1</sup> However, recently, the attention has shifted towards the use of other less explored oxyanions like sulfates, sulfites, selenates *etc.*<sup>2</sup> to synthesize open-framework materials. Thus main objective of this thesis is synthesis of new open framework materials based on sulfate anions and their applications. The part of this thesis divided in to three chapters.

## Chapter-1: Open-Framework Materials: A Brief Overview

A general introduction of open-framework materials, which includes open-framework zeolite materials, non aluminosilicates which are aluminophosphates, hydrothermal synthesis of zeolites, mechanism of formation of the open-framework materials, different synthetic techniques used for open-framework materials, characterization tools and techniques for synthesized open-framework materials and some of the reported open-framework metal phosphates and sulfates have been discussed in this chapter.

## Chapter-2: Open-Framework Main Group Metal Sulfates

This chapter describes the synthesis of main group (light and heavy weight) metal sulfates, their crystal dimensionalities and applications in adsorption and photoluminescence properties. Here depict the two Magnesium (light weight) sulfate frameworks, two Bismuth and four Tin (heavy weight) sulfate frameworks with different crystal dimensionalities. Two Mg(II) sulfate frameworks with composition of  $[\text{NH}_4]_8[\text{Mg}_8(\text{SO}_4)_{12}]_3$  (**1**) and  $[\text{NH}_4]_2[\text{Mg}_3(\text{OH})_2(\text{SO}_4)_3(\text{H}_2\text{O})_2]$ , (**2**) have been synthesized by hydro/solvothermal method in which both the compounds ammonium ion act as structure directing agent. Compound **1** crystallized with 3D-framework structure in cubic with chiral space group of  $P2(1)3$ . The anionic layer of **1** has 4-, 6-, and 8-membered apertures formed by corner sharing of  $\text{MgO}_6$  octahedra and  $\text{SO}_4$  tetrahedra through Mg-O-S linkages. From the first principle calculations suggest structure remains retain even after removal of ammonium ion. Compound **1** exhibits hydrogen adsorption in the order of 0.7 wt% at 77 K. Compound **2** crystallized with 2D-layered structures in orthorhombic with space group of  $Cmc2$ . Anionic 2D-layered structure formed with diamond chains consisting of  $\text{Mg}_3(\mu_3\text{-OH})_2$  units.

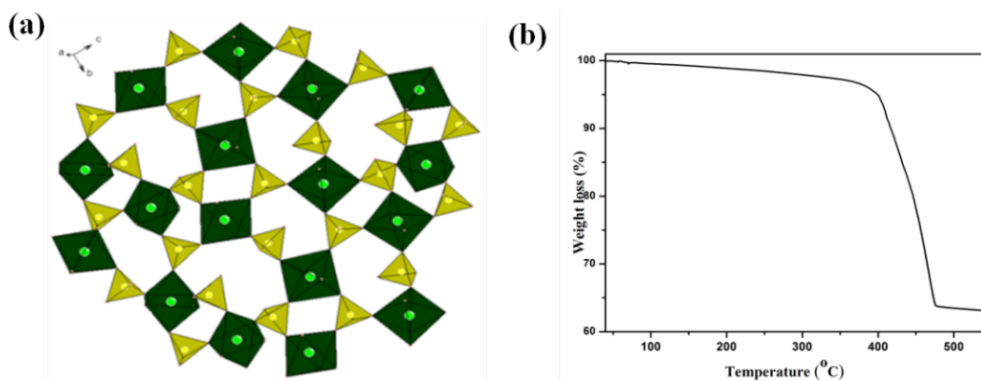


**Figure 1.** (a) Polyhedral representation of the Inorganic layer of **1** in the *bc*-plane forming 4-, 6- and 8- membered aperture and (b) Thermogravimetric data for  $[\text{NH}_4]_8[\text{Mg}_8(\text{SO}_4)_{12}]$ , (**1**).

Two organically-templated bismuth sulfates of the compositions,  $[\text{C}_6\text{N}_2\text{H}_{14}][\text{Bi}(\text{SO}_4)_2(\text{NO}_3)]$ ,<sup>4</sup> (**3**) and  $[\text{C}_4\text{N}_2\text{H}_{12}]_4[\text{Bi}_4(\text{SO}_4)_{10}(\text{H}_2\text{O})_4]$ ,<sup>4</sup> (**4**), with open architecture and their structures determined by single-crystal X-ray diffraction. These two compounds synthesized by slow evaporation method by using DABCO and Piperazine as structure directing agents. Compound **3** has a corrugated layered structure with 8- membered aperture where in the  $\text{SO}_4$  tetrahedra and the  $\text{BiO}_8$  polyhedra join together to form (4, 4) net sheets of the metal centers while **4** has a three-dimensional structure possessing 8- and 12- membered channels. Both the compounds show good fluorescence properties exhibiting blue luminescence. Time-resolved fluorescence behavior of **3** and **4** shows mean fluorescence lifetime of 0.9 and 1.0ns, respectively.

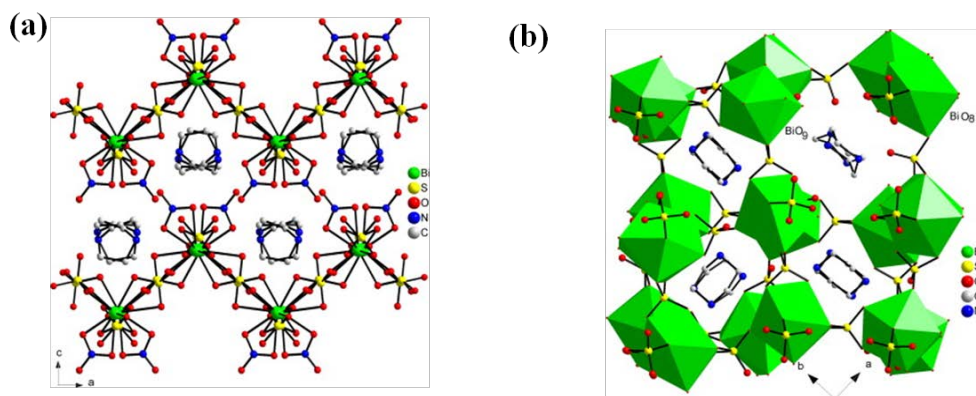


**Figure 2.** (a) The stacking of the alternate inorganic layers along the *c*-axis of the unit cell. The protonated DABCO molecules reside in the crest and trough regions of the inorganic layer for

[C<sub>6</sub>N<sub>2</sub>H<sub>14</sub>][Bi(SO<sub>4</sub>)<sub>2</sub>(NO<sub>3</sub>)], (**3**) and (b) 8- membered and 12- membered channels in *ab*- plane for [C<sub>4</sub>N<sub>2</sub>H<sub>12</sub>]<sub>4</sub>[Bi<sub>4</sub>(SO<sub>4</sub>)<sub>10</sub>(H<sub>2</sub>O)<sub>4</sub>], (**4**) and extra amine molecules are sitting inside the channels.

Four new Sn(II) sulfate materials with the compositions [C<sub>3</sub>N<sub>2</sub>H<sub>12</sub>][Sn<sub>2</sub>(SO<sub>4</sub>)<sub>3</sub>], (**5**); [C<sub>2</sub>N<sub>2</sub>H<sub>10</sub>][Sn(SO<sub>4</sub>)<sub>2</sub>], (**6**); [C<sub>3</sub>N<sub>2</sub>H<sub>12</sub>][Sn(SO<sub>4</sub>)<sub>2</sub>], (**7**) and [C<sub>4</sub>N<sub>2</sub>H<sub>14</sub>][Sn(SO<sub>4</sub>)<sub>2</sub>][H<sub>2</sub>O], (**8**), have been synthesized by hydrothermal condition using 1,3-diaminopropane (for **5**, **7**), ethylenediamine (for **6**) and 1,4-diaminobutane (for **8**) as structure directing organic amines and characterized by single-crystal X-ray diffraction. The ratio of Sn/S for all the four compounds is <1. In compound **5**, Sn<sup>II</sup> ions have three coordination with trigonal-pyramidal geometry where as in **6-8**, four coordination with truncated square-pyramidal. All the structures are slightly distorted due the presence of lone pair of electrons on Tin atoms which are occupied in the base vertex. The organic templates are present in between the anionic layers and render hydrogen bond through N-H...O for extra stability of the polymer. Compounds have been well characterized by FTIR spectra, elemental analysis, powder X-ray diffraction (PXRD), energy-dispersive X-ray spectroscopy (EDAX), and Thermogravimetric analyses (TGA).

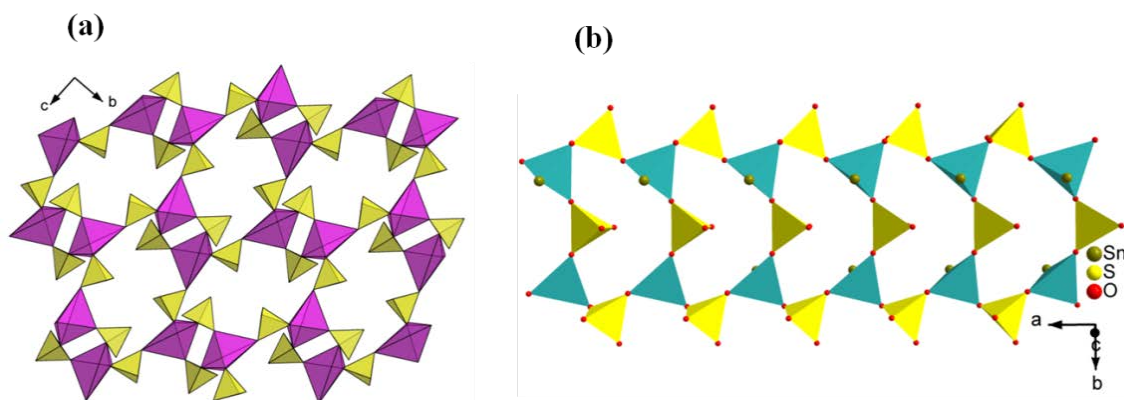


**Figure 3.** (a) The anionic layer of the compound [C<sub>2</sub>N<sub>2</sub>H<sub>10</sub>][Sn(SO<sub>4</sub>)<sub>2</sub>], (**6**), with 4- and 12-membered apertures in *bc*-plane and (b) Anionic chain of [C<sub>3</sub>N<sub>2</sub>H<sub>12</sub>][Sn(SO<sub>4</sub>)<sub>2</sub>], (**7**), with 8-membered running along *a*-axis.

### Chapter-3: Open-Framework Transition Metal Sulfates

This chapter describes the synthesis of open-frame work transition metal (Mn, Co and Ni) sulfates, their crystallographic signatures and applications in adsorption, magnetic and proton conductivity measurements. The 3D-frame work of  $[\text{NH}_4]_8[\text{Mn}_8(\text{SO}_4)_{12}]$ ,<sup>3</sup> (**9**) crystallize in the cubic chiral space group  $P2(1)3$  which is isostructural with 3D-Mg sulfate. In the presence of  $\text{NH}_4^+$  cations the framework has three-dimensional framework structures formed by corner sharing of metal octahedra and sulfate tetrahedra through Mn-O-S linkages, which leads the pinwheel arrangement of metal octahedra surrounded by six sulfate tetrahedra. This framework retain crystalline phase upon the thermal decomposition of ammonium ion resulting into the composition of  $[\text{H}]_8[\text{Mn}_8(\text{SO}_4)_{12}]$  which is confirmed by first principle calculations. Magnetic measurement of compound **9** exhibit paramagnetic behavior and hydrogen adsorption shows 0.45 wt% at 77 K.

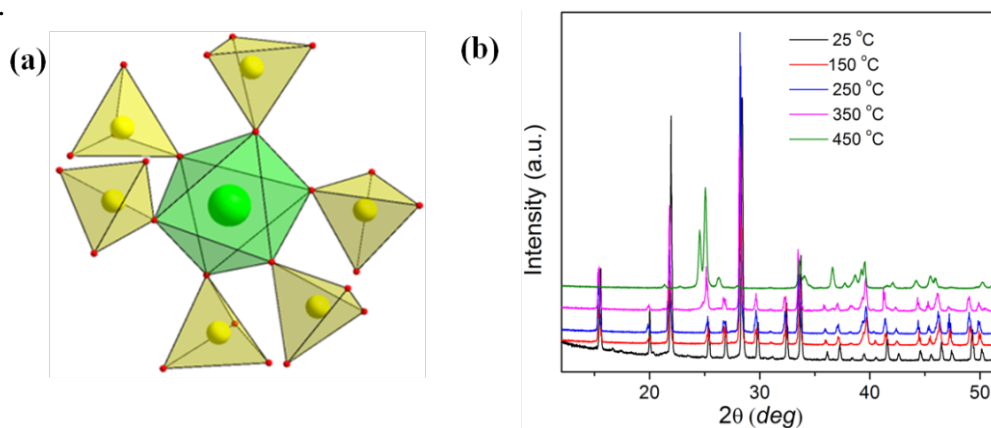


**Figure 4.** Pinwheel arrangement of  $\text{MnO}_6$  octahedra and  $\text{SO}_4$  tetrahedra in  $[\text{NH}_4]_8[\text{Mn}_8(\text{SO}_4)_{12}]$ , (**9**) and (b) Temperature dependent PXRD pattern for compound **9**.

The 2D-layer of  $[\text{C}_4\text{N}_2\text{H}_{12}]_2[\text{Co}_3\text{F}_2(\text{SO}_4)_3(\text{H}_2\text{O})_2]$ , **10** was synthesized by hydro/solvothermal condition by using Piperazine as structure directing agent. This compound is isostructural with 2D- Mg layered structure. Compound **10** was characterized by all the complementary techniques like PXRD, EDX, TGA, X-ray single-crystal diffraction. The layered structure was formed by the diamond chains comprising of  $\text{Co}_3(\mu_3\text{-F})_2$  units. Magnetic studies of **10** reveals its ferrimagnetic nature with a transition at 10.8 K and does not exhibit spin-glass freezing. Isothermal magnetization shows hysteresis loop at 3.5 K with a coercive field of 1200 Oe and remnant magnetization of  $0.1\mu_B$ .

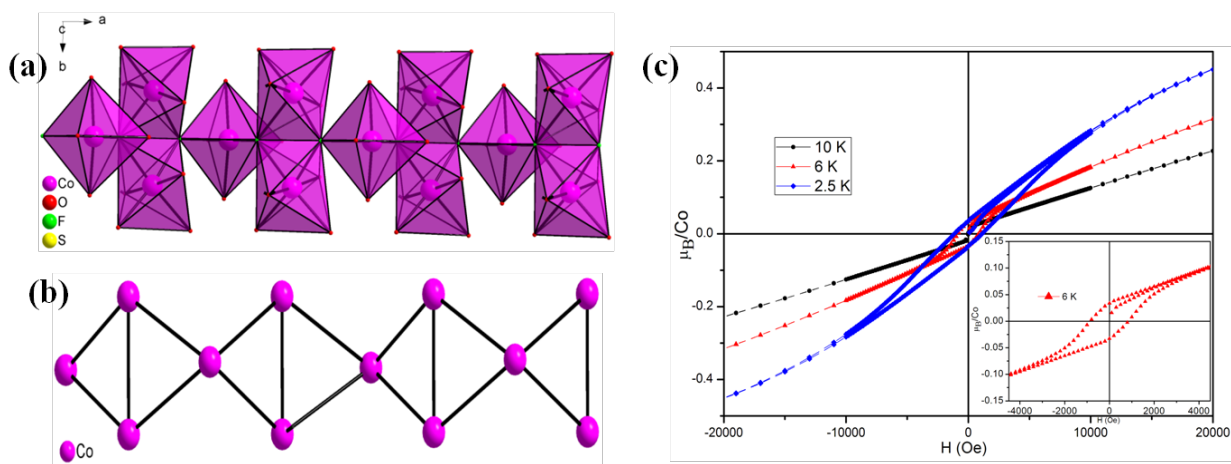


**Figure 5.** (a) The infinite diamond chain formed by the connectivity of the metal polyhedral. (b) Presence of triangular units in the diamond chain and (c) Magnetization as a function of magnetic field at 2.5, 6 and 10 K for  $[\text{C}_4\text{N}_2\text{H}_{12}]_2[\text{Co}_3\text{F}_2(\text{SO}_4)_3(\text{H}_2\text{O})_2]$ , **10**.

Two isostructural 3D-Kagome type structures with composition of  $[\text{H}_3\text{O}][\text{MSO}_4\text{F}]$  (where  $\text{M}=\text{Co}$  (**11**);  $\text{Ni}$  (**12**) and  $\text{Zn}$  (**13**)) were synthesized by solvothermal method and structurally characterized by single-crystal X-ray diffraction, FTIR, TGA and PXRD. In both 3D-crystal lattice consists of Kagome type entity where sulfate groups replaced one of the metal nodes when compared with true Kagome structures.<sup>5</sup> Magnetic studies of these ( $\text{Co}$  (**11**) and  $\text{Ni}$  (**12**))

frameworks) 3D-framework structures revolve the paramagnetic nature and shows weak antiferromagnetic interactions due to their orbital contribution.

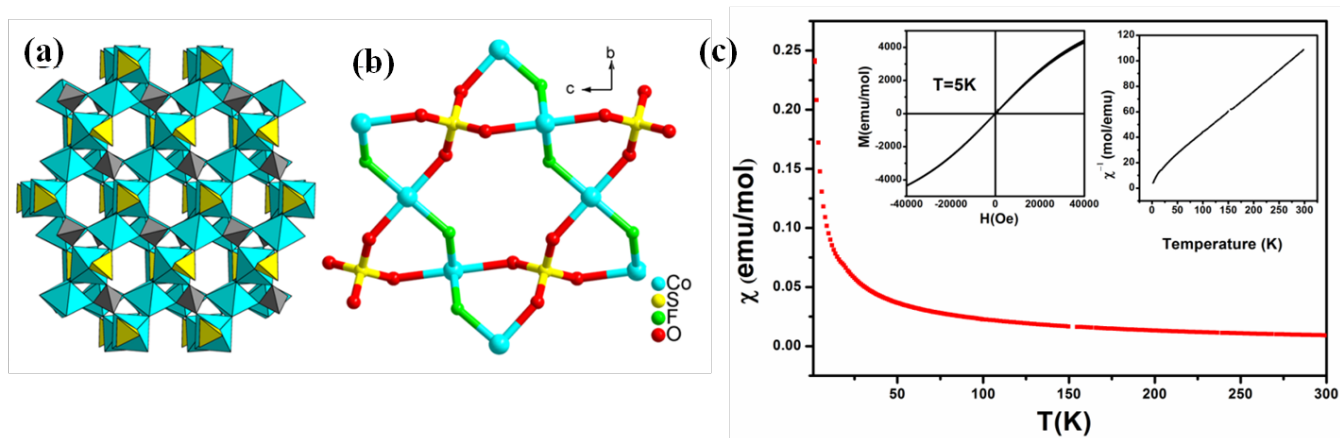


**Figure 6.** (a) Polyhedral view of 3D-crystal lattice (b) Kagome type structure building block and (c) magnetization curves for [H<sub>3</sub>O][CoSO<sub>4</sub>F], (11).

## Part-2

### Supercapacitors Based on Vanadium Chalcogenides-RGO/CNT Hybrids

The development of excellent supercapacitors is well sought because the consumption of fossil fuels and consequent global warming and increase in pollution has forced the research towards the development of more viable and energy efficient power storage devices. In this regards, supercapacitors are significantly important because of their high energy density, power density and long life cycle.<sup>6</sup> Recent developments have shown the propensity of TMCs-carbonaceous hybrid materials to perform as alternative electrode materials because of their unique property like combination of both electrical double layer and Pseudocapacitance behavior.<sup>7</sup> Hence the main objective of this thesis is synthesis of vanadium chalcogenides-carbonaceous composite

hybrid electrodes which exhibits high performance supercapacitance, high energy density and power density. The part of this thesis organized in to three chapters.

### **Chapter-1: Introduction of Supercapacitor**

A general introduction of supercapacitors, which includes comparison of properties and performance of battery, capacitor and Supercapacitor, various electrolytes used in supercapacitors, types of electrode materials, calculation of supercapacitance, types of mechanisms, metal chalcogenides and composite hybrids of TMCs-RGO and TMCs-CNTs hybrids have been described in this chapter.

### **Chapter-2: Supercapacitors Based on Vanadium Chalcogenides/RGO Hybrids**

This chapter describes the facile hydrothermal synthesis and high performance supercapacitance measurements of two Vanadium chalcogenides ( $VS_4$ ,  $VSe_2$ ) - RGO composite hybrids. The foremost hybrid  $VS_4$ /RGO synthesized by a facile one-step hydrothermal method and its supercapacitor performance is tested. The results obtained so far have shown the great potential of the  $VS_4$ /RGO hybrids with the specific capacitance as high as 877 F/g.<sup>8</sup> Simulations based on density functional theory confirms an enhanced quantum capacitance when  $VS_4$  is hetero structured with graphene, primarily due to the location of the graphene Dirac cone relative to the band gap of  $VS_4$ . The hybrids exhibited an enhanced energy density of 117 Wh/kg and a power density of 20 KW/kg which are compared with some of the reported metal sulfides and their graphene based hybrids. The second hybrid which is  $VSe_2$ /RGO where sulfur atom in foremost hybrid replaced by selenium.  $VSe_2$ /RGO hybrid exhibits very high specific capacitance in the order of 500 F/g at current density of 1 A/g, energy density of 128 Wh/kg and power density of 32.81 KW/kg. These experimental and theoretical findings provide useful insights in the design of supercapacitors for potential high performance energy storage application.

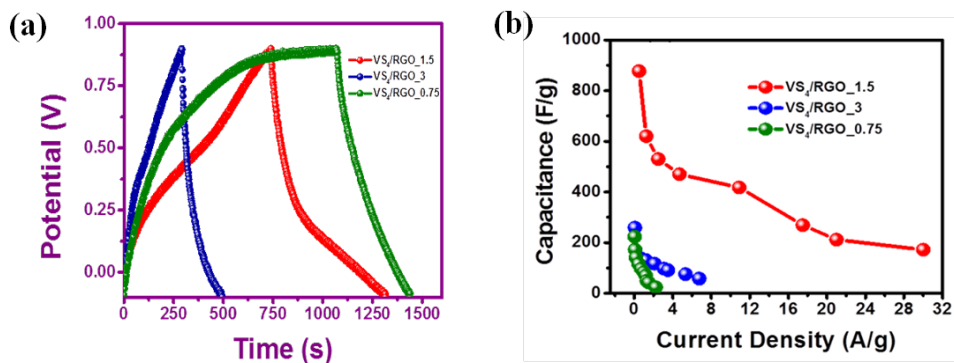


**Figure 7.** (a) Comparison of charge-discharge curves at different current densities of VS<sub>4</sub>/RGO hybrids and (b) comparison of capacitance for three composite hybrids.

### Chapter-3: High Energy Density Supercapacitors Based on Patronite /CNTs/ RGO Hybrids

Initially the electrodes used in the supercapacitors are carbonaceous materials which are reduced graphene oxide, carbon nanotubes and activated carbons *etc.*<sup>9</sup> The problem of carbonaceous materials is having less energy density as compared to rechargeable batteries due to their low value of energy per unit weight ratio. There are different ways we can enhance the energy density of the supercapacitor. By increasing the charge storage and /or working potential window surely enhance the energy density of supercapacitor. The working potential window can be increased by using the pseudocapacitive materials. But, they don't have the advantage of long cyclic stability as in case of carbonaceous materials.<sup>10</sup> This chapter describes the facile synthesis and supercapacitance measurements of high energy density material *i.e* Patronite/CNTs/RGO composite hybrid. The prepared hybrid is resulted because of the nucleation of VS<sub>2</sub>, in presence of CNTs/RGO as an active template.<sup>11</sup> Other intermediary samples such as VS<sub>2</sub>, bare CNTs, bare RGO, CNTs/RGO, VS<sub>4</sub>/CNTs and VS<sub>4</sub>/RGO were also obtained under different controlled experimental procedures. Structural and morphological properties of the hybrid, VS<sub>4</sub>/CNTs/RGO were studied and its electrochemical properties towards supercapacitor application were

investigated using a swagelok type two-electrode setup using 0.5 M aqueous solution of  $K_2SO_4$  as the electrolyte.<sup>12</sup> A thorough comparison was carried out for the supercapacitive properties of all experimentally obtained samples mentioned above, under similar testing conditions. The hybrid,  $VS_4/CNTs/RGO$  showed an impressive energy density of  $\sim 174$  Wh/kg and a moderate power density of  $\sim 13.8$  KW/kg.

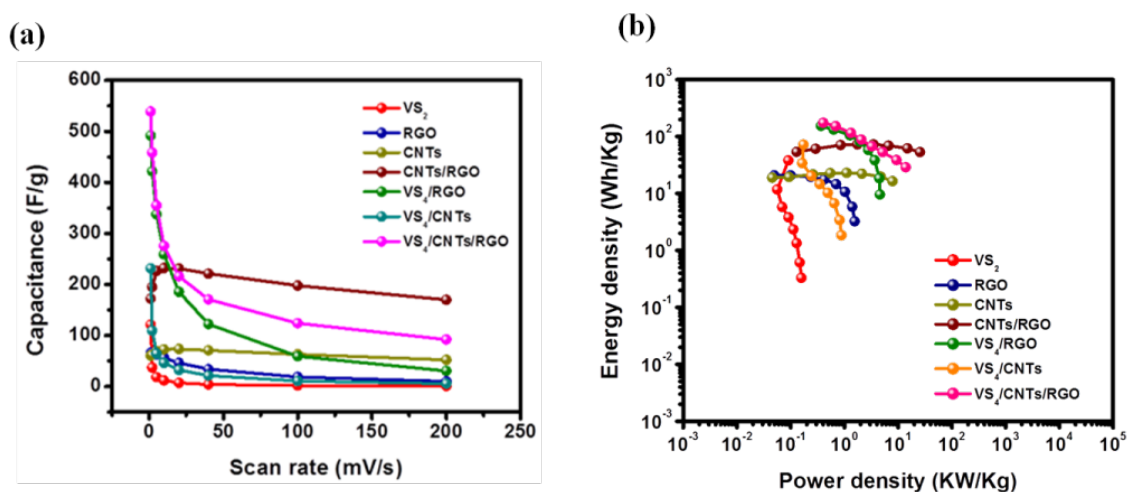


**Figure 8.** (a) comparison of specific capacitance for all the hybrids from cyclic voltmetry method and (b) Comparison of power densities and energy densities for all hybrids by using typical Ragone plot.

## References

1. Maspoch, D.; Ruiz-Molina, D.; Veciana, J., *Chem. Soc. Rev.* **2007**, *36*, 770.
2. (a) Rao, C. N. R.; Behera, J. N.; Dan, M., *Chem. Soc. Rev.* **2006**, *35*, 375; (b) Behera, J. N.; Gopalkrishnan, K. V.; Rao, C. N. R., *Inorg. Chem.* **2004**, *43*, 2636; (c) Behera, J. N.; Rao, C. N. R., *J. Am. Chem. Soc.* **2006**, *128*, 9334; (d) Behera, J. N.; Ayi, A. A.; Rao, C. N. R., *Chem. Commun.* **2004**, 968; (e) Tiwari, R. K.; Kumar, J.; Behera, J. N., *Chem. Commun.* **2016**, *52*, 1282.

3. Behera, J. N.; Bhattacharjee, J.; Horike, S.; Marri, S. R.; Dahiya, P. P., *RSC Advances* **2014**, *4*, 50435.
4. Marri, S. R.; Behera, J. N., *J. Solid State Chem.* **2014**, *210*, 15.
5. Behera, J. N.; Paul, G.; Choudhury, A.; Rao, C. N. R., *Chem. Commun.* **2004**, 456.
6. (a) Lu, X.; Li, G.; Tong, Y., *Science China Technological Sciences* **2015**, *58*, 1799; (b) Zhong, C.; Deng, Y.; Hu, W.; Qiao, J.; Zhang, L.; Zhang, J., *Chem. Soc. Rev.* **2015**, *44*, 7484.
7. (a) Late, D. J.; Rout, C. S.; Chakravarty, D.; Ratha, S., *Can. Chem. Trans* **2015**, *3*, 118; (b) Tan, C.; Zhang, H., *Chem. Soc. Rev.* **2015**, *44*, 2713.
8. Ratha, S.; Marri, S. R.; Lanzillo, N. A.; Moshkalev, S.; Nayak, S. K.; Behera, J. N.; Rout, C. S., *Journal of Materials Chemistry A* **2015**, *3*, 18874.
9. Wu, X.-L.; Xu, A.-W., *Journal of Materials Chemistry A* **2014**, *2*, 4852.
10. (a) Brownson, D. A. C.; Kampouris, D. K.; Banks, C. E., *J. Power Sources* **2011**, *196*, 4873; (b) Yang, M.; Cheng, B.; Song, H.; Chen, X., *Electrochim. Acta* **2010**, *55*, 7021.
11. Rout, C. S.; Kim, B.-H.; Xu, X.; Yang, J.; Jeong, H. Y.; Odkhuu, D.; Park, N.; Cho, J.; Shin, H. S., *J. Am. Chem. Soc.* **2013**, *135*, 8720.
12. Ratha, S.; Marri, S. R.; Behera, J. N.; Rout, C. S., *Eur. J. Inorg. Chem.* **2016**, *2016*, 259.

## List of Figures

### (Part-1)

### Page No

1	Figure 1.1	PBUs of Zeolites (a) $\text{TO}_4$ polyhedra (b) $\text{TO}_4$ tetrahedra sharing common vertex with oxygen atoms (where T=Si, P, Al and S).	41
2	Figure 1.2	SBUs with different number of tetrahedral cations. Codes are given below.	42
3	Figure 1.3	Some important chains that are occur in several Zeolite frameworks (a) Double <i>zig-zag</i> chain, (b) double sawtooth chain, (c) double crankshaft chain, (d) narsarsukite chain, (e) pentasil chain.	42
4	Figure 1.4	Structure of Zeolite FAU type framework.	44
5	Figure 1.5	Structural units in ZSM-5 (a) $5^8$ units, (b),pentasil chains which are present in ZSM-5 and (c) view of ZSM-5 with 10-ring channels.	45
6	Figure 1.6	Schematic diagrams of $\text{AlPO}_4$ -18, $\text{AlPO}_4$ -34, $\text{AlPO}_4$ -36 and $\text{AlPO}_4$ -5 Aluminophosphate molecular sieves with three-dimensional narrow pore structures.	47
7	Figure 1.7	Structure of ND-1 viewed along <i>c</i> -axis with 24-ring channels.	48
8	Figure 1.8	The anionic layer of $[(\text{C}_4\text{N}_3\text{H}_{16}) (\text{C}_4\text{N}_3\text{H}_{15})] [\text{Fe}_5\text{F}_4(\text{H}_2\text{PO}_4)(\text{HPO}_4)_3(\text{PO}_4)_3] \cdot \text{H}_2\text{O}$ , showing the one-dimensional Fe-O/F-Fe chains and their Connectivity with the $\text{PO}_4$ units.	49
9	Figure 1.9	View of 3D-framework of $[\text{C}_4\text{N}_2\text{H}_{12}][\text{Ni}_2\text{F}_4(\text{SO}_4)\text{H}_2\text{O}]$ with 11-membered apertures in [101] plane.	51
10	Figure 1.10	Inorganic-framework structure of $[\text{H}_2\text{N}(\text{CH}_2)_4\text{NH}_2]_{0.5}[\text{Zn}(\text{HSeO}_3)]$	52

(Se<sub>2</sub>O<sub>5</sub>)] formed with 4 and 10- membered ring channels in *bc*-plane and the amine molecules are resides in the 10- membered ring channels.

11	Figure 1.11	View of the structure of the compound [H <sub>2</sub> bipy][Zn(SeO <sub>4</sub> )(H <sub>2</sub> O)] in <i>ac</i> -plane.	53
12	Figure 1.12	Amine molecules inside the pores of the frameworks color code: blue; amine molecules; yellow; framework material (b) After activation of the framework material	55
13	Figure 1.13	Schematic representations for the crystallization mechanism of Si-TPA-MFI.	57
14	Figure 1.14	Schematic diagrams for the Teflon-lined stainless steel autoclave which we used regularly in our laboratory.	58
15	Figure 1.15	The schematic diagram for the autoclave.	60
16	Figure 1.16	General TGA plot for single step weight loss of the material.	62
17	Figure 1.17	Diffraction of X-rays by crystal planes.	63
18	Figure 1.18	The schematic diagram for different types of adsorptions (I-V)	66
19	Figure 2.1	Asymmetric unit of compound [NH <sub>4</sub> ] <sub>2</sub> [Mg <sub>3</sub> (OH) <sub>2</sub> (SO <sub>4</sub> ) <sub>3</sub> (H <sub>2</sub> O) <sub>2</sub> ], <b>1</b> .	83
20	Figure 2.2	View of inorganic layers of <b>1</b> in <i>bc</i> -plane with eight- membered apertures.	84
21	Figure 2.3	View of packing layers in <b>1</b> . Hydrogen bonding interactions between ammonium ions and the framework oxygen are shown by dotted lines.	85
22	Figure 2.4	Asymmetric unit of compound [NH <sub>4</sub> ] <sub>8</sub> [Mg <sub>2</sub> (SO <sub>4</sub> ) <sub>12</sub> ], <b>2</b> .	85
23	Figure 2.5	(a) Pinwheel arrangement of MO <sub>6</sub> octahedra and SO <sub>4</sub> tetrahedra (b)	87

		Top view of the layer parallel to the <i>ac</i> -plane of the unit cell in <b>2</b> .	
24	Figure 2.6	(a) View of 4-, 6- and 8- membered aperture in <i>bc</i> -plane for <b>2</b> . (b) Inorganic layers of the compound <b>2</b> in <i>c</i> -axis. Ammonium ions removed for clarity.	87
25	Figure 2.7	Hydrogen adsorption isotherms for $[\text{NH}_4]_8[\text{Mg}_8(\text{SO}_4)_{12}]$ , <b>2</b> at 77K.	88
26	Figure 2.8	The asymmetric unit of $[\text{C}_6\text{N}_2\text{H}_{14}][\text{Bi}(\text{SO}_4)_2(\text{NO}_3)]$ , <b>3</b> .	89
27	Figure 2.9	(a) Top view of the layer parallel to the <i>ab</i> -plane in <b>3</b> , formed by joining the $\text{BiO}_8$ polyhedra and $\text{SO}_4$ tetrahedra (b) (4, 4) net sheet formed by the joining of the metal centers.	90
28	Figure 2.10	Stacking of the alternate inorganic layers and protonated DABCO molecules along <i>c</i> -axis. Note the wave like pattern of the inorganic layers.	91
29	Figure 2.11	The asymmetric unit of $[\text{C}_4\text{N}_2\text{H}_{12}]_4[\text{Bi}_4(\text{SO}_4)_{10}(\text{H}_2\text{O})_4]$ , <b>4</b> with atom labeled.	91
30	Figure 2.12	(a) View down 8- membered and 12- membered rings along <i>a</i> -axis. (b) Protonated amine molecules are sitting inside the channels. Hydrogen atoms omitted for clarity.	93
31	Figure 2.13	(4, 6) net sheet in <b>4</b> formed by joining of the metal centers.	94
32	Figure 2.14	Excitation and emission spectra of compounds <b>3</b> and <b>4</b> . In set show an optical image of the blue luminescent compound of <b>4</b> using confocal microscope.	95
33	Figure 2.15	Time-resolved fluorescence behavior of <b>3</b> and <b>4</b> at $\lambda_{\text{exc}} = 375$ nm. In the figure, (i) instrument response function and (ii) monitoring wave-	97

lengths at 420 nm decay profile measured at 298 K.

34	Figure 2.16	Asymmetric unit of $[\text{C}_3\text{N}_2\text{H}_{12}][\text{Sn}_2(\text{SO}_4)_3]$ , <b>5</b> .	97
35	Figure 2.17	(a) The anionic chain of the compound $[\text{C}_3\text{N}_2\text{H}_{12}][\text{Sn}(\text{SO}_4)_2]$ , <b>5</b> in <i>ab</i> -plane. (b) The protonated amine molecules are resided in between the two chains in the <i>ac</i> -plane.	98
36	Figure 2.18	Asymmetric unit of $[\text{C}_2\text{N}_2\text{H}_{10}][\text{Sn}(\text{SO}_4)_2]$ , <b>6</b> shown with atom labeling.	99
37	Figure 2.19	(a) The anionic layer of the compound $[\text{C}_2\text{N}_2\text{H}_{10}][\text{Sn}(\text{SO}_4)_2]$ , <b>6</b> in <i>bc</i> -plane. (b) Packing of the amine molecules and anionic layers in compound <b>6</b> in <i>ab</i> -plane	100
38	Figure 2.20	Asymmetric unit of $[\text{C}_3\text{N}_2\text{H}_{12}][\text{Sn}(\text{SO}_4)_2]$ , <b>7</b> shown with atom labeling.	100
39	Figure 2.21	(a) View of 4- membered ring along <i>c</i> -axis. (b) Organic templates are resided in between the two anionic chains in <i>ac</i> -plane.	101
40	Figure 2.22	Asymmetric unit of $[\text{C}_4\text{N}_2\text{H}_{14}][\text{Sn}(\text{SO}_4)_2]\cdot\text{H}_2\text{O}$ , <b>8</b> .	102
41	Figure 2.23	The anionic layer of the compound $[\text{C}_4\text{N}_2\text{H}_{14}][\text{Sn}(\text{SO}_4)_2][\text{H}_2\text{O}]$ , <b>8</b> in <i>bc</i> -plane. (b) (4, 12) net sheet formed by the joining of the metal centers for compound <b>8</b> .	103
42	Figure 2.24	(a) Possible hydrogen bonding interactions between the two anionic layers and amine molecules in <i>ba</i> -plane (b) With water molecules in <b>8</b> .	103
43	Figure 2.25	Experimental and simulated PXRD patterns of compounds from <b>1-6</b> .	114
44	Figure 2.26	Thermogravimetric analysis for the compounds <b>1-6</b> .	115
45	Figure 2.27	FTIR spectra for the compounds <b>1-6</b> .	116

46	Figure 3.1	Asymmetric unit of $[\text{H}_3\text{O}][\text{MSO}_4\text{F}]$ , <b>9</b> . The disordered extra framework hydronium ion is omitted for clarity.	127
47	Figure 3.2	One-dimensional Co-F chains in <b>9</b> running in <i>bc</i> -planes; (b) Formation of 2D-layer in <i>bc</i> -plane by connecting each layer through sulfate anions (S(1)O <sub>4</sub> ); (c) Interconnection of 2D-layer as highlighted with different color <i>via</i> sulfate anions (S(2)O <sub>4</sub> ); (d) 3D-lattice as a results of interconnection <i>via</i> crystallographically distinct sulfate anions which are highlighted with different color.	129
48	Figure 3.3	(a) Polyhedral view of the 3D-crystal lattice; (b) Magnified view of the Kagome type structural building block in <b>9</b> .	130
49	Figure 3.4	Temperature dependence of the magnetic susceptibility for both <b>9</b> and <b>10</b> compounds measured at 1000 Oe. Inset (a) shows the isothermal M–H cycles at 5 K (b) shows the $\chi^{-1}$ vs T.	131
50	Figure 3.5	Asymmetric unit of $[\text{C}_4\text{N}_2\text{H}_{12}]_2[\text{Co}_3\text{F}_2(\text{SO}_4)_3(\text{H}_2\text{O})_2]$ , <b>12</b> .	131
51	Figure 3.6	(a) The infinite diamond chain formed by the connectivity of the metal polyhedra. (b) Presence of triangular units in the diamond chain. (c) Anionic inorganic layer in <b>12</b> in the <i>ac</i> -plane. Note the presence of eight- membered apertures.	132
52	Figure 3.7	View down the crystallographic <b>12</b> .	134
53	Figure 3.8	Temperature dependence of the DC-magnetic susceptibility of <b>12</b> measured at 100 Oe under FC and ZFC conditions. Inset shows the variation of inverse susceptibility.	135

54	Figure 3.9	Magnetization as a function of magnetic field at 2.5, 6 and 10 K.	135
55	Figure 3.10	<i>ac</i> -susceptibility as a function of temperature for a number of frequencies. Note that the position of the peak does not shift with frequency. (b) Specific heat data in the 2–25 K range.	136
56	Figure 3.11	Asymmetric unit of $[\text{NH}_4]_8[\text{Mn}_8(\text{SO}_4)_{12}]$ , <b>13</b> .	137
57	Figure 3.12	Top view of the layer parallel to the <i>ac</i> -plane of the unit cell in <b>13</b> .	139
58	Figure 3.13	PXRD patterns of compound <b>13</b> at different temperatures. The structure remains intact when it is heated at 350 °C.	140
59	Figure 3.14	Structure showing hydrogen bonding between adjacent –S-O-M-O-S- bridges in de-ammoniated compound $[\text{H}]_8[\text{Mn}_8(\text{SO}_4)_{12}]$ (b) Histogram showing the bond distances of Mn-O, and S-O for the ammoniated compounds $[\text{NH}_4]_8[\text{Mn}_8(\text{SO}_4)_{12}]$ , <b>13</b> and bond distances of Mn-O-[H] and S-O-[H] in the de-ammoniated compound $[\text{H}]_8[\text{Mn}_8(\text{SO}_4)_{12}]$ (c) Histogram showing O-H bond length and O-H···O bond angles in the de-ammoniated compound of $[\text{H}]_8[\text{Mn}_8(\text{SO}_4)_{12}]$ .	141
60	Figure 3.15	Fit of Murnagan equation of state to cohesive energy per atom calculated from first principles using PBE exchange-correlation to obtain equilibrium lattice constant.	143
61	Figure 3.16	Histogram showing the O-Mn-O and S-Mn-S bond angles of $[\text{NH}_4]_8[\text{Mn}_8(\text{SO}_4)_{12}]$ , <b>12</b> and their de-ammoniated products $[\text{H}]_8[\text{Mn}_8(\text{SO}_4)_{12}]$ .	144
62	Figure 3.17	Temperature dependence of the magnetic susceptibility of <b>13</b> measured at 1000 Oe. Inset shows the isothermal M–H cycles of <b>13</b> at 5 K.	145

63	Figure 3.18	Hydrogen adsorption isotherm for $[\text{NH}_4]_8[\text{Mn}_8(\text{SO}_4)_{12}]$ , <b>13</b> at 77 K.	146
64	Figure 3.19	(a) $\text{H}_2\text{O}$ vapour adsorption isotherm for <b>13</b> at 298 K. (b) Nyquist plot of the proton conductivity of <b>13</b> under relative humidity of 85% at 298 K.	147
65	Figure 3.20	PXRD patterns of $[\text{NH}_4]_8[\text{Mn}_8(\text{SO}_4)_{12}]$ , <b>13</b> (a) after and (b) before Impedance spectroscopy measurements under various RH at 298 K.	147
66	Figure 3.21	Experimental and simulated PXRD patterns: for $[\text{H}_3\text{O}][\text{MSO}_4\text{F}]$ [ $\text{M}=\text{Co}$ ( <b>9</b> ) and $\text{Ni}$ ( <b>10</b> )], $[\text{C}_4\text{N}_2\text{H}_{12}]_2[\text{Co}_3\text{F}_2(\text{SO}_4)_3(\text{H}_2\text{O})_2]$ , <b>12</b> and for $[\text{NH}_4]_8[\text{Mn}_2(\text{SO}_4)_{12}]$ , <b>13</b> .	158
67	Figure 3.22	TGA for $[\text{H}_3\text{O}][\text{CoSO}_4\text{F}]$ , <b>9</b> ; $[\text{H}_3\text{O}][\text{NiSO}_4\text{F}]$ , <b>10</b> ; $[\text{C}_4\text{N}_2\text{H}_{12}]_2[\text{Co}_3\text{F}_2(\text{SO}_4)_3(\text{H}_2\text{O})_2]$ , <b>12</b> and $[\text{NH}_4]_8[\text{Mn}_2(\text{SO}_4)_{12}]$ , <b>13</b> .	159
68	Figure 3.23	FTIR spectra for $[\text{H}_3\text{O}][\text{CoSO}_4\text{F}]$ , <b>9</b> ; $[\text{H}_3\text{O}][\text{NiSO}_4\text{F}]$ , <b>10</b> .and $[\text{C}_4\text{N}_2\text{H}_{12}]_2[\text{Co}_3\text{F}_2(\text{SO}_4)_3(\text{H}_2\text{O})_2]$ , <b>12</b> .	159
69	Figure 3.24	FTIR spectra of $[\text{NH}_4]_8[\text{Mn}_8(\text{SO}_4)_{12}]$ , <b>13</b> .	160

## (Part-2)

1	Figure 1.1	Schematic diagrams for the electrochemical supercapacitor.	165
2	Figure 1.2	CV curves for $\text{MoS}_2$ different scan rates (10, 25, 50,100 mV/s).	173
3	Figure 1.3	CD curves at different current densities for the $\text{MoS}_2$ in the 1 M KCl electrolyte.	174
4	Figure 1.4	Cyclic stability curves for the $\text{MoS}_2$ layers in the 1 M KCl electrolyte solution with 3000 cycles at the current density of 1 A/g.	174
5	Figure 1.5	EIS for $\text{MoS}_2$ layers at 1st and 100th cycle.	175

6	Figure 1.6	Schematic representation of a model for the electrical double-layers.	177
7	Figure 1.7	Electrical double-layer models at the interface of electrode and electrolyte solutions. (a) Diffusion layer of Gouy-Chapman model. (b) Helmholtz layer of model: $d$ represents the thickness of the double layer. (c) Stern-Grahame layer of model in which IHP represents the Inner Helmholtz plane and OHP represents the outer Helmholtz plane.	177
8	Figure 1.8	Layered structures of MCs. (a) Single nanocrystal are composed of multiple layers stacked along the $c$ -axis by weak van der Waals force. (b) Single layer of metal chalcogenides exists as various polymorphs. Each layer may have tri-, tetra- or penta-atomic layers of metal and chalcogen. (c) Rare GeS type of 2D layered metal chalcogenides.	181
9	Figure 2.1	(a) Low and (b) high magnification FESEM images of VS <sub>4</sub> /RGO <sub>1.5</sub> hybrid. (c) EDAX spectrum, atomic percentage and weight percentage of the elements.	203
10	Figure 2.2	Elemental analysis of VS <sub>4</sub> /RGO <sub>1.5</sub> . (a) Electron image of the hybrid over which the mapping has been done. Presence of (b) Carbon, (c) Sulfur and (d) Vanadium in the hybrid. (e) XRD pattern of VS <sub>4</sub> /RGO <sub>1.5</sub> showing prominent growth along (110).	203
11	Figure 2.3	Low (a) and high (b) magnified images of VS <sub>2</sub> micro flakes showing numerous protruding edges and (c) XRD pattern for VS <sub>2</sub> .	204
12	Figure 2.4	(a) XRD patterns for VS <sub>4</sub> /RGO hybrids containing 0.75 wt% (black), 1.5 wt% (blue) and 3 wt% (red) of RGO. (b) XPS showing C1s spectra for GO, RGO and VS <sub>4</sub> /RGO. (c) Raman spectra for GO, bare RGO and	204

RGO content in the hybrid with  $I_D/I_G$  ratio.

- |    |             |   |     |
|----|-------------|---|-----|
| 13 | Figure 2.5  | (a) CV curves for VS <sub>4</sub> /RGO_1.5 at different scan rates, (b) Specific capacitance vs scan rate showing a gradual decrease of capacitance at higher scan rates. (c) CD curves at different current densities and (d) Variation of capacitance with different values of current densities.   | 207 |
| 14 | Figure 2.6  | Supercapacitor data for VS <sub>4</sub> /RGO_0.75. (a) CV curves at different scan rates (b) plot between specific capacitance and scan rate, (c) CD curves at different current densities, (d) plot between specific capacitance and current density.  | 207 |
| 15 | Figure 2.7  | Supercapacitor data for VS <sub>4</sub> /RGO_3. (a) CV curves, (b) plot of specific capacitance against scan rate, (c) CD curves at different current densities, (d) specific capacitance vs current density plot.  | 208 |
| 16 | Figure 2.8  | (a) Supercapacitance data for VS <sub>2</sub> layers. (a) CV curves for VS <sub>2</sub> , (b) variation of specific capacitance with scan rate. (c) CD curves for different current densities symmetric curves depicting reversible redox (Faradic) reaction. (d) plot between specific capacitance and current density for VS <sub>2</sub> . | 208 |
| 17 | Figure 2.9  | Supercapacitor data for RGO. (a) CV curves, (b) graph showing variation of specific capacitance with scan rate, (c) CD curves at different current densities, (d) plot between specific capacitance and current density.  | 209 |
| 18 | Figure 2.10 | Supercapacitor performance of VS <sub>4</sub> /RGO_1.5 (red), VS <sub>4</sub> /RGO_3  | 209 |

		(blue), and VS <sub>4</sub> /RGO_0.75 (green). (a) CV curves, (b) comparison of capacitance vs scan rate and (c) Capacitance vs current density plot.	
19	Figure 2.11	(a) Ragone plot for VS <sub>4</sub> /RGO_1.5. (b) Last 5 cycles taken from the long cycle stability test to show no variation of symmetry in the CD pattern even after 1000 cycles. (c) Capacity retention of the hybrid showing much better stability even after 1000 cycles.	210
20	Figure 2.12	(a) Three electrode data (CV curves) for VS <sub>4</sub> /RGO_1.5 (red) and VS <sub>2</sub> (blue), (b) Ragone plot for VS <sub>4</sub> /RGO_0.75 (green), VS <sub>4</sub> /RGO_1.5 (red) and VS <sub>4</sub> /RGO_3 (blue). (c) Ragone plot comparison VS <sub>4</sub> /RGO_1.5 (red), RGO (blue) and VS <sub>2</sub> (green).	210
21	Figure 2.13	(a) Low and (b) high magnification FESEM images of VSe <sub>2</sub> /RGO_0.3 hybrid, (c) PXRD patterns for VSe <sub>2</sub> /RGO_0.3 hybrid and (d) EDAX spectrum.	212
22	Figure 2.14	(a) Low and (b) high magnification FESEM images of VSe <sub>2</sub> . (c) PXRD pattern for VSe <sub>2</sub> and (d) EDAX spectrum.	213
23	Figure 2.15	Supercapacitor performance of VSe <sub>2</sub> /RGO_0.3. (a) CV curves at different scan rates, (b) plot between specific capacitance and scan rate, (c) CD curves at different current densities and (d) plot between specific capacitance and current density.	214
24	Figure 2.16	Comparison of capacitance vs. current density.	214
25	Figure 2.17	Ragone plot for VSe <sub>2</sub> /RGO_0.3 hybrid.	215
26	Figure 3.1	Low (a) and high (b) magnified FESEM images of VS <sub>4</sub> /CNTs/RGO.	228

(c) EDAX spectroscopy showing the characteristic peaks for constituents of the hybrid with the atomic and weight percentage of the constituent elements.

27	Figure 3.2	Elemental mapping data of VS <sub>4</sub> /CNTs/RGO hybrid. (a) Electron image of the region of the sample for which mapping has been done showing the presence of elemental carbon (b), oxygen (c), sulphur (d) and vanadium (e).	229
28	Figure 3.3	PXRD patterns for VS <sub>4</sub> /CNTs/RGO.	230
29	Figure 3.4	PXRD patterns for RGO (yellow), CNTs (blue), and CNTs/RGO (red).	231
30	Figure 3.5	PXRD patterns for VS <sub>2</sub> .	231
31	Figure 3.6	Comparison of PXRD patterns for VS <sub>4</sub> /CNTs, VS <sub>4</sub> /RGO and VS <sub>4</sub> /CNTs/RGO.	232
32	Figure 3.7	CV data for the hybrid VS <sub>4</sub> /CNTs/RGO at (a) slower scan rates (i.e. 1 mV/s, 2 mV/s and 5 mV/s) and (b) fast scan rates (i.e. 10, 20, 40, 100 and 200 mV/s). (c) CD curves of the hybrid at different values of current densities.	233
33	Figure 3.8	Variation of specific capacitance with (a) scan rate and (b) current density. (c) Retention capability/ cyclic stability of the hybrid represented by the graph between cycle number and capacity retention in percentage with inset showing the long cycle data.(d) Ragone plot for the hybrid VS <sub>4</sub> /CNTs/RGO.	234
34	Figure 3.9	CV and (b) CD data for VS <sub>2</sub> . Variations of specific capacitance with (c) scan rate and (d) current density.	236

35	Figure 3.10	Two-electrode data for RGO. (a) CV and (b) CD curves along with graphs showing variation in specific capacitance value with (c) scan rate and (d) current density.	236
36	Figure 3.11	Two-electrode data for CNTs showing (a) CV and (b) CD curves. (c) and (d) show the variation of specific capacitance with scan rate and current density, respectively.	237
37	Figure 3.12	Two-electrode data for CNTs/RGO. (a) CV and (b) CD curves. (c) and (d) respectively show different values of specific capacitance at different scan rate and current density.	237
38	Figure 3.13	Two-electrode measurement data for VS <sub>4</sub> /RGO. (a) CV and (b) CD curves. Variations of specific capacitance with (c) scan rate and (d) current density.	238
39	Figure 3.14	Two-electrode data for VS <sub>4</sub> /CNTs. (a) CV and (b) CD curves. Variations of specific capacitance with (c) scan rate and (d) current density have been illustrated.	238
40	Figure 3.15	Graphs showing variation of capacitance with (a) scan rate and (b) current density for VS <sub>2</sub> , RGO, CNTs, CNTs/RGO, VS <sub>4</sub> /RGO, VS <sub>4</sub> /CNTs and VS <sub>4</sub> /CNTs/RGO.	239
41	Figure 3.16	Comparison of power densities and energy densities of VS <sub>2</sub> , RGO, CNTs, CNTs/RGO, VS <sub>4</sub> /RGO, VS <sub>4</sub> /CNTs and VS <sub>4</sub> /CNTs/RGO using a typical Ragone plot.	239

## List of Tables

### (Part-1)

1	Table 2.1	Synthetic conditions of compounds <b>5-8</b>	79
2	Table 2.2	Crystal data structure refinement parameters for <b>1-8</b> compounds.	109
3	Table 2.3	The Hydrogen Bonding Interactions for the compound <b>1-4</b>	112
4	Table 2.4	The Hydrogen Bonding Interactions for the compound <b>5-8</b>	113
5	Table 3.1	Lowdin charges for semicore and valance orbitals of atoms	144
6	Table 3.2	Crystal data structure refinement parameters for <b>9-11</b>	156
7	Table 3.3	Crystal data structure refinement parameters for <b>12-13</b>	157
8	Table 3.4	The Hydrogen Bonding Interactions for $[C_4N_2H_{12}]_2[Co_3F_2(SO_4)_3(H_2O)_2]$ , <b>12</b>	158

### (Part-2)

1	Table 1.1	Comparison of the properties and performance of Battery, Capacitor and supercapacitor	165
2	Table 2.1	Comparison of supercapacitor performance of $VS_4/RGO_{0.75}$ , $VS_4 / RGO_{1.5}$ , $VS_4/RGO_3$ , RGO and $VS_2$	211
3	Table 2.2	Comparison of supercapacitor performance of $VS_4/RGO_{1.5}$ with the reported metal sulfides/graphene hybrids	211
4	Table 3.1	Comparison data of supercapacitive performance of all the samples	240
5	Table 3.2	Comparison of supercapacitive performance of $VS_4/CNT/RGO$ with those reported in other literatures	241

## List of Abbreviations

PBU <sub>s</sub>	Primary bulding units
SBU <sub>s</sub>	Secondery bulding units
AlPO <sub>4</sub> <sub>s</sub>	Aluminophosphates
AlSiO <sub>4</sub> <sub>s</sub>	Aluminosilicates
DACH	Diamino cyclohexane
SDA	Structure directing agent
SHG	Second hormonic generation
PIP	Piperzine
bipy	4, 4' bipyridine
en	Ethylene diamine
DETA	Diethylenetriamine
1, 5-pda	1, 5-pentadamine
DABCO	1, 4-diaza bicycle [2, 2, 2] octane
EG	Ethylene glycol
DMF	Dimethyl formamide
DMA	Dimethyl acetamide
TGA	Thermogravmetric analysis
PXRD	Powder X-ray diffraction
SXRD	Single crystal X-ray diffraction
FTIR	Fourier transform infrared
SQUID	Sperconducting quantum device

EDAX	Energy dispersive analysis of X-rays
1,3-dap	1, 3-Diaminopropane
1,4-dab	1, 4-Diaminobutane
BVS	Bond valance sum
TCSPC	Time-corelated single-photon counting
FWHM	Full width half maximum
RH	Relative humidity
3D	Three-dimensional
2D	Two-dimensional
ZFC	Zero field-cooled
FC	Field-cooled
DFT	Density functional theory
LC	Lowdin charges
SC	Supercapacitor
$P_d$	Power density
$E_d$	Energy density
PPC	Propylene carbonate
ILs	Ionic liquids
CNTs	Carbon nanotubes
RGO	Reduced graphene oxide
TMOs	Transition metal oxides
CPs	Conducting polymers
PANI	Polyaniline

PPY	Polypyrrole
CV	Cyclic voltammetry
CCCD	Constant current charge/discharge
EIS	Electro chemical impedance spectroscopy
EDLC	Electrical double-layer capacitance
PC	Pseudocapacitance
PCS	Pseudocapacitance supercapacitor
HS	Hybrid supercapacitors
MCs	Metal chalcogenides
TMDCs	Transition metal dichalcogenides
CVD	Chemical vapor deposition
SWCNTs	Single walled carbon nanotubes
MWCNTs	Multi walled carbon nanotubes
GCE	Glassy carbon electrode
DI	De-ionized

## **Part-1**

### **Investigations of Open-Framework Metal Sulfates**

# CHAPTER-1

## Open-Framework Materials: A Brief Overview

<b>1.1</b>	Introduction	40
<b>1.2</b>	Zeolites and Zeolite like materials	40
<b>1.3</b>	Aluminosilicate Zeolites	43
<b>1.4</b>	Open-framework metal phosphates	46
<b>1.4.1</b>	Transition metal phosphates	47
<b>1.5</b>	Open-framework metal sulfates, selenate and selenites	49
<b>1.5.1</b>	Open-framework metal sulfates	49
<b>1.5.2</b>	Open-framework metal selenites	51
<b>1.5.3</b>	Open-framework metal selenates	52
<b>1.6</b>	Templating agents	53
<b>1.7</b>	Mineralizing agents	55
<b>1.8</b>	Mechanism of the formation of open-framework materials	55
<b>1.9</b>	Hydrothermal approach for the synthesis of Zeolites	57
<b>1.10</b>	Synthetic techniques for open-framework materials	59
<b>1.10.1</b>	Hydro/solvothermal method	59
<b>1.10.2</b>	Solvent diffusion method	61
<b>1.10.3</b>	Slow evaporation method	61
<b>1.10.4</b>	Sealed tube method	61
<b>1.10.5</b>	Microwave method	61
<b>1.11</b>	Characterization tools and techniques	62
<b>1.11.1</b>	Thermogravimetric analysis	62
<b>1.11.2</b>	Single crystal X-ray diffraction	63
<b>1.11.3</b>	Powder X-ray diffraction	64
<b>1.11.4</b>	Fourier transform infrared spectroscopy	64
<b>1.11.5</b>	Surface area and adsorption analysis	65
<b>1.11.6</b>	Superconducting quantum interference device	66
<b>1.12</b>	Future direction	67
<b>1.13</b>	References	68

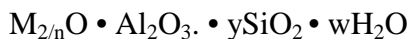
## 1.1 Introduction

The synthesis of inorganic materials with open architecture is one of the major activities in contemporary solid state chemistry for their applications in the areas of catalysis, ion-exchange, separation and sorption process.<sup>1-3</sup> At the bottom of the synthesis of such structures lies the idea of rational design that involves the assemblage of small molecular units to obtain the desired solid. Open-framework materials often referred to as molecular sieves or microporous materials are a class of inorganic solids, which possess regular pores, or void in the size range 5-20 Å. During the last two decades or so large number of new materials with novel architectures have been synthesized and characterized. Attempts are being made to exploit some of the exciting properties of the newly discovered open-framework systems and the results appear to be promising. In this chapter we have includes a brief history and summarize the various types of inorganic open-framework materials and their properties.

## 1.2 Zeolites and Zeolite like materials

Microporous materials such as open-framework materials, metal-organic frameworks (MOFs), covalent-organic frameworks (COFs) with having pore diameter  $< 2 \text{ \AA}$  are great interest because of their broad applications in industrial purpose. Among all these, open-framework inorganic materials (Zeolite, phosphates, sulfates arsenates *etc*) are great interest due to their interesting pore structures and surface area. Zeolites are the oldest open-framework materials, which were discovered in 1756 Swedish mineralogist A. F. Cronstedt.<sup>4</sup> When he was heating the silicate mineral “*Stilbite*” it produced large amounts of steam from water that has been adsorbed the material, based on this he called Zeolite. Zeolite word came from Greek word *Zeo* means “*boil*” litho means “*stone*”.

Zeolites are crystalline aluminosilicates ( $\text{AlSiO}_4\text{s}$ ) of a group IA and group IIA elements of sodium, potassium, magnesium and calcium. Chemically Zeolites are represented by the following formula



Where M = IA or IIA group elements, n is the cation valance, y is varies from 2 to 10 and w represents the no of water molecules presents in the voids of the Zeolite.

Zeolites are formed by three-dimensional (3D) four-connected framework of  $\text{TO}_4$  (T = Al, Si, P, S) tetrahedra linked through the corner sharing of oxygen atoms. These  $\text{SiO}_4$ ,  $\text{AlO}_4$ ,  $\text{PO}_4$  tetrahedra are the primary building unit (PBU) of the Zeolite frameworks. Zeolites form uniformly sized pores of molecular dimensions. The preferentially adsorb molecules that are fit in to pores and neglect the molecules which are large. So these molecules act as molecular sieves. In Zeolites, at some places  $\text{Al}^{3+}$  has been replaced by the  $\text{Si}^{4+}$  atoms. So the Charge neutrality of the framework was balanced by the loosely held positive charged ions which are present in the voids. These positive ions can be utilized for the ion exchange process.<sup>5</sup>

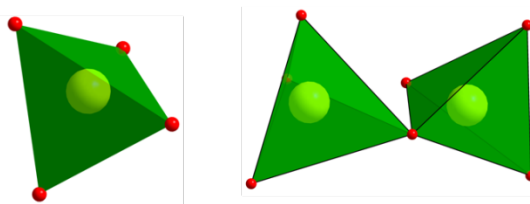


**Figure 1.1.** PBUs of Zeolites (a)  $\text{TO}_4$  tetrahedra, (b)  $\text{TO}_4$  tetrahedra sharing common vertex with oxygen atoms (where T=Si, P, Al and S).

The framework of Zeolites formed by the infinite component units or infinite component units like-chains (Figure 1.2) and layers (Figure 1.3) called as secondary building units (SBUs). In one type of framework can contain different types of SBUs *i.e* It is not necessary to contain only one type of SBUs.

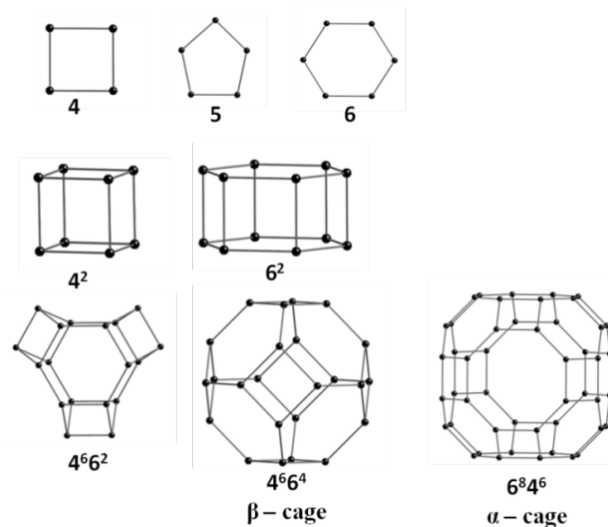


**Figure 1.2.** SBUs with different number of tetrahedral cations. Codes are given below.

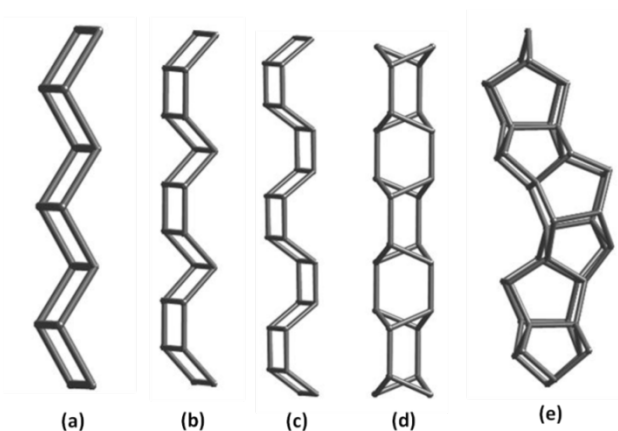


**Figure 1.3.** Some important chains that occur in several Zeolite frameworks (a) Double zig-zag chain, (b) double sawtooth chain, (c) double crankshaft chain, (d) narsarsukite chain, (e) pentasil chain.

## Applications of Zeolites

Zeolites contribute to a cleaner, safer environment in a great number of ways. In fact nearly every application of Zeolite has been driven by environmental concern, or plays a significant role in reducing toxic waste and energy consumption.

(1) Zeolites can be used as catalyst for chemical reactions due to their unique pore size and proton which is bounded to framework used for increasing the acidity. This is exploited in many chemical reactions, Oil refinements (Crude oil cracking), isomerisation and fuel synthesis. Zeolites can be used for oxidation and reduction reactions *i.e.* Titanium ZSM-5 can be used for the production of caprolactam, and copper Zeolites used in the  $\text{NO}_x$  decomposition.

(2) Zeolites have loosely bounded cationic ions which are more often used for the exchange properties. This is exploited in softening of water where the hard metal atoms (Calcium or Magnesium) can be exchanged with soft metal atoms (Na or K) which are present in the voids.

(3) Zeolites can be used for adsorption and separation of the gaseous mixtures due to their shape-selectivity properties and high surface area. The framework preferentially adsorbed the gas having diameter which are matches with pore diameter of Zeolite.<sup>4,6</sup>

### 1.3 Aluminosilicate Zeolites

Zeolites are crystalline  $\text{AlSiO}_4$  with three-dimensional framework structures. Depends upon the composition of Si/Al ratio,  $\text{AlSiO}_4$  Zeolites are classified as four types.<sup>5</sup>

(1) Low Zeolite: The ratio of Si/Al ratio range between 1-1.5. Zeolite A, X comes under low Zeolite. (2) Intermediate Zeolite: The ratio of Si/Al ratio range between 2 to 5. Natural Zeolite (erionite, clinoptilolite etc) and synthetic Zeolite (Zeolite Y, L etc) are comes under intermediate Zeolite. (3) High Zeolite: The ratio of Si/Al rage between 10 to100. The natural synthesized ZSM-5 and beta comes under high Zeolite. (4) Silica molecular sieves which are silicalite come

under this category. The thermal stability increase from about 700 °C in the low Zeolite to 1300 °C for the silica molecular sieves. The surface selectivity, which is hydrophilic nature in low Zeolite and hydrophobic nature in high silica Zeolites and silica molecular sieves. The acidity tendency was increases with increasing Si/Al ratio. As the concentration of Si/Al ratio increase the cation concentration and ion exchange properties decrease. Generally low silicate Zeolites formed with 4-, 6-, and 8- membered rings of tetrahedra. In the intermediate Zeolite we see the one set of 5- membered tetrahedra. High silica Zeolite and the silicate molecular sieves are formed with predominance of 5- rings of tetrahedra. Here we have given two different types of  $\text{AlSiO}_4$  Zeolites.



As with LTA, the FAU framework also featured by sodalite cages. In FAU Zeolite, the sodalite cages are arranged same way as the carbon atoms in diamond. This is one of the reason these materials are thermally stable.<sup>7</sup>



**Figure 1.4.** Structure of Zeolite FAU type framework.<sup>8</sup>

These materials are formed by connecting the  $\beta$ - cages through 6- membered rings, producing the so-called supercages with four, tetrahedral oriented 12- ring pore openings (Figure 1.4). Si/Al ratio of the FAU was greater than one. FAU frame work was formed with three-dimensional channel system with free aperture is  $7.4 \times 7.4 \text{ \AA}$ .



Zeolite ZSM-5 formed with orthorhombic arrangement. The number of Al atoms in the unit cell can vary from 0-27, so the ratio of Si/Al ratio can be changed. This framework contains characteristic  $5^8$  units. These  $5^8$  units linked via edge sharing to form a pentasil chain parallel to  $c$ -axis (Figure 1.5). These pentasil chains related by a mirror plane are connected via oxygen bridges to form corrugated 10- ring channels ( $5.5 \times 5.1 \text{ \AA}$ ). Adjacent sheets that are related by an inversion center are linked by oxygen bridges to the next, forming a three-dimensional framework. Zeolite-11 framework is closely related to ZSM-5. The corrugated pentasil chains that are found in ZSM-5 are also present in the ZSM-11 framework. However, in ZSM-11, the adjacent sheets are related to one other by a mirror plane instead of an inversion center as in ZSM-5 by mirror planes.<sup>7</sup>

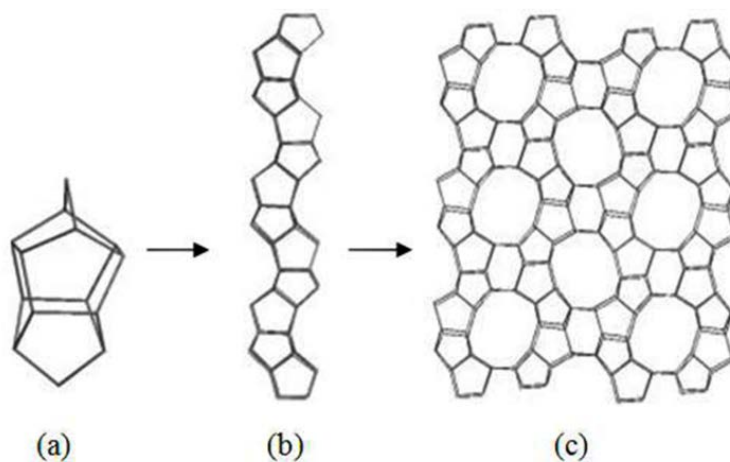


**Figure 1.5.** Structural units in ZSM-5 (a)  $5^8$  units, (b) pentasil chains which are present in ZSM-5 and (c) view of ZSM-5 with 10- ring channels.<sup>8</sup>

## 1.4 Open-framework metal phosphates

In 1982, Wilson, Lok, and Flanigen *et al*<sup>9</sup> synthesized novel family of molecular sieves called aluminophosphates (AlPO<sub>4</sub>s). AlPO<sub>4</sub> materials are similar to Zeolites with crystalline microporous 3D-polymeric structures but the difference in chemical composition. The discovery of AlPO<sub>4</sub>s is novel milestone for the development of other microporous materials. The pores of the Zeolites and AlSiO<sub>4</sub>s are narrow. Only limited space is available for industrial applications. To improve the porosity, numbers of microporous crystalline AlPO<sub>4</sub>s are widely reported and applied in catalysis and adsorption studies.<sup>10-15</sup> These materials are fine tuned to obtain ordered porosity by using larger organic amines or quaternary ammonium cations as templates during the synthesis.<sup>16-17</sup> Not only large-, medium-, and small pore AlPO<sub>4</sub>s molecular sieves prepared, but also SAPO (S=Si),<sup>18</sup> MAPO (M= Fe, Mg, Zn, Co *etc*),<sup>19-21</sup> MASO, EAPO (E= Ba, Ga, Ge, Li, As *etc*) and EAPSO<sup>22</sup> could be also obtained through the introduction of the elements other than the Al and P in to the microporous frameworks of AlPO<sub>4</sub>s. At present 200 numbers of AlPO<sub>4</sub>s based microporous materials are known. These compounds can be synthesized through the hydro or solvothermal synthesis by introducing the Al, P and other material sources. The main drawback of the AlPO<sub>4</sub>s is thermally unstable and structure get collapse after removal of the template during their calcination. It is difficult to synthesize the materials with Al/P ratio equal to 1. Generally, acidic-basic properties of the AlPO<sub>4</sub>s depend up on the ratio of the Al/P ratio.

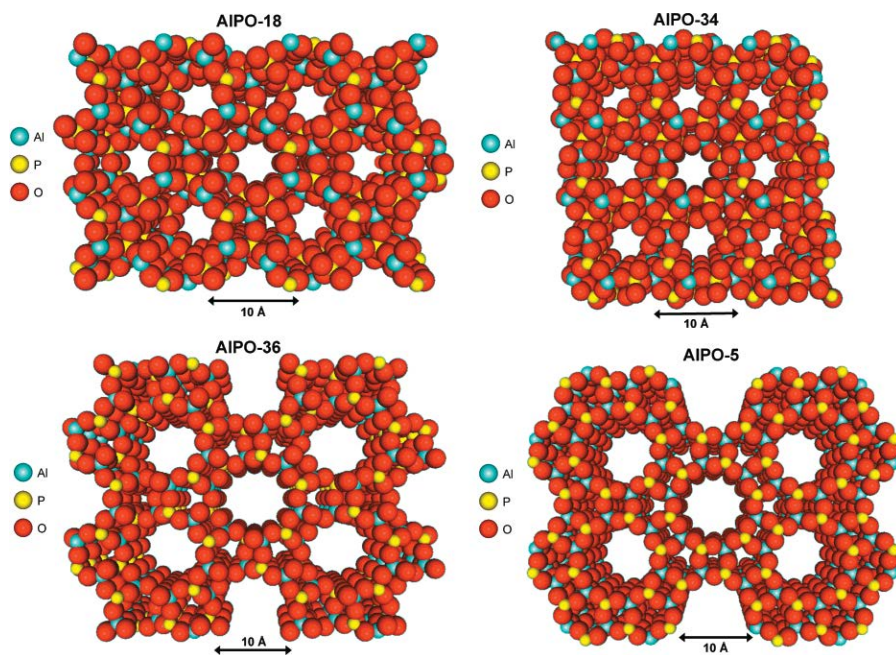


**Figure 1.6.** Schematic diagrams of  $\text{AlPO}_4$ -18,  $\text{AlPO}_4$ -34,  $\text{AlPO}_4$ -36 and  $\text{AlPO}_4$ -5 Aluminophosphate molecular sieves with three-dimensional narrow pore structures.<sup>13</sup>

Till now maximum number of reports on SAPO-34<sup>18, 22-25</sup> because of their narrow pore openings, easy to synthesize and high purity of synthetic products. Takeguchi *et al*<sup>26</sup> recently reports the incorporated  $\text{Cu}^{2+}$ ,  $\text{Fe}^{3+}$ ,  $\text{Ni}^{2+}$  into the SAPO-34 framework to separate the  $\text{CO}_2$  from the  $\text{N}_2$  and  $\text{CO}_2$  gaseous mixture.

#### 1.4.1 Transition metal phosphates

Due to the thermal unstableness of  $\text{AlPO}_4$ s and increasing the demand of industrial applications peoples are start to search the other phosphate framework materials. Many attempts are made to introduce the heteroatom in the microporous materials. Compared to other heteroatom, transition metal atoms are good due their attractive properties like catalysis and magnetic properties. Transition metal atoms have flexible coordination which can lead to the structural diversity of the framework. Here we had shown the some of the reported metal phosphates with their structural dimensionalities.

**[Zn<sub>3</sub>(PO<sub>4</sub>)<sub>2</sub>(PO<sub>3</sub>H)(H<sub>2</sub>DACH)].2H<sub>2</sub>O (DACH=1,2-diaminocyclohexane)(ND-1)**

ND-1 contains 24- ring channels. It crystallizes in the rhombohedral space group R-3. The anionic polymer of ND-1 was formed by ZnO<sub>4</sub> tetrahedra and PO<sub>4</sub> tetrahedra via corner sharing of oxygen atoms. Anionic layer of ND-1 exit μ<sub>3</sub>-O atoms by connecting the two Zn atoms and one P atom.<sup>27</sup> The three-dimensional framework of compound ND-1 contains 24- ring channels close-packed in hexagonal, honeycomb arrays, which are oriented parallel to the *c*-axis shown in the Figure 1.7. P-OH groups are oriented towards the center of channels. The extra amine guest (DACH) and water molecules are present near walls of the polymers.

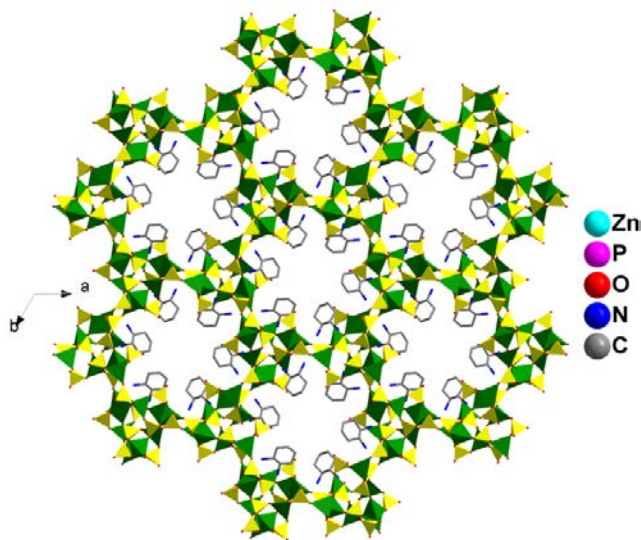


**Figure 1.7.** Structure of ND-1 viewed along *c*-axis with 24- ring channels.

**[(C<sub>4</sub>N<sub>3</sub>H<sub>16</sub>)(C<sub>4</sub>N<sub>3</sub>H<sub>15</sub>)] [Fe<sub>5</sub>F<sub>4</sub>(H<sub>2</sub>PO<sub>4</sub>)(HPO<sub>4</sub>)<sub>3</sub>(PO<sub>4</sub>)<sub>3</sub>].H<sub>2</sub>O**

This compound was prepared by hydrothermal method by using DETA as SDA. Compound was crystallized with monoclinic with space group P2<sub>1</sub>/n. The anionic framework formed by corner sharing of FeO<sub>6</sub>, FeO<sub>5</sub>F and FeO<sub>4</sub>F<sub>2</sub> octahedra and PO<sub>4</sub> tetrahedra with 3D-framework with unusually large 24- membered rings shown in the Figure 1.8. The extra protonated amine

molecules reside in the channels through hydrogen bond for making the charge balance and acquiring the extra stability of the polymer. This polymer shows spin-crossover behavior.<sup>28</sup>

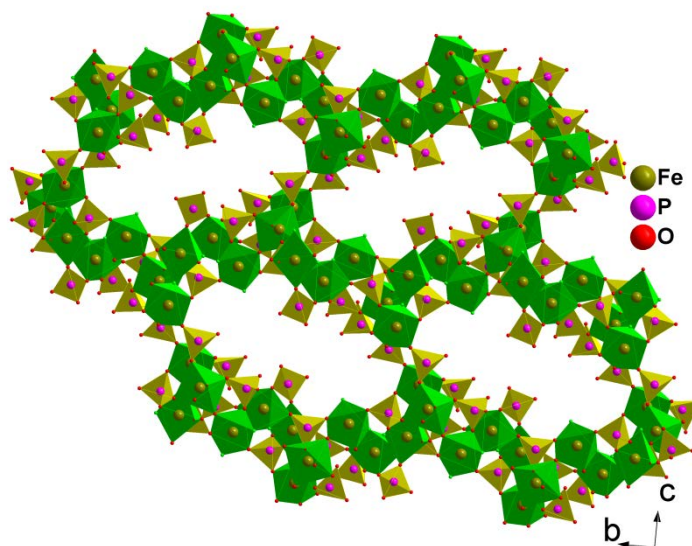


**Figure 1.8.** The anionic layer of  $[(C_4N_3H_{16})(C_4N_3H_{15})][Fe_5F_4(H_2PO_4)(HPO_4)_3(PO_4)_3] \cdot H_2O$ , showing the one-dimensional Fe-O/F-Fe chains and their connectivity with the  $PO_4$  units.

## 1.5 Open-Framework metal Sulfates, Selenite and Selenates

The research work on transition metal and rare earth metal based open-framework materials with sulfate, selenite and selenates are serving as linkers has been explored in the literature.<sup>29-32</sup>

Several of the frameworks with good adsorption, magnetic, ion exchange, catalytic properties have been studied extensively.<sup>33-35</sup> Here we have given few of the examples from literature.

### 1.5.1 Open-framework metal Sulfates

In Sulfate ions, Sulfur atom has tetrahedral coordination like in silicates, phosphates, arsenates etc. Using this analogy there has been considerable interest to study sulfate-based open-framework materials. Nevertheless, there are some difficulties to overcome. The S-O bonds have less charge (0.5) than the P-O bonds (0.75), which could create difficulties in forming extended network structures. In addition, the  $SO_4^{2-}$  ions may be similar to  $C_2O_4^{2-}$  ions and have similar

reactivity.<sup>32, 36</sup> The S-O bonds are also less covalent and thus poly sulfate units are less readily formed than polyborates, -phosphates, and -silicates. In spite of these issues, there are only few reports of open-framework sulfate structures with different dimensionalities. So, we are interested to explore the open-framework metal sulfates. Most of the sulfate structures are prepared employing a large excess of fluoride ions to form an M-O/F-M network, which forms the basis for all the structures. The sulfate anions generally link the M-O/F-M network. Here we had shown one of the example reported metal sulfate framework with their crystallographic signature.

### **[C<sub>4</sub>N<sub>2</sub>H<sub>12</sub>][Ni<sub>2</sub>F<sub>4</sub>(SO<sub>4</sub>)H<sub>2</sub>O]**

The three-dimensional framework of the compound [C<sub>4</sub>N<sub>2</sub>H<sub>12</sub>][Ni<sub>2</sub>F<sub>4</sub>(SO<sub>4</sub>)H<sub>2</sub>O]<sup>34</sup> formed by edge sharing of NiF<sub>4</sub>O<sub>2</sub> octahedra and SO<sub>4</sub> tetrahedra. The Ni(1) and Ni(2) octahedral units share edges through fluorine (Ni(1)-F(1), F(2) and Ni(2)-F(3), F(4)) to form the dimer units of Ni<sub>2</sub>(1)F<sub>6</sub>O<sub>2</sub>(H<sub>2</sub>O)<sub>2</sub> and Ni<sub>2</sub>(2)F<sub>6</sub>O<sub>4</sub> respectively. The dimers are linked by sharing octahedral edges to form two distinct infinite sinusoidal chains along the [001] direction. These chains are alternately stacked one over the other along the [100] direction and are interlinked by sharing corners with the tetrahedral corners of the SO<sub>4</sub> groups to form a layer with an 11- membered aperture in the [101] plane. The protonated amine molecules reside within the pores shown in the Figure 1.9.

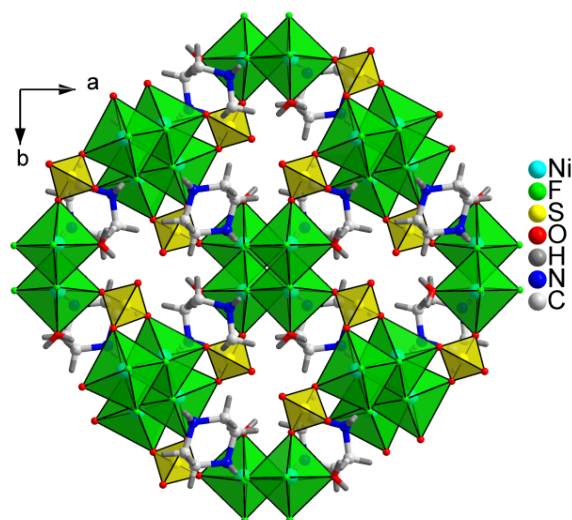
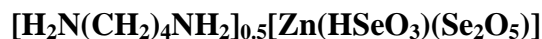


**Figure 1.9.** View of 3D-framework of  $[C_4N_2H_{12}][Ni_2F_4(SO_4)H_2O]$  with 11- membered apertures in  $[101]$  plane.

### 1.5.2 Open-framework metal selenites

Open-framework selenite based materials are great interest because of their invisible lone pair of electrons which can acts as SDA. Due to the presence of lone pair of electrons these materials crystallize in non-centrosymmetric structures give rise to interesting physical properties such as non-linear optical second harmonic generation (SHG).<sup>32, 36</sup> Due to the low reduction potential difference of  $Se^{IV}/Se^0$ , Selenite can be easily converted to metallic Se in hydrothermal method. Hence, reports on open-framework metal selenite are less explored. Here we have shown crystal structure for one of the reported metal selenite.



The three-dimensional framework of the compound  $[H_2N(CH_2)_4NH_2]_{0.5}[Zn(HSeO_3)(Se_2O_5)]$ <sup>37</sup> was synthesized by hydrothermal method in the presence of PIP as template. This compound was formed by two-dimensional sheets which are made up of  $ZnO_6$  octahedra and the diselenite units. The  $ZnO_6$  dimers are bridged by two diselenite units through  $-Zn-O-Se-O-Zn-$  linkages, which create a four- membered ring propagating in a zig-zag fashion in the  $bc$ -plane. The four

membered rings are fused by the diselenite units in a head to tail fashion (-Zn-O-Se-O-Se-O-Zn) by satisfying the coordination of the diselenite unit, creating a six- membered ring. Each ZnO<sub>6</sub> octahedron is connected to an adjacent layer of ZnO<sub>6</sub> octahedron through two selenite units, leaving a terminal Se-OH bond. This connectivity results a 10- membered two-dimensional channels in *bc*-plane. The protonated amine molecules are resides in the 10- membered ring channels shown in Figure 1.10 for acquiring the extra stability of the polymer.

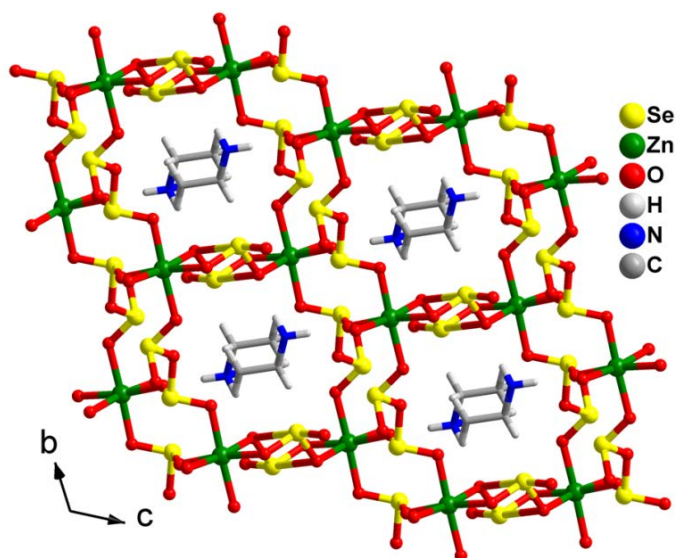


**Figure 1.10.** Inorganic-framework structure of  $[H_2N(CH_2)_4NH_2]_{0.5}[Zn(HSeO_3)(Se_2O_5)]$  formed with 4 and 10- membered ring channels in *bc*-plane and the amine molecules are resides in the 10- membered ring channels.

### 1.5.3 Open-framework metal selenates

Open-framework materials with selenate and selenite have been explored in literature. Selenate containing open-frameworks is not well known. Unlike the sulfur in sulfite +4 oxidation state is more stable for selenium (selenites) due to inert pair effect; hence the selenate is difficult to be stabilized in framework system. So, reports on metal selenates not explored much compared with selenite, phosphate and sulfates. Here we have shown one example of reported metal selenate with their crystal structure.

**[H<sub>2</sub>bipy][Zn(SeO<sub>4</sub>)(H<sub>2</sub>O)]** (bipy = 4, 4' bipyridine)

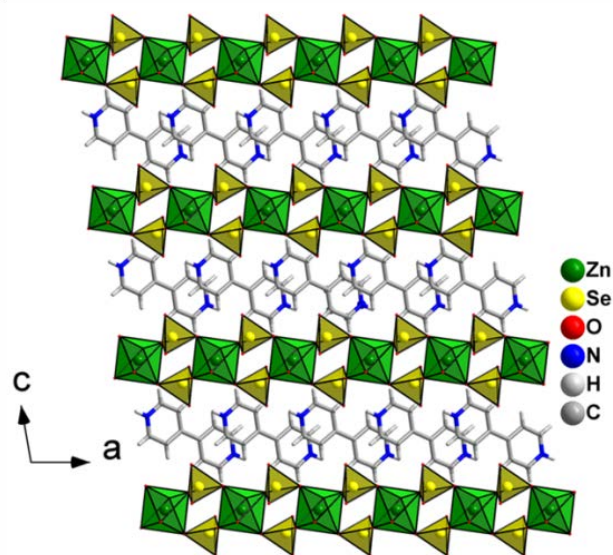


**Figure 1.11.** View of the structure of the compound [H<sub>2</sub>bipy][Zn(SeO<sub>4</sub>)(H<sub>2</sub>O)] in *ac*-plane.

The linear chain of the compound [H<sub>2</sub>bipy][Zn(SeO<sub>4</sub>)(H<sub>2</sub>O)]<sup>38</sup> was synthesized by solvothermal method where H<sub>2</sub>bipy acts as template. The anionic chain of this compound was formed by two neighbouring Zinc octahedra are bridging between the pair of selenate tetrahedra via corner-sharing to form a 4- membered chains along *a*-axis. These neighbouring chains are further interlinked by [H<sub>2</sub>bipy]<sup>2+</sup> cations via strong hydrogen bond through N-H···O forms 2D-layer in *ac*-plane shown in the Figure 1.11.

## 1.6 Templating agents

During synthesis of open-framework materials some additional compounds are added which goes to the porous cavity of material during the reaction and crystallizes along with. This approach has proven good in synthesizing these materials with ease. The templating agent commonly known as SDA used for the purpose of stabilizing the structure, charge balances, directing the size and shape of pore. Computational studies have concluded<sup>39-42</sup> the role of

templating agents in directing the size of porous cavity. These are held inside the cavity through ionic, hydrogen bonding or van der Waals interactions. After the formation of framework material templating agents can be removed by thermal treatment. Commonly used templating agents in our laboratory are protonated amines, say ethylenediamine (en), 1, 5-pentanediamine (1, 5-pda), diethylenetriamine, cyclohexylamine, cyclopentylamine, 1, 4-diaza bicycle [2, 2, 2] octane (DABCO) and piperazine etc. The choice of selection of particular templating agent is dependent on the ligand which is going to be used. For example, for lengthy ligand the size of the template should also be large such that it can make significant interaction with the moieties of the cavity. Smaller ligand in such case may stick to side way of the cavity or more number of templates can occupy the cavity.<sup>43</sup> A template can make interaction from one or more than one site. For example ethylenediamine in diprotonated form can interact from both the ends and DETA can form from three protonated nitrogen ends.

A templating agent serves the purpose of charge balance, directing the structure of pores, stabilizing the structure through electrostatic interaction. The size of the cavity sometimes is highly influenced by the choice of SDA. Large sized SDA can lead to large pore size.<sup>44</sup> The protonated amines balance the charge of the overall complex. Some of the frameworks are not stable and generally collapse, if SDA occupies the cavity, the structure is stabilized and SDA present in the cavity doesn't allow the framework to collapse. Figure 1.12 shows how a template is occupying the porous cavity.

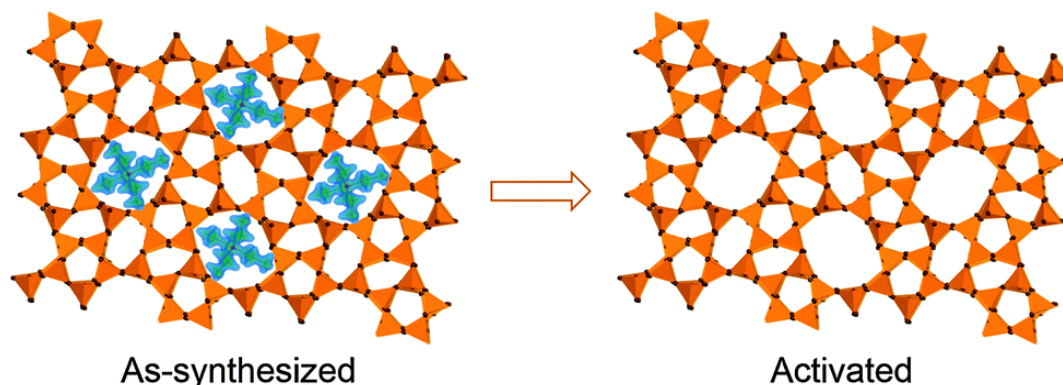


**Figure 1.12.** (a) Amine molecules inside the pores of the frameworks color code: blue; amine molecules; yellow; framework material (b) After activation of the framework material.

### 1.7 Mineralizing agents

Mineralizer is facilitates the lowering of crystallization kinetics that they induces indeed to give more homogeneous and crystallized phase. Generally Fluoride ( $F^-$ ) ion is used as mineralizer for the synthesis of open-framework materials. Flanigen and Patton were first used  $F^-$  ion as mineralizer for the synthesis of silicalite-I.<sup>45</sup> For the  $F^-$  ion, general sources are hydrofluoric acid (HF), Sodium fluoride (NaF), and Potassium fluorides (KF) etc are used. Mineralizer plays a several roles for the synthesis of microporous compounds which are (1) enabling the crystallization by changing the pH (3~10). (2) Balancing the positive charge of SDA, which would, reduces the framework defects created by the positive charge SDAs. (3) Helping the transition metal atoms enter the framework via the formation of a complex. (4) By using the mineralizer we can get different kind of structural frameworks. (5) Sometimes mineralizer can act as SDA for stabilizing the framework which can sit between the cavities of the framework.<sup>5</sup>

### 1.8 Mechanism of formation of open-frame work materials

Crystalline molecular sieves are usually synthesized by hydrothermal method by taking the mixture of water, a source of T atoms (T= Al, Si, P, and S *etc*), a mineralizing agent (Generally  $OH^-$  or  $F^-$ ) and SDAs. All these reagents are mixed well and heated ( $< 200\text{ }^\circ\text{C}$ ) and, over time, formed a self assembled crystalline Zeolite structures. Till now there is numerous number of

Zeolite structures have been synthesized successfully. It is still necessary to design and synthesis of more new Zeolite structures with specific architectures and properties. For that we need a full understanding of the crystallization process and mechanism for the formation Zeolites.<sup>5</sup> The procedure for the synthesis of Zeolites is not complicated but the crystallization mechanism involved is very complicated. Till now numerous groups have investigated the assembly process of Zeolite synthesis. So far, there is no well expected mechanism for the formation of Zeolite crystals. In 1990s Regev and co-workers,<sup>46</sup> Schoeman,<sup>47</sup> Thompson and co-workers,<sup>48</sup> and Iton and White and their co-workers<sup>49</sup> monitored Zeolite synthesis by *in situ* methods. It is impossible to isolate the intermediate products due to their weak interactions between them. So, conduction of *In situ* method is essential for the synthesis of crystalline Zeolite materials. Breck<sup>50</sup> has given first time for the mechanism of the crystallization called Solid-phase mechanism or solid-hydrogel transformation mechanism. He proposed that gel structure was firstly depolymerized and then the polyhedral formed through the rearrangement of  $AlSiO_4$ s and silicate anions in the gel. These polyhedral connect to form Zeolite framework. Beside this mechanism another mechanism called solution-mediated transport mechanism proposed by the Kerr and Ciric group.<sup>51</sup> This mechanism says that aluminosilicate hydrogel will be redissolved and the Zeolites are formed by the recrystallization of silicate and aluminate ions in the solution. Again in 1980, a dual phase transition mechanism which proposed that the formation of Zeolites might follow different mechanisms under different crystallization conditions.

Recently the Moor *et al*<sup>52</sup> gave the first crystallization mechanism for the formation of the pure-silica Zeolite (Si-TPA-MFI). The mechanism was investigated by using the complementary techniques like small-angle and wide angle X-ray diffraction scattering which is shown in the Figure 1.13. Initial process, hydrophobic spheres are formed surrounding the both SADs and

silicates. Then the overlap of these spheres forms an nanometer sized PBUs having both silicates and SDAs. During the nucleation, PBUs are aggregate to form ordered structures with the size of 10 nm. Martens and co-workers<sup>53</sup> proposed mechanism for nucleation and growth in Zeolite synthesis. In this mechanism he proposed the silica species initially forms into a series of small “building blocks” that has the same topology for the final crystalline framework. These building blocks then aggregates to form the final Zeolite structure.

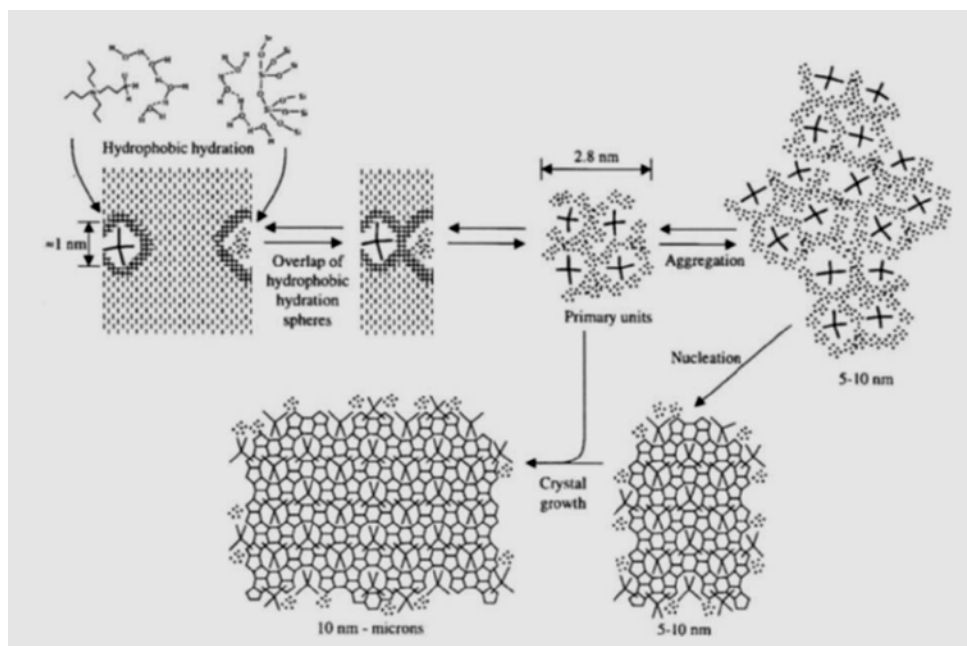


**Figure 1.13.** Schematic representations for the crystallization mechanism of Si-TPA-MFI.

## 1.9 Hydrothermal approach for the synthesis of Zeolites

The synthesis of microporous Zeolites started in the middle of 19<sup>th</sup> century. Till now Zeolite materials are mainly synthesized by two approaches (1) solid-state method and (2) Hydro (solvo) thermal method. The earliest synthesis of Zeolites were at high temperature (>200 °C) and pressure (10 MPA). However, the efforts are not very successful. The real success for the synthesis of Zeolite molecular sieves was happened in 1940s by R. M Barrer and J. Sameshima.<sup>5</sup> After that chemist at Union carbide Corporation (UCC), R. M. Milton and D.W. Breck,

employed mild hydrothermal synthesis and achieved a great success in developing a synthetic approach for the synthesis of Zeolites. By using the hydrothermal synthesis they successfully synthesized the unnatural Zeolites of types A, X and Y. Hydrothermal synthesis means reactions conducted at above 100 °C in aqueous solvents within a specially sealed container or high-pressure autoclaves shown in Figure 1.14. Under these conditions, autogeneous pressure (*i.e.* self-developing not external applied) is developed. Due to this autogeneous pressure the properties of water will be significantly changed. For example, the vapor pressure and ion product will be higher, and the density, surface tension and viscosity of water will be lower. The main difference between the hydrothermal and solid-state method was reaction mechanism. In hydrothermal conditions all the reactant molecules like silicon and aluminum sources, SDAs, and sources of other elements existing in the liquid phase can react with each other, whereas in solid-state synthesis occurs only on the surface by diffusion of the reactants at the interface. By varying the reaction mechanisms leads to formation of different structures from the same and similar starting materials. The main advantage of the hydrothermal method was we can synthesize materials with special structures and properties, or phases, types and morphologies which cannot be synthesized by other methods.<sup>54-55</sup>

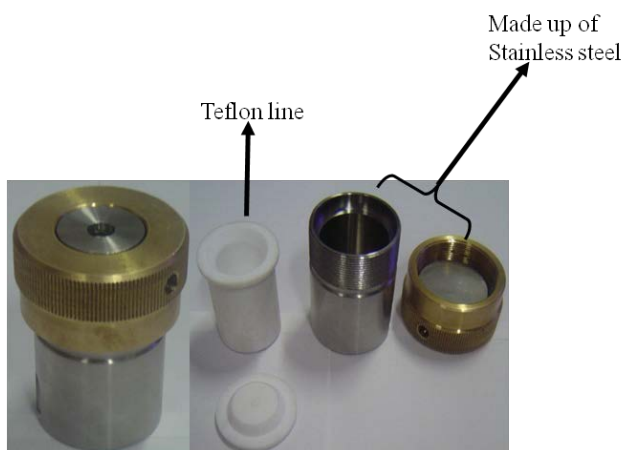


**Figure 1.14.** Schematic diagrams for the Teflon-lined stainless steel autoclave which we used regularly in our laboratory.

The main features of hydrothermal method in the synthesis of Zeolite materials are (1) From hydrothermal method we can synthesize new compounds of phases with special valance states, metastable structures which we cannot synthesized from solid-state reaction method. (2) We can get very nice large and single crystals from hydrothermal method. (3) We can crystallize the materials with low melting point, high vapor pressure, or low thermal stability, which we cannot get from traditional solid-state method. (4) We can control the morphology and particle size of the products from hydrothermal method. (5) To get uniform doping of hetero atoms to the crystalline structures very good from hydrothermal method. (6) We can conduct synthetic reactions which cannot carry out in solid-state phase. So, hydrothermal method was the best way to synthesize microporous materials. From hydrothermal method can enhance the effective solvation ability of water, increase the solubility of the reactants and activate the reactivity of the source materials, leading to the rearrangement and dissolution of the primary gel formed from the first stage and resulting in an increased nucleation and crystallization rate.<sup>5</sup>

## **1.10 Synthetic techniques for open-framework inorganic structures**

There are different techniques employed for the synthesis of open-framework materials which were briefly described below.

### **1.10.1 Hydro/solvothermal method**

Up to now most of the open-framework crystalline materials are synthesized by using Hydro/solvothermal method. Both the methods have same principle except solvent changes. In hydrothermal, water as solvent but in solvothermal solvent was organic solvents *i.e.* ethylene glycol (EG), ethanol, acetonitrile, dimethylformamide (DMF) and diethylacetamide (DMA) etc. Hydro/solvothermal synthesis refers to the synthetic reactions conducted at particular

temperature (50~200 °C) and pressure (1~5 MPa) in aqueous or organic solvents within a specially sealed container called autoclave (Figure 1.15).

To withstand the pressures involved in hydrothermal synthesis the use of autoclaves is usually required. The fundamental properties of solvent will change significantly at high temperature and pressure. When reaction can take place at high temperature, most thermodynamic stable product is formed. Sometimes if metal salts and ligands are not soluble at room temperature, they can form supersaturated solution at high temperature-pressure conditions and reaction can happen. Generally the steps used for the hydro/solvothermal method. (1) Addition of metal source in appropriate solvent and stir the whole solution for making homogenous. (2) Addition of ligand salts with continued stirring. (3) Addition of SDA. (4) Adjustment of pH. (5) Stirring from half an hour to 2 hours depending upon condition of solution. (6) The reaction mixture has been heated in a sealed autoclave at low temperature. (7) After appropriate time period, all the reactant materials will be converted to desired products as crystals. These crystals recovered by filtration, wash if we need and dry.

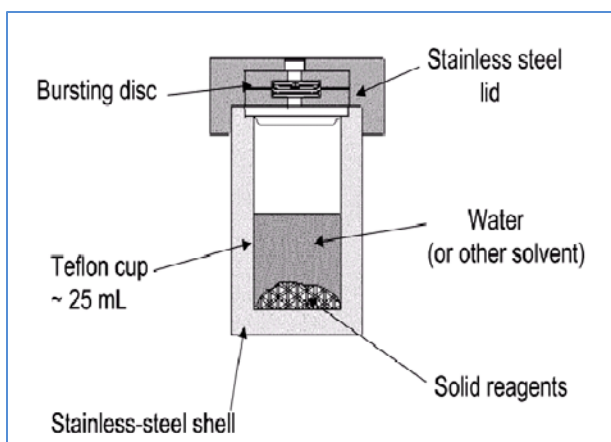


**Figure 1.15.** The schematic diagram for the autoclave.

### **1.10.2 Solvent diffusion method**

This method is used to prepare the milligram quantity of the sample. The solvent which is placed in the tube dissolved the metal salts and the second solvent (generally less denser than first solvent) in which ligand was dissolved carefully dripped down the side of the tube using either a pipette or a syringe to form a discreet layer. The desired compound forms at the boundary where the solvents slowly diffuse.

### **1.10.3 Slow evaporation method**

This method is the simplest method for the synthesis of open-framework materials. First prepared saturated solution in a suitable solvent, transfer the solution into a clean container which is having high surface area, and cover. We should not cover it too tightly (covered aluminum foil with punched holes good). Keep the solution at room temperature, after some particular days solvent would evaporate and we can observe the framework materials. Disadvantage of this method was we need a lot of starting material and not so good for the air-sensitive compounds.

### **1.10.4 Sealed tube method**

This method is good for the preparation of mesoporous materials. Principle of this method same as hydrothermal method only the difference is experimental container which is glass tube. First prepare the saturated solutions and transfer in a tube with the length of 10 mm. Before sealing the tube first freeze the tube in liquid nitrogen and apply vacuum for removing air. After sealing keep in programmable oven at particular temperature for required days and cool it to room temperature. While cooling we can observe desired compounds at sides of the tube.

### **1.10.5 Microwave method**

This method was developed in 1976. Microwave radiation was used in microwave method. In this method microwave oven is used with a specific, fixed frequency of 250 MHz with a 100%

power rating of 650 W. The synthesis was performed for 5-20 min with a 10 -50% power level. This method has many advantages for the synthesis of open-framework materials than the other conventional methods, such as shorter crystallization time, morphology can be controllable, narrow particle size distribution and low energy consumption.

## 1.11 Characterization tools and techniques

Characterization means the use of the external technique to probe of internal structure and properties of the materials. In this thesis the following main techniques are used to characterize the synthesized open-framework materials. (1) Single crystal X-ray diffraction (SXRD). (2) Powder X- ray diffraction (PXRD). (3) Thermogravimertic analysis (TGA) (4) Fourier transform infrared spectroscopy (FTIR). (5) Superconducting quantum interference device (SQUID) and (6) Surface area analysis.

### 1.11.1 Thermogravimertic analysis

TGA involves the measurements of certain physical and chemical properties as a function of temperature. TGA measures the amount of weight change of a material, either as a function of temperature or isothermally as a function of time in the presence of atmosphere of nitrogen ( $N_2$ ) or argon (Ar) or other gases. TGA analysis can be used to find the material decomposition temperature, phase change, glass phase change *etc.*

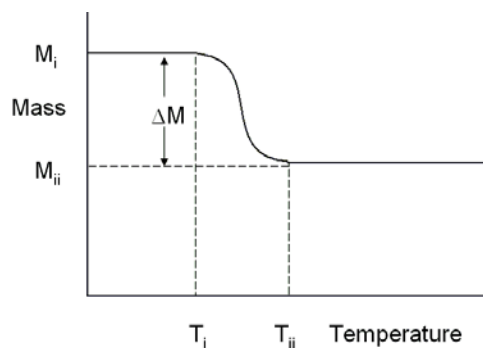


**Figure 1.16.** General TGA plot for single step weight loss of the material.

when the material is heated at constant heat flow of 5-10 °C/min with initial mass of  $M_i$ . The weight of the sample is constant up to  $T_i$  temperature. In TGA, heating is dynamic, heat is supplied continuously there was  $M_{ii}$  weight was changed at the temperature of  $T_{ii}$ . From the temperature  $T_i$  to  $T_{ii}$  there was new plateau was observed. The difference of weight  $\Delta M$  is change of weight (decomposed weight) from temperature  $T_i$  to  $T_{ii}$  shown in the Figure 1.16. In this thesis we studied to the thermal decomposition of open-framework metal sulfate materials.

### 1.11.2 Single crystal X-ray diffraction

SXRD is most widely used technique to know the crystal structure of system and constituent elements present in the structure. This experiment can be conduct only with crystal size larger than the 5  $\mu\text{m}$ . The basic principle is the diffraction of X-rays by planes on atoms in the crystal structure. The wavelength of X-ray falls in the range of interplanar spacing in the crystal and hence gets diffracted by it forming diffraction spots. The phenomenon of diffraction is accounted by Bragg's equation shown below and Figure 1.17 illustrates the diffraction phenomenon.

$$2d\sin\theta = n\lambda$$

Where  $d$  is interplanar spacing,  $\theta$  is the Bragg's angle,  $\lambda$  is the wavelength of X-rays and  $n$  is order.

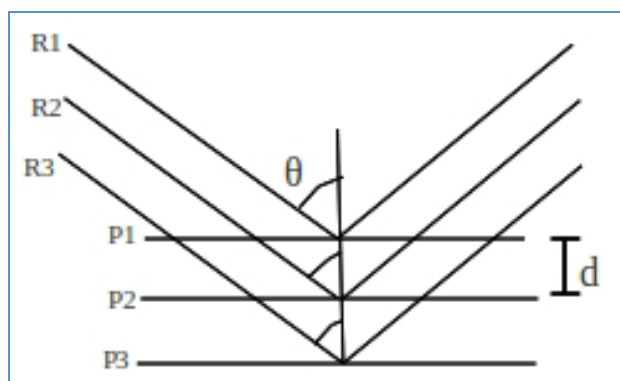


**Figure 1.17.** Diffraction of X-rays by crystal planes.

The detailed description of refining parameters involved and structure solving is given in short. First the data is collected from the single-crystal using Cu-target X-ray tube or Mo-target X-ray tube. The data is processed through reduction and absorption correction using programme SAINT and SADBAS respectively. Then the structure is solved using the SHELXL or WINGX software suite.

### **1.11.3 Powder X-ray diffraction**

As we discussed SXRD works only with crystal size of 5  $\mu\text{m}$ . Due to the nature of crystal, limitations on synthesis always we cannot get good quality of crystals. In these cases powder X-ray diffraction will help. The principle of PXRD is same as the SXRD. PXRD technique is extensively used for the many fields, e.g. crystallinity, crystalline parameters, phase identifications, expansion tensors, bulk modulus and phase transition. In this thesis used for the phase purity and phase identifications. The diffraction pattern is fingerprint of any crystalline phase and powder diffraction pattern has been extensively used to identify the mixture of phases. The phase purity of the material conformed by comparing the experimental powder pattern (PXRD) and simulated powder pattern which is generated after solving the single-crystal X-ray diffraction data. Phase identifications based on the comparison of experimental powder pattern with that of pure phase or with a data base.

### **1.11.4 Fourier transform infrared spectroscopy**

FTIR Spectroscopy that deals with the infrared region ( $4000\text{-}400\text{ cm}^{-1}$ ) of the electromagnetic spectrum, that is light with a longer wave length and lower than the visible light.<sup>56</sup> The technique involves the study of vibrational bands. The presence of a particular group in sample can be confirmed by checking the presence of some specific vibrational bands related to group in the FTIR spectra of sample. The frequency in the infrared region is scanned through the sample and

sample shows absorptions at particular frequencies specific to particular group. For example, the –O-H group in alcohols shows peaks in range 3200-3400  $\text{cm}^{-1}$ (stretch), –O-H group in carboxylic acids, 3500-3560  $\text{cm}^{-1}$ ; C=C, 1640-1680  $\text{cm}^{-1}$  (stretch) and CN 2220-2260  $\text{cm}^{-1}$ (stretch). Hence presence of specific group can be confirmed if its characteristic peak is observed. In this thesis we used to study the stretching and bending vibrations for organic template open-framework metal sulfates.

#### **1.11.5 Surface area and adsorption analysis**

The determination of surface area is a considered important technique for the open-framework materials. In addition, it is necessary to know the specific nature of pore structures of the solids since this may control the transport of the species of a catalytic and electro chemical reaction process. Gas adsorption is the often used technique for the determination of surface area and pore size of the solids. Generally  $\text{N}_2$  or Ar gas is used for measuring these properties.

Depends up on the degree of adsorption, mechanism of adsorption and relative strength adsorbate and adsorbent, adsorption of isotherms are divided in to five types shown in the Figure 1.18. Type 1 isotherms generally show the microporous materials whose pore size does not exceed the adsorbate molecular diameters. This isotherm is occurred by chemisorptions by strong attractive interactions between the adsorbate and adsorbent and week interactions between the adsorbate themselves. Type II isotherms are nonporous powders with pore diameters larger than the micropores. This isotherm occurred by strong interaction between the adsorbate molecule which leads multilayer adsorption. Complete monolayer coverage attains first then multilayer begins start. Type IV isotherms are occurred by ones the pores are filled then there was a weak interactions between the adsorbate molecules. Type III and V isotherms are occurred due to the initially the adsorption of gas molecules slow and then full surface coverage is

sufficient so that interactions between the adsorbed and free molecules begins to dominate the process.

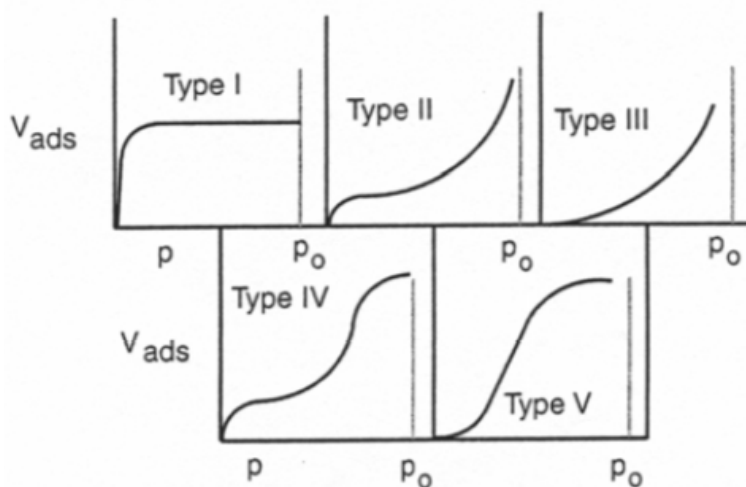


**Figure 1.18.** The schematic diagram for different types of adsorptions (I-V).<sup>57</sup>

### 1.11.6 Superconducting quantum interference device

SQUID is a very sensitive magnetometer used to measure subtle magnetic fields, based on superconducting loops containing Josephson junctions. SQUID magnetometer can monitor very small changes in magnetic flux and so discover the magnetic properties of samples. It is extremely sensitive for all kinds of AC and DC magnetic measurements. The SQUID detects and measures the magnetic moment of the sample. From this the magnetization and magnetic susceptibility can be determined. Sample was typically 20 to 40 mg required for the measurement, but strongly magnetic materials can be measured even with less amount of the material. Data can be collected between  $H = 0$  to  $\pm 50$  kOe and  $T = 1.7$  to 400 K. The maximum sensitivity of the instrument is in the range of  $10^{-9}$  emu. The main applications of the SQUID magnetometer include measurements of small quantities of paramagnetic ions, characterization of all kinds of magnetic materials, and quantitative determination of the number of unpaired electrons in samples.

## 1.12 Future direction

Template-directed synthesis of open-framework materials is a convenient and versatile method. By changing the different templates we can get different dimensions of the pores and structures. Ordered microporous materials exhibit tunable pore size, high surface area and pore volume, ease of surface functionalization, all these being highly promising properties for the numerous applications. For synthesis of open-framework materials, the following are still challenges for researchers in future direction.

- (1) The synthesis of open-framework materials should be an environmental friendly, low toxicity, low-cost and simple synthetic procedure.
- (2) The formation mechanisms are not clearly settled and active investigations should be done.
- (3) The use of the open-framework materials is still rather lacking.
- (4) Synthesize the useful materials targeting the special industrial applications, although some achievements have been reached in functional materials, physical properties and catalyst applications field.
- (5) The framework materials should be mechanically, thermally stable and have a long lifetime.
- (6) The pore system and wall composition are controllable and available.

## 1.13 References

1. Jiménez-Gallegos, J.; Rodríguez-Hernández, J.; Yee-Madeira, H.; Reguera, E., *J. Phys. Chem. C* **2010**, *114*, 5043.
2. Britt, D.; Furukawa, H.; Wang, B.; Glover, T. G.; Yaghi, O. M., *Proc. Natl. Acad. Sci. USA* **2009**, *106*, 20637.
3. Fletcher, A. J.; Cussen, E. J.; Bradshaw, D.; Rosseinsky, M. J.; Thomas, K. M., *J. Am. Chem. Soc.* **2004**, *126*, 9750.
4. Yang, R. T., *Adsorbents: fundamentals and applications*. John Wiley & Sons: 2003.
5. Xu, R.; Pang, W.; Yu, J.; Huo, Q.; Chen, J., *Chemistry of zeolites and related porous materials: synthesis and structure*. John Wiley & Sons: 2009.
6. Csicsery, S. M., *Zeolites* **1984**, *4*, 202.
7. Čejka, J. i.; Bekkum, H. v., *Zeolites and ordered mesoporous materials*. Elsevier: 2005.
8. Cejka, J., *Zeolites and ordered mesoporous materials: progress and prospects: the 1st FEZA School on Zeolites, Prague, Czech Republic, August 20-21, 2005*. Gulf Professional Publishing: 2005; Vol. 157.
9. Flanigen, E. M.; Lok, B. M.; Patton, R. L.; Wilson, S. T., *Pure Appl. Chem.* **1986**, *58*, 1351.
10. Cheung, O.; Hedin, N., *Rsc Advances* **2014**, *4*, 14480.
11. De Vos, D. E.; Sels, B. F.; Jacobs, P. A., *Adv. Synth. Catal.* **2003**, *345*, 457.
12. Panov, G., *Cattech* **2000**, *4*, 18.
13. Thomas, J. M.; Raja, R.; Sankar, G.; Bell, R. G., *Acc. Chem. Res.* **2001**, *34*, 191.
14. Davis, M. E., *Nature* **2002**, *417*, 813.
15. Thomas, J. M.; Raja, R., *Proc. Natl. Acad. Sci. USA* **2005**, *102*, 13732.

16. Han, Z.; Picone, A. L.; Slawin, A. M.; Seymour, V. R.; Ashbrook, S. E.; Zhou, W.; Thompson, S. P.; Parker, J. E.; Wright, P. A., *Chem. Mater.* **2009**, *22*, 338.
17. Li, J.; Corma, A.; Yu, J., *Chem. Soc. Rev.* **2015**, *44*, 7112.
18. Xi, D.; Sun, Q.; Chen, X.; Wang, N.; Yu, J., *Chem. Commun.* **2015**, *51*, 11987.
19. Song, X.; Li, J.; Guo, Y.; Pan, Q.; Gan, L.; Yu, J.; Xu, R., *Inorg. Chem.* **2008**, *48*, 198.
20. Grandjean, D.; Beale, A. M.; Petukhov, A. V.; Weckhuysen, B. M., *J. Am. Chem. Soc.* **2005**, *127*, 14454.
21. Akolekar, D.; Kaliaguine, S., *J. Chem. Soc., Faraday Trans.* **1993**, *89*, 4141.
22. Li, J.; Yu, J.; Xu, R., *Proc. R. Soc. London, Ser. A* **2012**, *468*, 1955.
23. Dahl, I. M.; Kolboe, S., *J. Catal.* **1994**, *149*, 458.
24. Prakash, A.; Unnikrishnan, S., *J. Chem. Soc., Faraday Trans.* **1994**, *90*, 2291.
25. Li, S.; Falconer, J. L.; Noble, R. D., *J. Membr. Sci.* **2004**, *241*, 121.
26. Takeguchi, T.; Tanakulrungsank, W.; Inui, T., *Gas Sep. Purif.* **1993**, *7*, 3.
27. Yang, G.-Y.; Sevov, S. C., *J. Am. Chem. Soc.* **1999**, *121*, 8389.
28. Choudhury, A.; Natarajan, S.; Rao, C. N. R., *Chem. Commun.* **1999**, 1305.
29. Choudhury, A.; Krishnamoorthy, J.; Rao, C. N. R., *Chem. Commun.* **2001**, 2610.
30. Choudhury, A.; Kumar, D.; Rao, C. N. R., *Angew. Chem. Int. Ed.* **2002**, *41*, 158.
31. Harrison, W. T.; Phillips, M. L.; Stanchfield, J.; Nenoff, T. M., *Angew. Chem. Int. Ed.* **2000**, *39*, 3808.
32. Rao, C.; Behera, J.; Dan, M., *Chem. Soc. Rev.* **2006**, *35*, 375.
33. MasPOCH, D.; Ruiz-Molina, D.; Veciana, J., *Chem. Soc. Rev.* **2007**, *36*, 770.
34. Behera, J.; Gopalkrishnan, K.; Rao, C., *Inorg. Chem.* **2004**, *43*, 2636.

35. Paul, G.; Choudhury, A.; Sampathkumaran, E. V.; Rao, C. N. R., *Angew. Chem. Int. Ed.* **2002**, *41*, 4297.
36. Natarajan, S.; Mandal, S., *Angew. Chem. Int. Ed.* **2008**, *47*, 4798.
37. Udayakumar, D.; Rao, C., *J. Mater. Chem.* **2003**, *13*, 1635.
38. Feng, M.-L.; Mao, J.-G.; Song, J.-L., *J. Solid State Chem.* **2004**, *177*, 3529.
39. Davis, M. E.; Lobo, R. F., *Chem. Mater.* **1992**, *4*, 756.
40. Jackowski, A.; Zones, S. I.; Hwang, S.-J.; Burton, A. W., *J. Am. Chem. Soc.* **2009**, *131*, 1092.
41. Lewis, D.; Freeman, C.; Catlow, C., *J. Phys. Chem.* **1995**, *99*, 11194.
42. Gómez-Hortigüela, L.; Hamad, S.; López-Arbeloa, F.; Pinar, A. B.; Pérez-Pariente, J.; Corà, F., *J. Am. Chem. Soc.* **2009**, *131*, 16509.
43. Xin, L.; Sun, H.; Xu, R.; Yan, W., *Sci. Rep.* **2015**, *5*.
44. Chien, H.-T.; Chen, M.-C.; Huang, P.-S.; Lai, J.-Y.; Hsu, C.-C.; Kang, D.-Y., *Chem. Commun.* **2015**, *51*, 13910.
45. Flanigen, E.; Patton, R., US Patent 4073865 (1978). In *Chem. Abstr*, 1978; Vol. 88, p 138653.
46. Regev, O.; Cohen, Y.; Kehat, E.; Talmon, Y., *Zeolites* **1994**, *14*, 314.
47. Schoeman, B. J., *Zeolites* **1997**, *18*, 97.
48. Twomey, T.; Mackay, M.; Kuipers, H.; Thompson, R., *Zeolites* **1994**, *14*, 162.
49. Iton, L. E.; Trouw, F.; Brun, T.; Epperson, J.; White, J.; Henderson, S., *Langmuir* **1992**, *8*, 1045.
50. Breck, D., *J. Chem. Educ.* **1964**, *41*, 678.
51. Kerr, G. T., *J. Phys. Chem.* **1966**, *70*, 1047.

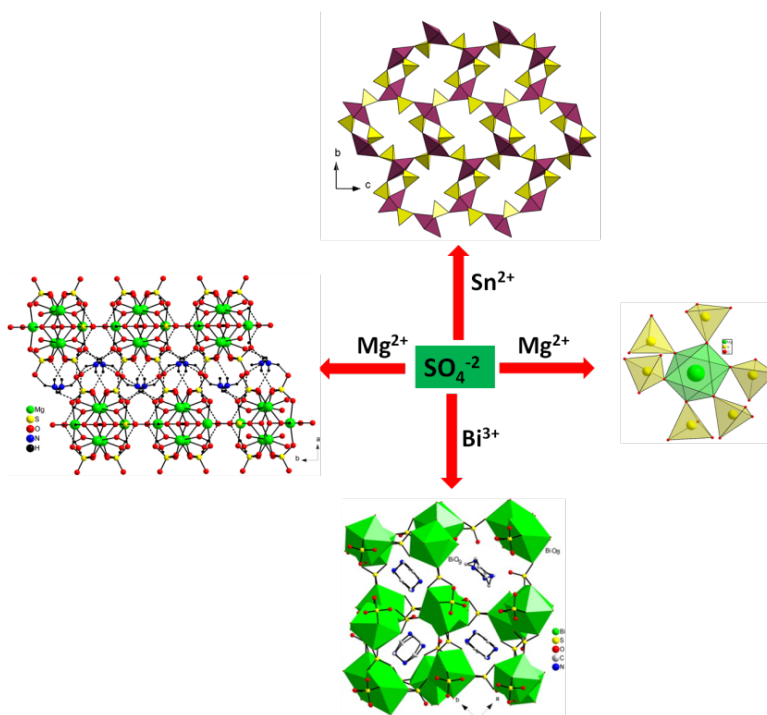
52. de Moor, P. P. E.; Beelen, T. P.; Komanschek, B. U.; Beck, L. W.; Wagner, P.; Davis, M. E.; van Santen, R. A., *Chem. Eur. J.* **1999**, *5*, 2083.
53. Kirschhock, C. E.; Ravishankar, R.; Looveren, L. V.; Jacobs, P.; Martens, J., *J. Phys. Chem. B* **1999**, *103*, 4972.
54. Cundy, C. S.; Cox, P. A., *Chem. Rev.* **2003**, *103*, 663.
55. Cundy, C. S.; Cox, P. A., *Microporous Mesoporous Mater.* **2005**, *82*, 1.
56. Nakamoto, K., *Infrared and Raman spectra of inorganic and coordination compounds*. Wiley Online Library: 1986.
57. Sing, K.; Everett, D.; Haul, R.; Moscou, L.; Pierotti, R.; Rouquerol, J.; Siemieniewska, T., *Pure Appl. Chem.* **1985**, *57*, 603.

## CHAPTER-2

### Open-Framework Main group Metal Sulfates

2.1	Abstract	73
2.2	Introduction	74
2.3	Experimental section	77
2.3.1	Mg(II) sulfate frameworks	77
2.3.2	Bi(III) sulfate frameworks	77
2.3.3	Sn(II) sulfate frameworks	78
2.4	Characterization	79
2.5	Single-crystal structure determination	82
2.6	Results and discussion	83
2.6.1.	Structural analysis of $[\text{NH}_4]_2[\text{Mg}_3(\text{OH})_2(\text{SO}_4)_3(\text{H}_2\text{O})_2]$ , <b>1</b>	83
2.6.2.	Structural analysis of $[\text{NH}_4]_8[\text{Mg}_2(\text{SO}_4)_{12}]$ , <b>2</b>	85
2.6.2.1	Adsorption Properties of $[\text{NH}_4]_8[\text{Mg}_2(\text{SO}_4)_{12}]$ , <b>2</b>	88
2.6.3	Structural analysis of $[\text{C}_6\text{N}_2\text{H}_{14}][\text{Bi}(\text{SO}_4)_2(\text{NO}_3)]$ , <b>3</b>	88
2.6.4.	Structural analysis of $[\text{C}_4\text{N}_2\text{H}_{12}]_4[\text{Bi}_4(\text{SO}_4)_{10}(\text{H}_2\text{O})_4]$ , <b>4</b>	91
2.6.4.1	Photoluminescence studies	94
2.6.4.2	Lifetime studies	96
2.6.5	Structural analysis of $[\text{C}_3\text{N}_2\text{H}_{12}][\text{Sn}_2(\text{SO}_4)_3]$ , <b>5</b>	97
2.6.6	Structural analysis of $[\text{C}_2\text{N}_2\text{H}_{10}][\text{Sn}(\text{SO}_4)_2]$ , <b>6</b>	99
2.6.7	Structural analysis of $[\text{C}_3\text{N}_2\text{H}_{12}][\text{Sn}(\text{SO}_4)_2]$ , <b>7</b>	100
2.6.8	Structural analysis of $[\text{C}_4\text{N}_2\text{H}_{14}][\text{Sn}(\text{SO}_4)_2] \cdot \text{H}_2\text{O}$ , <b>8</b>	102
2.7	Conclusions	104
2.8	References	105
2.9	Appendix	109

## 2.1 Abstract



In this chapter we describe 8 open-framework main group metal sulfates with different crystal dimensionalities. Two Mg(II) Compounds with composition  $[\text{NH}_4]_2[\text{Mg}_3(\text{OH})_2(\text{SO}_4)_3(\text{H}_2\text{O})_2]$ , **1** and  $[\text{NH}_4]_8[\text{Mg}_2(\text{SO}_4)_{12}]$ , **2** were synthesized by hydro/solvothermal method. Compound **1** crystallized with two-dimensional layered structure where as compound **2** crystallized with three-dimensional with chirality. Compound **2** shows hydrogen adsorption in the order of 0.7 wt%. Two Bi(III) sulfate frameworks with composition  $[\text{C}_6\text{N}_2\text{H}_{14}][\text{Bi}(\text{SO}_4)_2(\text{NO}_3)]$ , **3**, and  $[\text{C}_4\text{N}_2\text{H}_{12}]_4[\text{Bi}_4(\text{SO}_4)_{10}(\text{H}_2\text{O})_4]$ , **4** were synthesized by slow evaporation method. Both the compounds show good photolumiscence properties with blue light emission. Four Sn(II) sulfates with composition  $[\text{C}_3\text{N}_3\text{H}_{12}][\text{Sn}_2(\text{SO}_4)_3]$ , **5**;  $[\text{C}_2\text{N}_2\text{H}_{10}][\text{Sn}(\text{SO}_4)_2]$ , **6**;  $[\text{C}_3\text{N}_2\text{H}_{12}][\text{Sn}(\text{SO}_4)_2]$ , **7** and  $[\text{C}_4\text{N}_2\text{H}_{14}][\text{Sn}(\text{SO}_4)] \cdot \text{H}_2\text{O}$ , **8** were synthesized by hydro/solvothermal method. We observed four different Sn(II) sulfate framework structures by varying the different structure directing agents, reaction time and temperature.

## 2.2 Introduction

The synthesis of complex inorganic materials with open architecture is one of the major activities in contemporary solid state chemistry for their applications in the areas of catalysis, ion-exchange, sorption and separation process. During the last two decades or so large number of new materials with novel architectures have been synthesized and characterized. Accordingly, inorganic open-framework structures involving silicates, phosphates<sup>1-2</sup> and carboxylates<sup>3-5</sup> have been investigated widely in the past few years. It has been demonstrated recently that oxyanions such as selenite,<sup>6-7</sup> selenate<sup>8-9</sup> and sulfate<sup>10-14</sup> can also be used to build up open architectures. As we mentioned in previous chapter S-O bonds has less charge than the P-O bonds, which creates the difficulties for the extended networks. The S-O bond has very less covalent nature so poly sulfate units are very less readily formed as compared with polyborates, phosphates and silicates.<sup>15</sup> Thus, the reports on sulfate frameworks are very less explored. So, we are interested to explore the open-framework materials by using sulfate anions. Nevertheless, inorganic open-framework metal sulfates based on main group metals (light main group metal in particular) have not been synthesized hitherto.<sup>16</sup> Compared to f- and d-block cations, s-block cations are far less popular as building blocks owing to their unpredictable coordination numbers and geometries in the absence of ligand field stabilization affects.<sup>17</sup> So, the main objective of this thesis is to synthesize the open-framework metal sulfates by using main group metal atoms. The main problem for framework assembly with s-block ions is their high affinity for oxygen donors. In this chapter, we reports the open-framework metal sulfates by using the light weight (Mg) and heavy weight (Bi, Sn) main group metal atoms by changing the different structure directing agents.

We are interesting on light weight Magnesium atoms because Mg(II) ion has a number of similarities with transition metal ions as it prefers octahedral coordination, and has a comparable ionic radius (72 pm for Mg<sup>2+</sup> compared to 80 pm for Mn<sup>2+</sup>, 74 pm for Zn<sup>2+</sup> and 73 pm for Cu<sup>2+</sup>) despite having a much smaller molar mass. Use of such light metals in porous materials is appealing as they predictably have strong binding affinities for small molecules such as dihydrogen, methane, thus presenting new possibilities for light weight sorption materials.<sup>1, 18-20</sup> Due to these reasons we are concern on Mg(II) metal atoms for the synthesis of open-framework sulfates. In this chapter we report synthesis, crystal dimensionalities and gas adsorption studies of [NH<sub>4</sub>]<sub>2</sub>[Mg<sub>3</sub>(OH)<sub>2</sub>(SO<sub>4</sub>)<sub>3</sub>(H<sub>2</sub>O)<sub>2</sub>], **1** and [NH<sub>4</sub>]<sub>8</sub>[Mg<sub>2</sub>(SO<sub>4</sub>)<sub>12</sub>], **2**. Here we also concerns on heavy weight Bismuth metal atoms because Bi<sup>3+</sup> cation accommodating the lone pair of electrons which can be lead to the rich structural chemistry. The Bi<sup>3+</sup> ion with its ionic radius of 1.16 Å has one inert 6s<sup>2</sup> electron pair and forms non-transition metal center complexes with higher coordination-number atoms. Therefore, bismuth is expected to form higher dimensional frameworks. Bismuth containing compounds can have their low-toxicity; low-cost and good chemical stability and these materials have potential application in medicine treatment, catalyst and luminescence.<sup>21-23</sup> Also, bismuth can exist in a wide variety of coordination environment that can lead structures of different dimensionalities. So, we are interested in exploring the use of SO<sub>4</sub><sup>2-</sup> tetrahedra to build open-framework materials by using heavy weight main group Bismuth metal atom. Open-framework materials are usually synthesized by employing hydro/solvothermal techniques that require the reaction mixture to be heated at a particular temperature in a sealed autoclave.<sup>24</sup> We have been able to prepare both layered and three-dimensional bismuth sulfates employing simple aqueous mediated reaction at room temperature. In this

chapter, we report the synthesis, structure, and luminescence properties of  $[\text{C}_6\text{N}_2\text{H}_{14}][\text{Bi}(\text{SO}_4)_2(\text{NO}_3)]$ , **3** and  $[\text{C}_4\text{N}_2\text{H}_{12}]_4[\text{Bi}_4(\text{SO}_4)_{10}(\text{H}_2\text{O})_4]$ , **4**.

The Number of tin oxalates and phosphates/phosponates were synthesized from Cheetham and Rao's group <sup>25-29</sup> and their crystallographic findings are reported. In most of the cases, protonated structure directing amines reside within the cavities of anionic layers. The main structural feature was present in all the tin phosphates/phosponates materials comprises  $\text{Sn}_2\text{P}_2\text{O}_4$  unit in which tin atoms were linked either through three coordinate and/or four coordinate with oxygen from  $\text{PO}_4$  tetrahedra forming chains, layers, two-dimensional and three-dimensional structures. Due to presence of lone pair electrons on tin atom, structures are slightly distorted. In most of the reported structures of tin phosponates/phosphates, the ratio of Sn: P was  $>1$ .<sup>30</sup> A Small concentration of tin can be substituted into the open-framework of aluminosilicates<sup>31-32</sup> then after can be used as sorbents, ionic conductors and catalysts<sup>31</sup>. In most of the tin phosphates, Sn was in +IV oxidation state, with very fewer reports on  $\text{Sn}^{2+}$  oxidation state. The main advantage of  $\text{Sn}^{2+}$  is due to the presence of lone pair of electrons which can act as redox center or as a host for base-catalyzed reactions *e.g.* zeolites and  $\text{AlPO}_4\text{s}$  are used for acid- catalyzed reactions.<sup>28</sup> Till date, only two reports were found on tin(II) sulfates, which are  $[\text{C}_6\text{N}_2\text{H}_{14}][\text{SnCl}_2\text{SO}_4]$ <sup>33</sup> and  $[\text{C}_{10}\text{H}_{10}\text{N}_2]_{0.5}[\text{SnF}(\text{SO}_4)]$ <sup>34</sup>. Interestingly, there are no reports on pure O-Sn-O linkage based anionic polymers to the best of our knowledge. So, the motivation of our work to synthesize the new tin sulfate frameworks with +2 oxidation state. In this chapter, we report synthesis, structure and characterization of four tin(II) sulfate frameworks with composition of  $[\text{C}_3\text{N}_3\text{H}_{12}][\text{Sn}_2(\text{SO}_4)_3]$ , **5**;  $[\text{C}_2\text{N}_2\text{H}_{10}][\text{Sn}(\text{SO}_4)_2]$ , **6**;  $[\text{C}_3\text{N}_2\text{H}_{12}][\text{Sn}(\text{SO}_4)_2]$ , **7** and  $[\text{C}_4\text{N}_2\text{H}_{14}][\text{Sn}(\text{SO}_4)] \cdot \text{H}_2\text{O}$ , **8**. In all the polymers have pure O-Sn-O linkage and ratio of Sn and S was  $<1$ .

## 2.3 Experimental section

### 2.3.1 Mg(II) sulfate frameworks

Compounds **1** and **2** were synthesized by employing hydro/solvothermal methods. We have used ammonium sulfite as the source of sulfate that gets oxidized to sulfate easily during the synthetic conditions. Efforts of getting the same phase using  $\text{H}_2\text{SO}_4$  as the source of sulfate was unsuccessful. It seems the pH of the reaction mixture is playing an important role for the synthesis of both **1** and **2**. In a typical synthesis of **1**, 0.19 gm of  $\text{MgCl}_2$  was dispersed in an EG/ $\text{H}_2\text{O}$  mixture (3.5 and 1.5 mL, respectively) under constant stirring. To this mixture, 0.268 gm of  $(\text{NH}_4)_2\text{SO}_3$  and 0.12 mL of en were added and the mixture was stirred for 20 min to obtain the clear solution. The final mixture with the molar composition of  $\text{MgCl}_2/(\text{NH}_4)_2\text{SO}_3/\text{H}_2\text{O}/\text{en}/\text{EG}$  (2:2:80:40) was transferred into a 15-mL Teflon-lined acid digestion bomb and heated at 180 °C for 48 h. The reaction mixture after above heat treatment did not show any appreciable change in pH and remains at pH 6. After cooling white block-shaped crystals were obtained with 75% yield. Compound **2** was prepared in the same way and the final mixture with the molar composition of  $\text{Mg}(\text{OAc})_2 \cdot 4\text{H}_2\text{O}/(\text{NH}_4)_2\text{SO}_3/\text{EG}/\text{H}_2\text{O}$  (1:2:70:80) was transferred into a 15-mL Teflon-lined acid digestion bomb which was subjected to heat treatment similar as above. The product containing white block-shaped crystals were obtained with 80% yield.

### 2.3.2 Bi(III) sulfate frameworks

Compounds **3** and **4** were synthesized by slow evaporation at room temperature. In a typical synthesis of **3**, 0.485 gm of  $\text{Bi}(\text{NO}_3)_3 \cdot 4\text{H}_2\text{O}$  was dissolved in 10 mL of distilled water in a 20 mL scintillation vial under constant stirring. To this mixture, 0.5 mL of  $\text{H}_2\text{SO}_4$  followed by 0.162 gm of PIP were added and the mixture was stirred for 30 min to obtain the clear solution. The final mixture with the molar composition of  $\text{Bi}(\text{NO}_3)_3 \cdot 4\text{H}_2\text{O}/\text{H}_2\text{SO}_4/\text{PIP}/\text{H}_2\text{O}$  (1:9:2:55) was kept at

room temperature in open air. After one month needle-shaped white crystals were collected after filtration, washed with water and dried in air (yield 80% with respect to Bi). Compound **4** was synthesized in a similar way to that of **3** by using DABCO as the structure directing amine. 0.485 gm of  $\text{Bi}(\text{NO}_3)_3 \cdot 4\text{H}_2\text{O}$  was dissolved in 10 mL of distilled water in a 20 mL scintillation vial under constant stirring. To this mixture, 0.5 mL of  $\text{H}_2\text{SO}_4$  followed by 0.228 gm of DABCO were added and the mixture was stirred for 30 min to obtain the clear solution. The scintillation vial containing the reaction mixture with the molar composition of  $\text{Bi}(\text{NO}_3)_3 \cdot 4\text{H}_2\text{O}/\text{H}_2\text{SO}_4/\text{DABCO}/\text{H}_2\text{O}$  (1:9:2:55) was kept at room temperature in open air. After one month needle-shaped crystals were collected with 73% yield.

### 2.3.3 Sn(II) sulfate frameworks

Compounds **5-8** were synthesized by using hydro/solvothermal methods. All compounds were synthesized by using tin source has tin(II) oxalate by taking different organic amines. In a typical synthesis, compounds were synthesized by taking 1 mM of tin(II) oxalate in 1 mL of water followed by addition of 0.165 mL of  $\text{H}_2\text{SO}_4$  and 0.22 mL of 1,3-Diaminopropane (1,3-dap) for **5**, 0.33 mL of  $\text{H}_2\text{SO}_4$  and 0.145 mL of en for compound **6**, 0.33 mL of  $\text{H}_2\text{SO}_4$  and 0.22 mL of 1,3-dap for **7**, 0.33 mL of  $\text{H}_2\text{SO}_4$  and 0.33 mL of 1,4-Diamino butane (1,4-dab) for **8**, were taken in the 23 mL of PTFE lined acid digestion bomb stirred for 30 min for making homogenous solution and heated at 150 °C for 2-3 days. Colorless crystals were observed for all the reaction mixture. The molar composition of the reactants, time and temperature conditions for compounds **5-8** were given in the Table 2.1.

**Table 2.1.** Synthetic conditions of compounds **5-8**

S. No	Reactants and molar composition (mM)	Temperature (°C)	Time (h)	Compound
1	Tin(II) oxalate/H <sub>2</sub> SO <sub>4</sub> /1,3-dap/H <sub>2</sub> O (1:6:3:55)	150	62	[C <sub>3</sub> N <sub>2</sub> H <sub>12</sub> ][Sn <sub>2</sub> (SO <sub>4</sub> ) <sub>2</sub> ], <b>5</b>
2	Tin(II) oxalate/H <sub>2</sub> SO <sub>4</sub> /en/H <sub>2</sub> O (1:6:3:55)	150	66	[C <sub>2</sub> N <sub>2</sub> H <sub>10</sub> ][Sn(SO <sub>4</sub> ) <sub>2</sub> ], <b>6</b>
3	Tin(II) oxalate/H <sub>2</sub> SO <sub>4</sub> /1,3 dap/H <sub>2</sub> O (11:6:3:55)	150	48	[C <sub>3</sub> N <sub>2</sub> H <sub>12</sub> ][Sn(SO <sub>4</sub> ) <sub>2</sub> ], <b>7</b>
4	Tin(II) oxalate/H <sub>2</sub> SO <sub>4</sub> /1,4 dab/H <sub>2</sub> O (1:6:3:55)	150	72	[C <sub>4</sub> N <sub>2</sub> H <sub>14</sub> ][Sn(SO <sub>4</sub> ) <sub>2</sub> ].H <sub>2</sub> O, <b>8</b>

## 2.4 Characterization

Initial characterization of all the compounds were carried out PXRD, energy dispersive analysis of X-rays (EDAX), chemical analysis, TGA and FTIR spectroscopy. PXRD patterns of compounds (**1-6**) were almost in good agreement with the simulated patterns based on their respective single-crystal data shown in Figure 2.25. Compounds **1-6** gave satisfactory elemental analysis. The experimental and calculated (in wt%) values of H, N and S were as follows. **1**, H = 3.7; N = 5.8 and S = 21.6 (calc. H = 3.3, N = 6.0 and S = 22); **2**, H = 5; N = 7.4 and S = 21.6 (calc.: H = 4.6 N = 7.2 and S = 22). EDAX indicated the ratios of M and S to be 1:1 in compound **1** and 2:3 for compound **2**, which are good agreement with the molecular formulae. These analytical data confirm the molecular formulae of **1** and **2** as obtained from crystallography. For the compound **3** and **4** experimental and calculated values were as follows C, 12.5; N, 7.3; H, 2.5 (calc.: C, 12.6; N, 7.4; H, 2.3) for **3**, C,8.5; N,5.2; H,2.2 (calc.:C,8.7; N,5.1; H,2.6) for **4**. EDAX, indicated the ratios of Bi and S to be 1:2, and 1:2.5 in **3** and **4**, respectively, in agreement with the molecular formulae. For the compounds **5** and **6**

experimental and calculated (in wt%) values of H, N, and S were as follows; for **4**, H = 2.39 ; N = 5.54 and S = 12.68 (calc. H = 2.32 , N = 5.48 and S =12.29 ); **5**, H = 2.70; N = 7.51 and S = 17.20 (calc.: H =2.72, N = 7.48 and S = 17.32) for **6**. From the EDAX, concludes ratio of Sn and S to be 1:1 and 1:2 in **5** and **6** respectively. TGA for **1-6** compounds were carried out under constant flow of N<sub>2</sub> at a heating rate of 2 °C min<sup>-1</sup> in the temperature range 25-750 °C. TGA for compound **1** showed there was a two-step weight loss, of water at 70-275 °C [obs = 9 %, calc = 7.6 %] and to the loss of SO<sub>3</sub> in the range 300 to 450 °C [obs = 21 %, calc = 20.8 %] (Figure 2.26). The PXRD pattern of the sample heated to 750 °C corresponded to a mixture of MgSO<sub>4</sub>, MgO and NH<sub>4</sub>(SO<sub>4</sub>)<sub>2</sub>. (JCPDS file card no. 01-074-1364). Compound **2** also two step weight loss in temperature range of 35-750 °C. First step corresponding to the loss of ammonia in the range of 70-380 °C (obs = 7.0%, calcd = 6.8%), followed by removal of SO<sub>2</sub> around 400 °C. The total observed weight loss of 60.5% corresponds to the loss of the amine along with sulfates is in good agreement with the calculated value of 59.5% (Figure 2.26). Compound **3** showed a two-step weight loss corresponding to the loss of DABCO and SO<sub>2</sub> in the range 200-375 °C (obs = 52.4%, calcd = 50.8%), followed by the removal of rest of SO<sub>3</sub> in the range 380-600 °C. The total observed weight loss of 60.5% corresponds to the loss of the DABCO along with sulfates is in good agreement with the calculated value of 59.5%. The PXRD pattern of the sample heated to 750 °C corresponded to Bi<sub>2</sub>O<sub>3</sub> (JCPDS: 00-029-0236). In **4**, there was a three-step weight loss corresponding to the loss of water in the range 100-200 °C (obs = 3.4%, calcd = 3.3%), the amine molecules at 320 °C followed by the decomposition of sulfate in the range 350-500 °C (obs=54%, calcd=54.5%). The small weight loss below 80 °C could be the presence of small amount of moisture in the sample (Figure 2.26). The PXRD pattern of the sample heated to 750 °C corresponded to Bi<sub>2</sub>O<sub>3</sub> (JCPDS: 00-029-0236). In both the compounds **5** and **6**, there was

continuously two step weight loss. In **5**, the range of 96-358 °C (obs =52.68%, calcd= 52.59%) corresponding to the loss of protonated amine molecules and sulfate groups. The PXRD pattern for the preheated sample at 800 °C corresponded to SnO (JCPDS: 00-026-0538). In **6**, initially small weight loss (3.36%) corresponds to the loss of moisture from sample and the major weight loss with continuous two steps in the range 263-438 °C which correspond to the loss of amine and sulfate groups (obs = 56.72%; calcd = 57.1). The PXRD for preheated sample at 800 °C correspond to SnO (JCPDS: 00-026-0538) shown in the Figure 2.26 (appendix).

The FTIR spectra of **1** and **2** showed characteristic bands for the sulfate as well as the ammonium moieties. The stretching mode of N-H bond (of the amine) is observed around 300-3300 cm<sup>-1</sup>. The N-H bending modes of the amine and NH<sub>4</sub><sup>+</sup> are observed in the range 1440-1586 cm<sup>-1</sup>. The characteristic stretching bands,  $\nu_3(\text{N-H})$  and  $2\nu_4(\text{N-H})$  of the NH<sub>4</sub><sup>+</sup> ion are observed at 3243 and 2830 cm<sup>-1</sup> respectively. Strong bands in the region 850-1015 cm<sup>-1</sup> correspond to  $\nu_1$  and  $\nu_3$  while bands in the region 583-644 cm<sup>-1</sup> can be assigned to  $\nu_2$  and  $\nu_4$  fundamental modes of sulfate ion. The stretching and bending modes of O-H bands were in the expected range for compound **1** (Figure 2.27). For compounds **3** and **4** the main IR bands are (KBr):  $\nu(\text{H}_2\text{O}) = 3230\text{-}3450\text{ cm}^{-1}$ ,  $\nu(\text{N-H}) = 3070\text{-}3110\text{ cm}^{-1}$ ,  $\nu(\text{C-H}) = 2670\text{-}2780\text{ cm}^{-1}$ ,  $\nu(\text{C-H}) = 1300\text{-}1500\text{ cm}^{-1}$ ,  $\nu_1(\text{SO}_4) = 950\text{-}1000\text{ cm}^{-1}$ ,  $\nu_3(\text{SO}_4) = 1100\text{-}1150\text{ cm}^{-1}$ ,  $\delta(\text{SO}_4) = 500\text{-}700\text{ cm}^{-1}$ . In general, the free sulfate ions exhibit two bands at 1105 and 615 cm<sup>-1</sup>, which are assigned to the  $\nu_3(\text{F}_2)$  stretching [ $\nu_d(\text{SO})$ ] and  $\nu_4(\text{F}_2)$  stretching [ $\delta_d(\text{OSO})$ ] modes, respectively. The coordination of the free sulfate group to the metal centers would lower the overall symmetry of the sulfate group and lead to the splitting of the  $\nu_3$  and  $\nu_4$  modes. The spectra show multiple strong bands in the 900-1040 cm<sup>-1</sup> region due to  $\nu_1$  and in the 1050-1250 cm<sup>-1</sup> region due to  $\nu_3$  vibration modes of the sulfate group. The bending modes of SO<sub>4</sub><sup>2-</sup> are found in the 500-550 and 600-795 cm<sup>-1</sup> region

(Figure 2.27). Same as in compounds **5** and **6** showed their stretching and bending modes of all bands were in their expected range. The bands in the 980-1010  $\text{cm}^{-1}$  region due to  $\nu_1$  and in the 1090-1140  $\text{cm}^{-1}$  region due to  $\nu_3$  of the sulfate group.<sup>35</sup> The bending mode of  $\text{SO}_4^{2-}$  was in the 450-600  $\text{cm}^{-1}$  region C-N stretching modes are observed in the range 1080-1220  $\text{cm}^{-1}$  (Figure 2.27).

## 2.5 Single-crystal structure determination

A suitable single crystal of each compound was carefully selected under a polarizing microscope and mounted at the tip of the thin glass fibre using cyanoacrylate (super glue) adhesive. Single crystal structure determination by X-ray diffraction was performed on a Siemens SMART-CCD diffractometer equipped with a normal focus, 2.4 kW sealed-tube X-ray source ( $\text{Mo-K}\alpha$  radiation = 0.71073Å) operating at 50 kV and 30 mA. Structures were solved by the direct method using SHELXS-97<sup>36</sup> and refined on  $F^2$  by a full-matrix least-squares technique using the SHELXTL-PLUS<sup>37</sup> programs package. An empirical absorption correction based on symmetry equivalent reflections was applied using SADABS.<sup>38</sup> The graphic programs DIAMOND<sup>39</sup> and ORTEP<sup>40</sup> were used to draw the structures. Non-hydrogen atoms were refined anisotropically. In the refinement, hydrogens were treated as riding atoms using the SHELXL default parameters. In all the compounds hydrogens are located through fourier map. Crystal data and structure refinement parameters for all compounds (**1-8**) were given in the appendix (Table.2. 2)

## 2.6 Results and discussions

### 2.6.1 Structural analysis of $[\text{NH}_4]_2[\text{Mg}_3(\text{OH})_2(\text{SO}_4)_3(\text{H}_2\text{O})_2]$ , **1**

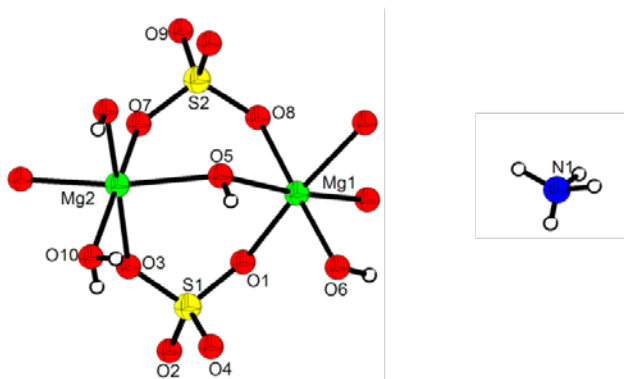


**Figure 2.1.** Asymmetric unit of compound  $[\text{NH}_4]_2[\text{Mg}_3(\text{OH})_2(\text{SO}_4)_3(\text{H}_2\text{O})_2]$ , **1**.

The asymmetric unit of **1** contains 15 non-hydrogen atoms out of which 14 belong to the inorganic framework and one belong to the extra framework ammonium ion (Figure 2.1). There are two crystallographically distinct Mg and S atoms, of which one Mg metal and one sulfur atom are in special positions with occupancy 0.5. The structure of **1** was constructed from macro anionic inorganic framework layers of  $[\text{Mg}_3(\text{OH})_2(\text{SO}_4)_3(\text{H}_2\text{O})_2]^{2-}$  held together by strong hydrogen bonds with the ammonium ions residing in the interlamellar space. The Mg atoms are octahedrally coordinated to six oxygens from four sulfates and two hydroxyl groups. For compound **1**, Mg-O bond distances are in the range 2.044(13)-2.149(18) Å and O-Mg-O bond angles in the range 79.76(6)-178.13(7)°. Of the two sulfur atoms, S(2) has four S-O-Mg linkages and S(1) has three such connections, with one terminal S(1)-O(4) bond. The S-O bond distances in **1** are in the range 1.444(11)-1.482(11) Å and the average O-S-O bond angle is 109.64°. In **1**, The S-O bond distances are in the range 1.462(12)-1.481(11) Å and the average O-S-O bond angle is 109.48°. The Bond valence sum (BVS) calculations for **1** based on the method of Brown and Altermatt,<sup>41</sup> using  $r_0(\text{Mg}-\text{O}) = 1.693$  Å, shown that valence sums for Mg(1) = 1.98, Mg(2) =

1.92 Å respectively. The charges on metal and sulfur atoms are clearly +2 and +6 respectively. These data are consistent with the stated composition. Selected bond distances and angles of **1** are listed in CCDC No: 1406125. The anionic framework of **1** was built up of Mg(1)(OH)<sub>2</sub>O<sub>4</sub>, Mg(2)(OH)<sub>2</sub>O<sub>4</sub> octahedra and SO<sub>4</sub> tetrahedra sharing edges as Mg-μ-(OH)-Mg bonds and vertexes as Mg-O-S bonds. The Mg(1)(OH)<sub>2</sub>O<sub>4</sub> octahedra get dimerized by sharing edges with two hydroxyl groups to form Mg<sub>2</sub>(OH)<sub>2</sub>O<sub>8</sub> moiety. Mg(2)(OH)<sub>2</sub>O<sub>4</sub> octahedra link to the dimer at one end of the shared edges through μ<sub>3</sub>-OH to form trimeric Mg<sub>3</sub>(OH)<sub>3</sub>O<sub>12</sub> units. These units are chains connected to one another through corner sharing Mg-O-S linkages there by forming the zig-zag chain shown in the Figure 2.2. Such chains run parallel to the *a*-axis and are covalently bonded to each other by the S(2)O<sub>4</sub> group resulting the two-dimensional layered structure. The S(2)O<sub>4</sub> tetrahedra from the adjacent connect alternatively via four Mg-O-S linkages to form four connected tetrahedra, leading to the formation of an eight- membered aperture in the *ab*-plane. The inorganic layers are stacked along the *c*-axis in the ABAB.... fashion and the interlayer space is occupied by the ammonium ion which ensures the stability of the structure through extensive hydrogen bonding as shown in the Figure 2.3. The hydrogen bond interactions are given in the Table 2.3.

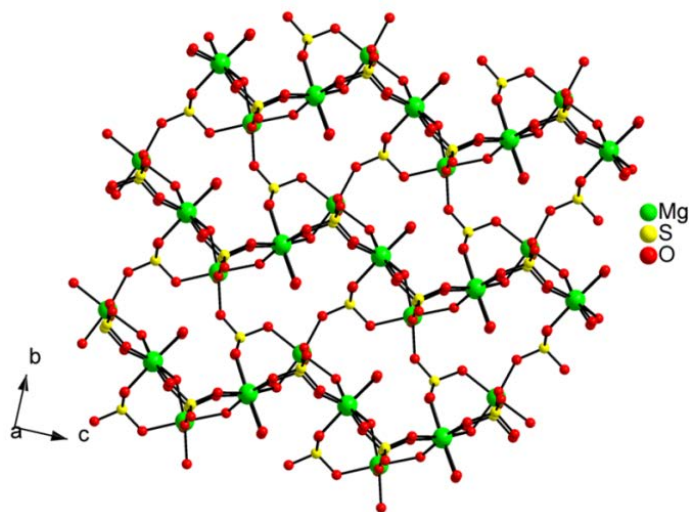


**Figure 2.2.** View of inorganic layers of **1** in *bc*-plane with eight- membered apertures.

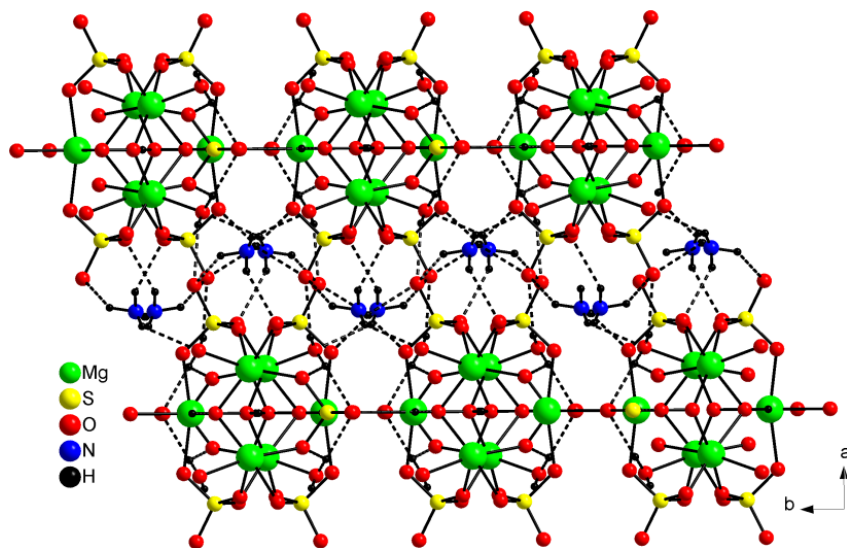


**Figure 2.3.** View of packing layers in **1**. Hydrogen bonding interactions between ammonium ions and the framework oxygen are shown by dotted lines.

### 2.6.2 Structural analysis of $[\text{NH}_4]_8[\text{Mg}_2(\text{SO}_4)_{12}]$ , **2**

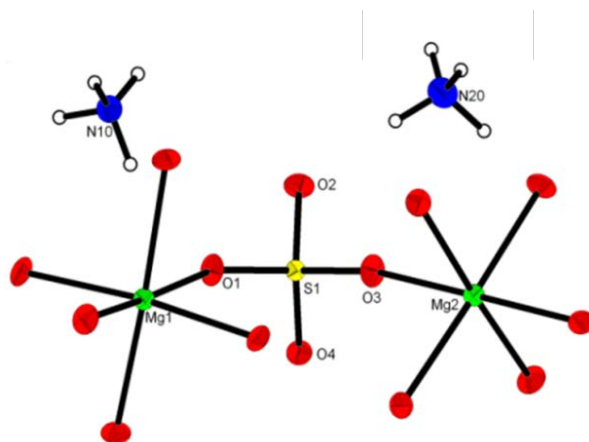


**Figure 2.4.** Asymmetric unit of compound  $[\text{NH}_4]_8[\text{Mg}_2(\text{SO}_4)_{12}]$ , **2**.

Compound **2** was three-dimensional chiral structure with cubic symmetry that crystallizes in the chiral space group  $P2(1)3$ . The asymmetric unit consists of 9 non-hydrogen atoms out of which 7 belong to the inorganic framework and 2 to the guest  $\text{NH}_4^+$  ions as shown in the Figure 2.4. There are two crystallographically distinct Mg atoms and one S atom with both the metal atoms in octahedral coordination with the O neighbours from the six sulfate groups. The Mg-O bond distances are in the range 2.070(4)-2.072(4) Å [ $\text{Mg}(1)\text{-O}_{\text{avg}} = 2.071$ ,  $\text{Mg}(2) - \text{O}_{\text{avg}} = 2.072$  Å].

The *trans* O-Mg-O bond angles are in the range 175.9(2)-168.7(2)° and the *cis* O-Mg-O are in the range 78.89(14)-101.1(2)° with an average of 172.4 and 85.06° respectively. Selected bond distances and angles of **2** are given in CCDC No: 1017043. Both Mg(1) and Mg(2) make six Mg-O-S linkages by sharing corner with six sulfate groups resulting into a pinwheel arrangement of MgO<sub>6</sub> octahedra and SO<sub>4</sub> tetrahedra (Figure 2.5a). The unique S atom is tetrahedrally coordinated by the oxygen neighbors with the S-O bond distance ranged between 1.489(4)-1.459(4) with an average bond distance of 1.474 Å. The S-atom makes four S-O-Mg linkages through four of its oxygen atoms. BVS<sup>41</sup> calculations (Mg(1) = 2.11, Mg(2) = 2.16) and the average Mg-O bond lengths indicate that the oxidation state of both Mg and S to be +2 and +6 although we expect deviations from these estimates due to the fully and partially covalent nature of the S-O and Mg-O bond respectively. Thus the framework structure [Mg<sub>2</sub>(SO<sub>4</sub>)<sub>12</sub>]<sup>8-</sup> is negatively charged and it gets neutralized by the presence of eight ammonium ions in the unit cell. The structures are built from strictly alternating MgO<sub>6</sub> octahedra and SO<sub>4</sub> tetrahedra units that linked through their vertexes throughout the structure. Both MgO<sub>6</sub> octahedra and SO<sub>4</sub> tetrahedra share corner alternatively to form four- and six- membered rings that form infinite chains. These chains are alternately stacked one over the other along the [100] direction and are interlinked by sharing corners with the tetrahedral corners of the SO<sub>4</sub> groups to form a layer as shown in Figure 2.5a. Within each layer, each sulfate tetrahedra shares three of its corners with the octahedra of three adjacent chains, one due to Mg(1) and two due to Mg(2) (Figure 2.6a). The layers thus formed are cross-linked by SO<sub>4</sub> tetrahedra along the *b*-axis through corner sharing S-O-Mg linkages to form the three-dimensional structure (Figure 2.6b). The interstitial ammonium ions interact with the framework oxygen through strong N-H···O hydrogen bonds.

The details of N-H $\cdots$ O hydrogen bonding interactions are given in (Table 2.3). This compound was thermally stable up to 380 °C which is confirmed by TGA experiment.

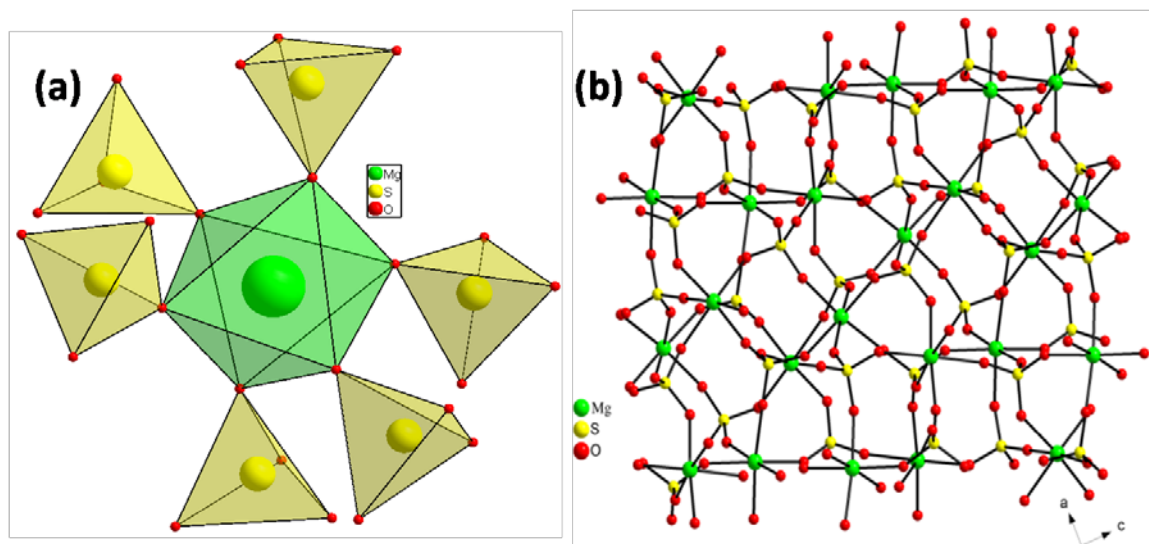


**Figure 2.5.** (a) Pinwheel arrangement of MO<sub>6</sub> octahedra and SO<sub>4</sub> tetrahedra. (b) Top view of the layer parallel to the *ac*-plane of the unit cell in **2**.

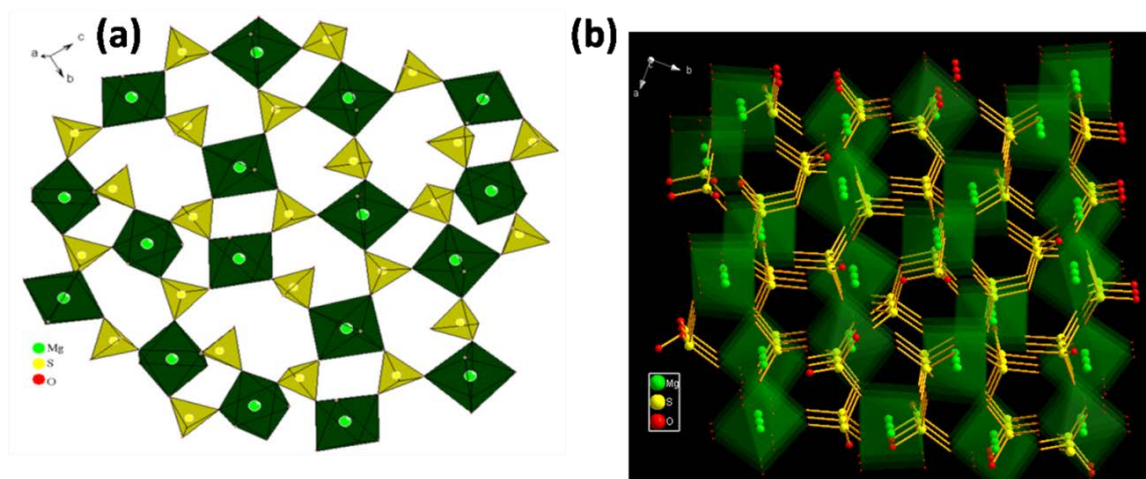


**Figure 2.6.** (a) View of 4-, 6- and 8- membered aperture in *bc*-plane for **2**. (b) Inorganic layers of the compound **2** in *c*-axis. Ammonium ions removed for clarity.

### 2.6.2.1 Adsorption Properties of $[\text{NH}_4]_8[\text{Mg}_2(\text{SO}_4)_{12}]$ , **2**

The rigidity and the porosity of the structure **2** were proven by gas-sorption analysis. Hydrogen adsorption measurements of **2** showed a fully reversible uptake of 0.7 wt% at 77 K and 890 Torr shown in Figure 2.7. However, they are nonporous to nitrogen as its channels size is very small and is almost equal to the kinetic diameter of nitrogen. Although the hydrogen sorption is somewhat less, but well with the value of 0.7 wt % obtained for the highest capacity Zeolite (ZSM-5) and some of Mg-MOFs reported in the literature.<sup>42-43</sup>

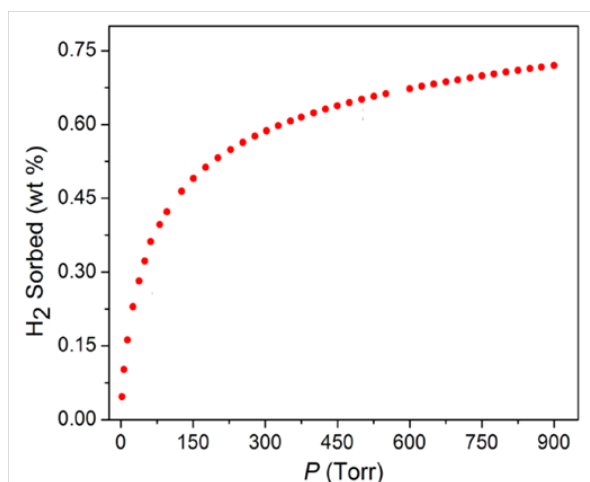


**Figure 2.7.** Hydrogen adsorption isotherms for  $[\text{NH}_4]_8[\text{Mg}_8(\text{SO}_4)_{12}]$ , **2** at 77 K.

### 2.6.3 Structural analysis of $[\text{C}_6\text{N}_2\text{H}_{14}][\text{Bi}(\text{SO}_4)_2(\text{NO}_3)]$ , **3**

The asymmetric unit of **3** contains 23 non-hydrogen atoms out of which 15 belong to the inorganic framework and 8 belong to the extra framework amine molecule. It has one crystallographically independent  $\text{Bi}^{3+}$  cation, two sulfate anions, one nitrate anion and one diprotonated DABCO cation.

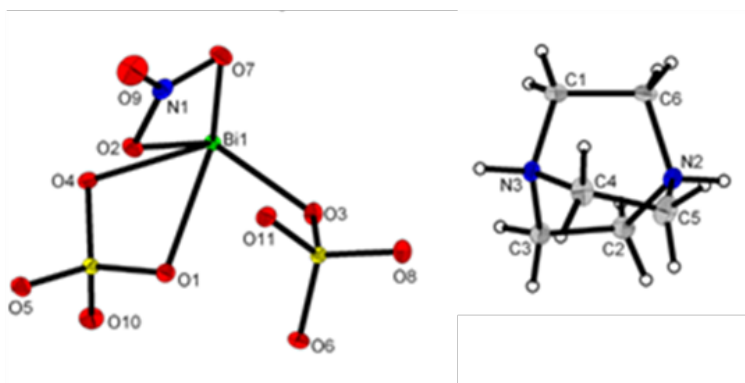
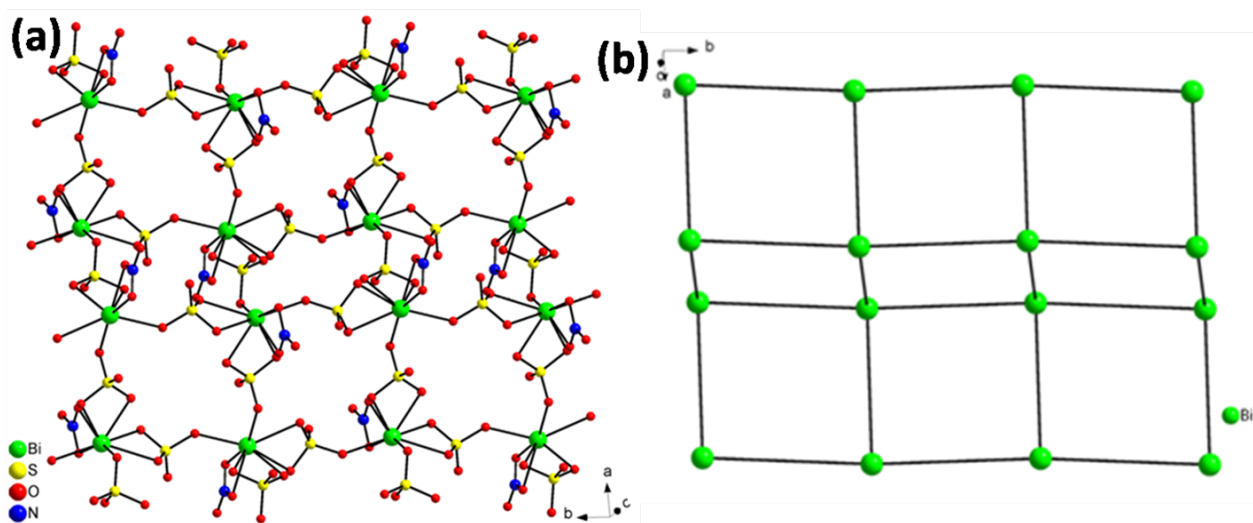


**Figure 2.8.** The asymmetric unit of  $[\text{C}_6\text{N}_2\text{H}_{14}][\text{Bi}(\text{SO}_4)_2(\text{NO}_3)]$ , **3**.

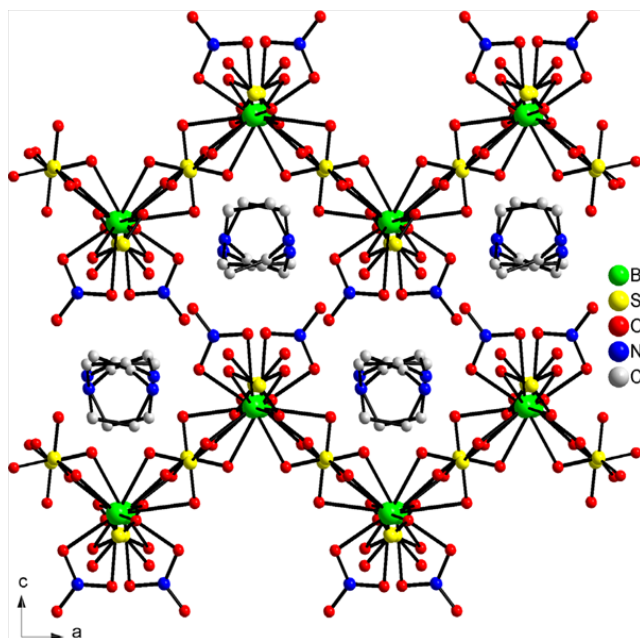
The  $\text{Bi}^{3+}$  cation in **3** is eight-coordinated to two sulfate and one nitrate ions in the bidentate fashion and two sulfate ions in the monodentate fashion. The Bi-O bond distances are in the range of 2.344(18)-2.740(2) Å [ $(\text{Bi-O})_{\text{avg}} = 2.490$  Å]. The O-Bi-O bond angles are in the range 59.03(7)-146.83(6). The selected bond lengths and bond angles are given in the CCDC No: 931288. Of the two framework sulfate anions, both bind to one  $\text{Bi}^{3+}$  cation in a bidentate fashion, and to another  $\text{Bi}^{3+}$  cation in a monodentate manner leaving a terminal S-O bond

Figure 2.8. Bond valence sum calculations for **3** based on the method of Brown and Altermatt,<sup>41</sup> using  $r_0(\text{Bi-O}) = 2.094$  Å, shown that the valence sums for Bi = 2.98 Å. The charges on Bi and S are clearly +3 and +6 respectively. These data are consistent with the stated composition. The linkage of the  $\text{BiO}_8$  polyhedra and the  $\text{SO}_4$  tetrahedra by sharing vertices and edges, gives rise to anionic inorganic layers parallel to the *ab*-plane of the unit cell, containing eight membered rings (Figure 2.9a). The three sulfate tetrahedra and one nitrate ion sharing edges with the  $\text{BiO}_8$  polyhedra bind to the  $\text{Bi}^{3+}$  cation in a *cis* fashion rendering the layers corrugated, with the terminal N-O of the nitrate group pointing out of the *zig-zag* layers. The protonated DABCO molecules reside in the crest and through regions which form hydrogen bonds with the framework oxygen that gives extra stability to the structure. The selected hydrogen bond interactions are given in the Table 2.3. The layer formed by the connectivity of the Bi centers and with the sulfate units can be visualized as (4,

4) net sheets with the Bi centers acting as nodes (Figure 2.9b). The entire structure is formed by the stacking of the (4, 4) net sheets along the *c*-axis of the unit cell. The anionic inorganic layers in **3** are stacked over one another along the *c*-axis of the unit cell in AAA.... fashion and are separated by a half unit cell length along the *c*-axis of the unit cell (Figure 2. 10). The structure of **3** can be compared with the structures of  $[\text{C}_6\text{N}_2\text{H}_{14}]_2 [\text{Ln}_2(\text{SO}_4)_4(\text{H}_2\text{O})_4]$   $[\text{SO}_4][\text{C}_2\text{N}_2\text{H}_8][\text{H}_2\text{O}]_3$ , (*Ln*=La, Pr or Nd),<sup>44</sup>  $[\text{A}] \text{La}_2(\text{H}_2\text{O})_2(\text{C}_2\text{H}_{10}\text{N}_2)_3(\text{SO}_4)_6 \cdot 4\text{H}_2\text{O}$ ,<sup>45</sup>  $\beta\text{-(NH}_4\text{)La(SO}_4\text{)}_2$ , and  $(\text{N}_2\text{H}_5)\text{Nd(H}_2\text{O)(SO}_4\text{)}$ <sup>46</sup> These compounds are built from corrugated anionic layers of rare earth sulfates, with the  $\text{NH}_4^+$ , organic amine and water molecules residing in the inter-lamellar space and interacting with the layers through hydrogen bonds. In (A), the isolated sulfate ion in the interlayer space also form hydrogen bonds with the layers.



**Figure 2.9.** (a) Top view of the layer parallel to the *ab*-plane in **3**, formed by joining the BiO<sub>8</sub> polyhedra and SO<sub>4</sub> tetrahedra, (b) (4, 4) net sheet formed by the joining of the metal centers.



**Figure 2.10.** Stacking of the alternate inorganic layers and protonated DABCO molecules along *c*-axis. Note the wave like pattern of the inorganic layers.

#### 2.6.4 Structural analysis of $[C_4N_2H_{12}]_4[Bi_4(SO_4)_{10}(H_2O)_4]$ , **4**

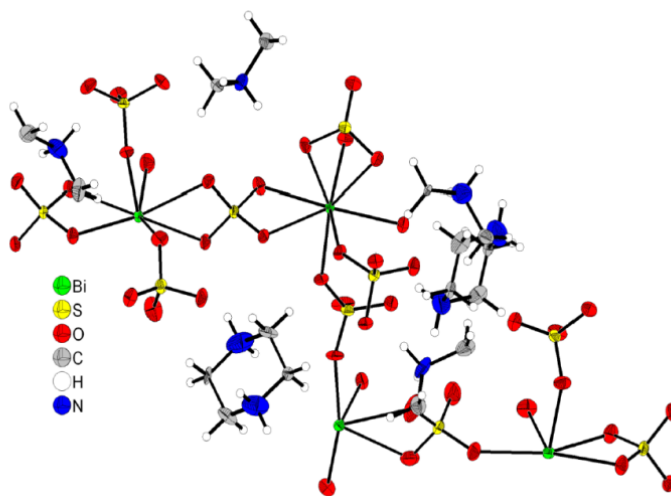


**Figure 2.11.** The asymmetric unit of  $[C_4N_2H_{12}]_4[Bi_4(SO_4)_{10}(H_2O)_4]$ , **4** with atom labeled.

The bismuth sulfate **4** is a three-dimensional net work structure made up of Bi(1)O<sub>9</sub>, Bi(2)O<sub>9</sub>, Bi(3)O<sub>8</sub>, Bi(4)O<sub>8</sub> polyhedra and SO<sub>4</sub> tetrahedra incorporating diprotonated piperazine molecules within the pores. The asymmetric unit of **4** contains 82 non-hydrogen atoms of which 58 belong

to the inorganic framework and 24 belong to the extra framework guest molecule. There are four crystallographically distinct  $\text{Bi}^{3+}$  cations and ten  $\text{SO}_4^{2-}$  anions as shown in Figure 2.11. Both  $\text{Bi}^{3+}(1)$  and  $\text{Bi}^{3+}(2)$  cations are nine-coordinated by the oxygens from five sulfate ions and one water molecule, with each one surrounded by three bidentate sulfate anions and two monodentate sulfate ions.  $\text{Bi}^{3+}(3)$  and  $\text{Bi}^{3+}(4)$  cations are eight coordinated by the oxygens from five sulfate ions and one water molecule, with each metal ion surrounded by two bidentate sulfate anions and three monodentate sulfate ions.  $\text{Bi}(1)\text{O}_9$  linked to the  $\text{Bi}(2)\text{O}_9$  polyhedra through sulfate tetrahedra by sharing edges and corners with  $\text{S}(10)\text{O}_4$  and  $\text{S}(7)\text{O}_4$ , respectively, there by forming an infinite chain along the [001] direction.  $\text{Bi}(2)\text{O}_9$  linked to  $\text{Bi}(3)\text{O}_8$  and  $\text{Bi}(4)\text{O}_8$  polyhedra through sulfate anions by sharing edges with  $\text{S}(4)\text{O}_4$  and corner with  $\text{S}(8)\text{O}_4$  tetrahedra along the *a*-axis.  $\text{S}(5)\text{O}_4$  and  $\text{S}(6)\text{O}_4$  tetrahedra share corners with  $\text{Bi}(3)\text{O}_8$  and  $\text{Bi}(4)\text{O}_8$  polyhedra respectively through Bi(3)-O-S linkages along the *c*-axis parallel to the Bi(1)-O-S-O-Bi(2) infinite chain.  $\text{S}(2)\text{O}_4$ ,  $\text{S}(9)\text{O}_4$ ,  $\text{S}(4)\text{O}_4$ ,  $\text{S}(3)\text{O}_4$  and  $\text{S}(8)\text{O}_4$  tetrahedra connect the infinite chains by sharing edges and corners with the  $\text{BiO}_n$  polyhedral of the adjacent chain along the *a*-axis to form a two-dimensional sheet in the *ac*-plane containing 8- and 12-membered aperture unit (Figure 2.12). A (4, 6) net sheet is formed by joining the metal centers of the four bismuth polyhedra (Figure 2.13). The layers are cross linked by the  $\text{S}(1)\text{O}_4$  and  $\text{S}(3)\text{O}_4$  tetrahedra along the *b*-axis to form the three-dimensional structure possessing channels along the *b*- and *c*-axes (Figure 2.12b). The channels are filled by the diprotonated amine cations which are in two different orientations interact with the framework oxygen through strong N-H $\cdots$ O and C-H $\cdots$ O hydrogen bonds (Selected hydrogen bond interactions given in Table 2.3). The Bi-O distances fall in the range 2.292(4)-2.632(5) Å with an average distance of 2.483 Å. The S atoms are at the centers of tetrahedral sulfate ions as expected. The S atoms

form (4-n) S-O-Bi bonds and n terminal S-O bonds, the actual number of the latter differing from one to another. The average lengths of the S-O bonds are 1.475(S-O-Bi) and 1.456 Å (terminal S-O) with the O-S-O bond angles in the range 103.3(3)-113.0(3) (details bond distances and bond angles are given in CCDC No: 931289). BVS calculations confirm the oxidation states of Bi and S to be +3 and +6, respectively. The framework stoichiometry of  $[\text{Bi}_4(\text{SO}_4)_{10}]^{8-}$ , with a net framework charge of -8, is balanced by the diprotonated four PIP molecules present inside the channels.

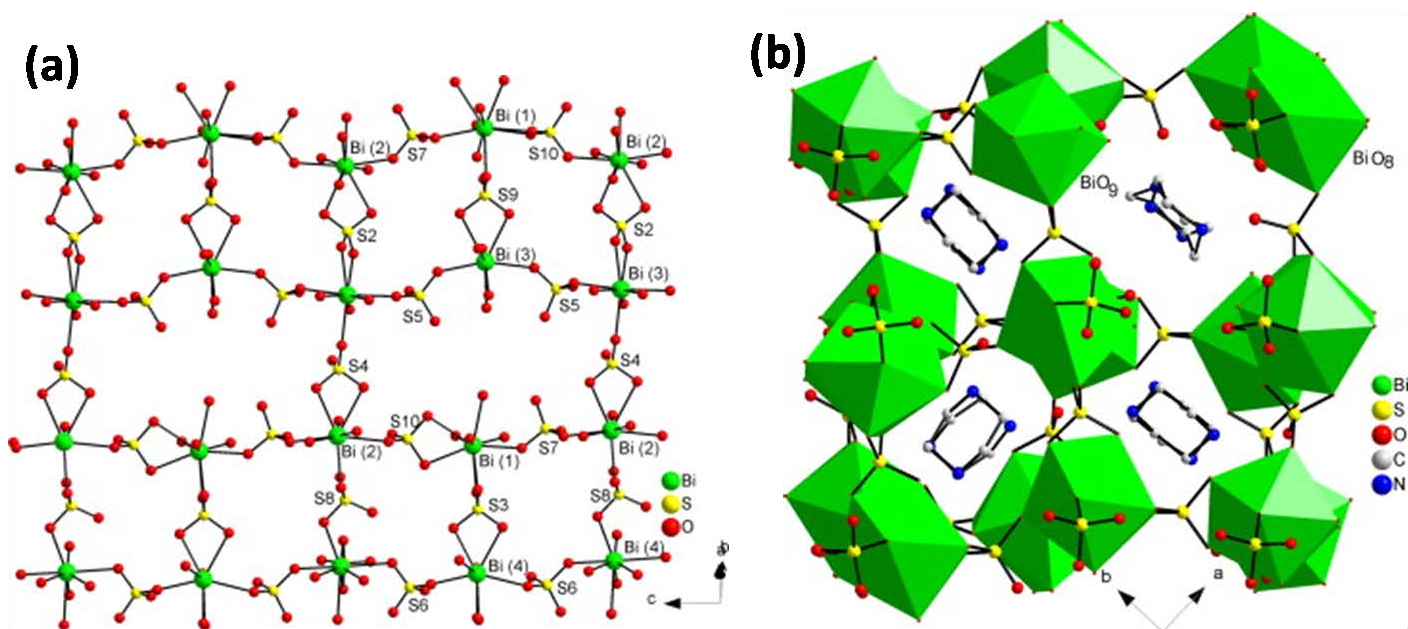


**Figure 2.12.** (a) View down 8- membered and 12- membered rings along *a*-axis. (b) Protonated amine molecules are sitting inside the channels. Hydrogen atoms omitted for clarity.

;

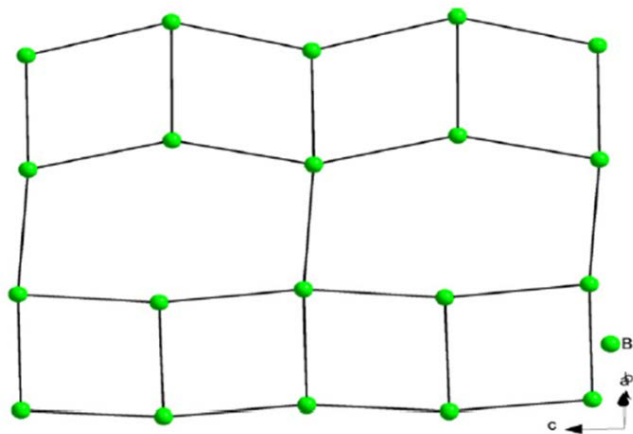


**Figure 2.13.** (4, 6) net sheet in **4** formed by joining of the metal centers.

#### 2.6.4.1 Photoluminescence studies

The optical properties of  $\text{Bi}^{3+}$  ions are governed, as a rule, to the electron transitions between the states  $6s^2$  and  $6s6p$ . Its luminescence properties are usually explained with respect to the energy-level scheme  $^1S_0 < ^3P_0 < ^3P_1 < ^3P_2 < ^1P_1$ .<sup>47-51</sup> The excited levels corresponding to the configuration  $6s6p$  are the triplet levels  $^3P_0$ ,  $^3P_1$ , and  $^3P_2$  and the singlet level  $^1P_1$  while the ground state is fully symmetric ( $^1S_0$ ). The transition  $^1S_0$ - $^3P_2$  is forbidden by the selection rule for the total momentum of the atom  $J$ . The transition  $^1S_0$ - $^3P_1$  is allowed owing to the spin-orbital interaction of the  $^3P_1$  and  $^1P_1$  states. The transitions  $^1S_0$ - $^3P_1$  and  $^1S_0$ - $^1P_1$ , the first of which is longer-wave, are realized in the bands of optical absorption and excitation of the photoluminescence of bismuth activated substances. The common property of bismuth compounds is the presence of wide-band luminescence, which is a nonradiative transition, and is attributed to the lowest-frequency allowed transition of  $^3P_1$ - $^1S_0$ . Also, the charge-transfer transition from the  $\text{SO}_4^{2-}$  ion to the empty  $6p$  level of the  $\text{Bi}^{3+}$  ion is possible. Generally the former is known to occur easily in many cases.<sup>52</sup> Furthermore, the luminescence of Bi ions usually appears in the visible wavelength region and bismuth containing organic/inorganic hybrid materials has been reported to display blue luminescence properties.<sup>53-55</sup> The room-temperature photoluminescence properties **3** and **4** were studied by exciting the sample at 280 nm. The emission spectra of them are almost similar

exhibiting blue photoluminescence (Figure 2.14). The optical image of the blue photoluminescence was taken in a confocal microscope (in set of Figure 2.14). On excitation at 280 nm, **3** and **4** show two intense emission peaks around 410, and 486 nm, respectively. The intense emission peak occurred at 410 nm, maybe assigned to the ligand to metal charge transfer or the  $^1P_1-^1S_0$  and  $^3P_1-^1S_0$  transition of the  $s^2$  electron of  $\text{Bi}^{3+}$  cation as discussed above. The less intense peak is likely arises from a combination of factors involving the presence of dinuclear  $\text{Bi}_2\text{O}_2$  unit, absence of organic amine and the different coordination sphere with respect to  $\text{Bi}^{3+}$  cation.  $\text{Bi}^{3+}$  is nine-coordinated in **3**, and both eight- and nine- coordinated in **4**. Similar blue luminescence has been seen for bismuth containing organic-inorganic hybrid materials.

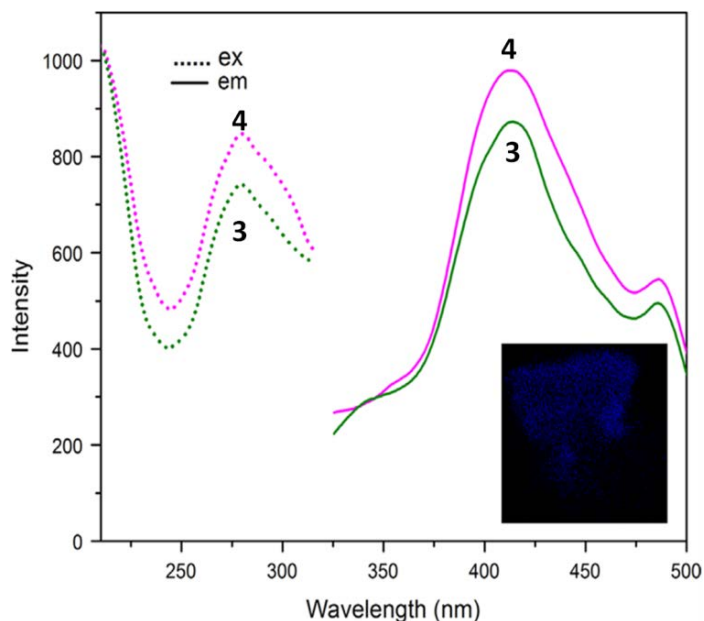


**Figure 2.14.** Excitation and emission spectra of compounds **3** and **4**. In set show an optical image of the blue luminescent compound of **4** using confocal microscope.

#### 2.6.4.2 Lifetime studies

Time-resolved fluorescence measurement was carried out using a time-correlated single-photon counting (TCSPC) spectrometer (Edinburgh, OB920). The samples were excited at 375 nm using a diode laser and the signals were collected at magic angle (54.7°) using a Hamamatsu micro channel plate photo multiplier tube (R3809U-50). The lamp profile was recorded by scatterer (dilute ludox solution in water) in place of the sample. The instrument response function of our setup is 75 ps for 375 nm diode laser which was determined from full width half maxima (FWHM) of the lamp profile. The decay curve was analyzed by nonlinear least-squares iteration procedure using F900 decay analysis software. The qualities of the fit were judged by the chi square ( $\chi^2$ ) value, and visual inspection of the residuals of the fitted function to the data. Mean fluorescence lifetime ( $\tau_f$ ) for the tri-exponential iterative fittings was calculated from the decay times ( $\tau_i$ ) and the relative amplitude ( $a_i$ ) using the following equation (2.1)

$$\langle \tau_f \rangle = a_1\tau_1 + a_2\tau_2 + a_3\tau_3 \quad (2.1)$$

The luminescence lifetimes of the excited states of both **3** and **4** were investigated. The emission band for samples was monitored for the lifetime studies employing 375 nm, excitation at room temperature. The fit of the curve for tri-exponential decay suggests a mean lifetime value of 0.9 and 1.0 ns for **3** and **4**, respectively (Figure 2.15).

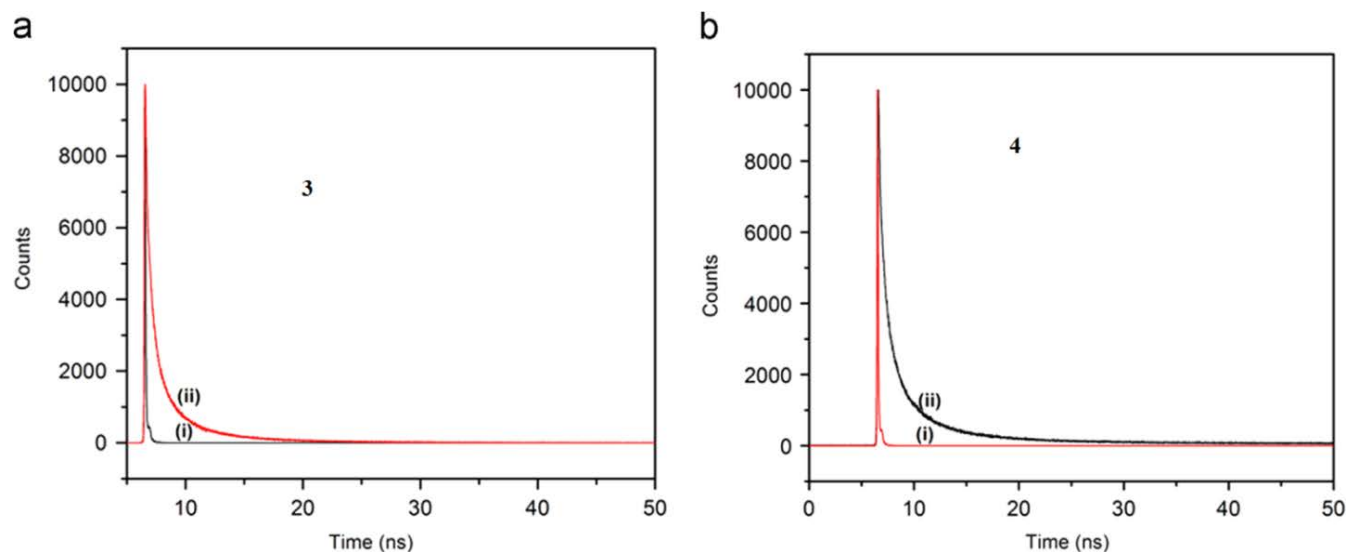


**Figure 2.15.** Time-resolved fluorescence behavior of **3** and **4** at  $\lambda_{\text{exc}}=375$  nm. In the figure, (i) instrument response function and (ii) monitoring wavelengths at 420 nm decay profile measured at 298 K.

### 2.6.5 Structural analysis of $[\text{C}_3\text{N}_2\text{H}_{12}][\text{Sn}_2(\text{SO}_4)_3]$ , **5**

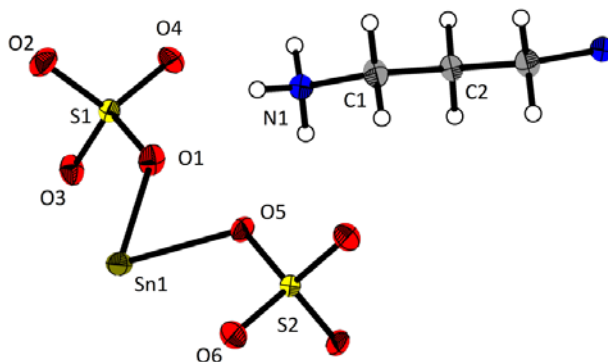


**Figure 2.16.** Asymmetric unit of  $[\text{C}_3\text{N}_2\text{H}_{12}][\text{Sn}_2(\text{SO}_4)_3]$ , **5**.

The asymmetric unit of the compound **5** contains 11 non-hydrogen atoms. Out of which, 9 belongs to inorganic framework and 3 belongs to protonated amine molecule. There are one crystallographically independent tin, two sulfur and 6 oxygen atoms are present. Tin atom is connecting with two oxygen atoms from two sulfate group by monodendate fashion through Sn-O-S linkage (Figure 2.16). In the anionic polymer, all the Sn atoms having trigonal pyramidal geometry with three oxygen atoms and one lone pair of the electrons which are presumably

occupies the base vertex of tetrahedron. The anionic chain structure is based on network strictly alternating the  $\text{SnO}_3$  and  $\text{SO}_4$  unit which forms a framework with formula  $[\text{Sn}(\text{SO}_4)_2]_n^{2-}$ . The infinite tin(II) sulfate chains are formed with 8- membered rings by vertex sharing of the  $\text{SnO}_3$  trigonal pyramidal with  $\text{SO}_4$  tetrahedra in  $ab$ -plane shown in Figure 2.17a. Of the one sulfate anion two oxygen atoms are connecting with  $\text{SnO}_3$  by leaving remaining two oxygen as  $\text{S}=\text{O}$ . The bonds which are coordinating with oxygen atoms are longer than the terminal  $\text{S}=\text{O}$  bond. The bond lengths for  $\text{Sn}-\text{O}$  are ranging between 2.157(17)-2.257(16) Å ( $\text{Sn}-\text{O}_{\text{avg}}-2.207\text{Å}$ ) and for  $\text{S}-\text{O}$  ranging between 1.4609(17)-1.4943(16) Å ( $\text{S}-\text{O}_{\text{avg}}-1.477\text{Å}$ ). The bond angles for  $\text{O}-\text{Sn}-\text{O}$  are 78.87(6)-84.59(6)° ( $\text{O}-\text{Sn}-\text{O}_{\text{avg}}-81.73^\circ$ ) and for  $\text{O}-\text{S}-\text{O}$  are 107.54(10) -113.35(15)° ( $\text{O}-\text{S}-\text{O}_{\text{avg}}-110.45^\circ$ ) (Detailed bond lengths and bond angles given in CCDC No: 1472106 ). From the BVS calculations by using Brown and Altermatt,<sup>41</sup>  $r_o(\text{Sn}-\text{O} = 1.984)$ , shown that the valence sum for  $\text{Sn}(1) = 2.05$ . The charges on both Sn and S are +2 and +6 respectively. The anionic  $[\text{Sn}(\text{SO}_4)_2]^{2-}$  part was neutralized by the cationic template amine  $[\text{C}_3\text{N}_2\text{H}_{12}]^{2+}$ . These template amines can make a hydrogen bond with anionic framework of oxygen atoms for acquiring the extra stability of the polymer (Figure 2.17b). (Detailed hydrogen bond interactions are given in Table 2.4).

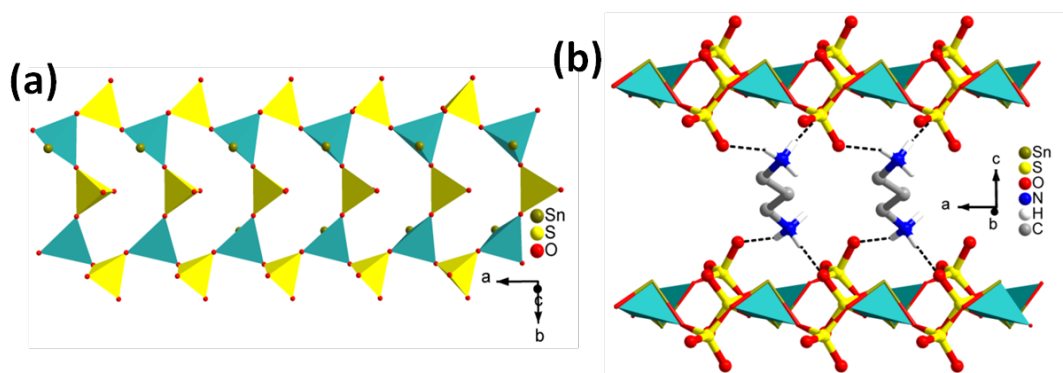


**Figure 2.17** (a) The anionic chain of the compound  $[\text{C}_3\text{N}_2\text{H}_{12}][\text{Sn}(\text{SO}_4)_2]$ , **5** in  $ab$ -plane. (b) The protonated amine molecules are resided in between the two chains in the  $ac$ -plane.

### 2.6.6 Structural analysis of $[\text{C}_2\text{N}_2\text{H}_{10}][\text{Sn}(\text{SO}_4)_2]$ , **6**

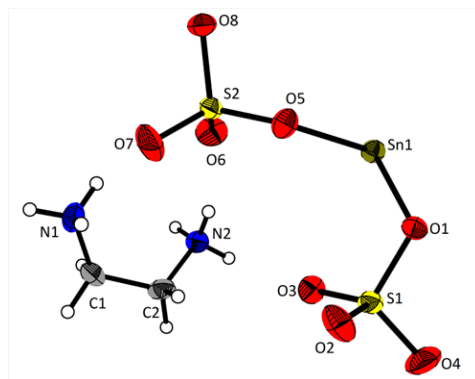


**Figure 2.18.** Asymmetric unit of  $[\text{C}_2\text{N}_2\text{H}_{10}][\text{Sn}(\text{SO}_4)_2]$ , **6** shown with atom labeling.

Asymmetric unit of compound **6** contains 15 non-hydrogen atoms out of which 11 belong to the anionic framework and 4 belong to the extra framework amine molecules. There is one crystallographically independent  $\text{Sn}^{2+}$  cation, two sulfate anions and one diprotanated 1, 3-dap cation. In asymmetric unit, Sn atom is coordinated with two oxygen atoms in a monodendate fashion from two different sulfate ions (Figure 2.18). From bond valance sum calculations<sup>41</sup> concludes that charges of both Sn and S were +2 and +6 respectively The average bond lengths for all Sn-O are 2.478-2.157Å ( $\text{Sn-O}_{\text{avg}}$ -2.317Å) and S-O 1.511(2)-1.441(3)Å ( $\text{S-O}_{\text{avg}}$  = 1.476 Å). The bond angles for O-Sn-O 121.57-76.11° ( $\text{O-Sn-O}_{\text{avg}}$ -98.84°) and for O-S-O 112.09(15)-106.69(13)° ( $\text{O-S-O}_{\text{avg}}$ -109.39°) (CCDC No: 1472107 ). All the Sn atoms in **6** square pyramidal geometry with four oxygen atoms from four different sulfates groups and one lone pair of electrons. Of the two framework sulfate anions, two oxygens bind to two adjacent  $\text{Sn}^{2+}$  cations by monodendate manner by leaving two terminal S=O. The anionic chain of  $[\text{Sn}(\text{SO}_4)_2]^{2-}$  was formed by infinite tin sulfate chains by 4- and 12- membered ring channels with corner sharing of  $\text{SnO}_4$  square pyramidal with  $\text{SO}_4$  tetrahedra shown in Figure 2.19a. The extra cationic organic template forms H-bonding interaction ( $\text{N-H}\cdots\text{O} = 148^\circ$ ,  $\text{H}\cdots\text{O} = 2\text{Å}$ ) (Total H-bond interactions

given in Table 2.4) between the anionic layers which induces extra stability to the polymer as shown in the Figure 2. 19b.

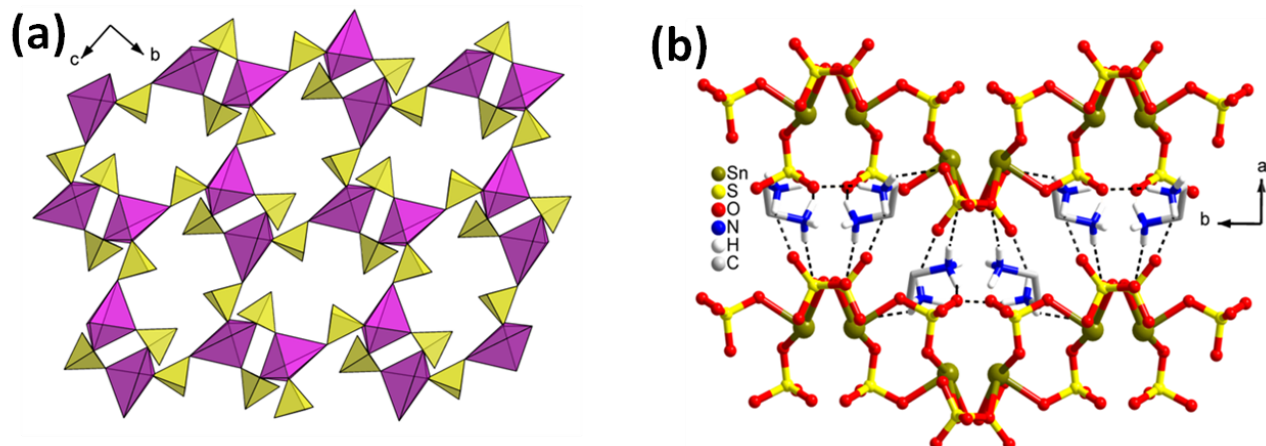


**Figure 2.19.** (a) The anionic layer of the compound  $[\text{C}_2\text{N}_2\text{H}_{10}][\text{Sn}(\text{SO}_4)_2]$ , **6** in *bc*-plane. (b) Packing of the amine molecules and anionic layers in compound **6** in *ab*-plane.

### 2.6.7 Structural analysis of $[\text{C}_3\text{N}_2\text{H}_{12}][\text{Sn}(\text{SO}_4)_2]$ , **7**

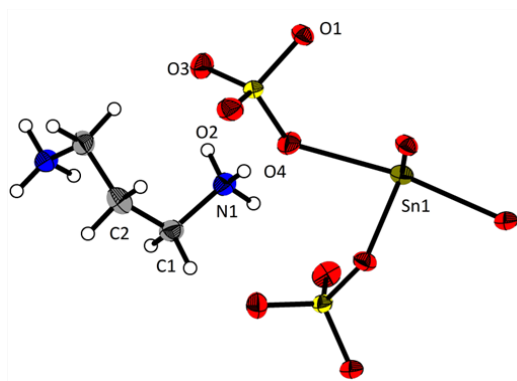


**Figure 2.20.** Asymmetric unit of  $[\text{C}_3\text{N}_2\text{H}_{12}][\text{Sn}(\text{SO}_4)_2]$ , **7** shown with atom labeling.

The asymmetric unit of the compound **7** contains 9 non-hydrogen atoms, out of which 6 belongs to the inorganic group and 3 belongs to the protonated amine molecules. In the inorganic group there are one crystallographically distinct tin and one sulfate group which was in tetrahedra. In the asymmetric unit, Sn atom was connected with one oxygen atom from sulfate group by

monodendate fashion through Sn-O-S linkage by leaving remaining three oxygen atoms (Figure 2.20). The Bond distance for Sn-O are ranging between 2.187(11)-2.402(12)Å (Sn-O<sub>avg</sub>-2.294Å) and for S-O ranging between 1.436(13)-1.525(11)Å (S-O<sub>avg</sub>-1.480Å). The Bond angles for O-Sn-O were 78.46-158-84° (O-Sn-O<sub>avg</sub>-118.65°) and for O-S-O 105.93(7)-113.18(8)° (O-S-O<sub>avg</sub>-109.55°). The selected bond lengths and bond angles are given in the CCDC No: 1472108. From BVS<sup>41</sup> calculations conclude that valances for both Sn and S atoms are +2 and +6 respectively. In the anionic chain of **7**, Sn atom was truncated square pyramidal geometry with four oxygen atoms from two sulfate groups and one invisible unpaired electron. The anionic chain of [Sn(SO<sub>4</sub>)<sub>2</sub>]<sup>2-</sup> was formed by infinite tin sulfate chains by 4- membered ring with corner sharing of SnO<sub>4</sub> square pyramidal with SO<sub>4</sub> tetrahedra (Figure 2. 21a). Two oxygen atoms of sulfate group is participating in the bonding with SnO<sub>4</sub> by leaving terminal S=O bonds. The corner shared chain structures are very interest because chain structures are important for considered secondary building for the open-framework materials. The protonated amine molecules are resided in between the individual layers through Hydrogen bond for making extra stability of the polymer (Detailed hydrogen bonds given in the Table 2.4) shown in the Figure 2.21b).

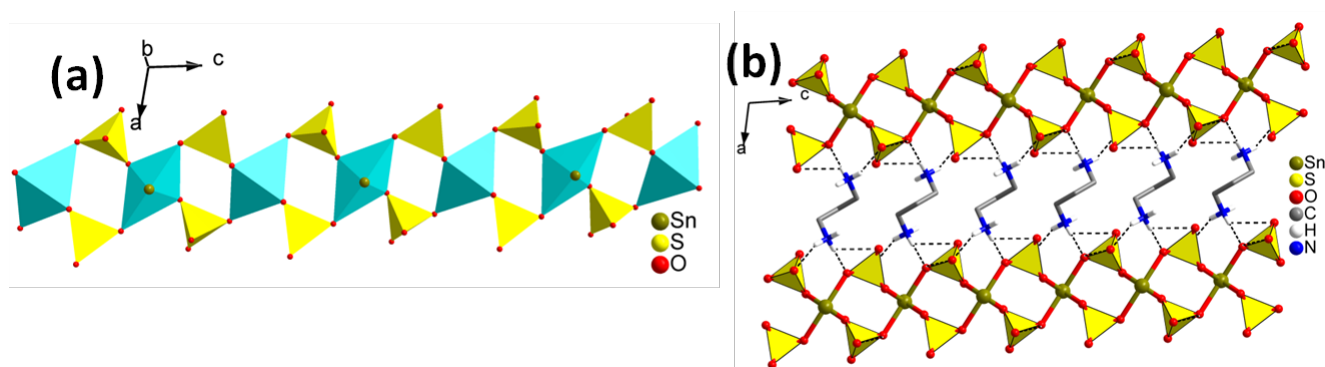


**Figure 2.21.** (a) View of 4- membered ring along *c*-axis. (b) Organic templates are resided in between the two anionic chains in *ac*-plane.

### 2.6.8 Structural analysis of $[\text{C}_4\text{N}_2\text{H}_{14}][\text{Sn}(\text{SO}_4)_2]\cdot\text{H}_2\text{O}$ , **8**

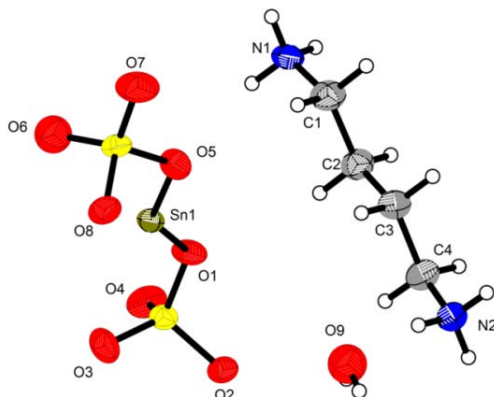


**Figure 2.22.** Asymmetric unit of  $[\text{C}_4\text{N}_2\text{H}_{14}][\text{Sn}(\text{SO}_4)_2]\cdot\text{H}_2\text{O}$ , **8**.

The asymmetric unit of the compound **8** contains 18 non-hydrogen atoms, in which 11 atoms belongs to the anionic group, 6 belongs to the protonated amine molecule and one non coordinated water molecule (Figure 2.22). In anionic group there are one crystallographic distinct Sn, two sulfur and 8 oxygen atoms present. The asymmetric unit of compound **8** similar to as **6** an extra water molecule is present in the compound **8**. From BVS calculations<sup>41</sup> indicating that valence states for various species in polymer are  $\text{Sn}^{2+}$  and  $\text{S}^{6+}$ . The bond distances for Sn-O are ranging between 2.165(3)-2.405(3) Å with ( $\text{Sn-O}_{\text{avg}}$ -2.285 Å) and bond angles for O-Sn-O ranging from 75.06(12)-148.67(11)° ( $\text{O-Sn-O}_{\text{avg}}$ -111.86°). The bond lengths and bond angles are given in the CCDC No: 1472116. The structure of **8** is constructed by altering network of  $\text{SnO}_4$  and  $\text{SO}_4$  units forming infinite anionic layers. All the Sn atoms in polymer having same coordination number with trigonal pyramidal geometry. The anionic layer of two sulfates have same connectivity by two oxygen atoms are bind to  $\text{Sn}^{2+}$  by bidentate manner, and to another oxygen by monodentate manner to adjacent tin ion by leaving terminal S=O bond.  $[\text{Sn}(\text{SO}_4)_2]_n^{2-}$  is formed with 4- and 12- membered rings by corner sharing of  $\text{SO}_4$  tetrahedra with  $\text{SnO}_4$  in *bc*-plane shown in the Figure 2. 23a. Connectivity of the  $\text{Sn}^{2+}$  centers and with sulfate unit of sulfur

can form 6- membered apertures with Sn atom acting as node (Figure 2.23b). The anionic inorganic layers of compound **8** stacked over one another along *c*-axis of the unit cell in AAA...fashion. The protonated amine and water molecules are resided in between the apertures which form hydrogen bond with inorganic framework oxygen atoms for making stability of the polymer (Figure 2.24).The selected hydrogen bond interactions are given in the Table 2.4.

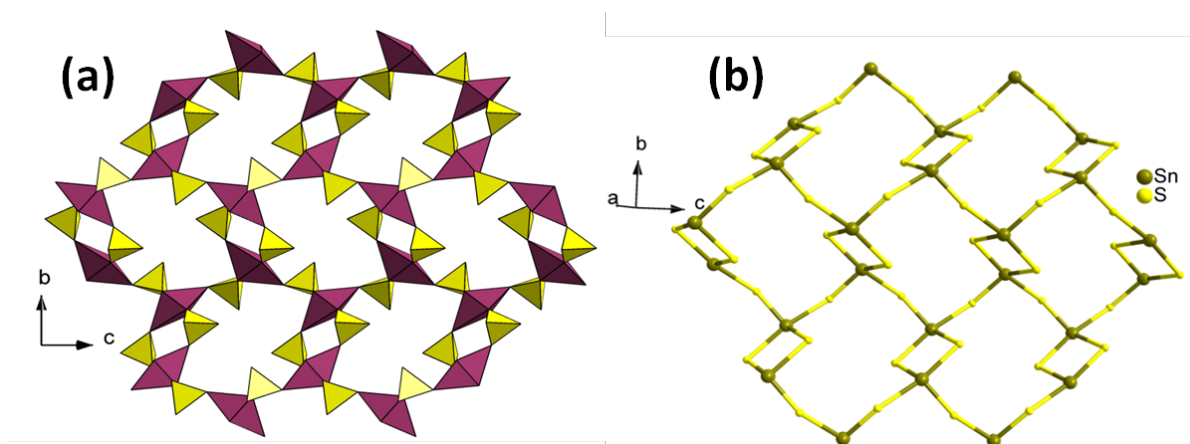


**Figure 2.23.** The anionic layer of the compound  $[C_4N_2H_{14}][Sn(SO_4)_2][H_2O]$ , **8** in *bc*-plane. (b) (4, 12) net sheet formed by the joining of the metal centers for compound **8**.

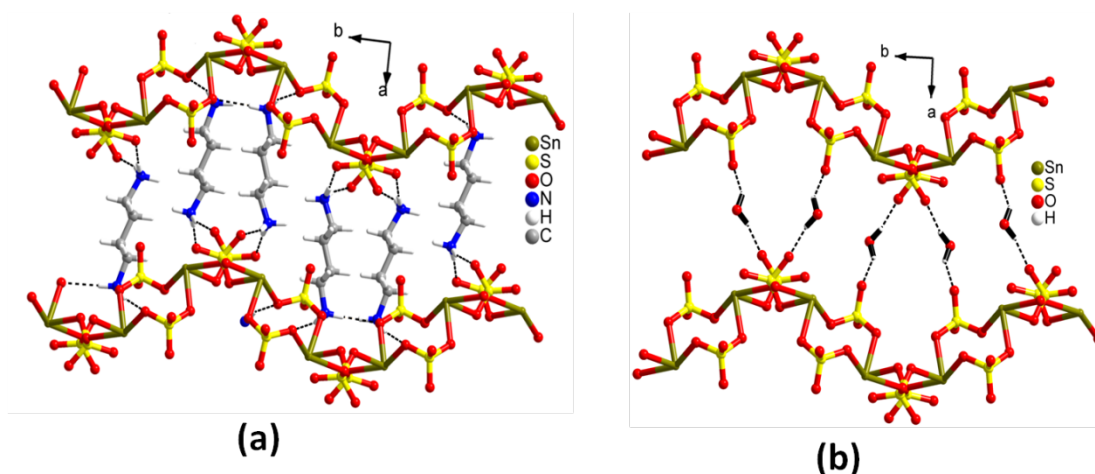


**Figure 2.24.** (a) Possible hydrogen bonding interactions between the two anionic layers and amine molecules in *ba*-plane (b) With water molecules in **8**

## 2.7 Conclusions

In summary, we synthesized 8 open-framework metal sulfates by using the light weight (Mg) and heavy weight (Bi, Sn) main group metal atoms by changing the different structure directing agents. All the compounds were well characterized by complementary techniques like PXRD, SCXRD, chemical analysis TGA, IR, and EDAX. Two Mg(II) compounds with composition  $[\text{NH}_4]_2[\text{Mg}_3(\text{OH})_2(\text{SO}_4)_3(\text{H}_2\text{O})_2]$ , **1** and  $[\text{NH}_4]_8[\text{Mg}_2(\text{SO}_4)_{12}]$ , **2** were synthesized by hydro/solvo thermal method where the ammonium ion acts as template. Compound **1** is formed by diamond kind of chains with four- and six- membered rings. Compound **2** is crystallized with three dimensional with chirality. This compound shows reversible hydrogen adsorption of 0.7 wt% respectively at 77 K. Two bismuth-sulfate frameworks with the compositions  $[\text{C}_6\text{N}_2\text{H}_{14}][\text{Bi}(\text{SO}_4)_2(\text{NO}_3)]$ , **3** and  $[\text{C}_4\text{N}_2\text{H}_{12}]_4[\text{Bi}_4(\text{SO}_4)_{10}(\text{H}_2\text{O})_4]$ , **4** were synthesized by slow evaporation method. Compound **3** has a corrugated layered structure with 8- membered aperture where in the  $\text{SO}_4$  tetrahedra and the  $\text{BiO}_8$  polyhedra join together to form (4, 4) net sheets of the metal centers while **4** has three-dimensional structure possessing 8- and 12- membered channels. Both the compounds show good fluorescence properties exhibiting blue luminescence. Time-resolved fluorescence behavior of **3** and **4** shows mean fluorescence life time of 0.9 and 1.0 ns, respectively. Four new Sn(II) sulfate materials with the compositions  $[\text{C}_3\text{N}_2\text{H}_{12}][\text{Sn}_2(\text{SO}_4)_3]$ , **5**;  $[\text{C}_2\text{N}_2\text{H}_{10}][\text{Sn}(\text{SO}_4)_2]$ , **6**;  $[\text{C}_3\text{N}_2\text{H}_{12}][\text{Sn}(\text{SO}_4)_2]$ , **7** and  $[\text{C}_4\text{N}_2\text{H}_{14}][\text{Sn}(\text{SO}_4)_2][\text{H}_2\text{O}]$ , **8** have been synthesized by hydrothermal condition using 1,3-diamino propane (for **5**, **7**), ethylenediamine (for **6**) and DABCO (for **8**) as structure directing organic amines. The ratio of Sn/S for all the four compounds is <1. In compound **5**,  $\text{Sn}^{\text{II}}$  ions three coordination with trigonal pyramidal geometry but in **6-8** four coordination with truncated square pyramidal. All the structures are slightly distorted due the presence of lone pair of electrons on tin atoms which are occupied in

the base vertex. The organic templates are present in between the anionic layers and render hydrogen bond through N-H...O for extra stability of the polymer.

## 2.8 References

1. Cheetham, A. K.; Ferey, G.; Loiseau, T., *Angew. Chem., Int. Ed.* **1999**, *38*, 3268.
2. Rao, C. N. R.; Natarajan, S.; Choudhury, A.; Neeraj, S.; Ayi, A. A., *Acc. Chem. Res.* **2001**, *34*, 80.
3. Livage, C.; Egger, C.; Ferey, G., *Chem. Mater.* **1999**, *11*, 1546.
4. Li, H.; Eddaoudi, M.; Groy, T. L.; Yaghi, O. M., *J. Am. Chem. Soc.* **1998**, *120*, 8571.
5. Guillou, N.; Pastre, S.; Livage, C.; Ferey, G., *Chem. Commun.* **2002**, 2358.
6. Choudhury, A.; Kumar D, U.; Rao, C. N. R., *Angew. Chem., Int. Ed.* **2002**, *41*, 158.
7. Udayakumar, D.; Rao, C. N. R., *J. Mater. Chem.* **2003**, *13*, 1635.
8. Pasha, I.; Choudhury, A.; Rao, C. N. R., *J. Solid State Chem.* **2003**, *174*, 386.
9. Udayakumar, D.; Dan, M.; Rao, C. N. R., *Eur. J. Inorg. Chem.* **2004**, 1733.
10. Paul, G.; Choudhury, A.; Sampathkumaran, E. V.; Rao, C. N. R., *Angew. Chem., Int. Ed.* **2002**, *41*, 4297.
11. Behera, J. N.; Paul, G.; Choudhury, A.; Rao, C. N. R., *Chem. Commun.* **2004**, 456.
12. Paul, G.; Choudhury, A.; Rao, C. N. R., *Chem. Mater.* **2003**, *15*, 1174.
13. Behera, J. N.; Rao, C. N. R., *J. Am. Chem. Soc.* **2006**, *128*, 9334.
14. Paul, G.; Choudhury, A.; Nagarajan, R.; Rao, C. N. R., *Inorg. Chem.* **2003**, *42*, 2004.
15. Natarajan, S.; Mandal, S., *Angew. Chem. Int. Ed.* **2008**, *47*, 4798.
16. Fu, Y.; Zhang, Y.; Xu, Z., *Dalton Trans.* **2008**, 4792.
17. Poonia, N. S.; Bajaj, A. V., *Chem. Rev.* **1979**, *79*, 389.
18. Cheon, Y. E.; Park, J.; Suh, M. P., *Chem. Commun.* **2009**, 5436.

19. Dinca, M.; Long, J. R., *J. Am. Chem. Soc.* **2005**, *127*, 9376.
20. Stergiannakos, T.; Tylianakis, E.; Klontzas, E.; Froudakis, G. E., *J. Phys. Chem. C* **2010**, *114*, 16855.
21. Sun, H.; Sadler, P. J., *Top. Biol. Inorg. Chem.* **1999**, *2*, 159.
22. Leonard, N. M.; Oswald, M. C.; Freiberg, D. A.; Nattier, B. A.; Smith, R. C.; Mohan, R. S., *J. Org. Chem.* **2002**, *67*, 5202.
23. Nikol, H.; Vogler, A., *J. Am. Chem. Soc.* **1991**, *113*, 8988.
24. Rao, C. N. R.; Behera, J. N.; Dan, M., *Chem. Soc. Rev.* **2006**, *35*, 375.
25. Natarajan, S.; Cheetham, A. K., *Chem. Commun.* **1997**, 1089.
26. Vaidhyanathan, R.; Natarajan, S., *J. Mater. Chem.* **1999**, *9*, 1807.
27. Natarajan, S.; Vaidhyanathan, R.; Rao, C. N. R.; Ayyappan, S.; Cheetham, A. K., *Chem. Mater.* **1999**, *11*, 1633.
28. Natarajan, S.; Attfield, M. P.; Cheetham, A. K., *Angew. Chem. Int. Ed* **1997**, *36*, 978.
29. Natarajan, S.; Eswaramoorthy, M.; N. R. Rao, C.; Natarajan, S.; K. Cheetham, A., *Chem. Commun.* **1998**, 1561.
30. Ramaswamy, P.; Natarajan, S., *Eur. J. Inorg. Chem.* **2006**, *2006*, 3463.
31. Skeels, G.; Flanigen, E., *Stud. Surf. Sci. Catal.* **1989**, *49*, 331.
32. Andersen, I. K.; Andersen, E. K.; Knudsen, N.; Skou, E., *Solid State Ionics* **1991**, *46*, 89.
33. Wang, Y.; Xu, J.-n.; Sun, J.-y.; Wang, L.; Sun, F.-x.; Fan, Y.; Xin, M.-h.; Shi, S.-h.; Zhu, G.-s., *J. Mol. Struct.* **2006**, *797*, 140.
34. Detkov, D. G.; Gorbunova, Y. E.; Kazarinova, A. S.; Mikhailov, Y. N.; Kokunov, Y. V., *RUSS J COORD CHEM* **2003**, *29*, 451.

35. Nakamoto, K., *Infrared and Raman spectra of inorganic and coordination compounds*. Wiley Online Library: 1986.
36. Sheldrick, G. M., *SHELXL-97, program for X-ray crystal structure refinement*, University of Göttingen, Germany **1997**.
37. Sheldrick, G. M., *SHELXTL-PLUS Program for Crystal Structure Solution and Refinement*, University of Göttingen, Göttingen, Germany.
38. Sheldrick, G. M., *SADABS Siemens Area Correction Absorption Program*, University of Göttingen, Göttingen, Germany **1994**.
39. Pennington, W., *J. Appl. Crystallogr.* **1999**, *32*, 1028.
40. Farrugia, L., *J. Appl. Crystallogr.* **1997**, *30*, 565.
41. Brown, I. D.; Altermatt, D., *Acta Cryst. B* **1985**, *41*, 244.
42. Mallick, A.; Saha, S.; Pachfule, P.; Roy, S.; Banerjee, R., *J. Mater. Chem.* **2010**, *20*, 9073.
43. Senkovska, I.; Kaskel, S., *Eur. J. Inorg. Chem.* **2006**, 4564.
44. Dan, M.; Behera, J. N.; Rao, C. N. R., *J. Mater. Chem.* **2004**, *14*, 1257.
45. Bataille, T.; Louer, D., *J. Mater. Chem.* **2002**, *12*, 3487.
46. Govindarajan, S.; Patil, K. C.; Manohar, H.; Werner, P. E., *J. Chem. Soc., Dalton Trans.* **1986**, 119.
47. Blasse, G.; Meijerink, A.; Nomes, M.; Zuidema, J., *J. Phys. Chem. Solids* **1994**, *55*, 171.
48. Peng, M.; Wang, C.; Chen, D.; Qiu, J.; Jiang, X.; Zhu, C., *J. Non-Cryst. Solids* **2005**, *351*, 2388.
49. Bordun, O. M., *J. Appl. Spectrosc.* **2002**, *69*, 67.

50. Meng, X.-g.; Qiu, J.-r.; Peng, M.-y.; Chen, D.-p.; Zhao, Q.-z.; Jiang, X.-w.; Zhu, C.-s., *Opt. Express* **2005**, *13*, 1635.
51. Komatsu, M.; Oyoshi, K.; Hishita, S.; Matsuishi, K.; Onari, S.; Arai, T., *Mater. Chem. Phys.* **1998**, *54*, 286.
52. Lin, J.; Su, Q.; Wang, S.; Zhang, H., *J. Mater. Chem.* **1996**, *6*, 265.
53. Yu, X.; Zhang, H.; Cao, Y.; Chen, Y.; Wang, Z., *J. Solid State Chem.* **2006**, *179*, 247.
54. Srivastava, A. M.; Beers, W. W., *J. Lumin.* **1999**, *81*, 293.
55. Folkerts, H. F.; Zuidema, J.; Blasse, G., *Chem. Phys. Lett.* **1996**, *249*, 59.

## 2.9 Appendix

**Table 2.2.** Crystal data structure refinement parameters for **1-8** compounds

Parameters	<b>1</b>	<b>2</b>	<b>3</b>
Empirical formula	$[\text{NH}_4]_2[\text{Mg}_3(\text{SO}_4)_3(\text{OH})_2(\text{H}_2\text{O})_2]$	$[\text{NH}_4]_8[\text{Mg}_2(\text{SO}_4)_{12}]$	$[\text{C}_6\text{N}_2\text{H}_{14}][\text{Bi}(\text{SO}_4)_2(\text{NO}_3)]$
$a$ (Å)	18.2294(13)	10.0022(8)	9.70(4)
$b$ (Å)	7.5534(5)	10.0022(8)	13.36(6)
$c$ (Å)	9.8334(6)	10.0022(8)	20.74(8)
$\alpha$ (°)	90	90	90
$\beta$ (°)	90	90	90
$\gamma$ (°)	90	90	90
$V$ (Å <sup>3</sup> )	1354(16)	1000.66(14)	2691(19)
$Z$	4	12	8
Formula weight	467.24	124.29	577.30
Space group	Cmc2(1)(36)	$P2(1)3(198)$	Pbca(61)
$T$ (°C)	23	23	23
$\lambda$ (MoK $\alpha$ ) Å	0.71073	0.71073	0.71073
$\rho_{\text{calc}}$ (gcm <sup>-3</sup> )	2.292	2.475	2.850
$\mu$ (mm <sup>-1</sup> )	0.786	0.943	13.484
R[I.>2 $\sigma$ (I)]	R1=0.0290 wR2=0.0688	R1 = 0.0162 wR2 = 0.0440	R1 = 0.0215 wR2 = 0.0531
R (all data)	R1=0.0344 wR2=0.0724	R1 = 0.0163, wR2 = 0.0441	R1 = 0.0273 wR2 = 0.0555

$$R_1 = \sum |F_o| - |F_c|; wR_2 = \{ [w(F_o^2 - F_c^2)^2] / [w(F_o^2)^2] \}^{1/2}, w = 1 / [\sigma^2(F_o)^2 + (aP)^2 + bP] P = [F_o^2 + 2F_c^2] / 3;$$

Where  $a = 0.0$ ;  $b = 0.0$  for **1**,  $a = 0.0176$ ;  $b = 0.713$  for **2** and  $a = 0.0300$ ;  $b = 0.3$  for **3**.

Parameters	<b>4</b>	<b>5</b>	<b>6</b>
Empirical formula	[C <sub>4</sub> N <sub>2</sub> H <sub>12</sub> ] <sub>4</sub> [Bi <sub>4</sub> (SO <sub>4</sub> ) <sub>10</sub> (H <sub>2</sub> O) <sub>4</sub> ]	[C <sub>3</sub> N <sub>2</sub> H <sub>12</sub> ][Sn <sub>2</sub> (SO <sub>4</sub> ) <sub>3</sub> ]	[C <sub>2</sub> N <sub>2</sub> H <sub>10</sub> ][Sn(SO <sub>4</sub> ) <sub>2</sub> ]
<i>a</i> (Å)	19.84(9)	4.5793(5)	8.41240(10)
<i>b</i> (Å)	19.35(9)	16.9707(17)	11.7070(2)
<i>c</i> (Å)	13.21(6)	8.8416(9)	10.1430(2)
α(°)	90	90	90
β(°)	91.93(10)	90	96.7270(10)
γ(°)	90	90	90
<i>V</i> (Å <sup>3</sup> )	5071.3(4)	687.12(12)	992.05(3)
<i>Z</i>	4	2	4
Formula weight	2213.14	601.71	372.93
Space group	P2 <sub>1</sub> /c (14)	P22(1)2(1)	P2(1)/C
<i>T</i> (°C)	23	23	23
λ(MoKα) Å	0.71073	0.71073	0.71073
ρ <sub>calc</sub> (gcm <sup>-3</sup> )	2.899	2.908	2.497
μ (mm <sup>-1</sup> )	14.381	4.159	3.025
R[I.>2σ(I)]	R1 = 0.0385, wR2 = 0.0761	R1 = 0.0149, wR2 = 0.0389	R1 = 0.0220, wR2 = 0.0546
R (all data)	R1 = 0.0628, wR2 = 0.0837	R1 = 0.0151, wR2 = 0.0389	R1 = 0.0260, wR2 = 0.0578

$$R_1 = \sum |F_o| - |F_c|; wR_2 = \{ [w(F_o^2 - F_c^2)^2] / [w(F_o^2)^2] \}^{1/2}, w = 1 / [\sigma^2(F_o)^2 + (aP)^2 + bP] P = [F_o^2 + 2Fc^2] / 3;$$

Where a = 0.0300; b = 2.50 for **4**, a = 0.0180; b = 0.2642 for **5** and a = 0.0330; b = 1.957 for **6**.

Parameters	<b>7</b>	<b>8</b>
Empirical formula	[C <sub>3</sub> N <sub>2</sub> H <sub>12</sub> ][Sn(SO <sub>4</sub> ) <sub>2</sub> ]	(C <sub>4</sub> N <sub>2</sub> H <sub>14</sub> )(Sn(SO <sub>4</sub> ) <sub>2</sub> ).H <sub>2</sub> O
<i>a</i> (Å)	11.7218(3)	10.6735(12)
<i>b</i> (Å)	10.2997(3)	13.8200(15)
<i>c</i> (Å)	9.3416(2)	9.6015(10)
α(°)	90	90
β(°)	100.985(2)	107.780
γ(°)	90	90
<i>V</i> (Å <sup>3</sup> )	1107.16(5)	1348.6(3)
<i>Z</i>	4	4
Formula weight	386.96	419.00
Space group	C2/C	P2(1)/c
<i>T</i> (°C)	23	23
λ(MoKα) Å	0.71073	0.71073
ρ <sub>calc</sub> (gcm <sup>-3</sup> )	2.321	2.064
μ (mm <sup>-1</sup> )	2.715	2.234
R[I.>2σ(I)]	R1 = 0.0177, wR2 = 0.0408	R1 = 0.0414, wR2 = 0.1024
R (all data)	R1 = 0.0196, wR2 = 0.0416	R1 = 0.0518, wR2 = 0.1155

$$R_1 = \frac{\sum |F_o| - |F_c|}{\sum |F_o|}; \quad wR_2 = \frac{\{[\sum w(F_o^2 - F_c^2)^2] / [\sum w(F_o^2)]\}^{1/2}}{[\sigma^2(F_o)^2 + (aP)^2 + bP]} \quad P = [\sum F_o^2 + 2F_c^2] / 3;$$

Where a= 0.0207; b= 0.2814 for **7** and a=0.0527; b= 1.2700 for **8**

**Table 2.3.** The Hydrogen Bonding Interactions for the compound **1-4**

<b>[NH<sub>4</sub>]<sub>2</sub>[Mg<sub>3</sub>(OH)<sub>2</sub>(SO<sub>4</sub>)<sub>3</sub>(H<sub>2</sub>O)<sub>2</sub>], <b>1</b></b>				
D-H...A	D...A(A°)	H...A(A°)	D...H(A°)	D-H...A(A°)
N(1)-H(1)···O(9)	2.936(2)	2.33(5)	0.71(5)	145(5)
N(1)-H(2)···O(7)	3.041(2)	2.28(3)	0.85(4)	149(3)
N(1)-H(3)···O(3)	3.162(2)	2.38(5)	0.86(5)	151(4)
N(1)-H(3)···O(10)	3.054(2)	2.40(5)	0.86(5)	132(4)
N(1)-H(4)···O(7)	3.166(2)	2.55(5)	0.89(5)	128(4)
N(1)-H(4)···O(10)	3.015(2)	2.43(6)	0.89(5)	124(4)
O(1)-H(6)···O(5)	3.130(2)	2.24(4)	0.89(4)	174(4)
O(9)-H(10A)···O(4)	3.0040(18)	2.17(3)	0.84(3)	174(3)
O(9)-H(10A)···O(8)	2.9808(19)	2.44(3)	0.84(3)	124(2)
O(9)-H(10B)···O(10)	2.8331(19)	2.26(4)	0.62(5)	154(5)
<b>[NH<sub>4</sub>]<sub>8</sub>[Mg<sub>2</sub>(SO<sub>4</sub>)<sub>12</sub>], <b>2</b></b>				
N(10)-H(1)···O(1)	2.9139(17)	2.09(3)	0.87(3)	158(3)
N(10)-H(2)···O(3)	3.0432(17)	2.37(2)	0.86(2)	135.6(17)
N(10)-H(2)···O(3)	3.0432(17)	2.37(2)	0.86(2)	135.6(17)
N(10)-H(2)···O(3)	3.0432(17)	2.37(2)	0.86(2)	135.6(17)
N(20)-H(3)···O(4)	2.9164(18)	2.10(3)	0.85(2)	161 (4)
<b>[C<sub>6</sub>N<sub>2</sub>H<sub>14</sub>][Bi(SO<sub>4</sub>)<sub>2</sub>(NO<sub>3</sub>)], <b>3</b></b>				
N(1)-H(20B)···O(9)	3.172(9)	2.29	0.9	166
N(1)-H(20C)···O(34)	3.126(8)	2.42	0.9	136
N(1)-H(20C)···O(38)	2.807(7)	2.11	0.9	134
N(2)-H(21B)···O(42)	2.978(8)	2.33	0.9	129
N(2)-H(21B)···O(31)	2.942(7)	2.13	0.9	149
N(2)-H(21C)···O(6)	2.951(7)	2.1	0.9	157
N(3)-H(22A)···O(15)	3.228(9)	2.47	0.9	142
N(5)-H(24A)···O(26)	2.888(7)	2.12	0.9	143
N(5)-H(24A)···O(43)	3.251(8)	2.59	0.9	166
<b>[C<sub>4</sub>N<sub>2</sub>H<sub>12</sub>]<sub>4</sub>[Bi<sub>4</sub>(SO<sub>4</sub>)<sub>10</sub>(H<sub>2</sub>O)<sub>4</sub>], <b>4</b></b>				
N(3)-H(7A)···O(2)	3.209(3)	2.58	0.91	166
N(3)-H(7A)···O(11)	2.776(3)	1.94	0.91	136
N(2)-H(8B)···O(4)	3.106(3)	2.4	0.91	134
N(2)-H(8B)···O(8)	2.813(3)	2.04	0.91	129
C(1)-H(1A)···O(7)	3.184(4)	2.41	0.97	149
C(2)-H(2A)···O(5)	3.390(3)	2.53	0.97	157
C(2)-H(2B)···O(4)	3.232(3)	2.29	0.97	142
C(3)-H(3A)···O(1)	3.310(3)	2.48	0.97	143
C(3)-H(3A)···O(5)	3.448(3)	2.56	0.97	130
C(3)-H(3B)···O(6)	3.163(3)	2.55	0.97	168
C(3)-H(3B)···O(1)	3.144(3)	2.35	0.97	169
C(4)-H(4A)···O(9)	3.244(4)	2.6	0.97	173

**Table 2.4.** The Hydrogen Bonding Interactions for the compound **5-8**

<b>[C<sub>3</sub>N<sub>2</sub>H<sub>12</sub>] [Sn(SO<sub>4</sub>)<sub>2</sub>], 5</b>				
D-H...A	D...A(A <sup>o</sup> )	H...A(A <sup>o</sup> )	D...H(A <sup>o</sup> )	D-H...A(A <sup>o</sup> )
N(1)-H(1A)...O(1)	2.791(3)	2.40	0.89	107
N(1)-H(1A)...O(4)	3.073(3)	2.22	0.89	160
N(1)-H(1A)...O(5)	2.884(3)	2.46	0.89	110
N(1)-H(1B)...O(6)	2.956(3)	2.08	0.89	166
N(1)-H(1C)...O(2)	2.995(3)	2.15	0.89	158
N(1)-H(1A)...O(3)	2.929(3)	2.39	0.89	119
C(1)-H(1E)...O(2)	3.395(3)	2.48	0.97	158
<b>[C<sub>2</sub>N<sub>2</sub>H<sub>10</sub>] [Sn(SO<sub>4</sub>)<sub>2</sub>], 6</b>				
N(1)-H(1C)...O(7)	2.925(4)	2.32	0.89	125
N(1)-H(1C)...O(6)	2.959(4)	2.29	0.89	132
N(1)-H(1D)...O(1)	2.903(4)	2.02	0.89	169
N(1)-H(1E)...O(2)	2.884(4)	2.36	0.89	118
N(1)-H(1E)...O(6)	3.285(4)	2.6	0.89	135
N(2)-H(1C)...O(4)	2.799(4)	2.65	0.89	148
N(2)-H(1C)...O(4)	2.948(4)	2.4	0.89	120
N(2)-H(1D)...O(3)	2.923(3)	2.21	0.89	137
N(2)-H(2D)...O(7)	2.797(4)	2.40	0.89	108
N(2)-H(1E)...O(6)	2.817(3)	1.95	0.89	165
<b>[C<sub>3</sub>N<sub>2</sub>H<sub>12</sub>] [Sn(SO<sub>4</sub>)<sub>2</sub>], 7</b>				
N(1)-H(3A)...O(1)	2.987(19)	2.11	0.89	168
N(1)-H(3A)...O(3)	3.117(19)	2.59	0.89	119
N(1)-H(3B)...O(2)	2.837(19)	1.96	0.89	167
N(1)-H(3B)...O(2)	2.964(2)	2.58	0.89	107
N(1)-H(3C)...O(4)	2.911(2)	2.02	0.89	179
C(1)-H(1A)...O(3)	3.410(2)	2.57	0.97	144
<b>[C<sub>4</sub>N<sub>2</sub>H<sub>14</sub>] [Sn(SO<sub>4</sub>)<sub>2</sub>][H<sub>2</sub>O], 8</b>				
N(1)-H(1C)...O(8)	2.932(5)	2.05	0.89	170
N(1)-H(1D)...O(7)	2.813(5)	2.05	0.89	144
N(1)-H(1E)...O(5)	2.963(5)	2.11	0.89	161
O(1W)-H(1W)...O(6)	2.726(6)	2.03	0.83	141
N(2)-H(2C)...O(3)	2.825(6)	1.94	0.89	175
N(2)-H(2D)...O(1)	3.113(5)	2.55	0.89	122
N(2)-H(2D)...O(4)	2.970(6)	2.1	0.89	165
N(2)-H(2D)...O(1W)	2.807(6)	1.92	0.89	173
O(1W)-H(2W)...O(4)	2.862(6)	2.08	0.83	157
C(4)-H(4A)...O(6)	3.336(7)	2.37	0.97	178

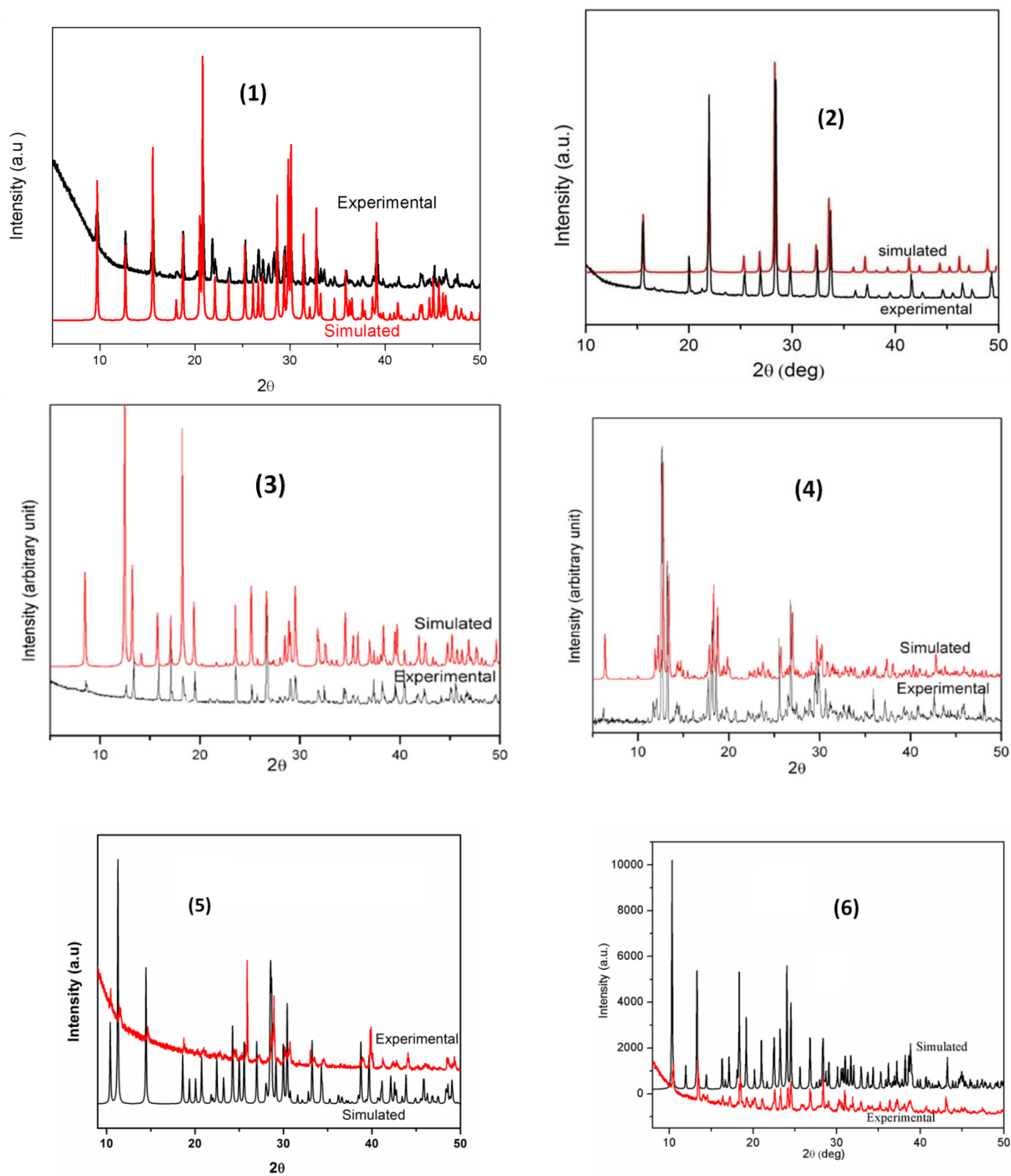


**Figure 2.25.** Experimental and simulated PXRD patterns of compounds from **1-6**

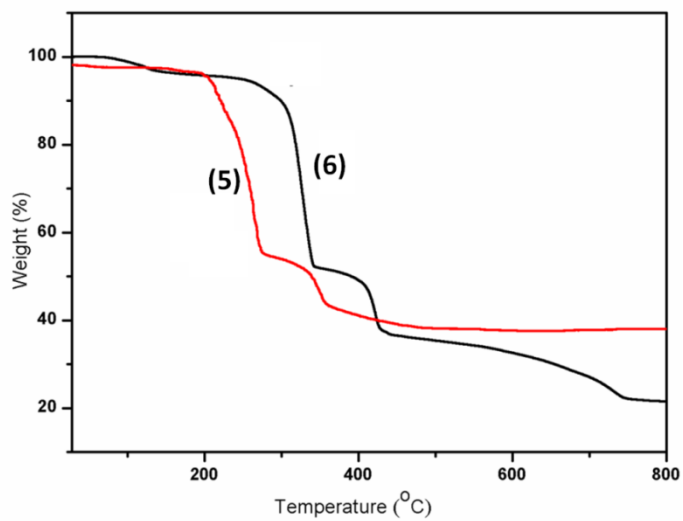
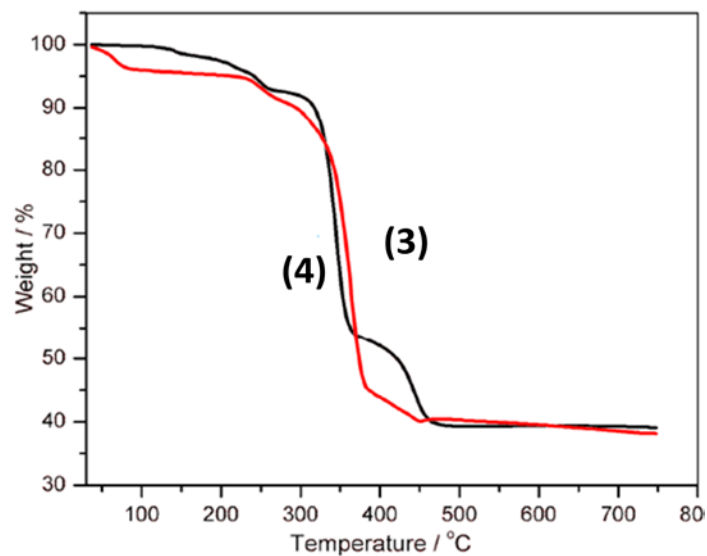
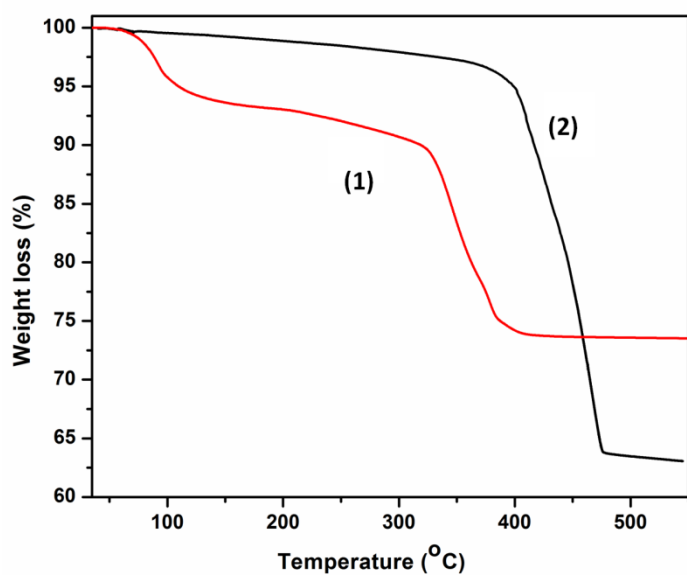


**Figure 2.26.** Thermogravimetric analysis for the compounds **1-6**.

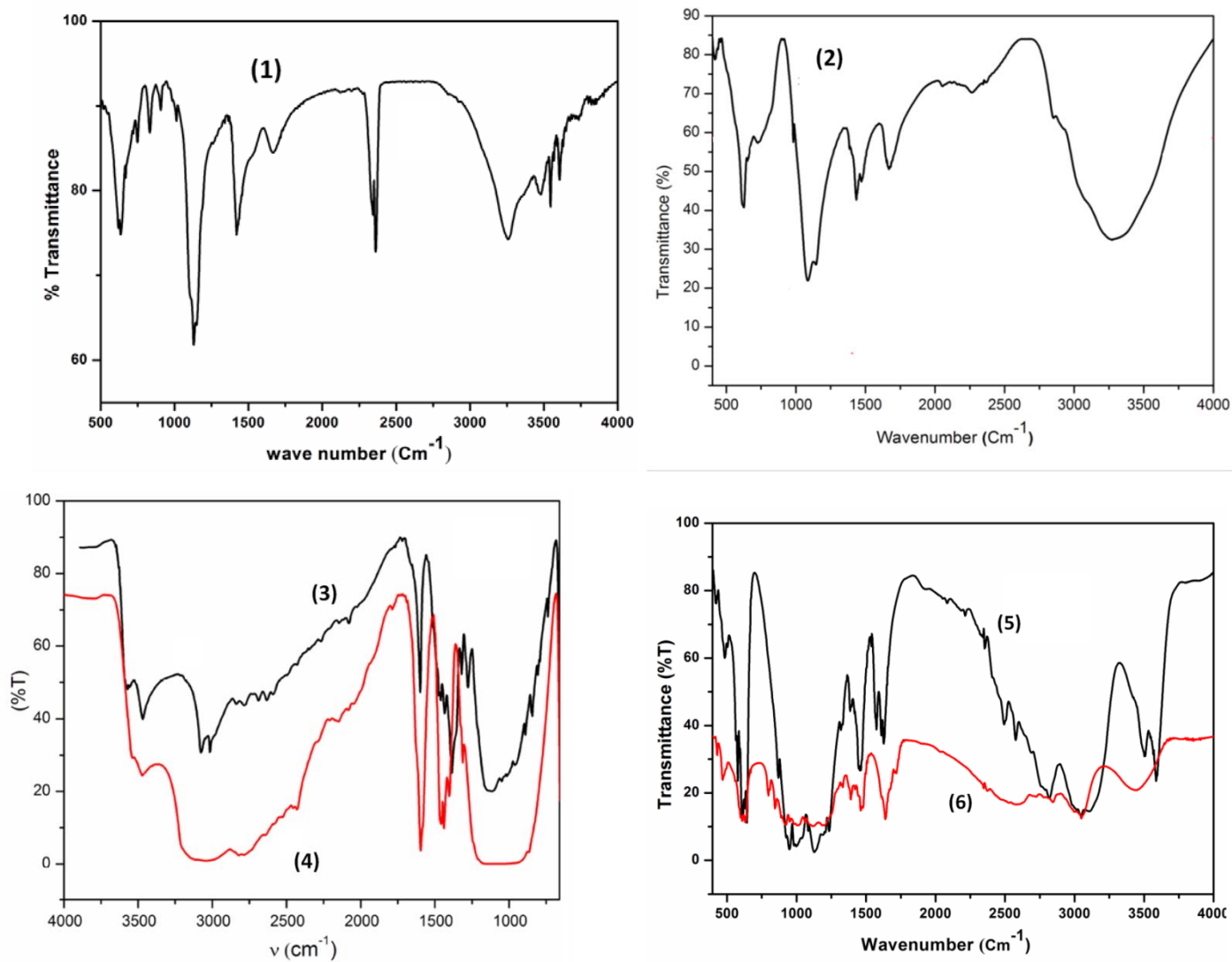


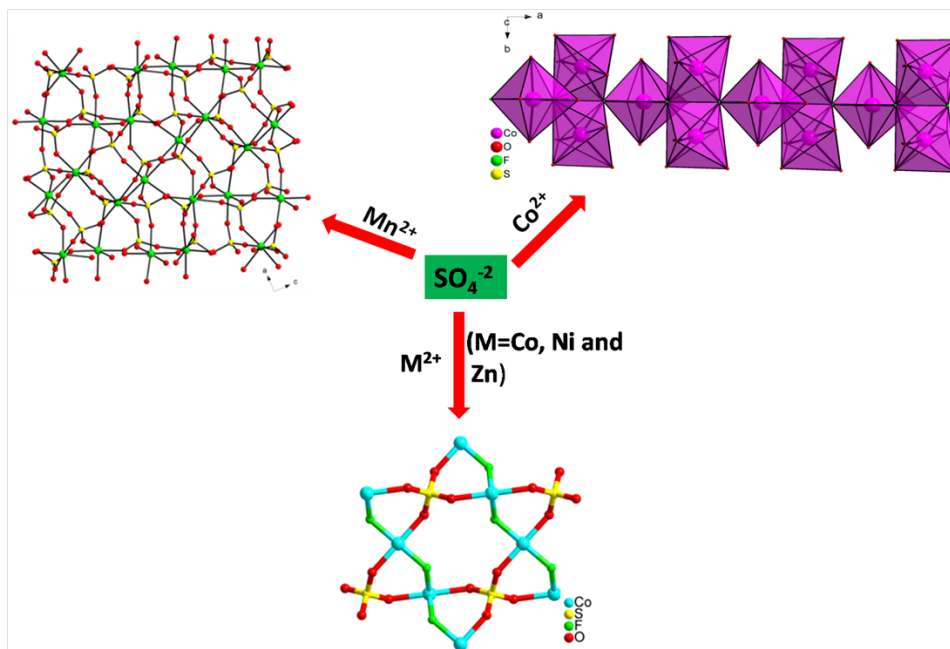
**Figure 2.27.** FTIR spectra for the compounds 1-6.

## CHAPTER-3

### Open-Framework Transition Metal Sulfates

3.1	Abstract	118
3.2	Introduction	119
3.3	Experimental section	122
3.3.1	[H <sub>3</sub> O][MSO <sub>4</sub> F][M=Co (9), Ni (10) and Zn (11)]	122
3.3.2	[C <sub>4</sub> N <sub>2</sub> H <sub>12</sub> ] <sub>2</sub> [Co <sub>3</sub> F <sub>2</sub> (SO <sub>4</sub> ) <sub>3</sub> (H <sub>2</sub> O) <sub>2</sub> ], 12	123
3.3.3	[NH <sub>4</sub> ] <sub>8</sub> [Mn <sub>8</sub> (SO <sub>4</sub> ) <sub>12</sub> ], 13	123
3.4	Characterization	124
3.5	Single-crystal structure determination	126
3.6	Results and discussion	127
3.6.1	Structural analysis of [H <sub>3</sub> O][MSO <sub>4</sub> F](where M= Co (9), Ni (10) and Zn (11))	127
3.6.1.1	Magnetic properties of [H <sub>3</sub> O][MSO <sub>4</sub> F](where M= Co (9) and Ni (10))	130
3.6.2	Structural analysis of [C <sub>4</sub> N <sub>2</sub> H <sub>12</sub> ] <sub>2</sub> [Co <sub>3</sub> F <sub>2</sub> (SO <sub>4</sub> ) <sub>3</sub> (H <sub>2</sub> O) <sub>2</sub> ], 12	131
3.6.2.1	Magnetic properties for [C <sub>4</sub> N <sub>2</sub> H <sub>12</sub> ] <sub>2</sub> [Co <sub>3</sub> F <sub>2</sub> (SO <sub>4</sub> ) <sub>3</sub> (H <sub>2</sub> O) <sub>2</sub> ], 12	134
3.6.3	Structural analysis of [NH <sub>4</sub> ] <sub>8</sub> [Mn <sub>8</sub> (SO <sub>4</sub> ) <sub>12</sub> ], 13	137
3.6.3.1	Temperature dependent PXRD for [NH <sub>4</sub> ] <sub>8</sub> [Mn <sub>8</sub> (SO <sub>4</sub> ) <sub>12</sub> ], 13	139
3.6.3.2	First Principle Studies for [NH <sub>4</sub> ] <sub>8</sub> [Mn <sub>8</sub> (SO <sub>4</sub> ) <sub>12</sub> ], 13	140
3.6.3.3	Magnetic Properties for [NH <sub>4</sub> ] <sub>8</sub> [Mn <sub>8</sub> (SO <sub>4</sub> ) <sub>12</sub> ], 13	144
3.6.3.4	Adsorption Properties for [NH <sub>4</sub> ] <sub>8</sub> [Mn <sub>8</sub> (SO <sub>4</sub> ) <sub>12</sub> ], 13	145
3.6.3.5	Proton Conductivity Study for [NH <sub>4</sub> ] <sub>8</sub> [Mn <sub>8</sub> (SO <sub>4</sub> ) <sub>12</sub> ], 13	146
3.7	Conclusions	148
3.8	References	149
3.9	Appendix	156

### 3.1 Abstract



In this chapter we reported 5 open-framework transition metal sulfates synthesised by hydro/solvothermal method. Compounds **9-11** with composition  $[H_3O][MSO_4F]$  ( $M=Co$  (**9**),  $Ni$  (**10**) and  $Zn$  (**12**)) were crystallized as three-dimensional framework with Kagome type structure. Both **9** and **10** shows paramagnetic behavior with weak antiferromagnetic nature. Compound **12** with composition  $[C_4N_2H_{12}]_2[Co_3F_2(SO_4)_3(H_2O)_2]$  was crystallized with diamond kind of structure. It shows ferrimagnetic nature with a transition at 10.8 K and does not exhibit spin-glass freezing. Compound **13** with composition  $[NH_4]_8[Mn_8(SO_4)_{12}]$  crystallized with three-dimensional framework with chirality. This Structure remains intact even after removal of ammonium ion which was confirmed by Temperature dependent PXRD and First principle calculations. It exhibits a paramagnetic nature and shows hydrogen adsorption in the order of 0.45 wt% at 77 K. Compound **13** shows proton conductivity under various relative humidity (RH) increases from  $2.6 \times 10^{-7} S cm^{-1}$  at  $RH = 80\%$  to  $3.1 \times 10^{-4} S cm^{-1}$  at  $RH = 90\%$ .

## 3.2 Introduction

The synthesis of complex inorganic materials with open architectures is one of the major activities in contemporary solid state chemistry for their applications in the areas of catalysis, ion-exchange, magnetism, multiferroics and separation process. There has been a considerable interest in smaller metal cluster, in particular the triangular system in which the interplay between isotropic and anisotropic exchange interactions gives a number of fascinating magnetic properties.<sup>1-3</sup> The use of metal ions with suitable choice of ligands leads to a variety of materials which behave as magnet.<sup>4</sup> There have been continuous efforts to design the magnetic materials with extended structures by using multifunctional bridging ligands, but it is still difficult to anticipate the structures and the magnetic behavior of such designed materials.<sup>5-9</sup> Usually short bridging ligands such as oxido, cyanide, azido, and small oxo-anions such as phosphate, carbonate and sulfate are commonly used to obtain strong magnetic interactions between paramagnetic centers due to the short distance between the moment carriers.<sup>10-12</sup> Tetrahedral anions are proven to be very attractive candidates who are being used as building unit for the construction of novel magnetic materials. We are interesting on sulfate oxo-anion because of  $\text{SO}_4^{2-}$  tetrahedra are being used for the synthesis of layered and three-dimensional compounds with the Kagome structures characteristics of showing magnetic frustration.<sup>13-18</sup> Since  $\text{SO}_4^{2-}$  can able to make different bridging mode ( $\mu_1$ -O1;  $\mu_2$ -O1, O2;  $\mu_3$ -O1, O2, O3;  $\mu_4$ -O1, O2, O3, O4) resulting both ferromagnetic and antiferromagnetic interactions between the metal centers.<sup>19</sup> The ligands are connected to the metal polyhedra in such a way that the moment are most likely retain in chains/layers through M-X-M linkages, where X = halide, N or O coordinating atoms.<sup>20</sup> The presence of organic amine in the interlamellar space also affects the magnetic properties of the material. The main objective of this chapter is synthesis of transition metal sulfates, their

crystal dimensionalities, applications in magnetism, adsorption and proton conductivity measurements. In this chapter, we report novel Kagome type three isostructural 3D-transition metal sulfates (Co, Ni and Zn), one diamond kind of chains with 2D-layered metal (Co) sulfate and one chiral 3D-metal (Mn) sulfate.

Transition metal compounds with the Kagome structures are one of the great academic interests because of the unusual magnetic properties. Kagome structures are essentially special arrangement of two-dimensional layers of corner sharing triangles where the neighbouring electronic interactions cannot be satisfied.<sup>21-22</sup> This results in spin frustration which gives rise to interesting magnetic properties by allowing the emergence of unusual ground state configurations particularly at low temperature. Thus, the Kagome lattice remains at the fore front for studying interesting phenomenon of magnetic frustration.<sup>23</sup> One of the most studied example is jarosite family with general formula of  $AM_3(SO_4)_2(OH)_6$  ( $A$  = monovalent cation;  $M = Fe^{3+}, Cr^{3+}$ ) for exploring magnetic frustration in two-dimensions.<sup>22, 24</sup> Various other Kagome structures have been reported in the literature with varied metal ions and with different mono anionic species which can replace the hydroxide anions effectively.<sup>25-32</sup> Thus, halide anions have been explored to generate Kagome type lattice, which is also advantageous in terms of minimizing the ambiguity of hydroxide composition.<sup>33</sup> To expand the area of synthesizing Kagome structures, various other anions like azide<sup>34-35</sup> and organic templates<sup>36-40</sup> have also been used which gave aesthetically pleasing structures with remarkable magnetic properties. Magnetic studies on Kagome compounds revealed that transition metal ion with integral spin have a different magnetic behavior from those with non-integer spins. Thus, Kagome compounds with integer spin show ferro/ferrimagnetic behaviour while those with non-

integer spins generally show magnetic frustration. And/or low temperature antiferromagnetism just as in  $\text{Fe}^{3+}$  jarosites. Theoretical prediction lends support these observations and suggested the crucial role of the magnitude of spin of the transition metal ions.<sup>36-37</sup> Although, there are various reports and magnetic studies on Kagome structures with 2D-layers, the reports on 3D-Kagome type structures are very rare.

Here we report synthesis, structure and magnetic properties of three Kagome type isostructural 3D-metal sulfates with composition of  $[\text{H}_3\text{O}][\text{MSO}_4\text{F}]$  (Where M= Co (**9**), Ni (**10**) and Zn (**11**)). We chose these two metal ( $\text{Co}^{2+}$  and  $\text{Ni}^{2+}$ ) ions because of spin 3/2 (odd-half integer) and 1 (integer), respectively which are good candidate for exhibiting interesting magnetic phenomenon.<sup>36-37</sup> Transition metal compounds with the layered structure which have diamond chains are considerable interest because of their novel magnetic properties. In diamond chains, metal atoms arranged as triangular fashion like in Kagome structures. Due to this arrangement we can observe unusual magnetic properties such as geometric frustration. So, our motivation to synthesize the layered diamond chains of transition metal sulfates frameworks. In this chapter we report the synthesis, crystal structure and magnetic properties of layered diamond chains of Co(II) sulfates with the composition of  $[\text{C}_4\text{N}_2\text{H}_{12}]_2[\text{Co}_3\text{F}_2(\text{SO}_4)_3(\text{H}_2\text{O})_2]$ , **12**.

Synthesis of new crystalline solids with unusual structures is a growing trend synthesis of higher-dimensional framework solids with chiral structures still remains a challenge.<sup>41-50</sup> Notwithstanding the modest progress in designing chiral structure of zeolite<sup>51</sup> and metal phosphate,<sup>52-55</sup> complete control of framework chirality has not been achieved due to the complexity and poor understanding of the reaction mechanisms involved in the process. Nevertheless, most of the transition metal sulfates reported in the literature have one- or two-dimensional structures in accordance with the observation that formation of three-dimensionally

extended robust sulfate networks is generally difficult.<sup>56-58</sup> Three-dimensional sulfate networks are most likely obtained by using the element which supports higher coordination number such as the lanthanides and actinides.<sup>59-64</sup> Chemistry of noncentrosymmetric sulfate materials is still in its infancy with very few compounds reported in the literature. Broadly, two synthetic strategies have been used so far to prepare chiral solids, one being the stereo selective synthesis<sup>65-75</sup> employing chiral organic ligands, while the other involves spontaneous resolution upon crystallization without chiral species.<sup>45-46, 76-81</sup> Chiral porous frameworks represent a novel class of recyclable and reusable solid asymmetric catalysts as a result of their truly single-site nature, and straightforward structural characterization by X-ray crystallography. Since the chirality of the compounds should be controlled in the molecular level, as well as in the entire crystal structure, there has been countable few chiral metal sulfates are reported till date.<sup>82-83</sup> Therefore, our motivation is synthesis of robust three-dimensional chiral transition metal sulfates. In this chapter we report synthesis, structure and electronic properties of chiral 3D-Mn sulfate with composition of  $[\text{NH}_4]_8[\text{Mn}_8(\text{SO}_4)_{12}]$ , **13**.

### 3.3 Experimental Section

#### 3.3.1 $[\text{H}_3\text{O}][\text{MSO}_4\text{F}][\text{M}=\text{Co}$ (**9**), Ni (**10**) and Zn (**11**)

The compounds **9-11** were Synthesized by hydro/solvothermal method by taking 1 mM of  $\text{M}(\text{NO}_3)_2 \cdot 6\text{H}_2\text{O}$  as metal source (M=Co (**9**), Ni (**10**) and Zn(**11**)). In a typical synthesis,  $\text{M}(\text{NO}_3)_2 \cdot 6\text{H}_2\text{O}$  [where M=Co, Ni and Zn] was dissolved in acetonitrile (2.6 mL) and water (0.9 mL) mixture followed by the addition of 0.165 mL of  $\text{H}_2\text{SO}_4$  and 0.09 mL of HF. Finally, the reaction mixture with molar composition 1:3:2:50:50 [ $\text{M}(\text{NO}_3)_2 \cdot 6\text{H}_2\text{O}/\text{H}_2\text{SO}_4/\text{HF}/$  acetonitrile / water ] was stirred for 1 h and transferred to a stainless steel autoclave of 23 mL capacity. The

autoclave was heated at 150 °C for 48 h and cooled naturally. The final product was filtered and washed with distilled water.

### 3.3.2 [C<sub>4</sub>N<sub>2</sub>H<sub>12</sub>]<sub>2</sub>[Co<sub>3</sub>F<sub>2</sub>(SO<sub>4</sub>)<sub>3</sub>(H<sub>2</sub>O)<sub>2</sub>], **12**

A compound **12** was synthesized by employing mild hydro/solvothermal methods. In a typical synthesis of **12**, 0.219 gm of Co(NO<sub>3</sub>)<sub>2</sub>·6H<sub>2</sub>O was dispersed in an EG (5 mL), under constant stirring. To this mixture, 0.334 gm of PIP, 0.22 mL of H<sub>2</sub>SO<sub>4</sub> and 0.336 mL of HF was added to mixture and stirred for 45 minutes to obtain the clear solution. The final mixture with the molar composition of Co(NO<sub>3</sub>)<sub>2</sub>·6H<sub>2</sub>O/H<sub>2</sub>SO<sub>4</sub>/pip /HF/EG (1:6:3:6: 90) was transferred into a 23-mL Teflon-lined acid digestion bomb and heated at 150 °C for 72 h. The reaction mixture after above heat treatment did not show any appreciable change in pH and remains at pH 2. After cooling pink-block shaped crystals were obtained with 66 % yield.

### 3.3.3 [NH<sub>4</sub>]<sub>8</sub>[Mn<sub>8</sub>(SO<sub>4</sub>)<sub>12</sub>], **13**

A compound **13** was synthesized by employing hydro/solvothermal method. In a typical synthesis of **13**, 0.251 gm of Mn(NO<sub>3</sub>)<sub>2</sub>·4H<sub>2</sub>O was dispersed in an EG/water mixture (2.8 and 0.9 mL, respectively) under constant stirring. To this mixture, 0.268 gm of (NH<sub>4</sub>)<sub>2</sub>SO<sub>3</sub> was added and the mixture was stirred for 20 min to obtain the clear solution. The final mixture with the molar composition of Mn(NO<sub>3</sub>)<sub>2</sub>·4H<sub>2</sub>O/(NH<sub>4</sub>)<sub>2</sub>SO<sub>3</sub>/H<sub>2</sub>O/EG (1:2:50:50) was transferred into a 15-mL Teflon-lined acid digestion bomb and heated at 180 °C for 48 h. The reaction mixture after above heat treatment did not show any appreciable change in pH and remains at pH 6. After cooling white block-shaped crystals were obtained with 75% yield.

### 3.4 Characterization

Initial characterization of all the compounds were carried out by PXRD, EDAX, chemical analysis, TGA and FTIR spectroscopy. The PXRD pattern exclusively exhibited signatures of a hitherto unknown material consistent with the structure determined by SXRD, which gave the compositions of  $[\text{H}_3\text{O}][\text{MSO}_4\text{F}](\text{M}=\text{Co}$  (**9**), Ni (**10**) and Zn (**11**)),  $[\text{C}_4\text{N}_2\text{H}_{12}]_2[\text{Co}_3\text{F}_2(\text{SO}_4)_3(\text{H}_2\text{O})_2]$ , **12** and  $[\text{NH}_4]_8[\text{Mn}_8(\text{SO}_4)_{12}]$ , **13**. PXRD patterns of all the compounds were almost in good agreement with the simulated patterns based on their respective single-crystal data given in appendix (Figure 3.21). All the compounds **9-13** gave satisfactory elemental analysis. The experimental and calculated (in wt%) values of H, N and S were as follows. For **9**, H = 1.48 and S = 15.95 (calc. H = 1.57 and S = 16.61); **10**, H = 1.45 and S = 15.5 (calc. H = 1.57 and S = 16.63); **11**, H = 1.48 and S = 15.90 (calc. H = 1.52 and S = 16.08); **12**, H = 3.78; N = 6.7 and S = 12.67 (calc. H = 3.95 N = 7.83 and S = 13.45) and **13**, H = 5; N = 7.4 and S = 21.6 (calc.: H = 4.6 N = 7.2 and S = 22). EDAX indicated the ratios of M and S to be 1:1 in compounds **9, 10, 11** and **12**, but for compound **13** has 2:3 which are good agreement with the molecular formulae. These analytical data confirm the molecular formulae of five compounds obtained from crystallography.

TGA experiment for all the five compounds were carried out under constant flow of  $\text{N}_2$  at a heating rate of  $2\text{ }^\circ\text{C min}^{-1}$  in the temperature range of 35-900  $^\circ\text{C}$ . Compounds **9-10** show multi-step decomposition and the TGA graph has striking similarity which is expected as the complexes are isostructural in nature. The first stage is the loss of hydronium anions and possibly the adsorbed moisture accounting for the loss of moisture in the temperature range of 50-100  $^\circ\text{C}$ . The second step involves the degradation of complex due to the loss of fluoride from the crystal lattice in the temperature range of 160-200  $^\circ\text{C}$  which accounts 31.3% (calcd 25.24%) weight

loss. Finally decomposition of  $\text{SO}_4$  group shows 26.86% (calcd 26.52%) weight loss in the temperature range of 240 to 400 °C (Figure 3.22). The PXRD analysis of the calcined product of **9** and **10** corresponds to the CoO oxide (JCPDS : 01-075-0576) and NiO (JCPDS : 01-077-2929) respectively. For **12**, two-step weight loss was observed corresponding to the loss of the water in the range 125 to 180 °C [obs = 5.4%, calc = 4.8%], and to the loss of amine, HF, and  $\text{SO}_3$  in the range 300 to 550 °C [obs, 57.7%; calc, 56.4%] (Figure 3.22). The PXRD pattern of the sample heated to 900 °C corresponded to a  $\text{Co}_3\text{O}_4$  (JCPDS file no. 01-074-1657) Compound **13** showed a two-step weight loss corresponding to the loss of ammonia in the range 70-380 °C (obs = 7.0%, calcd = 6.8%), followed by removal of  $\text{SO}_2$  around 400 °C. The total observed weight loss of 60.5% corresponds to the loss of the amine along with sulfates is in good agreement with the calculated value of 59.5% (Figure 3.22). The PXRD pattern of the sample heated to 550 °C diffracted very weakly and could not be recognized.

The FTIR spectra of all compounds showed characteristic bands for the sulfate as well as the guest ammonium moieties. FTIR spectrum of **9-10** showed the characteristic peaks for  $\text{SO}_4^{2-}$  anion around 1650, 1400, 1160, 1100, 605 and 460  $\text{cm}^{-1}$ . The broad peak around 3250-3500  $\text{cm}^{-1}$  are attributed to OH stretching vibrations of hydronium cation (Figure 3.23). Infrared spectra of **12** showed characteristic bands in the 980-1010  $\text{cm}^{-1}$  region due to  $\nu_1$  and in the 1090-1140  $\text{cm}^{-1}$  region due to  $\nu_3$  of the sulfate group<sup>84</sup>. The bending mode of  $\text{SO}_4^{2-}$  was in the 450-600  $\text{cm}^{-1}$  region. Multiple C-N stretching modes are observed in the range 1080-1220  $\text{cm}^{-1}$  shown in Figure 3.23. For compound **13** showed characteristic bands for the sulfate as well as the ammonium moieties. The stretching mode of -N-H bond (of the amine) is observed around 3004  $\text{cm}^{-1}$ . The N-H bending modes of the amine and  $\text{NH}_4^+$  are observed in the range 1440-1586  $\text{cm}^{-1}$ . The characteristic stretching bands,  $\nu_3(\text{N-H})$  and  $2\nu_4(\text{N-H})$  of the  $\text{NH}_4^+$  ion are observed at 3243

and 2830  $\text{cm}^{-1}$  respectively. Strong bands in the region 850-1015  $\text{cm}^{-1}$  correspond to  $\nu_1$  and  $\nu_3$  while bands in the region 583-644  $\text{cm}^{-1}$  can be assigned to  $\nu_2$  and  $\nu_4$  fundamental modes of sulfate ion shown in Figure 3.24.

### 3.5 Single-crystal structure determination

A suitable single-crystal of each compound was carefully selected under a polarizing microscope and mounted at the tip of the thin glass fibre using cyanoacrylate (super glue) adhesive. Single-crystal structure determination by X-ray diffraction was performed on a Siemens SMART-CCD diffractometer equipped with a normal focus, 2.4 kW sealed-tube X-ray source (*Mo-K $\alpha$*  radiation=0.71073Å) operating at 50 kV and 30 mA. Structures were solved by the direct method using SHELXS-97<sup>85</sup> and refined on  $F^2$  by a full-matrix least-squares technique using the SHELXTL-PLUS<sup>86</sup> programs package. An empirical absorption correction based on symmetry equivalent reflections was applied using SADABS.<sup>87</sup> The graphic programs DIAMOND<sup>88</sup> and ORTEP<sup>89</sup> were used to draw the structures. Non-hydrogen atoms were refined anisotropically. In the refinement, hydrogens were treated as riding atoms using the SHELXL default parameters. In all the compounds hydrogens are located through fourier map. In compounds **9-11**, hydronium oxygen atom was found to have positional disorder, thus the hydrogen although located on Fourier map were not refined and also the O-H bond lengths and H-O-H angles were fixed by applying restraints. Details of crystal structure refinement parameters for **9-13** given in the appendix (Table 3.2 and 3.3).

## 3.6 Results and discussion

### 3.6.1 Structural analysis of $[\text{H}_3\text{O}][\text{MSO}_4\text{F}]$ (where M= Co (9), Ni (10) and Zn (11))

The reaction of metal(II) nitrate with sulfuric acid in presence of HF under solvo/hydrothermal conditions afforded block shape crystal for each complex with composition  $[\text{H}_3\text{O}][\text{MSO}_4\text{F}]$  where M=Co, Ni and Zn for **9**, **10** and **11** respectively. All the three complexes were isostructural, hence crystal structure description of only **9** has been given in detail. Interestingly, in the crystal lattice, one hydronium ion was also found trapped which provides the extra positive charge required to balance the crystal lattice.

Block shape pink color crystals of **9** were obtained after solvo/hydrothermal treatment of  $\text{Co}(\text{NO}_3)_2 \cdot 6\text{H}_2\text{O}$  with  $\text{H}_2\text{SO}_4$  in presence of HF. Crystallographic analysis showed that **9** crystallizes in orthorhombic crystal system with  $Pnna$  space group. The asymmetric unit in **9** has 10 non-hydrogen atoms and 9 are involved in the formation of inorganic framework and the one hydronium ion is present as extraframework species. In the asymmetric unit (Figure 3.1), two distinct metal ions and two distinct sulfate ions are present at special position with 50% occupancy each. The interconnecting fluoride anion is present at general position.

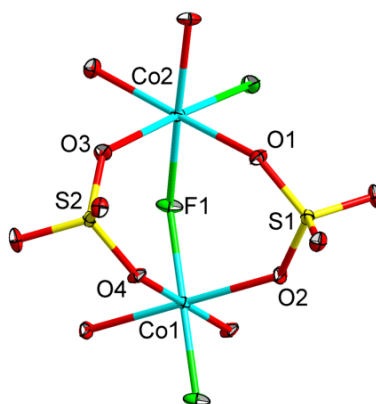


**Figure 3.1.** Asymmetric unit of  $[\text{H}_3\text{O}][\text{MSO}_4\text{F}]$ , **9**. The disordered extra framework hydronium ion is omitted for clarity.

Both the Co(II) ions adopt distorted octahedral geometry however the ligand arrangement around the metal ion is significantly different. Co(1) lies on an inversion centre, thus the fluoride on the Co(1) site adopts *trans*-configuration and the equatorial plane consists sulfate oxygen atoms whereas, in case of Co(2) fluoride anion are positioned *cis*-to each other as shown in Figure 3.1. The Co-O and Co-F bond lengths are in the range of 2.05-2.18 Å and 1.99-2.00 Å, respectively which are within the acceptable limits as reported for other similar compounds.<sup>40, 90-91</sup> Selected bond lengths and bond angles for **9-11** were given in CCDC No: 1442294, 1442295 and 1447992 respectively. The BVS calculations<sup>92</sup> suggested +2 oxidation state for Co (2.09 for Co(1) and 2.02 for Co(2)), Ni (1.96 for Ni(1) and 2.03 for Ni(2)) and Zn (2.02 for Zn(1) and 2.05 for Zn(2)) ions in **9**, **10** and **11** respectively. In the crystal lattice, each sulfate anion interacts with four metal ions in a  $\eta^1\mu^4$ -manner. Similarly, each metal ion is also interacting with four sulfate anions however; the geometrical parameters are different as described earlier. Part of the crystal lattice of **9** is shown in Figure 3.2 which can be dissected to visualize one dimensional chains of Co octahedron fused through fluoride vertices. Interestingly, in the lattice, these chains have two different orientations, which are running at approximate 63° angle with each other as shown in Figure 3.3. Symmetrically equivalent chains are interconnected through one type of crystallographically distinct sulfate anion (namely S(1)O<sub>4</sub>) to generate a 2D-layer in *bc*-plane as shown in Figure 3.2b. In the 2D layer, it can be seen that the cobalt centers have only four coordination sites occupied. The oxygen atoms contributed by other crystallographically distinct sulfate anions fulfill the other two sites around cobalt center. Thus, the 2D-layers comprising chains of different orientation are interconnected through other crystallographically distinct sulfate (S(2)O<sub>4</sub>) anions, which extend the lattice in *ab*-plane eventually generating a three-dimensional lattice as shown in Figure 3.2c where the 2D-layers are also highlighted with pink

and gray color. In Figure 3.2d part of the crystal lattice is shown which clearly depicts the interconnection of 2D-layers where crystallographically distinct sulfate anions are highlighted with different color showing the connectivity of pink and gray color. Thus, the  $\text{CoF}_2\text{O}_4$  octahedra and  $\text{SO}_4$  tetrahedra share their vertices to generate a 3D-assembly (Figure 3.3a) consisting of Kagome type lattice, which is shown in Figure 3.3b. However, in this case, one of the metal ion in the triangular lattice is substituted by sulfate anions compared to the normal Kagome structure.

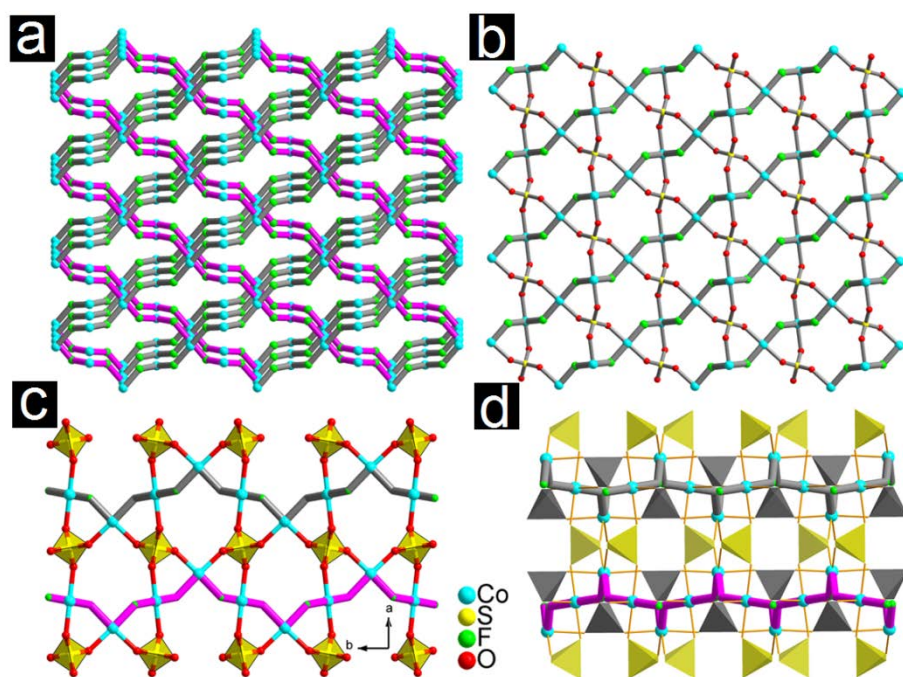


**Figure 3.2.** (a) One-dimensional Co-F chains in **9** running in  $bc$ -planes; (b) Formation of 2D-layer in  $bc$ -plane by connecting each layer through sulfate anions ( $\text{S}(1)\text{O}_4$ ); (c) Interconnection of 2D-layer as highlighted with different color *via* sulfate anions ( $\text{S}(2)\text{O}_4$ ); (d) 3D-lattice as a result of interconnection *via* crystallographically distinct sulfate anions which are highlighted with different color.

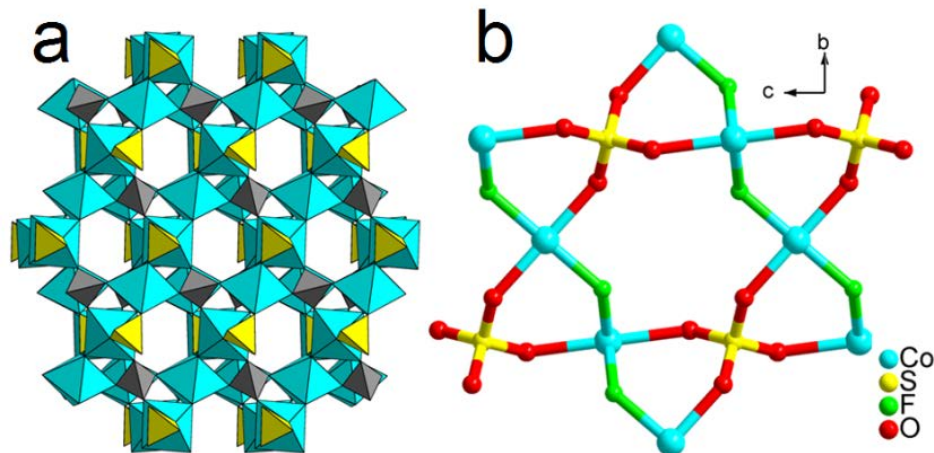


**Figure 3.3.** (a) Polyhedral view of the 3D-crystal lattice. (b) Magnified view of the Kagome type structural building block in **9**.

### 3.6.1.1 Magnetic properties for $[\text{H}_3\text{O}][\text{MSO}_4\text{F}]$ (where $\text{M} = \text{Co}$ (**9**) and $\text{Ni}$ (**10**))

The temperature dependence magnetic susceptibility ( $\chi$ ) data of **9** and **10** is shown in Figure 3.4. The paramagnetic region fitted well with Curie-Weiss law ( $\chi = C/(T - \theta)$ ) having Curie-Weiss temperature ( $\theta$ ) of -12 K for **9** and -10 K for **10**. The calculated effective magnetic moment ( $\mu_{\text{eff}}$ ) per  $\text{Co}^{+2}$  ions is  $4.78 \mu_{\text{B}}$  which is slightly higher than the expected spin only value of  $3.87 \mu_{\text{B}}$  for high spin  $\text{Co}^{+2}$  ion due to the orbital contribution as found in reported  $\text{Co}^{+2}$  compound.<sup>37</sup> And same as for Ni(II) compound  $2.95 \mu_{\text{B}}$  which is slightly higher than the expected spin only value of  $2.82 \mu_{\text{B}}$ . The negative  $\theta$  suggest that the exchange interaction is antiferromagnetic type

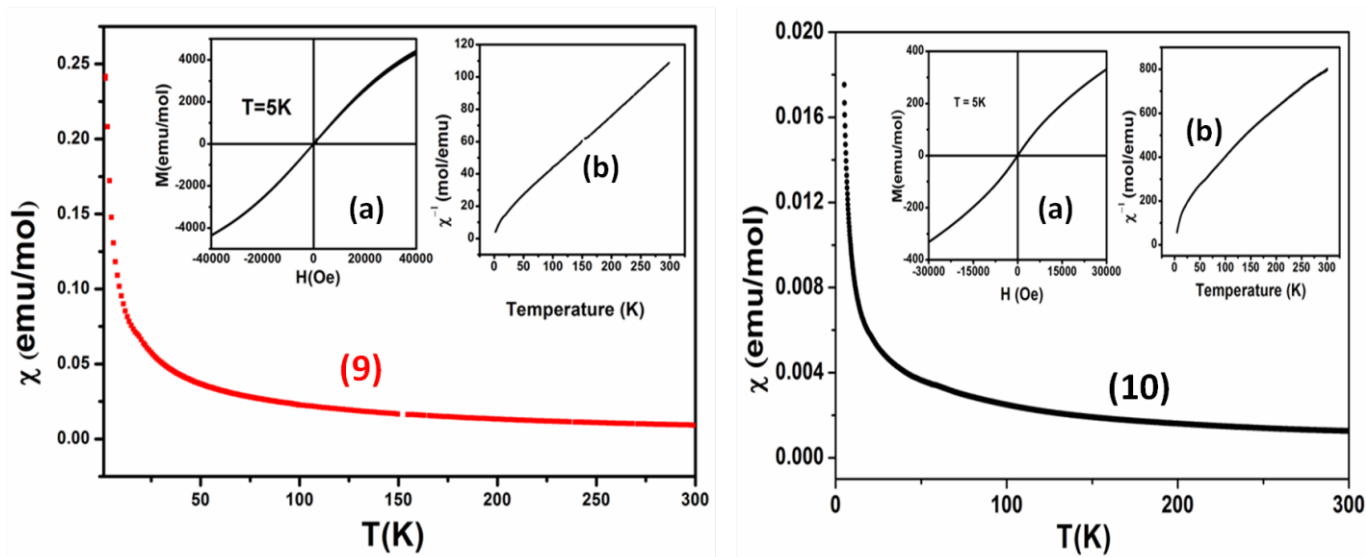


**Figure 3.4.** Temperature dependence of the magnetic susceptibility for both **9** and **10** compounds measured at 1000 Oe. Inset (a) shows the isothermal M-H cycles at 5 K (b) shows the  $\chi^{-1}$  vs T.

### 3.6.2 Structural analysis of $[\text{C}_4\text{N}_2\text{H}_{12}]_2[\text{Co}_3\text{F}_2(\text{SO}_4)_3(\text{H}_2\text{O})_2]$ , **12**

The asymmetric unit of **12** contains 17 non-hydrogen atoms, of which 14 belong to the inorganic framework and 3 belong to the extra framework amine molecule shown in Figure. 3.5.

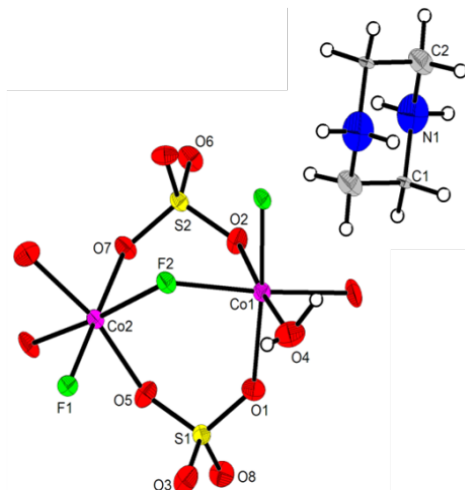


**Figure 3.5.** Asymmetric unit of  $[\text{C}_4\text{N}_2\text{H}_{12}]_2[\text{Co}_3\text{F}_2(\text{SO}_4)_3(\text{H}_2\text{O})_2]$ , **12**.

In the compound **12** two crystallographically two metal atoms and S atoms, of which one metal and one sulfur atom [Co(1) and S(1)] are in special positions with an occupancy 0.5. The framework structure of **12** constructed from macro anionic inorganic framework layer of

$[\text{Co}_3(\text{F})_2(\text{SO}_4)_3(\text{H}_2\text{O})_2]^{2-}$  held together by strong hydrogen bonds with the ammonium ions residing in the interlamellar space. The selected hydrogen bond interactions are given in the Table 3.4. The Co atoms in **12** are octahedrally coordinated to four oxygens from four sulfates and two fluorine atoms. The Co-O/F bond distances are in the range 2.015(12)-2.180(14) Å and O/F-Co-O/F bond angles in the range 78.02(3)-179.48(5) °. The S-O bond distances in **12** are in the range 1.444(11)-1.482(11) Å and the average O-S-O bond angle is 109.64°. The Bond valence sum calculations for **12** based on the method of Brown and Altermatt,<sup>92</sup> using  $r_0(\text{Co-O}) = 1.692$ , shown that the valence sums for Co(1) = 1.98, Co(2) = 1.92, The charges on metal and sulfur atoms are clearly +2 and +6 respectively. These data are consistent with the stated composition. Selected bond distances and angles of **12** given in CCDC NO: 1406154.

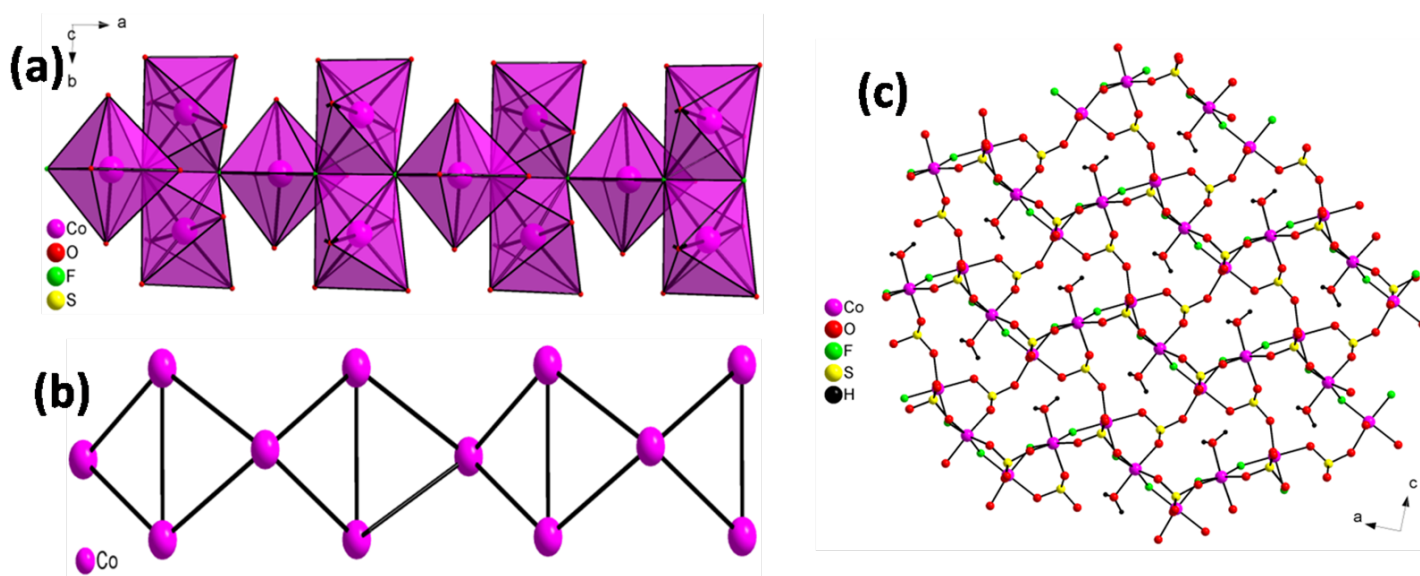


**Figure 3.6.** (a) The infinite diamond chain formed by the connectivity of the metal polyhedra. (b) Presence of triangular units in the diamond chain. (c) Anionic inorganic layer in **12** in the *ac*-plane. Note the presence of eight- membered apertures.

The framework of **12** built up of Co(1)/F)<sub>2</sub>O<sub>4</sub>, Co(2)/(F)<sub>2</sub>O<sub>4</sub> octahedra and SO<sub>4</sub> tetrahedra sharing edges as Co-μ-(/F)-Co bonds and vertexes as Co-O-S bonds. The Co(1)/(F)<sub>2</sub>O<sub>4</sub> octahedra get dimerized by sharing edges with two fluorine groups to form Co<sub>2</sub>(/F)<sub>2</sub>O<sub>8</sub> moiety. Co(2)(OH/F)<sub>2</sub>O<sub>4</sub> octahedra link to the dimer at one end of the shared edges through μ<sub>3</sub>-F to form trimeric Co<sub>3</sub>(F)<sub>3</sub>O<sub>12</sub> units. These units are connected to one another through corner sharing Co-O-S linkages there by forming the zig-zag chain shown in the Figure 3.6a. The presence of triangular units in the diamond chain is shown in Figure 3.6b. Such chains run parallel to the *a*-axis and are covalently bonded to each other by the S(2)O<sub>4</sub> group resulting the two-dimensional layered structure. The S(2)O<sub>4</sub> tetrahedra from the adjacent chains connect alternatively via four Co-O-S linkages to form four connected tetrahedra, leading to the formation of an eight-membered aperture in the *ab*-plane (Figure 3.6c). The inorganic layers are stacked along the *c*-axis in the ABAB.... fashion and the interlayer space is occupied by the diprotanated pip molecules which ensure the stability of the structure through extensive hydrogen bonding as shown in the Figure 3.7. The structures of **12** can be compared to the mineral sulphoborite<sup>93</sup> containing complex sheets of MgO<sub>6</sub> octahedra and (SO<sub>4</sub>) tetrahedra. In the mineral amaranthite, octahedral tetramers are polymerized to form octahedral chains parallel to [100] and linked by (SO<sub>4</sub>) tetrahedra, the linkage between sheets being provided by [B(OH)<sub>4</sub>] tetrahedra. This kind of diamond chain topology has also been found in several metal-organic hybrids of divalent transition metals. A two-dimensional nickel sulfates possessing the Ni<sub>3</sub>(μ<sub>3</sub>-F)<sub>2</sub> diamond chain topology has also been reported.<sup>16</sup> The diamond chain in **12** are similar and consistent with the diamond chain of azurite Cu<sub>3</sub>(OH)<sub>2</sub>(CO<sub>3</sub>)<sub>2</sub>,<sup>94</sup> which has alternating dimer-monomer sequence. In azurite, the connectivity of three CuO<sub>6</sub> octahedra leads to a triangular arrangement of the metal ions in the zig-zag chain.

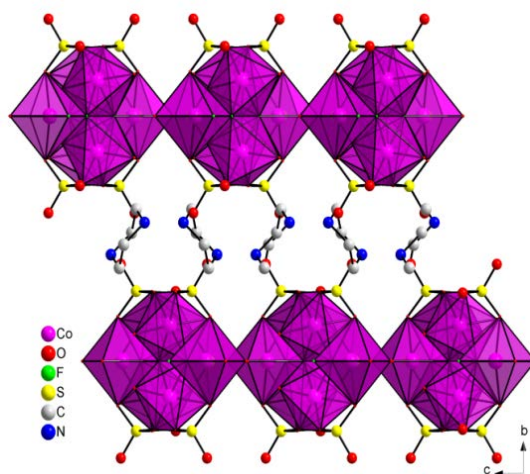


**Figure 3.7.** View down the crystallographic **12**.

### 3.6.2.1 Magnetic properties for $[\text{C}_4\text{N}_2\text{H}_{12}]_2[\text{Co}_3\text{F}_2(\text{SO}_4)_3(\text{H}_2\text{O})_2]$ , **12**

The temperature dependence magnetic susceptibility ( $\chi$ ) data of **12** at 100 Oe is shown in Figure 3.8. The paramagnetic region is fitted well with Curie-Weiss law ( $\chi = C/T - \theta$ ) having Curie-Weiss temperature ( $\theta$ ) of -25 K (inset of Figure 3.8). The calculated effective magnetic moment ( $\mu_{\text{eff}}$ ) per Co ion is  $4.89 \mu_{\text{B}}$ , which is slightly higher than the expected spin only value  $3.87 \mu_{\text{B}}$ , of high spin  $\text{Co}^{2+}$  ion due to the orbital contribution as found in many of the  $\text{Co}^{2+}$  compounds.<sup>13, 37, 95-96</sup> The negative  $\theta$  suggests that the exchange interaction is antiferromagnetic type. However, zero-field cooled (ZFC) and field-cooled (FC) magnetization show sharp rising  $T_c = 10.8$  K. This ferromagnetic-like behavior can arise from spin canting. Moreover, clear divergence of ZFC and FC curves suggests the low temperature behavior is ferrimagnetic. Interestingly, good magnetic hysteresis is observed at 2.5 and 6 K (Figure 3.9). In order to understand the irreversibility behavior in the ZFC-FC curve we performed ac-susceptibility measurement at different frequencies in the vicinity of the magnetic transitions as shown in Figure 3.10a. Both the real ( $\chi'$ ) and the imaginary ( $\chi''$ ) parts exhibit sharp peak near  $T_c$  having no frequency dependence. This rules out the spin glass behavior in the system. A sharp  $\lambda$ -like anomaly is also seen in heat capacity curve, favouring long range magnetic ordering below  $T_c$  (Figure 3.10b).

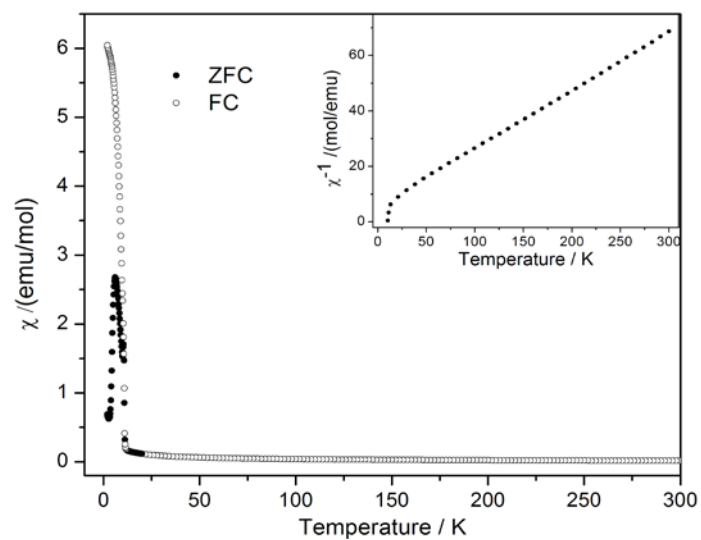


**Figure 3.8.** Temperature dependence of the DC-magnetic susceptibility of **12** measured at 100 Oe under FC and ZFC conditions. Inset shows the variation of inverse susceptibility.

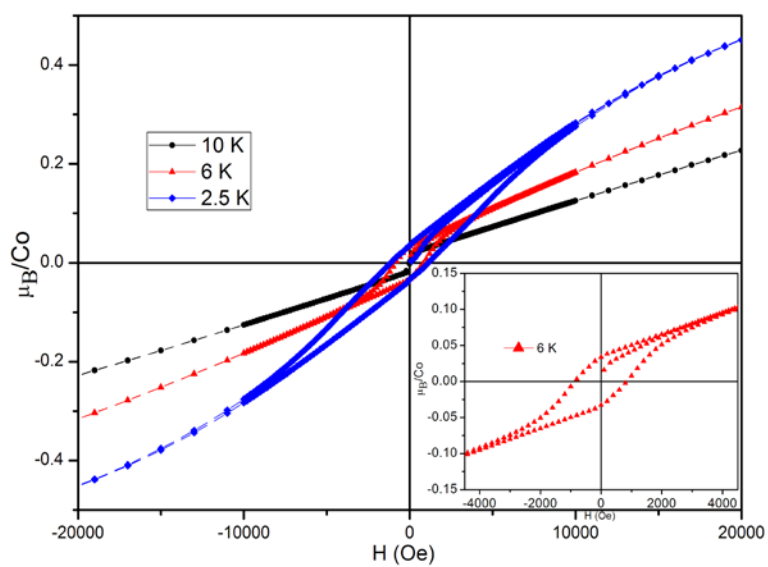
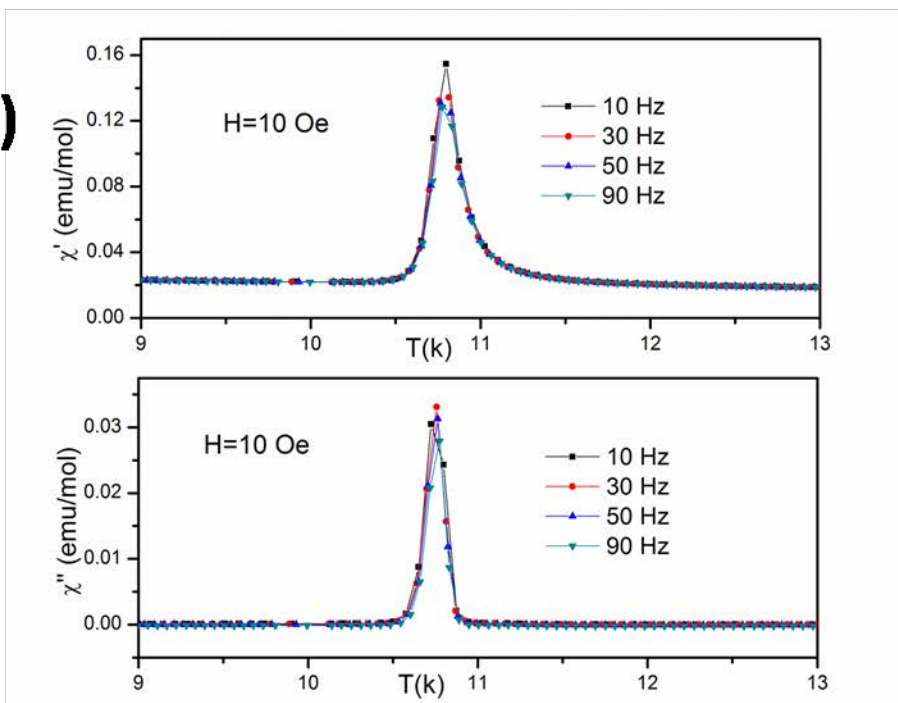


**Figure 3.9.** Magnetization as a function of magnetic field at 2.5, 6 and 10 K.

(a)



(b)

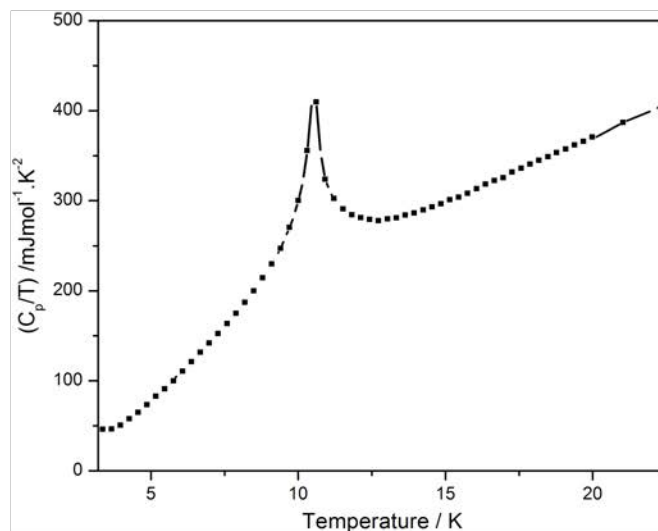


**Figure 3.10.** (a) ac-susceptibility as a function of temperature for a number of frequencies. Note that the position of the peak does not shift with frequency. (b) Specific heat data in the 2-25 K range.

### 3.6.3 Structural analysis of $[\text{NH}_4]_8[\text{Mn}_8(\text{SO}_4)_{12}]$ , **13**

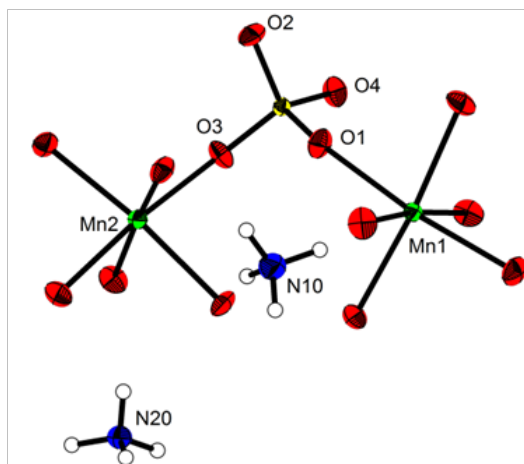


**Figure 3.11.** Asymmetric unit of  $[\text{NH}_4]_8[\text{Mn}_8(\text{SO}_4)_{12}]$ , **13**.

The synthesized Compound **13** has a three-dimensional network structure made up of  $\text{MnO}_6$  octahedra and  $\text{SO}_4$  tetrahedra with interstitial  $\text{NH}_4^+$  ions. The asymmetric unit consists of 9 non-hydrogen atoms out of which 7 belong to the inorganic framework and 2 to the guest  $\text{NH}_4^+$  ions as shown in the Figure 3.11. There are two crystallographically distinct Mn atoms and one S atom with both the metal atoms in octahedral coordination with the O neighbours from the six sulfate groups. The Mn-O bond distances are in the range 2.1585 (13)-2.1728(14) Å [Mn(1) -  $\text{O}_{\text{avg}} = 2.165$ , Mn(2)-  $\text{O}_{\text{avg}} = 2.164$  Å]. The *trans* O-Mn-O bond angles are in the range 173.7(6) - 174.2(5)° and the *cis* O-Mn-O are in the range 81.79(6)-94.93(5)° with an average of 173.9 and 70.14° respectively. Selected bond distances and bond angles for **13** given in the CCDC No: 1017343. The anionic framework of compound **13** formed by six Mn-O-S linkage by sharing corner with six sulfate groups resulting into a pinwheel arrangement of  $\text{MnO}_6$  octahedra and  $\text{SO}_4$  tetrahedra. From the Mn-O bond lengths, it can be seen that  $\text{MnO}_6$  octahedra are little distorted. The unique S atom is tetrahedrally coordinated by the oxygen neighbours with the S-O bond distance ranged between 1.489(4)-1.459(4) with an average bond distance of 1.474 Å. The S-

atom makes four S-O-Mn linkages through four of its oxygen atoms. BVS calculations<sup>92</sup> (Mn(1) = 2.17, Mn(2) = 2.17,) and the average Mn-O bond lengths indicate that the oxidation state of both manganese and Sulfur was +2 and +6 respectively. Thus the framework structure  $[\text{Mn}(\text{SO}_4)_{12}]^{8-}$  is negatively charged and it gets neutralized by the presence of eight ammonium ions in the unit cell

The prominent feature of **13** is the three-dimensional chiral structure with cubic symmetry that crystallizes in the space group  $P2(1)3$ . The structures are built from strictly alternating  $\text{MnO}_6$  octahedra and  $\text{SO}_4$  tetrahedra units that linked through their vertexes throughout the structure. Both  $\text{MnO}_6$  octahedra and  $\text{SO}_4$  tetrahedra share corner alternatively to form four- and six- membered rings that form infinite chains. These chains are alternately stacked one over the other along the [100] direction and are interlinked by sharing corners with the tetrahedral corners of the  $\text{SO}_4$  groups to form a layer. Within each layer, each sulfate tetrahedra shares three of its corners with the octahedra of three adjacent chains, one due to Mn(1) and two due to Mn(2) (Figure 3.12). The layers thus formed are cross-linked by  $\text{SO}_4$  tetrahedra along the *b*-axis through corner sharing S-O-Mn linkages to form the three-dimensional structure. The interstitial ammonium ions interact with the framework oxygen through strong N-H $\cdots$ O hydrogen bonds.

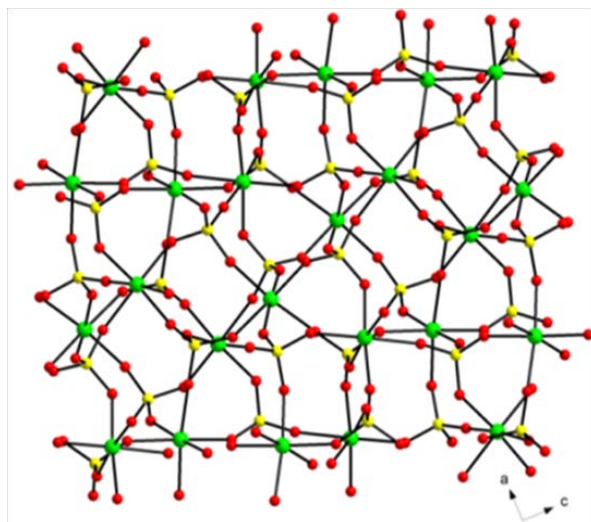


**Figure 3.12.** Top view of the layer parallel to the *ac*-plane of the unit cell in **13**.

### 3.6.3.1 Temperature dependent PXRD for $[\text{NH}_4]_8[\text{Mn}_8(\text{SO}_4)_{12}]$ , **13**

Compound  $[\text{NH}_4]_8[\text{Mn}_8(\text{SO}_4)_{12}]$ , **13** is isostructural with  $[\text{NH}_4]_8[\text{Mg}_8(\text{SO}_4)_{12}]$ , **2** which was described in the previous chapter-2. Hence, these two compounds are isostructural both are thermally stable up to 370 °C which was confirmed by TGA experiment. To check the thermal stability of the compound, high temperature X-ray studies of **13** were carried out at different temperatures on a Bruker D8 Advance with DAVINCI design fitted with HTK 16 temperature chamber. It was observed that the structure remains intact even after a thermal treatment at 350 °C, as can be seen from the powder pattern shown in Figure 3.13. The framework collapses when it is heated at 450 °C, which is also supported by the TGA data. So, here we can conclude that compound remains retain their structure even after removal of ammonium ion at high temperature.

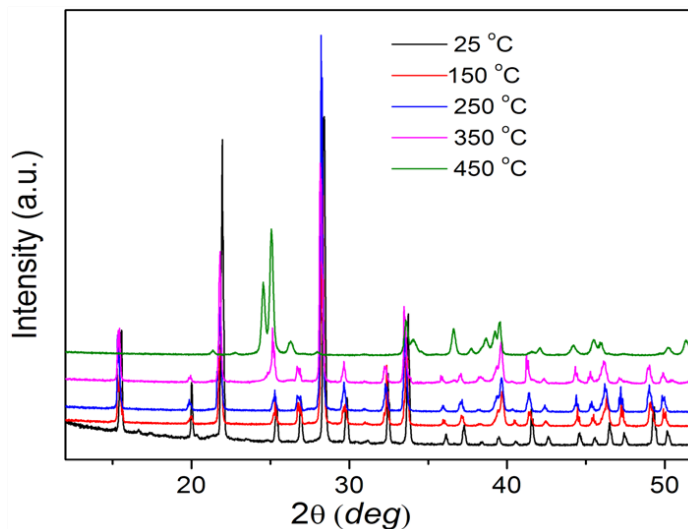


**Figure 3.13.** PXRD patterns of compound **13** at different temperatures. The structure remains intact when it is heated at 350 °C.

### 3.6.3.2 First Principles Studies for $[\text{NH}_4]_8[\text{Mn}_8(\text{SO}_4)_{12}]$ , **13**

The compound **13** was thermally stable confirmed by TGA, Temperature dependent PXRD. And also we stated the first principle calculations why this compound is stable at high temperature. Here we report the first principle calculations which are derived from density functional theory (DFT). We study the observed crystal structure from first principles within the framework of DFT which approximates the many-body exchange and correlation interactions by local functional of single particle density and its derivatives. In this section we attempt to address whether the experimentally observed ammoniated crystal  $[\text{NH}_4]_8[\text{Mn}_8(\text{SO}_4)_{12}]$ , **13** would retain their open-framework structure upon de-ammoniation or not. We use a gradient corrected exchange-correlation functional which inherently describes the lower-bound of crystal binding. Oxidation states of atoms are estimated in terms of Lowdin charges<sup>97</sup> (LC) which are obtained by projecting the occupied manifold of wave functions onto a set of orthonormalized atomic orbitals. While LCs are not logically expected to exactly add up to the total charge, they constitute more than 90% of total charge for all the systems studied in this work.

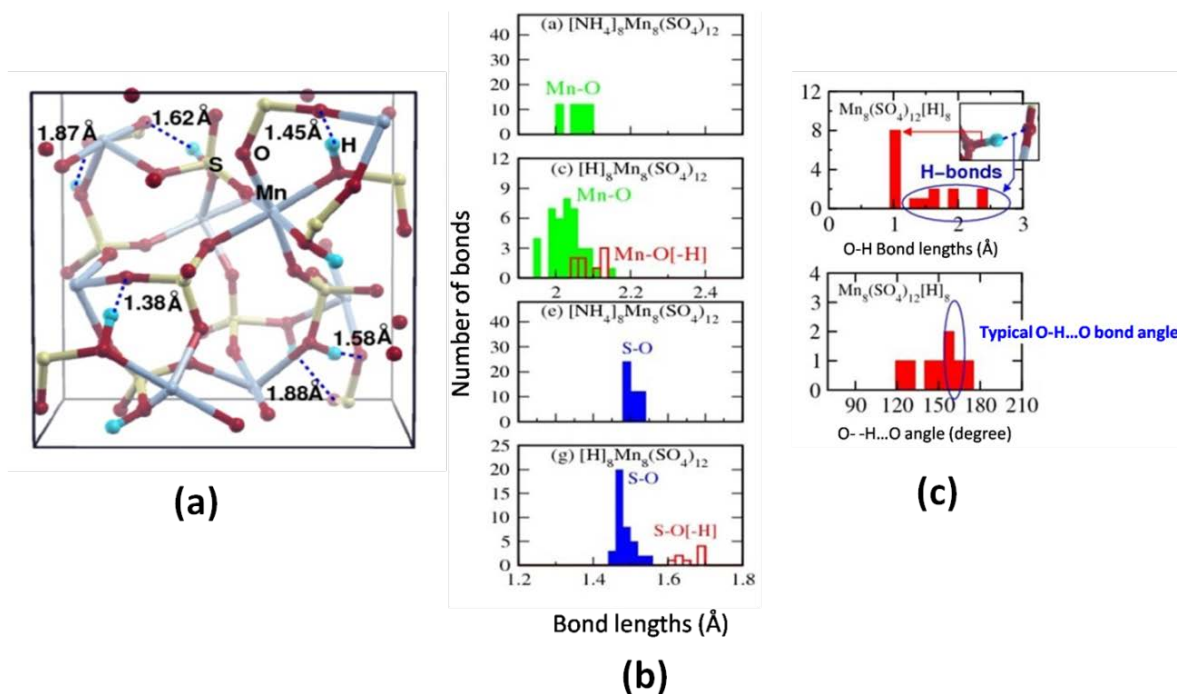


**Figure 3.14.** (a) Structures showing hydrogen bonding between adjacent -S-O-M-O-S- bridges in de-ammoniated compound  $[\text{H}]_8[\text{Mn}_8(\text{SO}_4)_{12}]$  (b) Histogram showing the bond distances of Mn-O, and S-O for the ammoniated compounds  $[\text{NH}_4]_8[\text{Mn}_8(\text{SO}_4)_{12}]$ , **13** and bond distances of Mn-O[-H] and S-O[-H] in the de-ammoniated compound  $[\text{H}]_8[\text{Mn}_8(\text{SO}_4)_{12}]$  (c) Histogram showing O-H bond length and O-H...O bond angles in the de-ammoniated compound of  $[\text{H}]_8[\text{Mn}_8(\text{SO}_4)_{12}]$ .

The de-ammoniated crystal structure is obtained by minimizing total energy as function of unit-cell volume and atomic positions starting from the respective ammoniated crystal structure with the  $\text{NH}_4^+$  ions replaced by H atoms. We choose cubic unit cells in order to allow lowering of symmetry through asymmetric chemisorption of the H atoms to the framework. With 48 O atoms and 8 H atoms per cubic unit-cell there exist a large number of such configurations without much variation of total energies and structural generalities. The H atoms, besides forming O-H bonds with the framework O atoms, also lead to intra-framework O-H...O hydrogen bonding as evident from the distribution of O-H...O angle and O-H bond lengths shown in Figure 3.14a. De-ammoniation is thus expected to increase the level of crystal binding which is evident in the resultant reduction of cohesive energies (Figure 3.15) of the Mn compound from -5.65eV/atom

to -5.85eV/atom. Relatedly, bulk-modulus values obtained by fitting the Murnaghan equation of state to total energies calculated as functions of unit cell volume for both the ammoniated compound is about 40 GPa, which increases marginally upon de-ammoniation accompanied by shrinkage of equilibrium unit-cell volume by about 6% for the Mn compound, implying that the compound may be expected to remain structurally as stable as the common oxide perovskites ( $ABO_3$ ) even after of de-ammoniation.

To assess the nature of structural changes and the degree of retention of their framework structure we note that the distribution of O-Mn-O and O-S-O angles in the ammoniated and de-ammoniated phases suggests modest distortions to the  $MnO_6$  octahedra and the  $SO_4$  tetrahedra primarily due to in-equivalence among the O atoms at their vertices owing to bonding to H by one or more of them. To assess whether these structural changes modify the open-framework nature of crystals we note that the distribution of the S-[O]-Mn-[O]-S angles imply gross retention of the framework except for admissible buckling of the S-O-Mn-O-S bridges primarily on account of the inter-bridge O-H $\cdots$ O hydrogen bonding, which nevertheless leaves 35%(30%)d of the unit-cell effectively empty as interstitial voids accounting for only 0.01% of total charge. Details of the M-O and S-O bond lengths for **13** and their de-ammoniated compounds are given in the form of histogram in Figure 3.14b and c. The O-Mn-O and S-Mn-S bond angles for **13** and their de-ammoniated products are given as histogram in Figure 3.16. Oxidation states implied by the Lowdin charges (Table 3.1), which are different from that implied by the semi-empirical BVS analysis, suggests major depletion of electrons from 3s(4s) states of Mn and from 3s and 3p states of S, leading to oxidation states about +2 and +2.5 for Mn and S atoms respectively. The remaining valence electrons of S undergo  $sp^3$  type hybridization leading to the  $SO_4$  tetrahedra with S-O covalent bonds. Thus the eight O atoms with O-H bonds achieve complete sub shell

filling without the electrons released by the Mn atoms, thus leading to longer Mn-O[-H] bonds owing majorly to their covalent interactions with the Mn atoms. Also the total number of electrons released by the Mn and S atoms are sufficiently enough for complete sub-shell filling of the rest of the O atoms. Thus the hydrogenated framework can indeed sustain charge neutrality throughout the structure due to complete sub shell of all constituent atoms without any of them requiring any additional coordination which otherwise would have resulted into major structural modification.

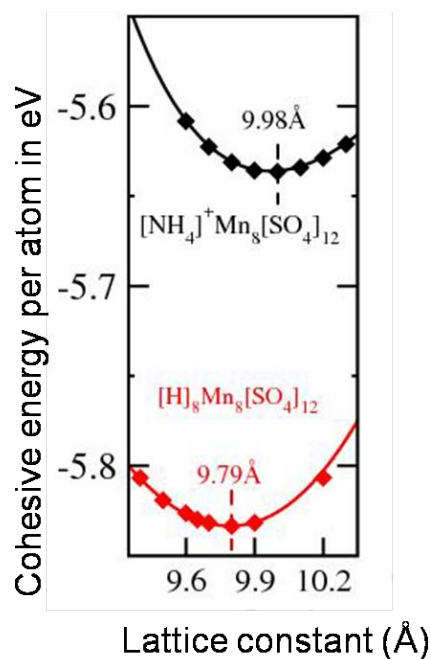


**Figure 3.15.** Fit of Murnagan equation of state to cohesive energy per atom calculated from first principles using PBE exchange-correlation to obtain equilibrium lattice constant.

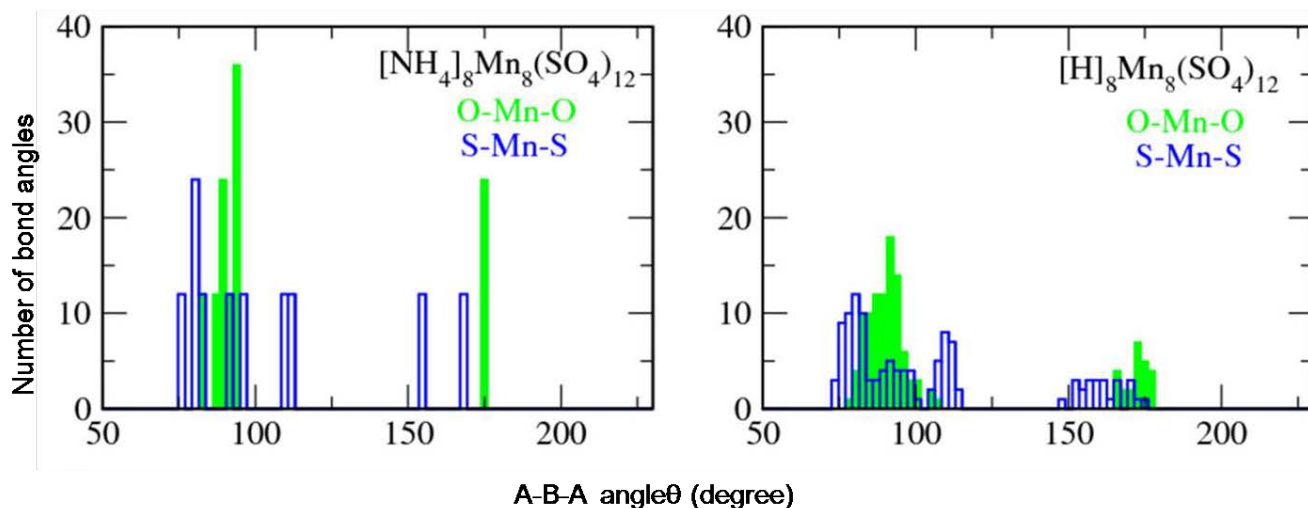


**Figure 3.16.** Histogram showing the O-Mn-O and S-Mn-S bond angles of  $[\text{NH}_4]_8[\text{Mn}_8(\text{SO}_4)_{12}]$ , **12** and their de-ammoniated products  $[\text{H}]_8[\text{Mn}_8(\text{SO}_4)_{12}]$ .

**Table 3.1.** Lowdin charges for semicore and valence orbitals of atoms

	$[\text{NH}_4]_8[\text{Mn}_8(\text{SO}_4)_{12}]$ , <b>13</b>							
Element	1s	2s	2p	3s	3p	3d	4s	4p
Mn				2.0	6.0	5.6	0.4	0.9
S				1.0	2.5			
O		1.7	4.9					
N		1.3	4.2					
Mn				2.0	6.0	5.6	0.4	0.9
S				1.0	2.5			
O		1.6	5.0					
H	0.6							

### 3.6.3.3 Magnetic Properties for $[\text{NH}_4]_8[\text{Mn}_8(\text{SO}_4)_{12}]$ , **13**

We show the variable temperature magnetic susceptibility ( $\chi$ ) data of **13** recorded at 1000 Oe in Figure 3.17. The compound is predominantly paramagnetic and the inverse susceptibility data show a linear behavior in the temperature range 50-300 K, yielding a negative Weiss temperature of -30 K, indicating weak antiferromagnetic interaction. The effective magnetic moment per manganese atom calculated from the fit of the  $\chi_M^{-1}$  versus T curve is  $5.6 \mu_B$ , almost equal to the spin only  $S = 5/2$  value of  $5.92 \mu_B$  since there is negligible orbital contribution to the moment

and is comparable to that of Mn(II) compounds reported in the literature.<sup>98-99</sup> Furthermore, no magnetic hysteresis was observed at 5 K (inset of Figure 3.17).

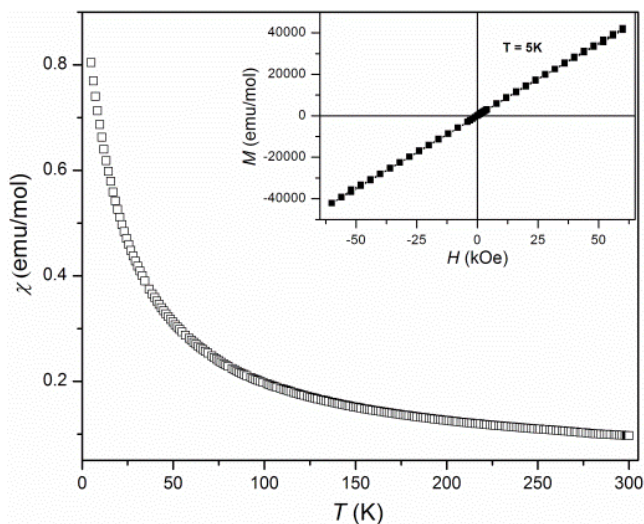


**Figure 3.17.** Temperature dependence of the magnetic susceptibility of **13** measured at 1000 Oe. Inset shows the isothermal M-H cycles of **13** at 5 K.

#### 3.6.3.4 Adsorption Properties for $[\text{NH}_4]_8[\text{Mn}_8(\text{SO}_4)_{12}]$ , **13**

The rigidity and the porosity of the structures **13** were proven by gas-sorption analysis. Hydrogen adsorption measurements of compound **13** showed only 0.45 wt% of hydrogen likely arises from the heavier atomic weight of manganese at 77 K and 890 Torr (Figure 3.18). However, they are nonporous to nitrogen as its channels size is very small and is almost equal to the kinetic diameter of nitrogen. So, we are unable to perform the  $\text{N}_2$  adsorption studies.

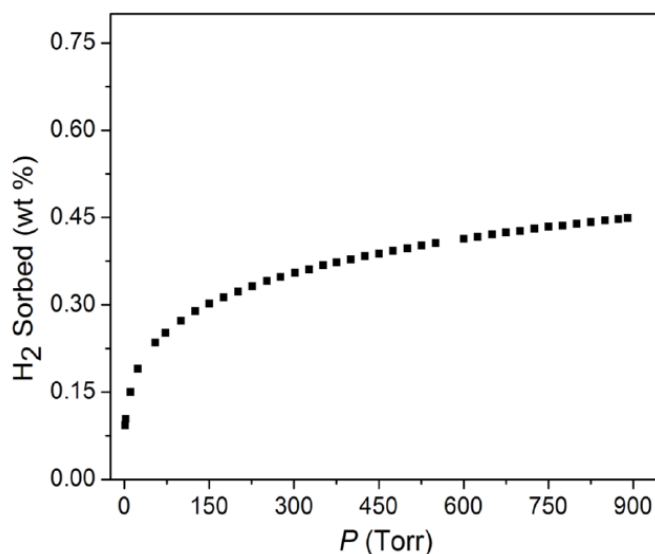


**Figure 3.18.** Hydrogen adsorption isotherm for  $[\text{NH}_4]_8[\text{Mn}_8(\text{SO}_4)_{12}]$ , **13** at 77 K.

### 3.6.3.5 Proton Conductivity Study for $[\text{NH}_4]_8[\text{Mn}_8(\text{SO}_4)_{12}]$ , **13**

We measured  $\text{H}_2\text{O}$  adsorption for **13** at 298 K as shown in Figure 3.19a. Because of the non-porosity of **13**, it does not adsorb  $\text{H}_2\text{O}$  until  $P = 2.7$  kPa ( $P/P_0 = 0.85$ ). This adsorption profile also suggests that the surface of **13** does not have  $\text{H}_2\text{O}$  condensation on the surface of crystals, because of the negligible uptake. We measured the hydrous proton ( $\text{H}^+$ ) conductivity for **13** under various RH at 298 K (Figure 3.19b). It does not show any  $\text{H}^+$  conductivity below RH = 80%, and it comes to show  $2.6 \times 10^{-7}$  S  $\text{cm}^{-1}$  at RH = 80%. The observed  $\text{H}^+$  conductivity reaches to  $3.1 \times 10^{-4}$  S  $\text{cm}^{-1}$  at RH = 90%. The proton conductivity of a  $\text{NH}_4^+$  ion containing MOF  $(\text{NH}_4)_2(\text{adp})[\text{Zn}_2(\text{ox})_3] \cdot 3\text{H}_2\text{O}^{100}$  was found to show  $8 \times 10^{-3}$  S  $\text{cm}^{-1}$  at 25 °C under 98% relative humidity (RH) conditions. The significant enhancement of  $\text{H}^+$  conductivity in the range of RH of 80 to 90% is not accountable from the  $\text{H}_2\text{O}$  adsorption uptake, because we do not observe an increase of uptake at this RH region. We assume that the  $\text{H}_2\text{O}$  molecules on the crystal surface of **13** above RH = 80% would form an effective  $\text{H}^+$  hopping pathway with the aid of ordered  $\text{SO}_4^{2-}$  groups, which contributes the  $\text{H}^+$  conductivity. We measured PXRD after the impedance spectroscopy measurements as shown in Figure 3.20 and the observed diffraction pattern was

identical to that of the original state of **13**. This indicates the crystal structure is intact even under the high RH conditions, and this supports that H<sub>2</sub>O molecules would locate on the crystal surface to promote the H<sup>+</sup>

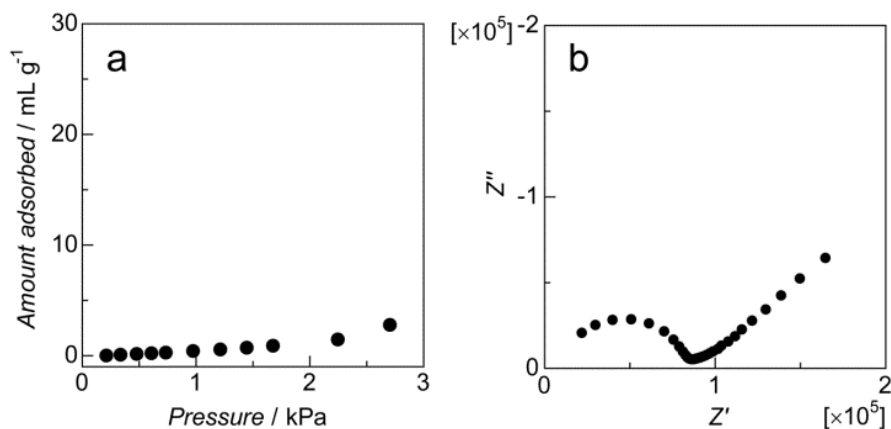


**Figure 3.19.** (a) H<sub>2</sub>O vapour adsorption isotherm for **13** at 298 K. (b) Nyquist plot of the proton conductivity of **13** under relative humidity of 85% at 298 K.

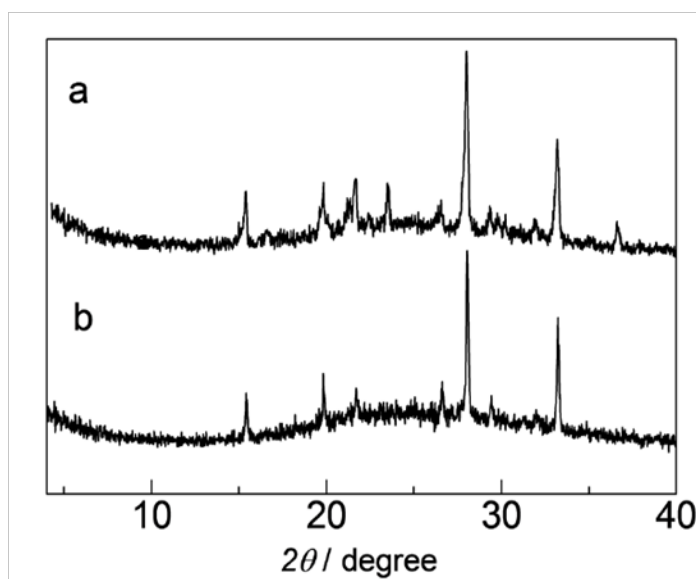


**Figure 3.20.** PXRD patterns of [NH<sub>4</sub>]<sub>8</sub>[Mn<sub>8</sub>(SO<sub>4</sub>)<sub>12</sub>], **13** (a) after and (b) before Impedance spectroscopy measurements under various RH at 298 K.

### 3.7 Conclusions

In conclusions, we synthesized open-framework metal sulfates by using transition metal atoms (Co, Ni, Zn and Mn) by changing the different structure directing agents. All the compounds were well characterized by all complementary techniques like PXRD, SXRD, chemical analysis TGA, FTIR, and EDAX. Three isostructural Kagome type 3D-metal sulfates with the composition of  $[\text{H}_3\text{O}][\text{MSO}_4\text{F}][\text{M}=\text{Co } \mathbf{9}, \text{Ni } \mathbf{10} \text{ and Zn } \mathbf{11}]$  were synthesized by hydro/solvo thermal method where the protonated water molecules are resides in the cavities. The strong complexation ability of sulfate anions were established where each sulfate anion interact with four metal ions to afford Kagome type of lattice. Magnetic studies of compounds **9** and **10** exhibits a paramagnetic behavior and shows weak antiferromagnetic interactions at low temperature. The layered structure comprising diamond chains of Co(II) sulfates with composition  $[\text{C}_4\text{N}_2\text{H}_{12}]_2[\text{Co}_3\text{F}_2(\text{SO}_4)_3(\text{H}_2\text{O})_2]$ , **12** has been synthesized under hydro/solvothermal conditions and structurally characterized. The magnetic behavior of the layered cobalt sulfate, with the diamond chains containing three CoO(F) octahedra is ferrimagnetic and shows magnetic hysteresis at low temperatures. The frequency dependence study shows **12** does not exhibit spin-glass freezing. 3D chiral Mn(II) sulfate with composition of  $[\text{NH}_4]_8[\text{Mn}_8(\text{SO}_4)_{12}]$ , **13** has been synthesized by hydro/solvothermal method. High temperature X-ray diffraction, Thermogravimetric analysis and DFT calculations suggest a gross retention of the framework structure **13** even after the thermal decomposition of the ammonium ion, which results in the formation of  $[\text{H}]_8[\text{Mn}_8(\text{SO}_4)_{12}]$ . Compound **13** is predominantly paramagnetic in nature and show reversible hydrogen adsorption of 0.45 wt% at 77 K. The proton conductivity of **13** under various RH increases from  $2.6 \times 10^{-7} \text{ S cm}^{-1}$  at RH= 80% to  $3.1 \times 10^{-4} \text{ S cm}^{-1}$  at RH= 90%.

### 3.8 References

1. Kinoshita, M., *Japanese journal of applied physics* **1994**, *33*, 5718.
2. Blundell, S. J.; Pratt, F. L., *J. Phys.: Condens. Matter* **2004**, *16*, R771.
3. Carlin, R. L.; De Jongh, L., *Chem. Rev.* **1986**, *86*, 659.
4. *See the Proceedings of the International Conference on Molecule-Based Magnets, Polyhedron* **2007, 2009, 2011**.
5. Kajiwara, T.; Kamiyama, A.; Ito, T., *Chem. Commun.* **2002**, 1256.
6. MasPOCH, D.; Ruiz-Molina, D.; Wurst, K.; Domingo, N.; Cavallini, M.; Biscarini, F.; Tejada, J.; Rovira, C.; Veciana, J., *Nat Mater* **2003**, *2*, 190.
7. Galán-Mascarós, J. R.; Dunbar, K. R., *Angew. Chem. Int. Ed.* **2003**, *42*, 2289.
8. MasPOCH, D.; Ruiz-Molina, D.; Veciana, J., *J. Mater. Chem.* **2004**, *14*, 2713.
9. Poulsen, R. D.; Bentien, A.; Chevalier, M.; Iversen, B. B., *J. Am. Chem. Soc.* **2005**, *127*, 9156.
10. Ohba, M.; Ōkawa, H., *Coord. Chem. Rev.* **2000**, *198*, 313.
11. Batten, S. R.; Murray, K. S., *Coord. Chem. Rev.* **2003**, *246*, 103.
12. Ribas, J.; Escuer, A.; Monfort, M.; Vicente, R.; Cortés, R.; Lezama, L.; Rojo, T., *Coord. Chem. Rev.* **1999**, *193*, 1027.
13. Powell, A. V.; Leyva-Bailen, P.; Vaqueiro, P.; Sanchez, R. D., *Chem. Mater.* **2009**, *21*, 4102.
14. Rujiwatra, A.; Kepert, C. J.; Claridge, J. B.; Rosseinsky, M. J.; Kumagai, H.; Kurmoo, M., *J. Am. Chem. Soc.* **2001**, *123*, 10584.
15. Rao, C.; Behera, J.; Dan, M., *Chem. Soc. Rev.* **2006**, *35*, 375.
16. Behera, J.; Gopalkrishnan, K.; Rao, C., *Inorg. Chem.* **2004**, *43*, 2636.

17. Paul, G.; Choudhury, A.; Rao, C. N. R., *Chem. Mater.* **2003**, *15*, 1174.
18. Fan, Y.; Hua Li, G.; Yang, L.; Ming Zhang, Z.; Chen, Y.; You Song, T.; Hua Feng, S., *Eur. J. Inorg. Chem.* **2005**, *2005*, 3359.
19. Rao, C. N. R.; Behera, J. N.; Dan, M., *Chem. Soc. Rev.* **2006**, *35*, 375.
20. Kurmoo, M., *Chem. Soc. Rev.* **2009**, *38*, 1353.
21. Shores, M. P.; Nytko, E. A.; Bartlett, B. M.; Nocera, D. G., *J. Am. Chem. Soc.* **2005**, *127*, 13462.
22. Grohol, D.; Matan, K.; Cho, J.-H.; Lee, S.-H.; Lynn, J. W.; Nocera, D. G.; Lee, Y. S., *Nat. Mater.* **2005**, *4*, 323.
23. Pati, S. K.; Rao, C. N. R., *Chem. Commun.* **2008**, 4683.
24. Bartlett, B. M.; Nocera, D. G., *J. Am. Chem. Soc.* **2005**, *127*, 8985.
25. Liu, D.; Huang, G.; Huang, C.; Huang, X.; Chen, J.; You, X.-Z., *Cryst. Growth Des.* **2009**, *9*, 5117.
26. Bala, S.; Bhattacharya, S.; Goswami, A.; Adhikary, A.; Konar, S.; Mondal, R., *Cryst. Growth Des.* **2014**, *14*, 6391.
27. Zhang, W.-X.; Xue, W.; Chen, X.-M., *Inorg. Chem.* **2011**, *50*, 309.
28. Liu, S.-S.; Yuan, S.; Li, X.-Y.; Miao, S.; Yu, Z.-W.; Wang, X.-P.; Sun, D., *Inorg. Chim. Acta* **2014**, *416*, 195.
29. Li, Y.-M.; Xiao, C.-Y.; Zhang, X.-D.; Xu, Y.-Q.; Lun, H.-J.; Niu, J.-Y., *CrystEngComm* **2013**, *15*, 7756.
30. Keene, T. D.; Murphy, M. J.; Price, J. R.; Sciortino, N. F.; Southon, P. D.; Kepert, C. J., *Dalton Trans.* **2014**, *43*, 14766.

31. Li, Z.-X.; Zhao, J.-P.; Sanudo, E. C.; Ma, H.; Pan, Z.-D.; Zeng, Y.-F.; Bu, X.-H., *Inorg. Chem.* **2009**, *48*, 11601.
32. Wibowo, A. C.; Smith, M. D.; zur Loye, H.-C., *Chem. Commun.* **2011**, *47*, 7371.
33. Aidoudi, F. H.; Downie, L. J.; Morris, R. E.; A. de Vries, M.; Lightfoot, P., *Dalton Trans.* **2014**, *43*, 6304.
34. Hu, B.-W.; Zhao, J.-P.; Tao, J.; Sun, X.-J.; Yang, Q.; Zhang, X.-F.; Bu, X.-H., *Cryst. Growth Des.* **2010**, *10*, 2829.
35. Yang, Q.; Zhao, J.-P.; Song, W.-C.; Bu, X.-H., *Dalton Trans.* **2012**, *41*, 6272.
36. Behera, J. N.; Rao, C. N. R., *J. Am. Chem. Soc.* **2006**, *128*, 9334.
37. Behera, J. N.; Paul, G.; Choudhury, A.; Rao, C. N. R., *Chem. Commun.* **2004**, 456.
38. Paul, G.; Choudhury, A.; Rao, C. N. R., *Chem. Commun.* **2002**, 1904.
39. Nagaraja, C. M.; Behera, J. N.; Maji, T. K.; Pati, S. K.; Rao, C. N. R., *Dalton Trans.* **2010**, *39*, 6947.
40. Powell, A. V.; Leyva-Bailen, P.; Vaqueiro, P.; Sanchez, R. D., *Chem. Mater.* **2009**, *21*, 4102.
41. Neeraj, S.; Natarajan, S.; Rao, C. N. R., *Chem. Commun.* **1999**, 165.
42. Monge, A.; Snejko, N.; Gutierrez-Puebla, E.; Medina, M.; Cascales, C.; Ruiz-Valero, C.; Iglesias, M.; Gomez-Lor, B., *Chem. Commun.* **2005**, 1291.
43. Wang, X.-L.; Qin, C.; Wang, E.-B.; Xu, L.; Su, Z.-M.; Hu, C.-W., *Angew. Chem., Int. Ed.* **2004**, *43*, 5036.
44. Wang, X.-L.; Qin, C.; Wang, E.-B.; Li, Y.-G.; Su, Z.-M., *Chem. Commun.* **2005**, 5450.
45. Perez-Garcia, L.; Amabilino, D. B., *Chem. Soc. Rev.* **2002**, *31*, 342.
46. Gao, E.-Q.; Bai, S.-Q.; Wang, Z.-M.; Yan, C.-H., *J. Am. Chem. Soc.* **2003**, *125*, 4984.

47. Wang, M.; Li, J.-y.; Yu, J.-h.; Pan, Q.-h.; Song, X.-w.; Xu, R.-r., *Inorg. Chem.* **2005**, *44*, 4604.
48. Moon, D.; Song, J.; Kim, B. J.; Suh, B. J.; Lah, M. S., *Inorg. Chem.* **2004**, *43*, 8230.
49. Taddei, M.; Donnadio, A.; Costantino, F.; Vivani, R.; Casciola, M., *Inorg. Chem.* **2013**, *52*, 12131.
50. Chen, X.-M.; Liu, G.-F., *Chem. - Eur. J.* **2002**, *8*, 4811.
51. Newsam, J. M.; Treacy, M. M. J.; Koetsier, W. T.; Gruyter, C. B. D., *Proc. R. Soc. A* **1988**, *420*, 375.
52. Stalder, S. M.; Wilkinson, A. P., *Chem. Mater.* **1997**, *9*, 2168.
53. Gray, M. J.; Jasper, J. D.; Wilkinson, A. P.; Hanson, J. C., *Chem. Mater.* **1997**, *9*, 976.
54. Bruce, D. A.; Wilkinson, A. P.; White, M. G.; Bertrand, J. A., *J. Solid State Chem.* **1996**, *125*, 228.
55. Chen, P.; Li, J.; Yu, J.; Wang, Y.; Pan, Q.; Xu, R., *J. Solid State Chem.* **2005**, *178*, 1929.
56. Rujiwatra, A.; Kepert, C. J.; Rosseinsky, M. J., *Chem. Commun. (Cambridge)* **1999**, 2307.
57. Rujiwatra, A.; Kepert, C. J.; Claridge, J. B.; Rosseinsky, M. J.; Kumagai, H.; Kurmoo, M., *J. Am. Chem. Soc.* **2001**, *123*, 10584.
58. Behera, J. N.; Rao, C. N. R., *Can. J. Chem.* **2005**, *83*, 668.
59. Akkari, H.; Benard-Rocherulle, P.; Merazig, H.; Roisnel, T.; Rocherulle, J., *Solid State Sci.* **2006**, *8*, 704.
60. Ding, S.; Xu, Y.; Nie, L.; Feng, W., *J. Cluster Sci.* **2006**, *17*, 627.
61. Bataille, T.; Louer, D., *J. Mater. Chem.* **2002**, *12*, 3487.
62. Norquist, A. J.; Doran, M. B.; Thomas, P. M.; O'Hare, D., *Dalton Trans.* **2003**, 1168.

63. Thomas, P. M.; Norquist, A. J.; Doran, M. B.; O'Hare, D., *J. Mater. Chem.* **2003**, *13*, 88.
64. Doran, M.; Norquist, A. J.; O'Hare, D., *Chem. Commun.* **2002**, 2946.
65. Kumagai, H.; Inoue, K., *Angew. Chem. Int. Ed.* **1999**, *38*, 1601.
66. Minguet, M.; Luneau, D.; Lhotel, E.; Villar, V.; Paulsen, C.; Amabilino, D. B.; Veciana, J., *Angew. Chem., Int. Ed.* **2002**, *41*, 586.
67. Inoue, K.; Imai, H.; Ghalsasi, P. S.; Kikuchi, K.; Ohba, M.; Okawa, H.; Yakhmi, J. V., *Angew. Chem., Int. Ed.* **2001**, *40*, 4242.
68. Knof, U.; von Zelewsky, A., *Angew. Chem. Int. Ed.* **1999**, *38*, 302.
69. Xin, F.; Pope, M. T., *J. Am. Chem. Soc.* **1996**, *118*, 7731.
70. Long, D.-L.; Kogerler, P.; Farrugia, L. J.; Cronin, L., *Chem. - Asian J.* **2006**, *1*, 352.
71. Long, D.-L.; Burkholder, E.; Cronin, L., *Chem. Soc. Rev.* **2007**, *36*, 105.
72. Streb, C.; Long, D.-L.; Cronin, L., *Chem. Commun.* **2007**, 471.
73. Kortz, U.; Savelieff, M. G.; Ghali, F. Y. A.; Khalil, L. M.; Maalouf, S. A.; Sinno, D. I., *Angew. Chem., Int. Ed.* **2002**, *41*, 4070.
74. Fang, X.; Anderson, T. M.; Hill, C. L., *Angew. Chem., Int. Ed.* **2005**, *44*, 3540.
75. Fang, X.; Anderson, T. M.; Hou, Y.; Hill, C. L., *Chem. Commun.* **2005**, 5044.
76. Sporer, C.; Wurst, K.; Amabilino, D. B.; Ruiz-Molina, D.; Kopacka, H.; Jaitner, P.; Veciana, J., *Chem. Commun.* **2002**, 2342.
77. Katsuki, I.; Motoda, Y.; Sunatsuki, Y.; Matsumoto, N.; Nakashima, T.; Kojima, M., *J. Am. Chem. Soc.* **2002**, *124*, 629.
78. Tabellion, F. M.; Seidel, S. R.; Arif, A. M.; Stang, P. J., *Angew. Chem., Int. Ed.* **2001**, *40*, 1529.

79. Sasa, M.; Tanaka, K.; Bu, X.-H.; Shiro, M.; Shionoya, M., *J. Am. Chem. Soc.* **2001**, *123*, 10750.
80. Tan, H.; Li, Y.; Zhang, Z.; Qin, C.; Wang, X.; Wang, E.; Su, Z., *J. Am. Chem. Soc.* **2007**, *129*, 10066.
81. Soghomonian, V.; Chen, Q.; Haushalter, R. C.; Zubieta, J.; O'Connor, C. J., *Science* **1993**, *259*, 1596.
82. Wang, W.-H.; Tian, H.-R.; Zhou, Z.-C.; Feng, Y.-L.; Cheng, J.-W., *Cryst. Growth Des.* **2012**, *12*, 2567.
83. Naili, H.; Hajlaoui, F.; Mhiri, T.; MacLeod, T. C. O.; Kopylovich, M. N.; Mahmudov, K. T.; Pombeiro, A. J. L., *Dalton Trans.* **2013**, *42*, 399.
84. Nakamoto, K., *Infrared and Raman spectra of inorganic and coordination compounds*. Wiley Online Library: 1986.
85. Sheldrick, G. M., *SHELXL-97, program for X-ray crystal structure refinement*, University of Göttingen, Germany **1997**.
86. Sheldrick, G. M., *SHELXTL-PLUS Program for Crystal Structure Solution and Refinement*, University of Göttingen, Göttingen, Germany.
87. Sheldrick, G. M., *SADABS Siemens Area Correction Absorption Program*, University of Göttingen, Göttingen, Germany **1994**.
88. Pennington, W., *J. Appl. Crystallogr.* **1999**, *32*, 1028.
89. Farrugia, L., *J. Appl. Crystallogr.* **1997**, *30*, 565.
90. Freedman, D. E.; Chisnell, R.; McQueen, T. M.; Lee, Y. S.; Payen, C.; Nocera, D. G., *Chem. Commun.* **2012**, *48*, 64.
91. Tang, Y.; Guo, W.; Zhang, S.; Yang, M.; He, Z., *Cryst. Growth Des.* **2014**, *14*, 5206.

92. Brown, I. D.; Altermatt, D., *Acta Cryst. B* **1985**, *41*, 244.
93. Hawthorne, F. C.; Krivovichev, S. V.; Burns, P. C., *Reviews in Mineralogy and Geochemistry* **2000**, *40*, 1.
94. Belokoneva, E.; Gubina, Y. K.; Forsyth, J., *Phys. Chem. Miner.* **2001**, *28*, 498.
95. Vilminot, S.; Baker, P. J.; Blundell, S. J.; Sugano, T.; André, G.; Kurmoo, M., *Chem. Mater.* **2010**, *22*, 4090.
96. Nagaraja, C. M.; Kumar, N.; Maji, T. K.; Rao, C. N. R., *Eur. J. Inorg. Chem.* **2011**, *2011*, 2057.
97. Lowdin, P. O., *Advan. Quantum Chem.* **1970**, *5*, 185.
98. Lethbridge, Z. A. D.; Smith, M. J.; Tiwary, S. K.; Harrison, A.; Lightfoot, P., *Inorg. Chem.* **2004**, *43*, 11.
99. Behera, J. N.; Rao, C. N. R., *Dalton Trans.* **2007**, 669.
100. Sadakiyo, M.; Yamada, T.; Kitagawa, H., *J. Am. Chem. Soc.* **2009**, *131*, 9906.

### 3.9 Appendix

**Table 3.2.** Crystal data structure refinement parameters for **9-11**

Parameters	<b>9</b>	<b>10</b>	<b>11</b>
Empirical formula	[H <sub>3</sub> O].[CoSO <sub>4</sub> F]	[H <sub>3</sub> O].[NiSO <sub>4</sub> F]	[H <sub>3</sub> O].[ZnSO <sub>4</sub> F]
<i>a</i> (Å)	13.1891(6)	13.0149(3)	13.184(5)
<i>b</i> (Å)	10.6850(6)	10.6079(3)	10.639(5)
<i>c</i> (Å)	6.6081(3)	6.5455(2)	6.626(5)
$\alpha$ ( <sup>0</sup> )	90	90	90
$\beta$ ( <sup>0</sup> )	90	90	90
$\gamma$ ( <sup>0</sup> )	90	90	90
<i>V</i> (Å <sup>3</sup> )	931.25(8)	903.68(4)	929.4
<i>Z</i>	8	8	8
Formula weight	193.01	192.79	191.65
Space group	P n n a	P n n a	P n n a
<i>T</i> (°C)	23	23	23
$\lambda$ (MoK $\alpha$ ) Å	0.71073	0.71073	0.71073
$\rho_{\text{calc}}$ (gcm <sup>-3</sup> )	2.753	2.834	2.913
$\mu$ (mm <sup>-1</sup> )	4.087	4.708	4.652
R[I.>2 $\sigma$ (I)]	R1 = 0.0541, wR2 = 0.1241	R1 = 0.0503, wR2 = 0.1143	R1 = 0.061, wR2 = 0.1213
R (all data)	R1 = 0.0563, wR2 = 0.1248	R1 = 0.0572, wR2 = 0.1164	R1 = 0.066, wR2 = 0.1256

$$R_1 = \frac{\sum |F_o| - |F_c|}{\sum |F_o|}; wR_2 = \left\{ \frac{[\sum w(F_o^2 - F_c^2)^2]}{[\sum w(F_o^2)^2]} \right\}^{1/2}, w = 1/[\sigma^2(F_o)^2 + (aP)^2 + bP] P = [F_o^2 + 2Fc^2]/3;$$

Where a= 0.0512; b= 0.5013 for **9**, a=0.0176; b= 0.713 for **10** and a=0.0734; b= 0.1237 for **11**.

**Table 3.3.** Crystal data structure refinement parameters for **12-13**.

Parameters	<b>12</b>	<b>13</b>
Empirical formula	[C <sub>4</sub> N <sub>2</sub> H <sub>12</sub> ] <sub>2</sub> [C <sub>03</sub> F <sub>2</sub> (SO <sub>4</sub> ) <sub>3</sub> (H <sub>2</sub> O) <sub>2</sub> ]	[NH <sub>4</sub> ] <sub>8</sub> [Mn <sub>2</sub> (SO <sub>4</sub> ) <sub>12</sub> ]
<i>a</i> (Å)	10.0475(2)	10.1846(2)
<i>b</i> (Å)	22.0781(4)	10.1846(2)
<i>c</i> (Å)	7.26340(10)	10.1846(2)
α(°)	90	90
β(°)	90	90
γ(°)	90	90
<i>V</i> (Å <sup>3</sup> )	1611.24(5)	1056.41(4)
<i>Z</i>	4	12
Formula weight	627.16	144.71
Space group	Pnma (62)	<i>P2(1)3(198)</i>
<i>T</i> (°C)	23	23
λ(MoKα) Å	0.71073	0.71073
ρ <sub>calc</sub> (gcm <sup>-3</sup> )	2.585	2.730
μ (mm <sup>-1</sup> )	3.545	3.056
R[I.>2σ(I)]	R1 = 0.0200 wR2 = 0.0508	R1 = 0.0150 wR2 = 0.0378
R (all data)	R1 = 0.0223 wR2 = 0.0530	R1 = 0.0153, wR2 = 0.0379

$$R_1 = \sum |F_o| - |F_c|; wR_2 = \{ [w(F_o^2 - F_c^2)^2] / [w(F_o^2)^2] \}^{1/2}, w = 1 / [\sigma^2(F_o)^2 + (aP)^2 + bP] P = [F_o^2 + 2F_c^2] / 3;$$

Where a=0.0286; b=0.8291 for **12** and a=0.0247; b= 0.1707 for **13**.

**Table 3.4.** The Hydrogen Bonding Interactions for  $[\text{C}_4\text{N}_2\text{H}_{12}]_2[\text{Co}_3\text{F}_2(\text{SO}_4)_3(\text{H}_2\text{O})_2]$ , **12**

D-H...A	D...A(A°)	H...A(A°)	D...H(A°)	D-H...A(A°)
N(1)-H(1)···O(8)	3.180(7)	2.56	0.92	125
N(1)-H(2)···O(8)	3.139(8)	2.59	0.92	119
O(4)-H(7)···O(7)	2.856(6)	2.15(9)	0.86(9)	140(7)
O(1)-H(8)···O(6)	2.910(6)	2.23(8)	0.90(5)	132(7)
O(4)-H(8)···O(2)	3.198(6)	2.32(5)	0.90(5)	164(8)
C(1)-H(5)···O(3)	3.107(7)	2.15	0.99	162
C(1)-H(6)···O(4)	3.034(7)	2.49	0.99	114
C(1)-H(6)···O(5)	3.529(7)	2.56	0.99	166
C(1)-H(6)···O(8)	2.938(7)	2.33	0.99	119

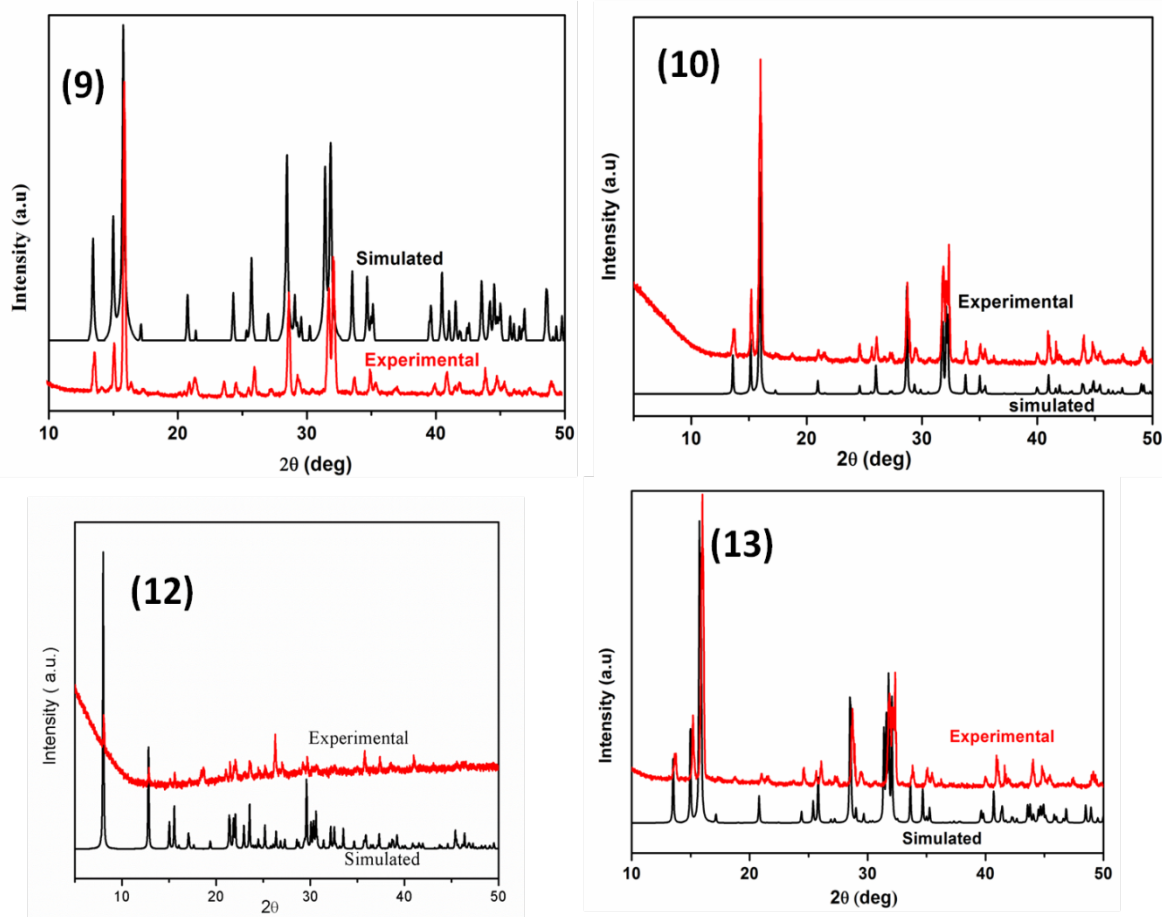


**Figure 3.21.** Experimental and simulated PXRD patterns: for  $[\text{H}_3\text{O}][\text{MSO}_4\text{F}]$  [ $\text{M}=\text{Co}$  (**9**) and  $\text{Ni}$  (**10**)],  $[\text{C}_4\text{N}_2\text{H}_{12}]_2[\text{Co}_3\text{F}_2(\text{SO}_4)_3(\text{H}_2\text{O})_2]$ , **12** and for  $[\text{NH}_4]_8[\text{Mn}_2(\text{SO}_4)_{12}]$ , **13**.

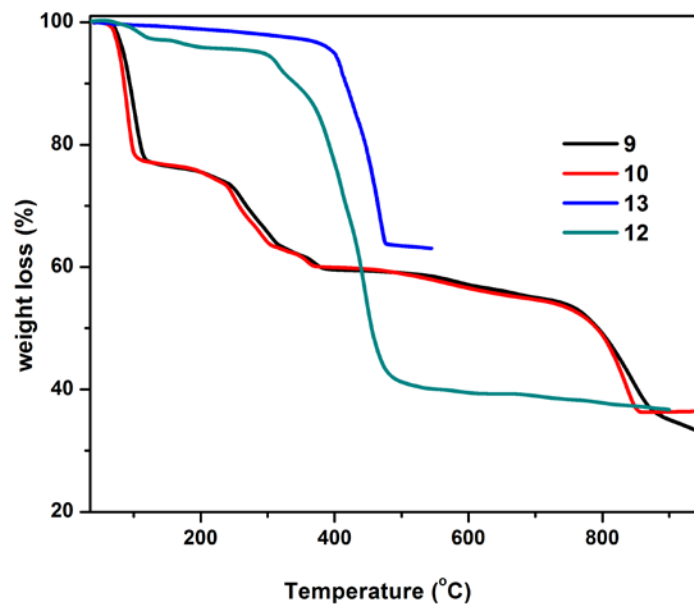


**Figure 3.22.** TGA for  $[\text{H}_3\text{O}][\text{CoSO}_4\text{F}]$ , **9**;  $[\text{H}_3\text{O}][\text{NiSO}_4\text{F}]$ , **10**;  $[\text{C}_4\text{N}_2\text{H}_{12}]_2 [\text{Co}_3\text{F}_2(\text{SO}_4)_3(\text{H}_2\text{O})_2]$ , **12** and  $[\text{NH}_4]_8[\text{Mn}_2(\text{SO}_4)_{12}]$ , **13**.

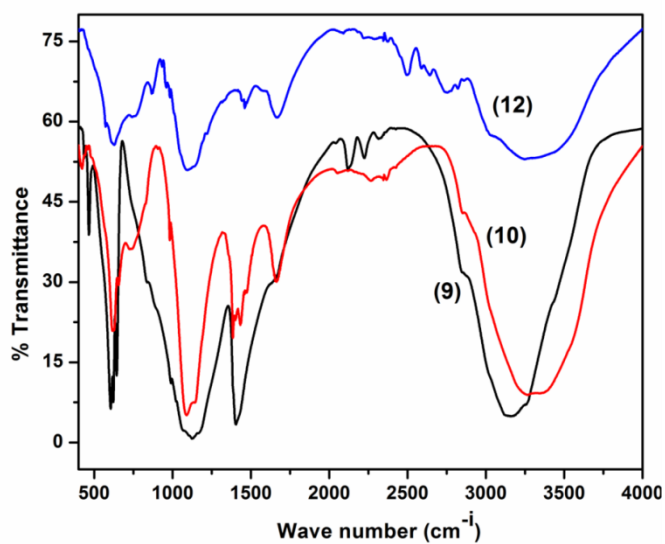


**Figure 3.23.** FTIR spectra for  $[\text{H}_3\text{O}][\text{CoSO}_4\text{F}]$ , **9**;  $[\text{H}_3\text{O}][\text{NiSO}_4\text{F}]$ , **10**.and  $[\text{C}_4\text{N}_2\text{H}_{12}]_2 [\text{Co}_3\text{F}_2(\text{SO}_4)_3(\text{H}_2\text{O})_2]$ , **12**.

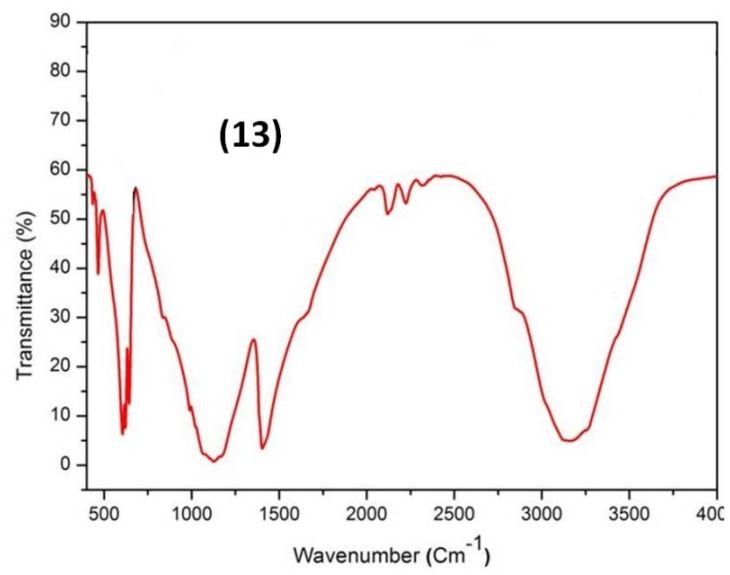
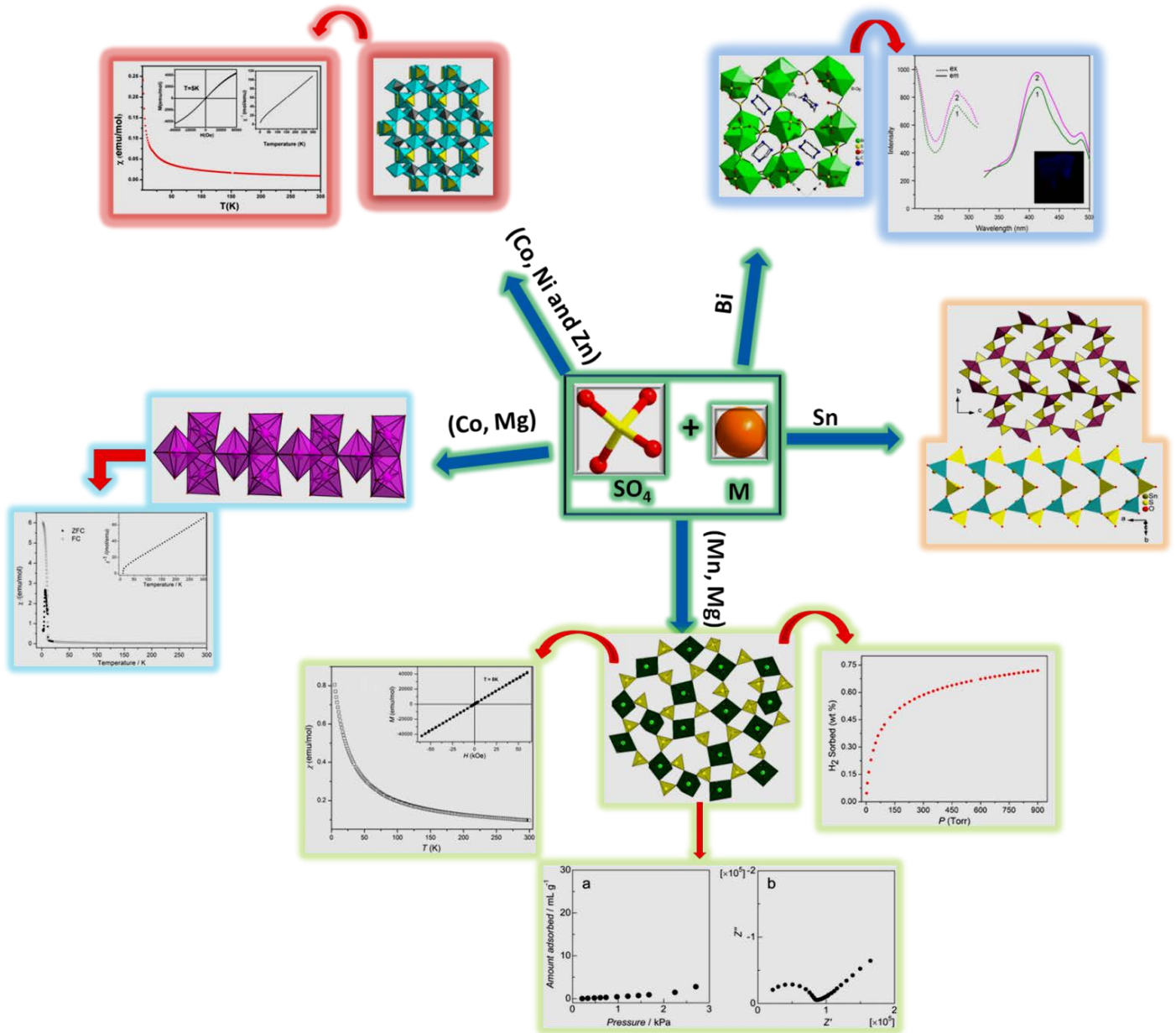


**Figure 3.24.** FTIR spectra of  $[\text{NH}_4]_8[\text{Mn}_8(\text{SO}_4)_{12}]$ , **13**.

# Summary of Part-1



## **PART-2**

# **Supercapacitors Based on Vanadium Chalcogenides-RGO/CNT Hybrids**

# CHAPTER-1

## Introduction of Supercapacitor

<b>1.1</b>	Introduction	164
<b>1.2</b>	Supercapacitor	165
<b>1.2.1</b>	Basic setup of supercapacitor	165
<b>1.2.2</b>	Common parameters in supercapacitor	166
<b>1.2.2.1</b>	Energy density and power density	166
<b>1.2.2.2</b>	Efficiency	166
<b>1.2.3</b>	Electrolytes used in supercapacitor	167
<b>1.2.3.1</b>	Aqueous electrolytes	167
<b>1.2.3.2</b>	Organic electrolytes	168
<b>1.2.3.3</b>	Ionic liquid electrolytes	168
<b>1.2.4</b>	Types of electrode materials	169
<b>1.2.4.1</b>	Carbon materials	169
<b>1.2.4.2</b>	Transition metal oxides	170
<b>1.2.4.3</b>	Conducting polymers	171
<b>1.2.5</b>	Calculation of supercapacitance for electrode materials	172
<b>1.2.5.1</b>	Cyclic voltammetry	172
<b>1.2.5.2</b>	Constant current charge/discharge	173
<b>1.2.5.3</b>	Electro chemical impedance spectroscopy	174
<b>1.2.6</b>	Types of mechanisms	176
<b>1.2.6.1</b>	Electrical double layer-mechanism	176
<b>1.2.6.2</b>	Pseudocapacitance mechanism	179
<b>1.2.6.3</b>	Hybrid supercapacitor	180
<b>1.3</b>	Metal chalcogenides in supercapacitor	180
<b>1.4</b>	Supercapacitance of TMCs/GO	182
<b>1.5</b>	Supercapacitance of TMCs/CNTs	184
<b>1.6</b>	References	186

## 1.1 Introduction

The consumption of the fossil fuel, and increasing global warming have been driving to the alternative efficient, clean and sustainable source of energy need to be developed. Due to fast grow of global economy we need an urgent demand for the environmentally friendly high-energy power source. Supercapacitor (SC) or electrochemical supercapacitor (ES) or ultra capacitor getting a great attention because of their high pulse power supply, long cycle life (>100,000 cycles), simple operating principle, and high dynamics of charge propagation.<sup>1</sup> Supercapacitor have (almost 1000 times) higher powder density ( $P_d$ ) than the lithium ion batteries and large energy density ( $E_d$ ) than the conventional capacitors. The comparison of properties and performance of the battery, supercapacitor and capacitor were given in Table 1.1.

**Table 1.1.** Comparison of the properties and performance of Battery, Capacitor and supercapacitor<sup>2</sup>

Parameters	Battery	Capacitor	Supercapacitor
Charge time	0.3 - 3hrs	$10^{-6} - 10^{-3}$ sec	1 - 30 sec
Discharge time	1 - 5hrs	$10^{-6} - 10^{-3}$ sec	1 - 30 sec
Cycle life	500 - 2,000	>500,000	>100,000
Energy density	20 - 100	<0.1	1 - 10
Charge/Discharge (CD) efficiency	0.7 - 0.85	~1.0	0.9 - 0.95
Power density	50 - 200	>10,000	1,000 - 2,000

From the Table1.1 Batteries have lower power density than the capacitor and supercapacitor but having high energy density. Conventional capacitor having high power density and long life

cycle than the battery but having less energy density, whereas in supercapacitor have combined properties of both high power density and energy density, and also having long life cycle due to the absence of chemical reactions.

## 1.2 Supercapacitor

### 1.2.1 Basic setup of supercapacitor

Supercapacitors are electrochemical energy storage devices. The basic setup of a supercapacitor is similar to a battery (Figure 1.1) it consists of two porous electrodes connected by a current collector. Two electrodes are immersed in a suitable electrolyte and separated by a dielectric separator. When a voltage is applied to the current collectors, positive ions are attracted by the negative electrode and negative ions are attracted by the positive ions. The charge will be accumulated on both the electrode surfaces, generating energy when it is discharged. The performance of the supercapacitor depends on the components made up of the supercapacitor, which are the type of electrodes, electrolyte, the separator, and the current collector. The performance of the supercapacitor is mainly evaluated on the basis of the following points.<sup>1</sup> (1) Higher power density greater than the battery. (2) High energy density. (3) Low cost (4) Safe operation. (5) Excellent cycle stability (more than 100 times greater than battery). (6) Fast charge/discharge within seconds and (7) Very slow self-discharge process.

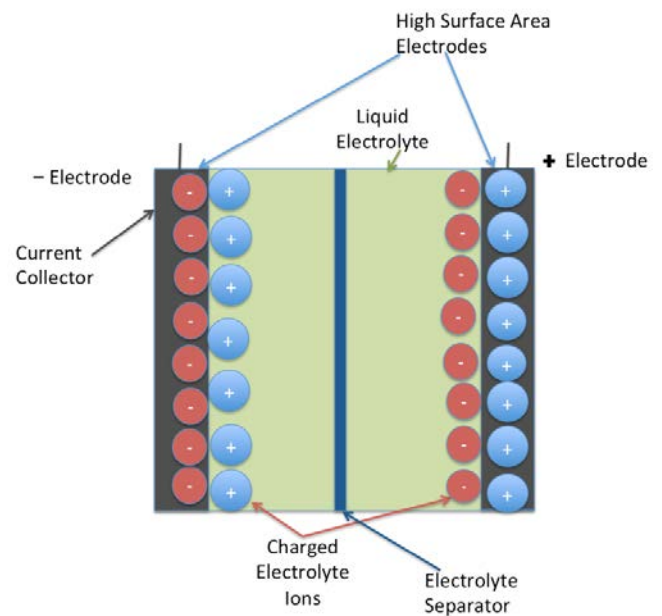


**Figure 1.1.** Schematic diagrams for the electrochemical supercapacitor.

## 1.2.2 Common parameters in supercapacitor

### 1.2.2.1 Energy density and Power density

The performance of the supercapacitor can be considered by looking the energy and power density values. The capacitor having high energy and power density then it has good performances. Notable, the energy density of the supercapacitor decrease with increasing the power density, therefore both of them inversely proportional to each other. Charge/discharge method is used to measure the energy and power density of the supercapacitance. Generally, Energy density of the supercapacitance is directly proportional to specific capacitance and operational potential voltage window shown in the equation (1.1)

$$E = \frac{1}{2} C (\Delta V)^2 \quad (1.1)$$

$$P = \frac{E}{T} \quad (1.2)$$

Power density of the supercapacitance directly proportional to energy density but inversely to the discharge time shown in equation (1.2)<sup>3-4</sup>

Where F is specific capacitance (F/g),  $\Delta V$  is the potential voltage window (V), T is discharge time, E is energy density (Wh/kg) and P is power density (KW/kg).

### 1.2.2.2 Columbic Efficiency ( $\eta$ )

The efficiency of the capacitor can be calculated by using the cyclic stability test by using the first and last cycle. It is defined as the ratio of time of discharging and time of charging given in equation (1.3)<sup>5-7</sup>

$$\eta = \frac{t_D}{t_C} \times 100 \% \quad (1.3)$$

Where  $t_D$  discharging time (s),  $t_C$  charging time (s) and  $\eta$  columbic efficiency.

### **1.2.3 Electrolytes used in supercapacitor**

The performance of the SC depends up on the electrolyte which was present inside the separator as well as the inside the active material layers. The main requirements for the electrolyte to used in the ES: High electrical stability, wide voltage window, high ionic concentration and low solvated ionic radius, low resistivity, low viscosity, low volatility, low toxicity, low cost as well as availability as pure form.<sup>1</sup> There are three types of electrolytes used in the ES which are

- (1) Aqueous electrolytes
- (2) Organic electrolytes
- (3) Ionic liquids

#### **1.2.3.1 Aqueous electrolytes**

There are many aqueous electrolytes are present which are  $H_2SO_4$ ,  $KOH$ ,  $K_2SO_4$ ,  $Na_2SO_4$ ,  $NH_4Cl$  *etc.* The main advantage of aqueous electrolyte has higher ionic concentration and lower resistance than the organic electrolyte. ES having aqueous electrolyte shows higher capacitance and power density probably due to the higher ionic concentration and lower ionic radius. For preparing the aqueous electrolytes no need of any special process and conditions to get pure form but Organic electrolytes need a strict process and separate conditions for getting the ultra-pure electrolyte.

The disadvantage of the aqueous electrolyte have lower working voltage window i.e. 1.2 V which is much lower than the organic electrolytes.<sup>1</sup> Hence, the aqueous electrolyte has large limitation on improving the both power and energy densities due to the narrow operational voltage window. So, the organic electrolytes are come in to the picture for rectifying all aqueous electrolyte disadvantages.

### **1.2.3.2 Organic electrolytes**

The operational working potential voltage window for the organic electrolytes as high as 3.5 V. This is the main advantage of the organic electrolyte over the aqueous electrolyte. There are many organic electrolytes among them acetonitrile and propylene carbonate (PPC) are the most commonly used electrolytes. Acetonitrile can dissolve large number of salts than the other electrolytes but it has toxic problems and environmentally not good. PPC based electrolytes are good for the environment and less toxic.<sup>1</sup> Organic electrolytes can offer wide electrochemical potential window, wide range of operational temperatures and good conductivity. In organic electrolytes water content always should be below 3-5 ppm otherwise the performance of SC will be significantly comes low.

### **1.2.3.3 Ionic liquids (ILs)**

ILs have recently emerged as “green” and environment friendly solvents for their use in the industrial manufacture of chemicals. From past few years ILs has been used for the diverse applications such as organic synthesis, catalysis, solvent extraction of the variety of the compounds and electrochemical device. ILs are composed of both cations and anions having low melting point (<100 °C).<sup>8</sup> The Cations may be organic or inorganic, anions are inorganic. Ionic liquids have some desirable properties which are low vapor pressure, high thermal and electrical stability,<sup>9-10</sup> low flammability, electrochemical stability, operational voltage window ranging from 2 to 6 V (order of 4.5 V) and high electrical conductivity with level of 10 mS/cm.<sup>11</sup> Due to all these properties Ionic liquids make them to use in the electrolyte in ES. Since ILs are solvent-free, there is no solvation shell in the ILs, so ILs can offer a well identified ion size.

The main ILs used for ES applications are imidazolium, pyrrolidinium aliphatic quaternary ammonium salts with anions such as tetrafluoroborate, trifluoromethanesulfate, bis(trifluoromethanesulfonyl) imide, and hexafluorophosphate.<sup>11-13</sup> The physical-chemical properties of ILs depend on the type of the cation and anion.<sup>1</sup> There are a number of reports on ILs as electrolytes in ES. *N*-Butyl-*N*-methyl pyrrolidinium bis-(trifluoromethane sulfonyl)imide (NBNMPBTSI), which operates with a potential window between 3.4 to 1.5 V.<sup>14</sup> 1-Ethyl 3-methyl imidazolium bistrifluoromethylsulfonyl imide showed better fluidity than the NBNMPBTSI.<sup>15</sup> The recently reported solvent free 1-butyl-3-methyl imidazolium hexafluorophosphate having good conductivity, wide electrochemical window and low vapor pressure, could help for mesoporous nickel-based mixed rare-earth oxide with higher power density of 458 W/kg, higher energy density of 50 Wh/kg and excellent cycle life.<sup>12</sup>

## **1.2.4 Types of Electrode materials**

The capacitance of charge storage of ES depends on the electrode materials. There are different types of electrode materials used for electrochemical supercapacitor measurements *e.g.* carbon materials, metal oxides, conducting polymers *etc.*

### **1.2.4.1 Carbon materials**

The main advantages of the carbon based materials are low cost, easy processing, non-toxicity, high abundance, high surface area, good electrical conductivity, high chemical stability and wide range of operating temperatures.<sup>16</sup> These materials are close to the electrical double-layer (EDL) capacitors. Generally, carbon materials store charge in an EDL formed at the interface between the electrode and electrolyte. Therefore, the capacity predominantly depends on the surface area of the electrode which is accessible to the electrolyte ions. The important factors affecting the capacitance were Specific surface area, pore size distribution, pore shape and structure,

electrical conductivity and surface functionality. Among all these, surface area and pore size distribution are two factors affecting the performance of supercapacitor.<sup>1</sup> Carbon materials mainly include activated carbon,<sup>17-19</sup> carbon aerogels,<sup>20</sup> carbon nanotubes (CNTs)<sup>21</sup> template porous carbons<sup>22-23</sup> and carbon nanofibers<sup>24</sup> have high surface area. Sometimes specific surface area is not directly related to specific capacitances because of all micropores in the electrode layers are not necessarily accessible by electrolyte ions. In addition to the surface area and pore size, surface functionalization of materials has also been considered to enhance the specific capacitance of carbon materials.<sup>25-27</sup> The recently reported reduced graphene oxide (RGO) shows the specific capacitance of 144 F/g.<sup>28</sup> The activated nonporous carbon has been used in supercapacitor applications with reported specific capacitance value of 240 F/g. Merino *et al* used activated carbon nanofibers as electrode material, which exhibited specific capacitance of about 60 F/g.<sup>29</sup> Portet *et al* evaluated activated carbon and carbon nanotube mixture in an organic electrolyte, which showed the specific capacitance value of 90 F/g.<sup>30</sup>

#### **1.2.4.2 Transition metal oxides (TMOs)**

TMOs are great important in the ES because of their superior pseudocapacitive (PC) behavior which is the potential candidate for the high performance of supercapacitor. The main advantage of metal oxide has high electrochemical stability than the other materials.<sup>31</sup> General requirements for Metal oxides in ES applications are<sup>32</sup> (1) metal oxide should be electronically conductive (2) the metal can exist in two or more oxidation states (3) the proton can be transferred into the oxide lattice for reduction, allowing facile inter conversion of  $O^{2-} \longleftrightarrow OH^-$ . Till date extensive research has been done on the ruthenium oxide, manganese oxide nickel oxide and cobalt oxide. The main disadvantage of  $RuO_2$  limited commercial availability due to the high cost.<sup>1</sup> Other metal oxides like NiO, CoO, and MnO are potential for good candidates as the supercapacitor

electrode due to low cost and ecofriendly. Hu *et al*<sup>33</sup> observed the supercapacitance of nanotubular array of RuO<sub>2</sub> · xH<sub>2</sub>O in aqueous system as high as 1300 F/g. The anhydrous RuO<sub>2</sub> which is prepared from sol-gel method showed a specific capacitance value of 390 F/g.<sup>34</sup> Similarly, chemically prepared RuO<sub>2</sub> showed lowest capacitance of value of 50 F/g.<sup>35</sup> The amorphous nanostructure MnO<sub>2</sub> electrode with specific capacitance of 250 F/g much stability up to 1200 cycles.<sup>36</sup> 2D-nanosheets of MnO<sub>2</sub> have been prepared by exfoliation-reassembling method achieved the specific capacitance value of 140-160 F/g and cyclic stability of 99% up to 1000 cycles.<sup>37</sup> Hexagonal nanosheets of Co<sub>3</sub>O<sub>4</sub> showed a specific capacitance of 227 F/g at 1.0 A/g.<sup>38</sup> Co<sub>3</sub>O<sub>4</sub> nanowire arrays prepared on nickel foam, showed a maximum specific capacitance of 746 F/g at a current density of 5 mA/cm<sup>2</sup>.<sup>39</sup>

#### **1.2.4.3 Conducting polymers (CPs)**

CPs having many advantages for ES, which are low cost, high electrical conductivity in doped state, low environmental impact, high voltage window, high storage capacity, and adjustable redox activity through chemical modifications.<sup>40-44</sup> CPs shows specific capacitance behavior through oxidation process. When oxidation takes place, ions are transferred to backbone of polymer and ions are released in electrolyte through this backbone.<sup>45</sup> The main advantage of these materials while charging and discharging process do not change any structural changes (phase changes), so the process is highly reversible.<sup>46</sup> The most common used conducting polymers in the supercapacitors are polyaniline (PANI),<sup>47</sup> polypyrrole (PPY),<sup>48</sup> p-dopedpoly (pyrrole) and poly (3, 4-ethylenedioxythiophene) (PEDOT) *etc.*<sup>49-50</sup> The main drawback of CPs is poor mechanical stability. When the cycling of the polymers take place, series of physical changes occur *e.g.* swelling, shrinkage, doping and undoping which degrades the performance of material over time. So, composite polymers are good choice for the enhancing the mechanical

property of conduction polymers.<sup>1</sup> Li *et al* reported the specific capacitance of PANI with 815 F/g.<sup>51</sup> Kim *et al*<sup>50</sup> reported the composite material of PPY, carbon fibers and carbon with a thickness of 5-10 nm by chemical polymerization and achieved the specific capacitance of ~ 588 and ~ 550 F/g with potential scan rate of 30 to 200 mV/s.

## **1.2.5 Calculation of supercapacitance for electrode materials**

There are various test methods are used to characterize the electrochemical performance of SC, which are cyclic voltammetry (CV), Constant current charge/discharge (CCCD), Electrochemical impedance spectroscopy (EIS). All these instruments are used to measure the fundamental parameters of voltage, current and time: other metrics, including the capacitance, operating voltage, equivalent series resistance, energy density and power density of SCs.

### **1.2.5.1 Cyclic voltammetry**

As we know mechanism of the supercapacitance are operates on EDLC and PC with different way. CV test is used to know the storage mechanism for SCs. When the capacitance is originated from EDLC and most of PC, the shape of CV curves are rectangular shape, where as some of PC materials, pronounced redox peaks may occur in a highly reversible manner. Therefore, it is not sufficient to differentiate by seeing the CV curves. Pseudocapacitance of metal oxide and conducting polymers has been evaluated by CV method. CVs were recorded at both two and three electrode systems. It can calculate the specific capacitance of supercapacitor at different scan rates with potential voltage operation window in the appropriate suitable electrolyte (alkali of acidic). It is notable that while increasing the scan rate capacitance will decrease. The following equation (1.4) is used to measure the specific capacitance of the supercapacitor.<sup>52-53</sup> Wang *et al*<sup>54</sup> calculated the specific capacitance of MoS<sub>2</sub> layers by using the cyclic voltammetry (Figure 1.2) with the order of 160 F/g at a current density of 1 A/g

$$C = \frac{1}{mv(V_a - V_b)} \int_{V_a}^{V_b} I(V) dV \quad (1.4)$$

Where  $\int_{V_a}^{V_b} I(V) dV$  is the area under the curve,  $m$  is the mass of electrode used,  $s$  is the scan rate and  $(V_a - V_b)$  is the potential working window.

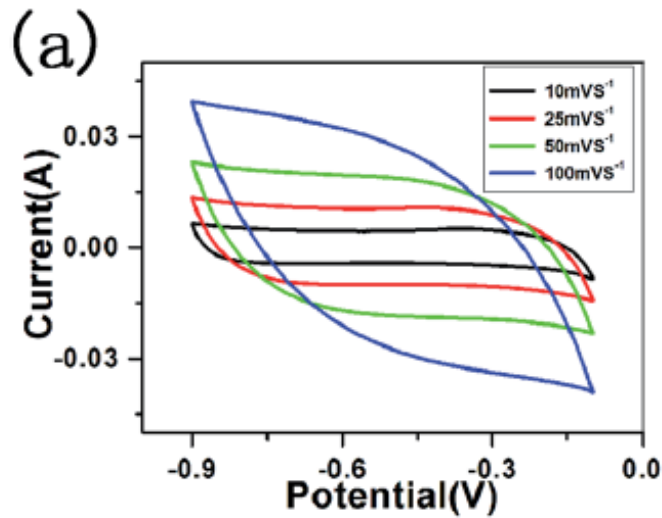


**Figure 1.2.** CV curves for MoS<sub>2</sub> different scan rates (10, 25, 50, 100 mV/s).

### 1.2.5.2 Constant current charge/discharge

CCCD test is the most accurate and versatile approach for characterizing the SCs device. Most of the core parameters like power density, energy density, leakage and peak current can be calculated from this technique. It can also be used to check the cyclic stability of the SC materials. Moreover, by using the three electrode setup, specific capacitance, reversibility and potential window for SC materials can be measured by CCCD test. The specific capacitance of the electrode can be evaluated from the equation (1.5).<sup>55-56</sup> The charge/discharge curves (Figure 1.3) and cyclic stability curves (Figure 1.4) for the reported MoS<sub>2</sub> layers are given below.

$$C = \frac{I \times \Delta t}{\Delta V \times m} \text{ F/g} \quad (1.5)$$

Where  $I$  is the discharge current (A),  $\Delta t$  is the discharging time (s),  $\Delta v$  is the discharging voltage and  $m$  is the active material.

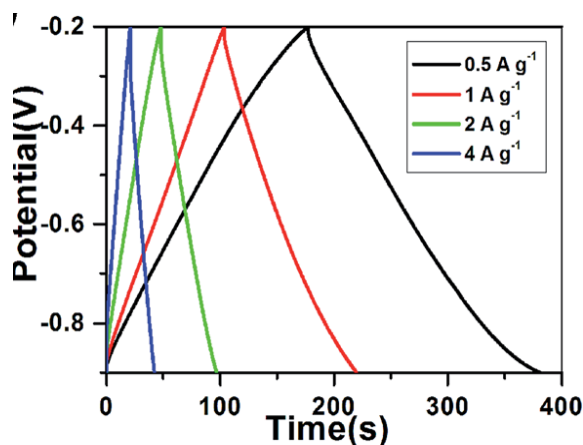


**Figure 1.3.** CD curves at different current densities for the  $\text{MoS}_2$  in the 1 M KCl electrolyte.<sup>54</sup>

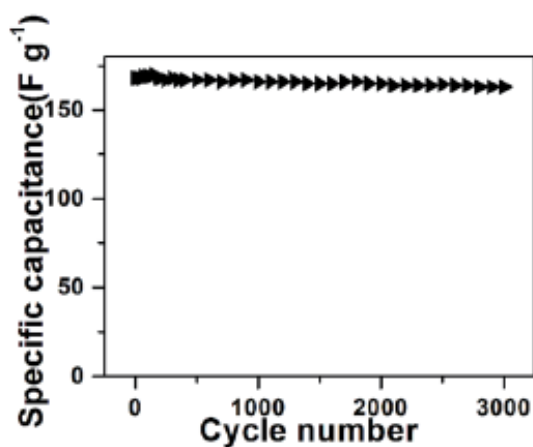


**Figure 1.4.** Cyclic stability curves for the  $\text{MoS}_2$  layers<sup>54</sup> in the 1 M KCl electrolyte solution with 3000 cycles at the current density of 1 A/g.

### 1.2.5.3 Electro chemical impedance spectroscopy

EIS has been used to measure the charge transfer, mass transport, charge storage mechanisms, specific capacitance, energy density and power density properties. Nyquist plots were plotted as  $Z''$  (imaginary part) versus  $Z'$  (real part) in a suitable electrolyte. A well defined semi-circle region at the high frequency range and a straight line at low frequency range measured for the

SC electrode materials. The diameter of the semi-circle represents the interfacial charge transfer of faradaic resistance. The faradaic resistance decreases by increasing power density of materials. Specific capacitance can be calculated from semi circle region of the plot. A plot through 45° phase angle corresponds to the Warburg impedance and it indicates a high ion diffusion resistance. The specific capacitance value can be evaluated from EIS by using the following equation (1.6).<sup>57-58</sup>

$$C_m = \frac{1}{m \times j \times 2\pi f \times Z''} \quad (1.6)$$

Where  $C_m$  specific capacitance of electrode from EIS,  $m$  is mass of the active electrode material,  $Z''$  is the imaginary part,  $f$  is the frequency.

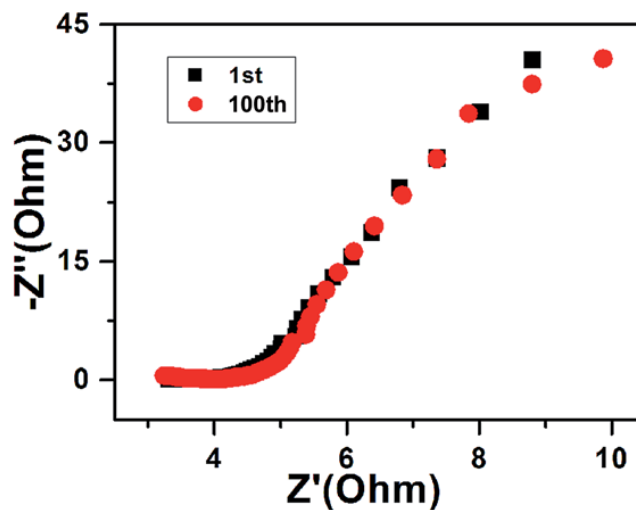
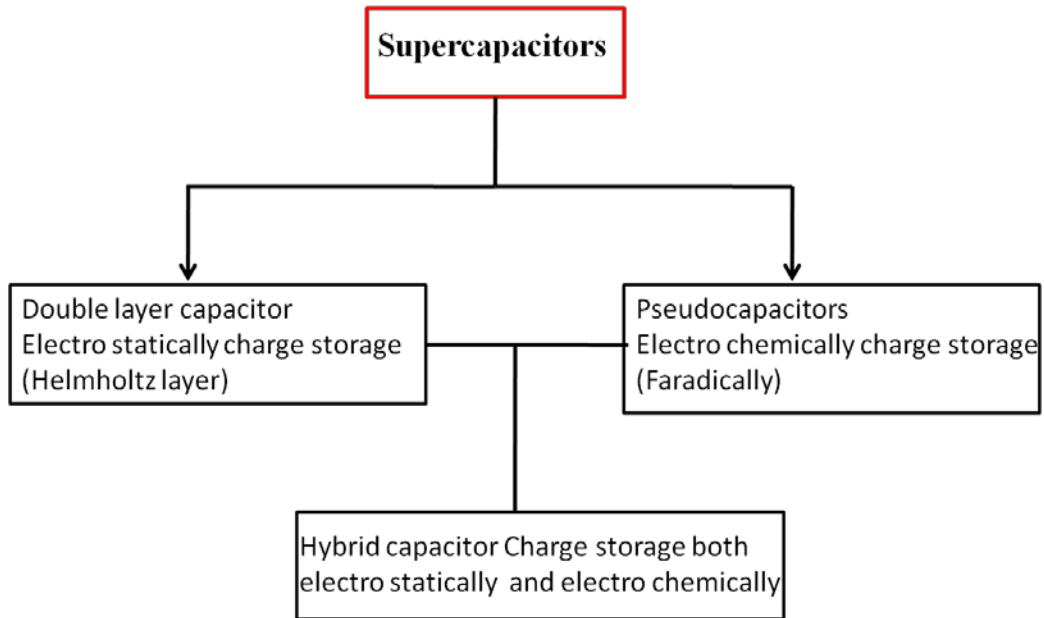


**Figure 1.5.** EIS for MoS<sub>2</sub> layers at 1st and 100th cycle.<sup>54</sup>

## 1.2.6 Types of mechanisms

Depends up on the storage of energy, supercapacitors are divided in to three types



### 1.2.6.1 Electrical double-layer mechanism.<sup>59</sup>

In EDL mechanism, stores energy as electro statically in the supercapacitor device. In all these type of capacitors energy stores as without any reactions take place unlike pseudocapacitor mechanism where redox reactions take place. In EDL mechanism double layer is formed by separation of charges in electrolyte and requires the presence of two electrodes accumulating the opposite charges to each other (Figure 1.6)

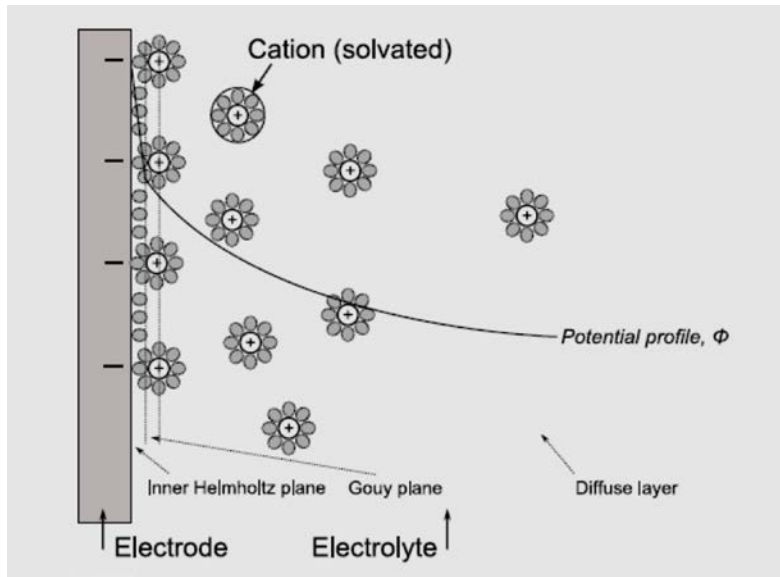


**Figure 1.6.** Schematic representation of a model for the electrical double-layers.<sup>59</sup>

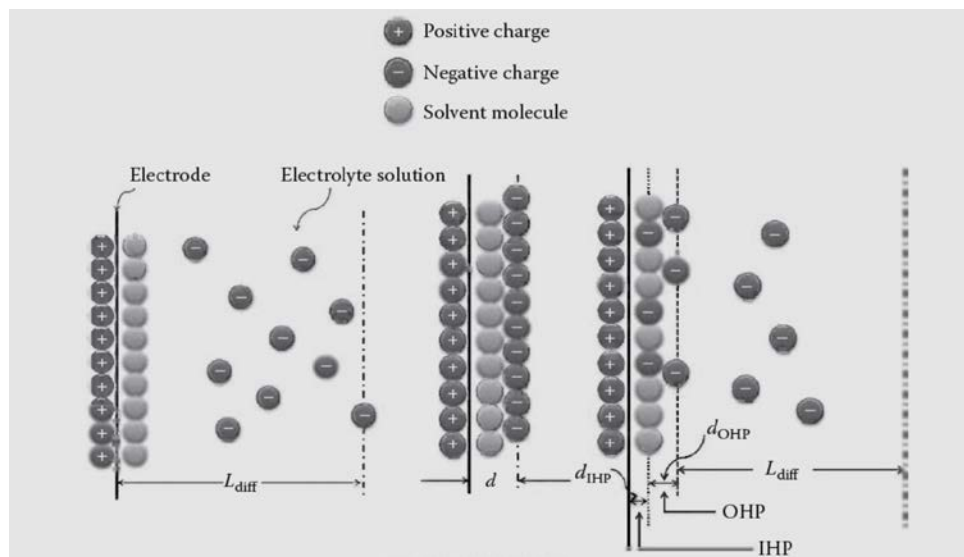


**Figure 1.7.** Electrical double-layer models at the interface of electrode and electrolyte solutions. (a) Diffusion layer of Gouy-Chapman model. (b) Helmholtz layer of model:  $d$  represents the thickness of the double layer. (c) Stern-Graphame layer of model in which IHP represents the Inner Helmholtz plane and OHP represents the outer Helmholtz plane.<sup>59</sup>

There are several models are proposed for explaining in EDL mechanism: Helmholtz<sup>60</sup>, Gouy-Chapman<sup>61</sup> and Stern-Grahame layer.<sup>62</sup> The first theoretical model for the electrochemical double layer was developed by Helmholtz in the 19<sup>th</sup> century. In this model describes the two layers of the charges at an electrode interface. The first layer in the solid material in the one sign (positive or negative) and other layer of the opposite sign in the electrolyte outside this solid electrolyte. The charge layers in the electrolyte was first considered static and the potential profile in the electrochemical double layer decreased linearly with distance from the electrode surface.<sup>59</sup>

Gouy introduced new thermal factor in 1910 further developing the concept of electrochemical double layer mechanism. In his consideration the idea of a double layer consist of a point charges, it also over estimated the capacitance and gave an incorrect potential profile. So, further work by Chapman in 1910. This model developed the idea of distribution of ions in the electrolyte. The main drawback of Gouy-Chapman model was overestimation of the capacitance value of the electrode.<sup>61</sup>

Stern proposed a model in 1924 to overcome the all disadvantages by considering the adsorption of ions according to the Langmuir at the surface of electrode solid.<sup>62</sup> And also including the hydration shells of the ions in the electrolyte solution improved the predictions of this model shown in the Figure 1.7. Stern also introduced the idea of the capacitance of the double layer consisting of two parts calculated from the equation (1.7). One component in the layer closest to the electrode ( $C_H$ ) and another in the diffuse layer ( $C_{diff}$ )

$$\frac{1}{C_{dl}} = \frac{1}{C_H} + \frac{1}{C_{diff}} \quad (1.7)$$

Later work by Grahame<sup>63</sup> introduced a difference in the Helmholtz layers, dividing them into the outer and inner Helmholtz layer and always considering a diffuse layer beyond these two layers close to the electrode/electrolyte interface. Another aspect of Grahame's work is the clarification he made in the concept of the ideally polarizable electrode. When charges are supplied to an ideally polarizable electrode from an outer source, only the double layer should be charged. Thus, no faradaic reactions should take place since no charges are passing across the double layer.

#### **1.2.6.2. Pseudocapacitance mechanism**

PC or Faradaic supercapacitor is different from the EDLC mechanism. When we apply the potential to PC, fast and reversible faradaic reactions (redox reactions) take place on the electrode materials and involve the passage of charge across the double layer.<sup>64</sup> PC materials are relatively low stability during the cycling process because of their redox reactions occurs at the electrode. However, PCs are usually having relatively lower powder density than the EDLC because faradaic process generally slower than the non-faradaic processes.<sup>65</sup> Conducting polymers and several metal oxides include RuO<sub>2</sub>, MnO<sub>2</sub>, and Co<sub>3</sub>O<sub>4</sub><sup>46, 66-68</sup> undergoes redox reactions at electrodes. There are three types of faradaic processes occur at PC electrodes: reversible adsorption (for example adsorption of hydrogen on surface of Platinum or gold), redox reactions of transition metal oxides (*e.g.*: RuO<sub>2</sub>), and reversible electrochemical doping-dedoping in the conductive polymers based electrodes.<sup>46</sup> These three faradaic electrochemical processes utilized for extending the working voltage and specific capacitance of the supercapacitor.<sup>16</sup> The electrochemical process in Pseudocapacitance supercapacitor (PCS) occurs both on the surface and in the bulk near the surface of the solid electrode, so PCS shows large values of capacitance

and energy density than the EDLC. Conway *et al*<sup>69</sup> reported the capacitance of PC can be 10-100 times higher than the electrostatic capacitance of the EDLC.

### **1.2.6.3 Hybrid supercapacitor (HS)**

HS having an asymmetric electrode configuration *i.e* one electrode consists of electrostatic carbon material and another consists of faradaic capacitance material. These HS have been studied recently with an advantage of high cell voltage, energy and power densities.<sup>70-72</sup> In this kind of hybrid supercapacitor, both electrical double-layer capacitance and faradaic capacitance mechanisms occur simultaneously, but one of them plays a greater role. In both the mechanisms, large surface area, appropriate pore-size distribution, and high conductivity are essential properties of the electrode materials to achieve large capacitance.<sup>1</sup>

## **1.3 Metal chalcogenides in supercapacitors**

Graphene is attracted significant attention in energy device due to the high specific area, carrier mobility, lightest charge carriers, low density, low cost, having a significantly high transparency and shows highly stretchable. However the use of graphene has been restricted in energy storage device applications due to the absence of a well-defined band-gap.<sup>73</sup> Researchers are devoted to identifying the two-dimensional semiconductors. There are lot of non graphene layered compounds received recent attention includes boron nitride, metal-chalcogenides, metal oxides, hydroxides, and oxychlorides, however only few of the layered structures are semiconductors , successfully isolated as air stable, high quality, and two dimensional crystals.<sup>74</sup> The 2D-layered semiconductor materials (metal oxides and metal chalcogenides (MCs)) especially MCs have gained the renewed interest because of their well defined band-gaps which can be tuned by controlling the number of layers.<sup>75</sup>

Transition metal dichalcogenides (TMDCs) have the chemical formula  $\text{MX}_2$ , where M is transition metal (M=Mo, Sn, W, Nb) and X is a chalcogen (X=S, Se, Te). The important structural features of MCs were metal is sandwiched between two chalcogen atoms by covalent bond forms a layered structures (*e.g.*: X-M-X where X= chalcogen, M=Metal). The individual layers are bounded by Van der Waals interactions through *c*-axis (Figure 1.8). Depending upon the atomic coordination occurring within the individual layers, these materials can exit in different polymeric forms, such as trigonal prismatic, octahedral and rhombohedral geometry and different stacking orders (*e.g.* AbA BaB, AcA CbC or Abc Abc).

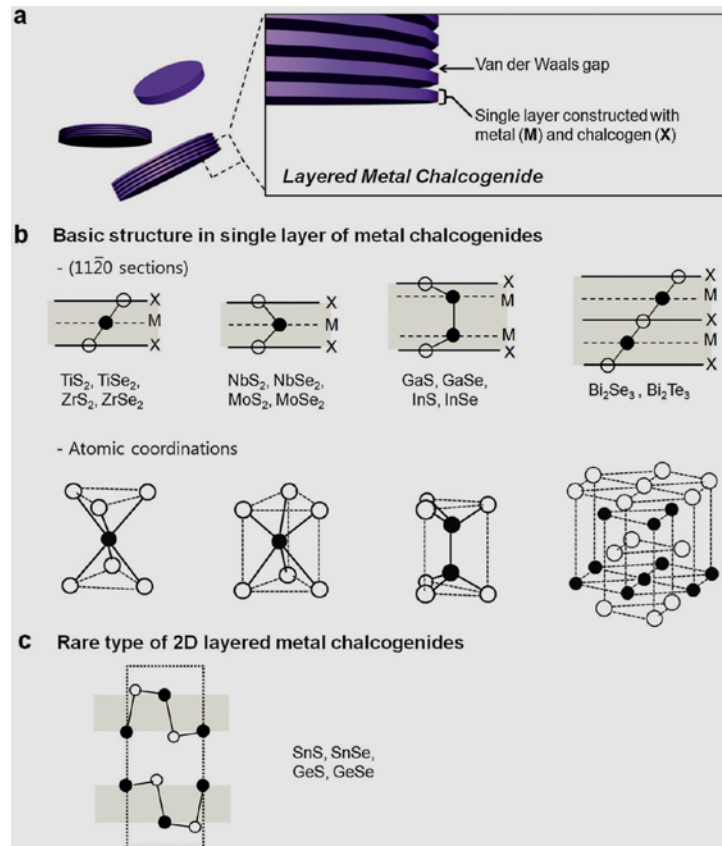


**Figure 1.8.** Layered structures of MCs. (a) Single nanocrystal are composed of multiple layers stacked along the *c*-axis by weak van der Waals force. (b) Single layer of MCs exits as various polymorphs. Each layer may have tri-, tetra- or penta-atomic layers of metal and chalcogen. (c) Rare GeS type of 2D-layered metal chalcogenides.<sup>76</sup>

Compounds of the TMDCs family exhibits a wide range of properties like electronic, magnetic as well as electrochemical which have attracted great attention for energy related device like supercapacitor, solar cell, lithium ion battery, and water splitting to generate hydrogen.<sup>75, 77-78</sup> TMDCs shows enhanced electrical, optical and mechanical properties due to their flat surface.<sup>74-75</sup> These layered materials also have a wide absorption range such as visible, infrared, ultraviolet and near infrared, so they possess this unique property of getting self-excited under light .The 2D- planar structures have large surface area and especially its insignificant thickness could be beneficial for reducing the recombination of the photo-generated electrons and holes. Therefore, the layered TMDC materials show interesting photoelectric and catalytic properties.<sup>79-80</sup> Because of their unique properties like high surface area and high conductivity MCs can be used in the Supercapacitors. In 2D-metal chalcogenides electrons transport through  $\text{MX}_2$  nanostructures, which provides easier and faster ion diffusion between  $\text{MX}_2$  layers/electrolyte produce high value of specific capacitance. The Reported  $\text{MoS}_2$  and  $\text{WS}_2$  having high supercapacitance due to the large specific area and interlayer space for the ion intercalation and wide range of oxidation states for metal ion which are tuned between  $\text{M}^{+2}$  to  $\text{M}^{+6}$  (M=Metal ion) in the redox reaction.<sup>75</sup> Rout *et. al.* reported the specific capacitance of  $\text{WS}_2$  layers with order of 70 F/g.<sup>81</sup> Wang *et al* reported the specific capacitance of  $\text{MoS}_2$  with 160 F/g.<sup>54</sup> Recently from our group reported the supercapacitance of  $\text{VS}_2$  layers with 137 F/g.<sup>28</sup>

#### **1.4 Supercapacitance of TMDCs/GO**

Electrochemical Supercapacitors are having great potential applications in high power devices like lasers and electric vehicles.<sup>1</sup> There are many electrode materials being developed for electrochemical Supercapacitors. The main electrode materials used for ES are carbon based materials (activated carbon, GO, CNTs etc),<sup>54, 82-83</sup> Transition metal oxides ( $\text{RuO}_2$ ,  $\text{MnO}$ ,  $\text{NiO}$

*etc*),<sup>33, 84</sup> Metal Chalcogenides (MoS<sub>2</sub>, WS<sub>2</sub>, VS<sub>2</sub> *etc*)<sup>28, 81</sup> Conduction polymers.<sup>85-86</sup> However new electrode materials with having both the combination of electrical double-layers and Pseudocapacitance called Composite materials. Composite materials mean the combination of two or more materials which exhibit unique properties like mechanical, electrical and chemical properties than the Individual materials. Up to now there are many composite materials are known which are metal oxide-polymer based composites, carbon-metal oxide based composites, carbon-polymer based composites and carbon-metal composite based composites.<sup>1</sup> We are interesting on carbon-TMDCs based composite materials. Carbon materials has high surface area and regular pore structures, because of which it makes a composite material with TMDCs very easily, and also it has both ionic and electronic conductivity of the electrode surface.<sup>87</sup> The composite electrode materials exhibit high energy and power densities. As we know 2D graphene sheet, having extraordinary electronic and mechanical properties are more preferable than the other carbon materials but the disadvantage is absence of a well-defined band-gap.<sup>73</sup> Nowadays composite materials of GO have attracted great importance from the researchers due to the GO materials act as filler material dispersed with in a continuous polymer or an inorganic polymer matrix. GO sheets containing TMDCs which are currently drawing significant attention due to their intricateness and tunable physical and chemical properties.<sup>75</sup> GO is structurally similar with TMDCs except the oxygen containing functional groups are oriented over the layers in GO.<sup>88</sup> TMDCs-GO nanocomposites mainly processed by the hydrothermal method, Chemical vapor deposition (CVD), solution method *etc*.<sup>77-78</sup> Unlike TMDCs, graphene oxide has many advantages to form nanocomposites, such as high surface area to volume ratio, high dispersibility in water as well as organic solvents, high mechanical strength and better chemical stability *etc*.<sup>88</sup> A large number of oxygen atoms on surface of graphene oxide facilitate the dispersibility in

solvent as well as reduce aggregation and enhance the interaction between fillers and polymers in composites.<sup>88</sup> TMDCs have been extremely popular not only for their wide range of applications but also for the facile route by which they synthesized.<sup>89</sup> They have been in pristine form as well as hybrid form with Graphene/RGO. Graphene/RGO as a platform provides mechanical support and facilitates fast charge transport in addition to that, hybrid structures comprising RGO, in most cases, result in formation of many active sites and tend to promote open edge growths, which greatly enhance their electrochemical and physical properties as compared to their pristine forms.<sup>28</sup> A number of hybrid materials containing graphene/RGO as the active template have shown much improved performance. For example, MoS<sub>2</sub>/RGO has shown a much better specific capacitance value of 282 F/g as compared to 156 F/g for pristine MoS<sub>2</sub>.<sup>54</sup> Similarly, WS<sub>2</sub>/RGO showed a specific capacitance of 350 F/g which is 5 times higher as compared to bare WS<sub>2</sub>.<sup>81</sup>

## **1.5 Supercapacitance of TMDCs/CNTs**

Depends up on their features carbon based materials are classified as activated carbon, template porous carbon, hetero atom containing carbons, carbon nanotubes carbon aerogels and xerogels *etc.* Among all carbon based materials CNTs are having good attention because of their good electrical conductivity, high thermal conductivity, high thermal stability and good mechanical properties and high surface area.<sup>90-93</sup> All these properties are reasons to use CNTs in many applications like energy storage, sensors and supercapacitor. Iijima was first discovered Carbon nanotubes in 1991.<sup>94</sup> CNTs have different forms like single wall carbon nanotubes (SWCNTs) and multiwall carbon nanotubes (MWCNTs). SWCNTs consist of a single graphene sheet wrapped into cylindrical tube and MWCNTs compose of an array of such nanotubes that are cylindrical nested. CNTs walls having the basal plane of graphite at outside surface so, there is no edge plane. Generally at the edge planes irreversible electrochemical reactions occur, such as

electrolyte decomposition, easily occur at high voltage potential, which prevent from using the capacitor at high voltage.<sup>95</sup> CNTs have high electrical conductivity, high mechanical stability, high charge transport capability, high mesoporosity high electrolyte accessibility and moderate surface area.<sup>96-98</sup> Due to all these properties CNTs can be lead to use for electrode material for supercapacitor. CNTs are easy to fabricate for supercapacitor applications. However, the electrode material composed with only CNTs have low energy density and capacitance.<sup>99</sup> So, the recent researchers are investigating the new kind of material called composite materials having CNTs with Transition metal dichalcogenides or transition-metal oxides or conducting polymers, which uses fast and reversible surface or near surface redox reactions for charge storage.<sup>100-101</sup> The ultrathin thickness and lateral morphology of the 2D-TMDCs nanosheet contribute to its high surface-to-volume ratio and short diffusion path, rendering it a brilliant electrode material for supercapacitance.<sup>1</sup> Due to the relative low conductivity, low theoretical specific capacity and easy restacking character of the TMDC sheet, the hybridization of it with other materials, such as graphene, 3D graphene networks, CNTs, nanoparticles, and carbon fibers, is one of the most attractive strategies to overcome its weaknesses and thus further optimize its performance in supercapacitance.<sup>102</sup> Both the electrode materials (CNTs and TMDCs) are having their own disadvantages. For rectifying these disadvantages composite materials of CNTs-TMDCs are good for enhancing the high energy density, power density and specific capacitance.

## 1.6 References

1. Wang, G.; Zhang, L.; Zhang, J., *Chem. Soc. Rev.* **2012**, *41*, 797.
2. [http://batteryuniversity.com/learn/article/whats\\_the\\_role\\_of\\_the\\_supercapacitor](http://batteryuniversity.com/learn/article/whats_the_role_of_the_supercapacitor).
3. Wang, Y.-G.; Wang, Z.-D.; Xia, Y.-Y., *Electrochim. Acta* **2005**, *50*, 5641.
4. Wang, Y.-G.; Cheng, L.; Xia, Y.-Y., *J. Power Sources* **2006**, *153*, 191.
5. Heinzl, A.; Vogel, B.; Hübner, P., *J. Power Sources* **2002**, *105*, 202.
6. Ganesh, V.; Pitchumani, S.; Lakshminarayanan, V., *J. Power Sources* **2006**, *158*, 1523.
7. Stoller, M. D.; Ruoff, R. S., *Energy & Environmental Science* **2010**, *3*, 1294.
8. Wasserscheid, P.; Welton, T., *Ionic liquids in synthesis*. Wiley Online Library: 2008; Vol. 1.
9. Ohno, H.; Fukumoto, K., *Electrochemistry* **2008**, *76*, 16.
10. Snook, G. A.; Kao, P.; Best, A. S., *J. Power Sources* **2011**, *196*, 1.
11. Galiński, M.; Lewandowski, A.; Stępnia, I., *Electrochim. Acta* **2006**, *51*, 5567.
12. Garche, J.; Dyer, C. K.; Moseley, P. T.; Ogumi, Z.; Rand, D. A.; Scrosati, B., *Encyclopedia of electrochemical power sources*. Newnes: 2013.
13. Lewandowski, A.; Galiński, M., *J. Phys. Chem. Solids* **2004**, *65*, 281.
14. Balducci, A.; Henderson, W. A.; Mastragostino, M.; Passerini, S.; Simon, P.; Soavi, F., *Electrochim. Acta* **2005**, *50*, 2233.
15. Randriamahazaka, H.; Plesse, C.; Teyssie, D.; Chevrot, C., *Electrochim. Acta* **2005**, *50*, 1515.
16. Zhang, Y.; Feng, H.; Wu, X.; Wang, L.; Zhang, A.; Xia, T.; Dong, H.; Li, X.; Zhang, L., *Int. J. Hydrogen Energy* **2009**, *34*, 4889.

17. Endo, M.; Maeda, T.; Takeda, T.; Kim, Y.; Koshihara, K.; Hara, H.; Dresselhaus, M., *J. Electrochem. Soc.* **2001**, *148*, A910.
18. Qu, D.; Shi, H., *J. Power Sources* **1998**, *74*, 99.
19. Raymundo-Pinero, E.; Kierzek, K.; Machnikowski, J.; Béguin, F., *Carbon* **2006**, *44*, 2498.
20. Fang, B.; Binder, L., *J. Power Sources* **2006**, *163*, 616.
21. Shiraishi, S.; Kurihara, H.; Okabe, K.; Hulicova, D.; Oya, A., *Electrochem. Commun.* **2002**, *4*, 593.
22. Lee, J.; Kim, J.; Hyeon, T., *Adv. Mater.* **2006**, *18*, 2073.
23. Morishita, T.; Soneda, Y.; Tsumura, T.; Inagaki, M., *Carbon* **2006**, *44*, 2360.
24. Xu, B.; Wu, F.; Chen, R.; Cao, G.; Chen, S.; Zhou, Z.; Yang, Y., *Electrochem. Commun.* **2008**, *10*, 795.
25. Frackowiak, E., *PCCP* **2007**, *9*, 1774.
26. Regisser, F.; Lavoie, M.-A.; Champagne, G. Y.; Bélanger, D., *J. Electroanal. Chem.* **1996**, *415*, 47.
27. Momma, T.; Liu, X.; Osaka, T.; Ushio, Y.; Sawada, Y., *J. Power Sources* **1996**, *60*, 249.
28. Ratha, S.; Marri, S. R.; Lanzillo, N. A.; Moshkalev, S.; Nayak, S. K.; Behera, J.; Rout, C. S., *J. Mater. Chem.A* **2015**, *3*, 18874.
29. Merino, C.; Soto, P.; Vilaplana-Ortego, E.; de Salazar, J. M. G.; Pico, F.; Rojo, J. M., *Carbon* **2005**, *43*, 551.
30. Portet, C.; Taberna, P.; Simon, P.; Flahaut, E., *J. Power Sources* **2005**, *139*, 371.
31. Zhao, D.-D.; Bao, S.-J.; Zhou, W.-J.; Li, H.-L., *Electrochem. Commun.* **2007**, *9*, 869.

32. Supercapacitors, E., Scientific Fundamentals and Technological Applications, ed. BE Conway. Plenum Publishing Co., New York: 1999.
33. Hu, C.-C.; Chang, K.-H.; Lin, M.-C.; Wu, Y.-T., *Nano Lett.* **2006**, *6*, 2690.
34. Chang, K.-H.; Hu, C.-C.; Chou, C.-Y., *Electrochim. Acta* **2009**, *54*, 978.
35. Patake, V.; Lokhande, C., *Appl. Surf. Sci.* **2008**, *254*, 2820.
36. Ragupathy, P.; Park, D. H.; Campet, G.; Vasan, H.; Hwang, S.-J.; Choy, J.-H.; Munichandraiah, N., *J. Phys. Chem. C* **2009**, *113*, 6303.
37. Song, M.-S.; Lee, K. M.; Lee, Y. R.; Kim, I. Y.; Kim, T. W.; Gunjekar, J. L.; Hwang, S.-J., *J. Phys. Chem. C* **2010**, *114*, 22134.
38. Fang, Z.; Liang, H.; Qing-Bin, F.; Xiao-Gang, Z., *CHIN J INORG CHEM* **2010**, *26*, 827.
39. Gao, Y.; Chen, S.; Cao, D.; Wang, G.; Yin, J., *J. Power Sources* **2010**, *195*, 1757.
40. Prasad, K. R.; Koga, K.; Miura, N., *Chem. Mater.* **2004**, *16*, 1845.
41. Jang, J., Conducting polymer nanomaterials and their applications. In *Emissive Materials Nanomaterials*, Springer: 2006; pp 189.
42. Zhou, Y.-k.; He, B.-l.; Zhou, W.-j.; Huang, J.; Li, X.-h.; Wu, B.; Li, H.-l., *Electrochim. Acta* **2004**, *49*, 257.
43. Gupta, V.; Miura, N., *Mater. Lett.* **2006**, *60*, 1466.
44. Fan, L.-Z.; Maier, J., *Electrochem. Commun.* **2006**, *8*, 937.
45. Sharma, P.; Bhatti, T., *Energy Convers. Manage.* **2010**, *51*, 2901.
46. Conway, B. E., *Electrochemical supercapacitors: scientific fundamentals and technological applications*. Springer Science & Business Media: 2013.
47. Ryu, K. S.; Kim, K. M.; Park, N.-G.; Park, Y. J.; Chang, S. H., *J. Power Sources* **2002**, *103*, 305.

48. Clemente, A.; Panero, S.; Spila, E.; Scrosati, B., *Solid State Ionics* **1996**, 85, 273.
49. Lota, K.; Khomenko, V.; Frackowiak, E., *J. Phys. Chem. Solids* **2004**, 65, 295.
50. Kim, J.-H.; Lee, Y.-S.; Sharma, A. K.; Liu, C. G., *Electrochim. Acta* **2006**, 52, 1727.
51. Li, H.; Wang, J.; Chu, Q.; Wang, Z.; Zhang, F.; Wang, S., *J. Power Sources* **2009**, 190, 578.
52. Dar, R. A.; Giri, L.; Karna, S. P.; Srivastava, A. K., *Electrochim. Acta* **2016**, 196, 547.
53. Zhang, S.; Pan, N., *Adv. Energy Mater.* **2015**, 5.
54. Wang, X.; Ding, J.; Yao, S.; Wu, X.; Feng, Q.; Wang, Z.; Geng, B., *J. Mater. Chem.A* **2014**, 2, 15958.
55. Yang, Z.; Chen, C.-Y.; Chang, H.-T., *J. Power Sources* **2011**, 196, 7874.
56. Xu, M.; Kong, L.; Zhou, W.; Li, H., *J. Phys. Chem. C* **2007**, 111, 19141.
57. Zang, J.; Bao, S.-J.; Li, C. M.; Bian, H.; Cui, X.; Bao, Q.; Sun, C. Q.; Guo, J.; Lian, K., *J. Phys. Chem. C* **2008**, 112, 14843.
58. Liang, Y.-Y.; Li, H. L.; Zhang, X.-G., *J. Power Sources* **2007**, 173, 599.
59. Bard, A. J.; Faulkner, L. R., *Electrochemical Methods, 2nd ed.*; Wiley: New York **2001**.
60. von Helmholtz, H., *Ann. Phys. Chem* **1853**, 89, 211.
61. Chapman, D. L., *The London, Edinburgh, and Dublin philosophical magazine and journal of science* **1913**, 25, 475.
62. Stein, O., *Zeit. Elektrochem* **1924**, 30, 508.
63. Grahame, D. C., *Chem. Rev.* **1947**, 41, 441.
64. Simon, P.; Gogotsi, Y., *Nat. Mater.* **2008**, 7, 845.
65. Chuang, C.-M.; Huang, C.-W.; Teng, H.; Ting, J.-M., *Energy & Fuels* **2010**, 24, 6476.
66. Wu, M.-S.; Chiang, P.-C. J., *Electrochem. Solid-State Lett.* **2004**, 7, A123.

67. Sugimoto, W.; Iwata, H.; Murakami, Y.; Takasu, Y., *J. Electrochem. Soc.* **2004**, *151*, A1181.
68. Dong, X.; Shen, W.; Gu, J.; Xiong, L.; Zhu, Y.; Li, H.; Shi, J., *J. Phys. Chem. B* **2006**, *110*, 6015.
69. Conway, B. E.; Birss, V.; Wojtowicz, J., *J. Power Sources* **1997**, *66*, 1.
70. Burke, A., *J. Power Sources* **2000**, *91*, 37.
71. Kisacikoglu, M.; Uzunoglu, M.; Alam, M., *Int. J. Hydrogen Energy* **2009**, *34*, 1497.
72. Ma, S.-B.; Nam, K.-W.; Yoon, W.-S.; Yang, X.-Q.; Ahn, K.-Y.; Oh, K.-H.; Kim, K.-B., *Electrochem. Commun.* **2007**, *9*, 2807.
73. Geim, A. K.; Novoselov, K. S., *Nat. Mater.* **2007**, *6*, 183.
74. Miro, P.; Audiffred, M.; Heine, T., *Chem. Soc. Rev.* **2014**, *43*, 6537.
75. Late, D. J.; Rout, C. S.; Chakravarty, D.; Ratha, S., *Can. Chem. Trans* **2015**, *3*, 118.
76. Han, J. H.; Lee, S.; Cheon, J., *Chem. Soc. Rev.* **2013**, *42*, 2581.
77. Gao, M.-R.; Xu, Y.-F.; Jiang, J.; Yu, S.-H., *Chem. Soc. Rev.* **2013**, *42*, 2986.
78. Huang, X.; Zeng, Z.; Zhang, H., *Chem. Soc. Rev.* **2013**, *42*, 1934.
79. Wan, R.; Jia, C.; Zhang, W., *J. Alloys Compd.* **2012**, *544*, 1.
80. Zhong, H.; Yang, G.; Song, H.; Liao, Q.; Cui, H.; Shen, P.; Wang, C.-X., *J. Phys. Chem. C* **2012**, *116*, 9319.
81. Ratha, S.; Rout, C. S., *ACS Appl. Mater. Interfaces* **2013**, *5*, 11427.
82. Frackowiak, E.; Beguin, F., *Carbon* **2001**, *39*, 937.
83. Obreja, V. V., *Physica E: Low-dimensional Systems and Nanostructures* **2008**, *40*, 2596.
84. Wang, Y.-T.; Lu, A.-H.; Zhang, H.-L.; Li, W.-C., *J. Phys. Chem. C* **2011**, *115*, 5413.
85. Ghenaatian, H.; Mousavi, M.; Kazemi, S.; Shamsipur, M., *Synth. Met.* **2009**, *159*, 1717.

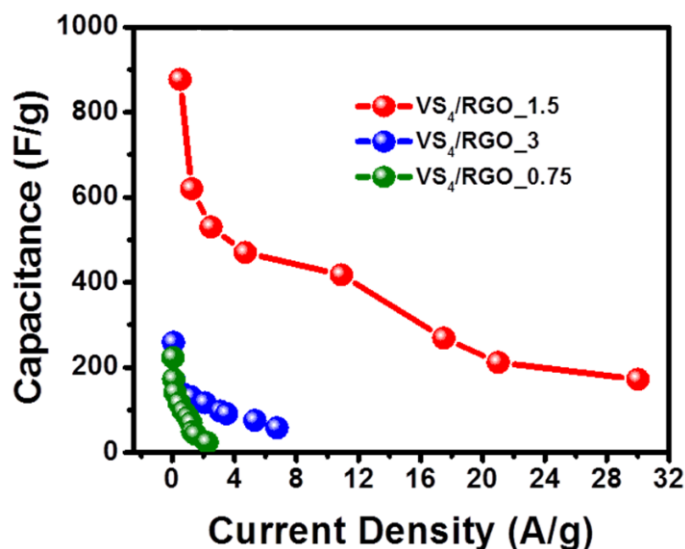
86. Sharma, R.; Rastogi, A.; Desu, S., *Electrochem. Commun.* **2008**, *10*, 268.
87. Huang, X.; Qi, X.; Boey, F.; Zhang, H., *Chem. Soc. Rev.* **2012**, *41*, 666.
88. Li, D.; Mueller, M. B.; Gilje, S.; Kaner, R. B.; Wallace, G. G., *Nat. Nanotechnol.* **2008**, *3*, 101.
89. Tan, C.; Zhang, H., *Chem. Soc. Rev.* **2015**, *44*, 2713.
90. Yurekli, K.; Mitchell, C. A.; Krishnamoorti, R., *J. Am. Chem. Soc.* **2004**, *126*, 9902.
91. Chen, J.; Hamon, M. A.; Hu, H.; Chen, Y.; Rao, A. M.; Eklund, P. C.; Haddon, R. C., *Science* **1998**, *282*, 95.
92. Mitchell, C. A.; Bahr, J. L.; Arepalli, S.; Tour, J. M.; Krishnamoorti, R., *Macromolecules* **2002**, *35*, 8825.
93. Garg, A.; Sinnott, S. B., *Chem. Phys. Lett.* **1998**, *295*, 273.
94. Ebbesen, T. W., *Carbon nanotubes: preparation and properties*. CRC press: 1996.
95. Inagaki, M.; Konno, H.; Tanaike, O., *J. Power Sources* **2010**, *195*, 7880.
96. Yakobson, B. I.; Avouris, P., Mechanical properties of carbon nanotubes. In *Carbon nanotubes*, Springer: 2001; pp 287.
97. Ajayan, P. M.; Zhou, O. Z., Applications of carbon nanotubes. In *Carbon nanotubes*, Springer: 2001; pp 391.
98. Endo, M.; Strano, M. S.; Ajayan, P. M., Potential applications of carbon nanotubes. In *Carbon nanotubes*, Springer: 2007; pp 13.
99. Wang, Y.; Shi, Z.; Huang, Y.; Ma, Y.; Wang, C.; Chen, M.; Chen, Y., *J. Phys. Chem. C* **2009**, *113*, 13103.
100. Pan, H.; Li, J.; Feng, Y. P., *Nanoscale Res. Lett.* **2010**, *5*, 654.
101. Du, C.; Pan, N., *Nanotech. L. & Bus.* **2007**, *4*, 3.
102. Rui, X.; Tan, H.; Yan, Q., *Nanoscale* **2014**, *6*, 9889.

## CHAPTER-2

### Supercapacitors Based On Vanadium Chalcogenides/RGO Hybrids

2.1	Abstract	193
2.2	Introduction	194
2.3	Objective of our work	197
2.4	Experimental section	197
	2.4.1 Synthesis of GO and RGO	197
	2.4.2 Synthesis of VS <sub>2</sub> and VS <sub>4</sub> /RGO hybrids	198
	2.4.3 Synthesis of VSe <sub>2</sub> and VSe <sub>2</sub> /RGO hybrids	198
2.5	Electrochemical measurmets	199
2.6	Determination of specific capacitance, energy density and power density	200
2.7	Results and discussions	201
2.8	Conclusions	215
2.9	References	216

## 2.1 Abstract



*This chapter describes the hydrothermal synthesis and detailed study on supercapacitor applications of Vanadium chalcogenides/RGO composite hybrids i.e VSe<sub>2</sub>/RGO and VS<sub>4</sub>/RGO. VSe<sub>2</sub>/RGO showed an enhanced specific capacitance in the order of ~500 F/g at current density of 1 A/g. In comparison with VSe<sub>2</sub> and RGO, the hybrid showed ~3 times and ~12 times higher value of capacitance respectively. The second hybrid which is VS<sub>4</sub>/RGO showed an enhanced specific capacitance of ~877 F/g at a current density of 0.5 A/g. In comparison to bare vanadium sulfide and RGO, the hybrid showed ~6 times and ~5 times higher value of specific capacitance respectively. Obtained energy density (117 Wh/kg) and power density (20.65 KW/kg) are comparable to other reported transition metal sulfides and their graphene hybrids. Results infer that the hybrid has the potential to be used as a high performance supercapacitor electrode.*

## 2.2 Introduction

Recent developments in the field of 2D-layered materials have drawn immense attention from the researchers, globally. The intriguing properties exhibited by graphene in terms of its unmatched mechanical strength,<sup>1-2</sup> exceptionally high surface area,<sup>3-4</sup> high electrical and thermal conductivity<sup>5-6</sup> and resistance towards any kind of chemical adversities,<sup>7</sup> has created a specific paradigm for it in the scientific community. In addition, there are other 2D-inorganic graphene analogues like layered TMDCs which are currently drawing significant attention due to their intricateness, tunable physical and chemical properties.<sup>7-11</sup> Because of their unique layered structures with each layer stacked onto another via weak Van der Waals force, they can be easily exfoliated to form few layered structures.<sup>12-14</sup> Because of these properties, they have been known to form excellent materials to be used in flexible and transparent electronics.<sup>15-16</sup> Some of the TMDCs like MoS<sub>2</sub>, SnS<sub>2</sub>, and WS<sub>2</sub>, have been studied extensively owing to their exceptional applicability in areas like electronics,<sup>17-18</sup> energy storage,<sup>19-22</sup> energy conversion,<sup>23-25</sup> optoelectronics *etc.*<sup>20, 26</sup> TMDCs have been extremely popular not only for their wide range of applications but also for the facile route by which they can be synthesized.<sup>27-28</sup> They have been studied in their pristine form as well as hybrid form with graphene/(RGO).<sup>22, 29-32</sup> Graphene/RGO as a platform provides mechanical support and facilitates fast charge transportation. In addition to that, hybrid structures comprising of RGO, in most cases, result in formation of many active sites and tend to promote open edge growths, which greatly enhances the electrochemical and physical properties as compared to their pristine forms. A number of hybrid materials containing graphene/RGO as active template, have shown much improved performances.<sup>30, 33-35</sup> For example, MoS<sub>2</sub>/RGO has shown much better specific capacitance value of 282 F/g as compared to 156 F/g for pristine MoS<sub>2</sub>.<sup>36</sup> Similarly WS<sub>2</sub>/RGO showed a specific capacitance of 350 F/g

which is 5 times higher as compared to bare WS<sub>2</sub>.<sup>22</sup> Other metal sulfides such as NiS<sub>2</sub>,<sup>37</sup> CoS<sub>2</sub><sup>38</sup> and FeS<sub>2</sub> etc.<sup>39-40</sup> have also been reported to show many intriguing applicability in various areas of research and it is highly expected that their graphene hybrids would yield even better results. In this chapter we report the one step hydrothermal synthesis and supercapacitance measurements of three types of Vanadium chalcogenides (VS<sub>2</sub>, VS<sub>4</sub> and VSe<sub>2</sub>) and their composite hybrids (VS<sub>4</sub>/RGO and VSe<sub>2</sub>/RGO) with different concentration of GO.

Vanadium sulfides are prominent group of TMDCs which have shown promising results in areas like energy storage,<sup>41-42</sup> sensing,<sup>43</sup> and spintronics.<sup>44-45</sup> Recently, few researchers have demonstrated that various stoichiometrically different forms of vanadium sulfides can be synthesized via facile hydrothermal routes.<sup>22, 46</sup> Many interesting properties of vanadium sulfides have been explored recently. In their report, Zhang *et al.*<sup>44</sup> have shown that vanadium sulfide nano-ribbons have the potential to be used as an active material in spintronics. Catalytic properties of vanadium sulfides have been detailed in a report by Guillard *et al.*<sup>47</sup> In another report, ultrathin nanosheets of VS<sub>2</sub> have shown exemplary moisture sensing properties. Few layered flower-like VS<sub>2</sub> has been reported to have high field emission properties.<sup>31</sup> Jing *et al.*<sup>42</sup> have concluded that 2D monolayered VS<sub>2</sub> has great potential as an anode material for Li-ion batteries.<sup>42</sup> Similarly, Feng *et al.* have inferred that VS<sub>2</sub> shows exceptional in-plane supercapacitor properties due to correlation between electrons of vanadium atoms. These reports suggest that vanadium sulfides do have the required physical and electrochemical properties to be used extensively in energy storage applications like supercapacitors and Li-ion batteries. Another such compound, VS<sub>4</sub>, is currently going under careful observation by a number of researchers due to its intriguing properties and unique morphology and composition. In VS<sub>4</sub>, the vanadium atoms<sup>41</sup> are present in an unusual geometry and form a linear chain containing two

$s_2^{-2}$  dimers, though the oxidation state of vanadium remains the same as in the case of  $VS_2$ .  $VS_4$  mineral is known as patronite and was first discovered in the year 1906.<sup>48-51</sup> Its crystallographic data were specified in 1964, and since then, many attempts have been made to synthesize it,<sup>52</sup> until recently, few reports depicted that it can be synthesized by a facile hydrothermal method in the presence of graphene as template,<sup>22, 53-54</sup> because graphene promotes nucleation process which facilitates the growth of  $VS_4$  instead of  $VS_2$ .  $VS_4/RGO$  is semiconducting in nature and possesses a band gap of the order 1.0 eV,<sup>22</sup> in contrast to  $VS_2$  which is metallic. Also various reports reveal that it has got potential applicability in the area of energy storage; especially the storage of lithium and it shows much better reaction mechanism and high rate capacity.<sup>54</sup> It has also been reported that  $VS_4/RGO$  has excellent photocatalytic activity under visible-light irradiation.<sup>53</sup>

Vanadium diselenide ( $VSe_2$ ) is also another TMDC material which is isostructural with  $VS_2$  where sulfur atom was replaced by Selenium atom.  $VSe_2$  is made up of the layers composing of metal V atoms sandwiched between two Se atom layers to give  $VSe_2$  formula (CdI<sub>2</sub>-type structure), and the Se-V-Se layers are further stacked by van der Waals interaction forming  $VSe_2$  crystal form.<sup>55</sup> Furthermore, in the  $VSe_2$  structure, the infinite  $V^{4+}$ - $V^{4+}$  chains along  $a$  and  $b$  axis forms a  $V^{4+}$ - $V^{4+}$  network structure in the  $ab$ -plane, and there is a strong electron coupling interaction for all neighboring  $V^{4+}$ - $V^{4+}$ , causing metallic character as well as the prototype charge density wave behavior. Moreover, the  $3d^1$  odd-electronic configuration of the  $V^{4+}$  ion also provides rich spin-related information. Recent theoretical investigations unraveled that the  $VSe_2$  monolayer exhibit intrinsic magnetic behavior, and its magnetic moments and strength of magnetic coupling even be tuned by isotropic strain.<sup>45</sup> Therefore, with these synergic effects of  $3d^1$  odd-electron configuration and their strong electron–electron correlations,  $VSe_2$  ultrathin

nanosheets would be a new type of 2D TMDC that possessing exotic electronic charge and spin properties. Due to these interesting properties  $VSe_2$  can be used in for future generation electronics like supercapacitors, spintronics and Li- ion batteries. Interestingly from the best of our knowledge there are no reports on  $VSe_2$  used as supercapacitor electrode materials. We first report the synthesis and supercapacitance measurements of  $VSe_2$  and composite hybrids of  $VSe_2/RGO$ .

### **2.3 Objective of our work**

From all the above discussions TMCs/RGO composite materials were good for high energy density, power density and specific capacitance. Till now most of the research carried out on  $MoS_2$  and  $WS_2$  layers and research on Vanadium layers are very less explored.  $VS_2$ ,  $VS_4$  and  $VSe_2$  layers have some interesting properties and unique morphology and composition. Hence we are interested to study the  $VS_4/RGO$  and  $VSe_2/RGO$  composite hybrids. In this chapter we mentioned detailed synthesis by facile one-step hydrothermal route of all hybrids, explanation of supercapacitor performance of  $VS_4/RGO$  and  $VSe_2/RGO$  and a thorough comparison with that of  $VS_2$ ,  $VSe_2$  and RGO.

### **2.4 Experimental section**

#### **2.4.1 Synthesis of GO and RGO**

GO was synthesized from graphite powder by a modified Hummer's method as detailed experiment was given in the report.<sup>22</sup> Further reduction of GO to form RGO was carried out by a hydrothermal reaction performed at 160 °C for 24 h.

### 2.4.2 Synthesis of VS<sub>2</sub> and VS<sub>4</sub>/RGO hybrids

VS<sub>2</sub> sheets were synthesized by a previously reported hydrothermal method involving reaction of sodium orthovanadate (Na<sub>3</sub>VO<sub>4</sub>, Sigma-Aldrich, 99.98%) and thioacetamide (C<sub>2</sub>H<sub>5</sub>NS, Sigma-Aldrich, ≥ 99%) at 160 °C.<sup>22, 56</sup> During hydrothermal reaction, hydrolysis of thioacetamide generates HS<sup>-</sup>, which acts as a reductant to reduce V<sup>5+</sup> into V<sup>4+</sup> and VS<sub>2</sub> layered structures are formed. VS<sub>4</sub> sheets were also synthesized by the same hydrothermal reaction in a GO solution (with varied GO concentration) at 160 °C and the final carbon content of the composite was estimated by elemental analysis.<sup>22, 56</sup> During the hydrothermal process, VS<sub>4</sub> sheets were formed on GO and the GO transformed to RGO.<sup>22</sup>

### 2.4.3 Synthesis of VSe<sub>2</sub> and VSe<sub>2</sub>/RGO hybrids

VSe<sub>2</sub> sheets were synthesized by small modification of a previously reported hydrothermal method.<sup>57</sup> In a typical procedure, 1.01 mM of Sodium Metavanadate (NaVO<sub>3</sub>), 2 mM of Selenium dioxide (SeO<sub>2</sub>) and 7mL of DI water were mixed together and stirred for 5 min in a Teflon-lined autoclave with a volume capacity of 23 mL, and then 1mL Formic acid (HCOOH) was drop wise added to this mixed solution and kept vigorously stirred for 10 min. Afterwards, the system was sealed and heated at 200 °C for 24h. Upon cooling to room temperature, the obtained samples were washed with DI water and absolute ethanol for several times, and then dried under vacuum at 60 °C. During the hydrothermal synthesis HCOOH act as reducing agent owing to the co-reduction processes from SeO<sub>2</sub> to H<sub>2</sub>Se which acts as a reducing agent to reduce the V<sup>+5</sup> into V<sup>+4</sup>. VSe<sub>2</sub>/RGO hybrids also synthesized by same hydrothermal method by varied concentration of GO. During the hydrothermal process GO transferred to RGO.

## 2.5 Electrochemical measurements

Two electrode measurements were carried out with the help of Swagelok type two electrode cells. The stainless steel electrodes were polished with emery paper and alumina powder ( $1\ \mu\text{m}\ \text{Al}_2\text{O}_3$ ) for about 30 min and then sonicated with DI water for about 1 h. In a typical procedure, 4 mg of the sample was taken and it was finely ground with the help of a mortar-pestle for about 1-2 h. Then it was equally divided and was taken in two different glass tubes and dispersed with viable amount of ethanol by ultrasonication in an ice bath for about 15 min in order to achieve nearly homogeneous mixture containing ethanol and the sample. The sample contained in one glass tube was drop-casted on to one electrode using a micropipette so that each electrode would carry 2 mg of the sample with uniform coverage. Both the electrodes were then dried in a vacuum desiccator for about 2-3 h. To provide separation between those electrodes, a porous cellulose nitrate membrane (Himedia Laboratories, Pvt. Ltd., India) having diameter equal to the diameter of the electrodes and pore size  $\sim 0.22\ \mu\text{m}$  was used. Before that, the membrane was thoroughly soaked in 1 M aqueous  $\text{Na}_2\text{SO}_4$  solution which acted as the electrolyte. All the measurements like CV at different scan rates, CD at different current densities and long cycle stability test were performed by a potentiostat/galvanostat (PG262A, Technoscience Ltd., Bangalore, India) while keeping the working potential range within the range of -0.1 V to 0.9 V.

Electrochemical property of the sample was also studied by a three electrode cell configuration. For that, a typical glassy carbon electrode (GCE) coated with sample was used as the working electrode, Ag/AgCl was taken as the reference electrode and a platinum wire was used as the counter electrode. The GCE was first properly polished with fine emery paper and alumina powder ( $0.3\ \mu\text{m}\ \text{Al}_2\text{O}_3$ ) for about 10-15 min and then sonicated in DI water for 30 min and dried in a vacuum desiccator for 1 h. The sample was dispersed in ethanol to get a

homogeneous mixture and then was drop-casted on to the GCE using a micropipette. 5  $\mu\text{l}$  of nafion was then drop-coated on to the as deposited sample and was kept in a vacuum desiccator, overnight. 1 M aqueous  $\text{Na}_2\text{SO}_4$  solution was taken as the electrolyte. Cyclic voltammetry at a particular scan rate was performed to verify the pseudocapacitive behavior of  $\text{VS}_4$ . Here the working potential range was kept within -0.1 V to 0.9 V.

## 2.6 Determination of specific capacitance, energy density and power density

Values of specific capacitance, energy density and power density were estimated by using the cyclic voltammetry and charge-discharge curves. Specific capacitance was calculated from the cyclic voltammetry curves by the following equation 2.1.

$$C_{sp}^{cv} = \frac{\oint I(V)dV}{2mr(V_f - V_i)} \quad (2.1)$$

Where  $C_{sp}^{cv}$  denotes specific capacitance from CV data, the integral in the numerator indicates the area under the CV curve,  $m$  is the mass of the sample,  $r$  is the scan rate and  $V_f - V_i$  is the working potential window (1.5 V). From the charge discharge curves, the specific capacitance was determined by the following equation 2.2.

$$C_{sp}^{cd} = \frac{I}{ms} \quad (2.2)$$

Where  $C_{sp}^{cd}$  denotes specific capacitance obtained from charge-discharge data,  $I$  is the discharge current and  $s$  is the slope of the discharge curve. Subsequent calculations for energy density and power density were done using equation 2.3 and equation 2.4.

$$E_d = \frac{1}{2} C_{sp}^{cv} (V_f - V_i)^2 \quad (2.3)$$

$$P_d = \frac{1}{2} C_{sp}^{cv} (V_f - V_i) r \quad (2.4)$$

## 2.7 Results and discussion

VS<sub>4</sub>/RGO containing 0.75 wt% of RGO, 1.5 wt% of RGO and 3 wt% of RGO has been denoted hereafter as VS<sub>4</sub>/RGO\_0.75, VS<sub>4</sub>/RGO\_1.5 and VS<sub>4</sub>/RGO\_3, respectively. Field emission scanning electron microscopy (FESEM) images of the VS<sub>4</sub>/RGO (1.5%) hybrid confirm uniform distribution of VS<sub>4</sub> over RGO layer (Figure 2.1a and 2.1b). Figure 2.1c shows the EDAX data of the VS<sub>4</sub>/RGO hybrid confirming the presence of the components with appropriate proportions. Elemental mapping of the hybrid has also been done (Figures 2.2a-d) depicting the uniformity of the elements in the hybrid. Figure 2.2e shows the PXRD pattern of the hybrid demonstrating a prominent growth along (110) direction with another peak along (020). In the XRD pattern of VS<sub>4</sub>/RGO, the suppressed carbon peak (at 2θ value of ~26°), characteristic of RGO, is due to the low thickness of the RGO layer and the sharp crystalline peak of VS<sub>4</sub>. Applying the Scherrer equation (to calculate the crystallite size over all FWHM values of diffraction peaks), the average grain size was found to be within the range of 24–29 nm. It confirms the uniformity of the VS<sub>4</sub> crystallites in the hybrid. All these diffraction peaks can be assigned to the patronite V(S<sub>2</sub>)<sub>2</sub> having a monoclinic structure (JCPDS file:72-1294). The FESEM studies and XRD analyses for pristine VS<sub>2</sub> confirms the formation of pure phase without any impurities (JCPDS file:89-1640) (Figure 2.3a-c). Furthermore, the diffraction patterns of VS<sub>4</sub>/RGO\_0.75 and VS<sub>4</sub>/RGO\_3 were compared with that of VS<sub>4</sub>/RGO\_1.5 (Figure 2.4a). The hybrid containing 0.75 wt% of RGO shows the poor uniformity of the VS<sub>4</sub> crystallites (hence larger grain boundaries) and also has additional peak of VS<sub>2</sub> (along the direction of (004), denoted by the asterisk mark in

Figure 2.4a) which may be due to the insufficiency of the RGO template which hindered the nucleation of  $\text{VS}_4$  significantly. However, better crystallinity of  $\text{VS}_4$  is clearly visible in the case of both  $\text{VS}_4/\text{RGO}_{1.5}$  and  $\text{VS}_4/\text{RGO}_3$ . To check the reduction quality of GO in the case of RGO and the hybrid, X-ray photoelectron spectroscopy (XPS) has been performed (Figure 2.4b). The characteristic C1s spectra of all the three samples were compared. As can be seen, the C1s spectrum of GO has two distinct peaks at 285 eV (C–C) and 289.48 (O–C=O). Whereas for RGO and the hybrid, only one distinct peak is observed at 284.48 eV (C–C) indicating the absence of oxygen containing functional groups (due to the thermal reduction process). Raman spectroscopy for GO, RGO and  $\text{VS}_4/\text{RGO}$  was performed to investigate the vibrational modes and the quality of reduction of GO in both the RGO sample and the hybrid. Figure 2.4c shows the Raman spectra of the samples. It shows the characteristic D and G bands for both GO and RGO. The D-band appears at  $\sim 1350 \text{ cm}^{-1}$  which confirms lattice distortions and the G-band appears at  $\sim 1590 \text{ cm}^{-1}$  which corresponds to the first order scattering ( $E_{2g}$  mode).<sup>58</sup> The  $I_D/I_G$  ratio of GO, bare RGO and RGO in the hybrid has also been calculated. The increased intensity ratio in the case of both bare RGO and RGO present in the hybrid is in good agreement with previously reported data.<sup>58-60</sup> It confirms the restoration of  $\text{sp}^2$  carbons and formation of smaller  $\text{sp}^2$  domains.

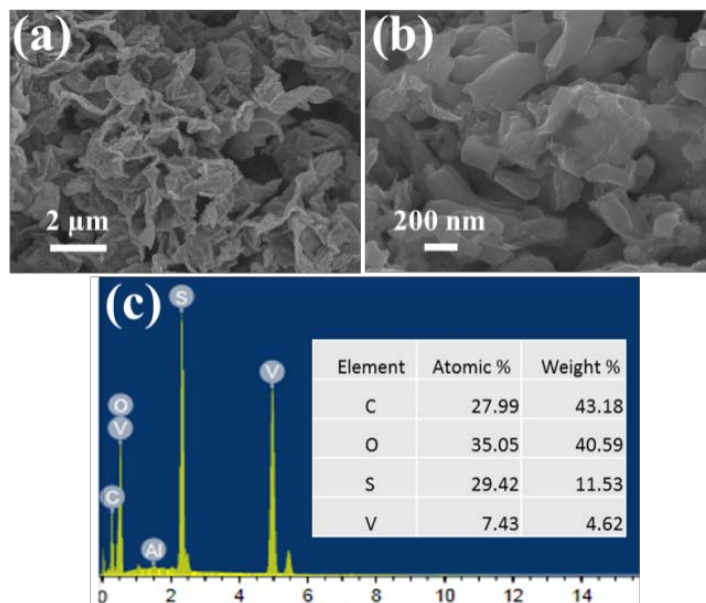


**Figure 2.1.** (a) Low and (b) high magnification FESEM images of VS<sub>4</sub>/RGO<sub>1.5</sub> hybrid. (c) EDAX spectrum, atomic percentage and weight percentage of the elements.

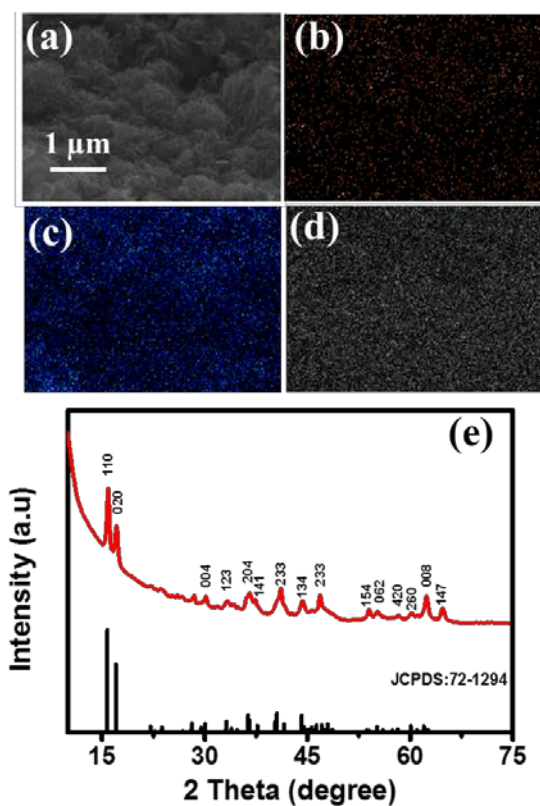


**Figure 2.2.** Elemental analysis of VS<sub>4</sub>/RGO<sub>1.5</sub>. (a) Electron image of the hybrid over which the mapping has been done. Presence of (b) Carbon, (c) Sulfur and (d) Vanadium in the hybrid. (e) XRD pattern of VS<sub>4</sub>/RGO<sub>1.5</sub> showing prominent growth along (110).

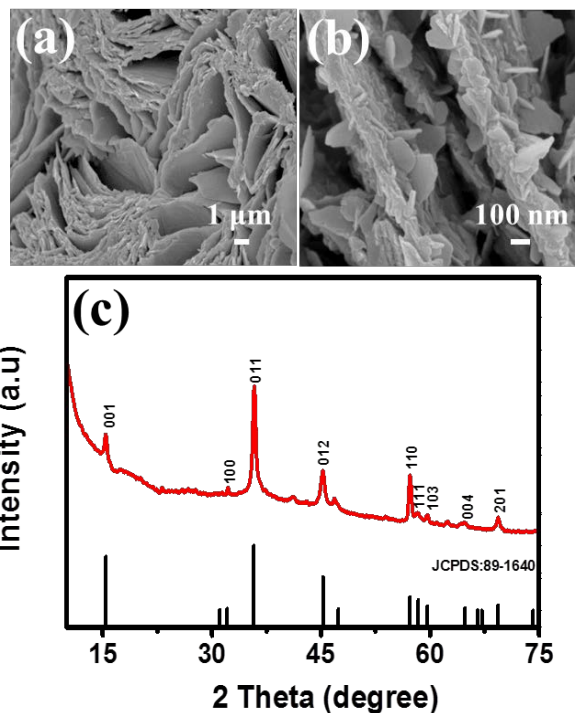


**Figure 2.3.** Low (a) and high (b) magnified images of  $\text{VS}_2$  micro flakes showing numerous protruding edges and (c) XRD pattern for  $\text{VS}_2$ .

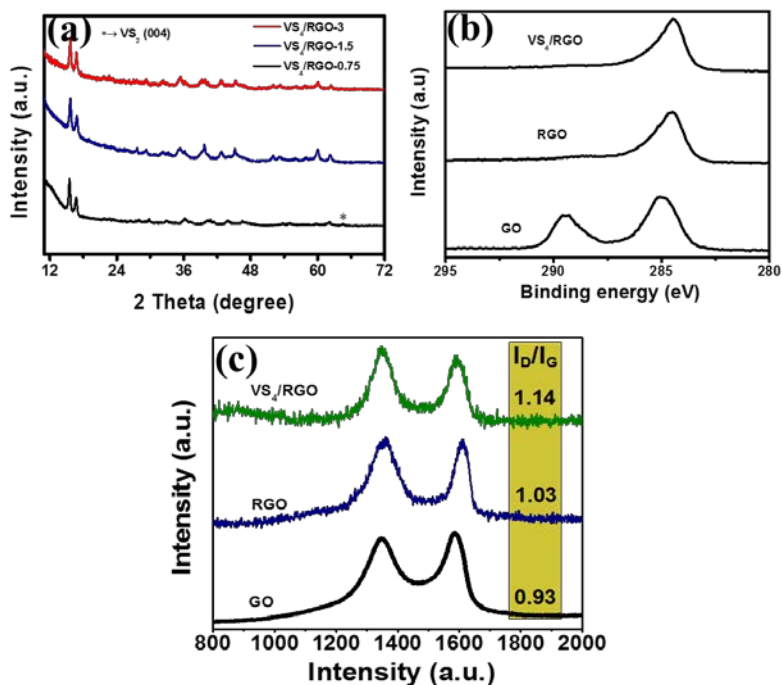


**Figure 2.4.** (a) XRD patterns for  $\text{VS}_4/\text{RGO}$  hybrids containing 0.75 wt% (black), 1.5 wt% (blue) and 3 wt% (red) of RGO. (b) XPS showing  $\text{C}1\text{s}$  spectra for GO, RGO and  $\text{VS}_4/\text{RGO}$ . (c) Raman spectra for GO, bare RGO and RGO content in the hybrid with  $I_D/I_G$  ratio.

The electrochemical measurements were performed for VS<sub>2</sub>, RGO and VS<sub>4</sub>/RGO at three different concentrations (i.e. 0.75 wt%, 1.5 wt% and 3 wt%) of RGO. Hybrid containing 0.75 wt% of RGO, 1.5 wt% of RGO and 3 wt% of RGO have been denoted as VS<sub>4</sub>/RGO\_0.75, VS<sub>4</sub>/RGO\_1.5 and VS<sub>4</sub>/RGO\_3, respectively. Figures 2.5a and 2.5b show the CV and CD curves of the VS<sub>4</sub>/RGO\_1.5 hybrid. At a scan rate of 2 mV/s, it showed a specific capacitance of 845 F/g. This high value of specific capacitance can be attributed to the EDLC from the RGO layer as well as pseudocapacitive contribution from VS<sub>4</sub>. Similar electrochemical measurements were also carried out for pristine VS<sub>4</sub>/RGO\_0.75 (Figure 2.6), VS<sub>4</sub>/RGO\_3 (Figure 2.7), VS<sub>2</sub> (Figure 2.8), and RGO (Figure 2.9), and Comparison between the supercapacitor performances of VS<sub>4</sub>/RGO\_1.5, RGO and VS<sub>2</sub> has been elucidated in Table 2.1. Dependence of specific capacitance on both scan rates and current densities is shown in Figures 2.5b and 2.5d respectively. Figure 2.5d shows that for a current density of 0.5 A/g, the hybrid shows its maximum calculated specific capacitance of 877 F/g. The obtained specific capacitance of VS<sub>4</sub>/RGO hybrid is found to be comparable to the best supercapacitors based on other metal sulfides reported in literature (Table 2.2). For example, NiS nanoparticles on graphene oxide sheets grown by a facile hydrothermal route have shown a specific capacitance of 800 F/g at a current density of 1 A/g. Wang *et al.*, have reported supercapacitors based on Co<sub>3</sub>S<sub>4</sub> hollow nanospheres on graphene which showed a maximum specific capacitance of ~675 F/g. At higher scan rates the capacitance values decreased as shown in Figure 2.5b. The phenomenon can be correlated to a relatively slower diffusion of charged ions as the scan rate goes higher, due to lower value of time constant. The values of specific capacitance for the hybrid obtained for different current densities (Figure 2.5d) are more or less comparable to the values obtained for different scan rates (Figure 2.4b). Also the CD curves are nearly symmetrical which explains that

the redox reaction (Faradaic reaction) is reversible in nature and the material possesses good capacitive property. Figure 2.10a shows the capacitive behavior of VS<sub>4</sub>/RGO hybrids at different concentrations of RGO. VS<sub>4</sub>/RGO\_1.5 shows a remarkable increase of the capacitive effect in comparison to VS<sub>4</sub>/RGO\_0.75 as well as VS<sub>4</sub>/RGO\_3. It shows that the capacitive effect of the hybrid depends strongly upon the concentration of RGO. Similarly, Figures 2.10b and 2.10c show variation of capacitance of the hybrid with scan rate and current density, respectively at different concentrations of RGO. Figure 2.11a shows the Ragone plot which depicts the energy density and power density of the hybrid material at different scan rates. At a scan rate of 2 mV/s, the hybrid material shows a maximum energy density in the order of ~117 Wh/kg and a maximum power density in the order of ~20.65 KW/kg. Stability is a factor of immense priority for the material, which is to be used as a supercapacitor electrode and therefore a long cycle CD measurement was performed in which the stability of the hybrid was tested for about 1000 cycles. Figure 2.11b shows the last 5 cycles of the long cyclic measurement, carried out at a current density of 9 A/g. Specific capacitance value for the hybrid was calculated at an interval of 50 cycles and the corresponding plot has been provided in Figure 2.11c shows the data containing 1000 cycles of CD. The data shown in Figure 2.11c elucidates that even after 1000 cycles, the degradation in specific capacitance of the hybrid material is merely ~10% of the original value. The corresponding Ragone plots for VS<sub>4</sub>/RGO\_0.75, VS<sub>4</sub>/RGO\_1.5 and VS<sub>4</sub>/RGO\_3 and comparison of the power density and energy density in ragone plots have been given Figure 2.12.

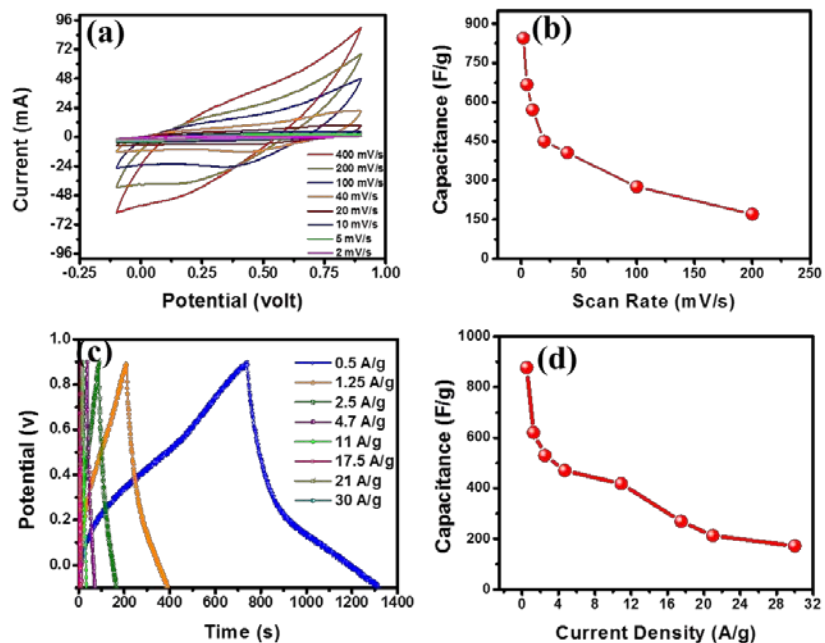


**Figure 2.5.** (a) CV curves for VS<sub>4</sub>/RGO<sub>1.5</sub> at different scan rates, (b) specific capacitance vs scan rate showing a gradual decrease of capacitance at higher scan rates. (c) CD curves at different current densities and (d) variation of capacitance with different values of current densities.

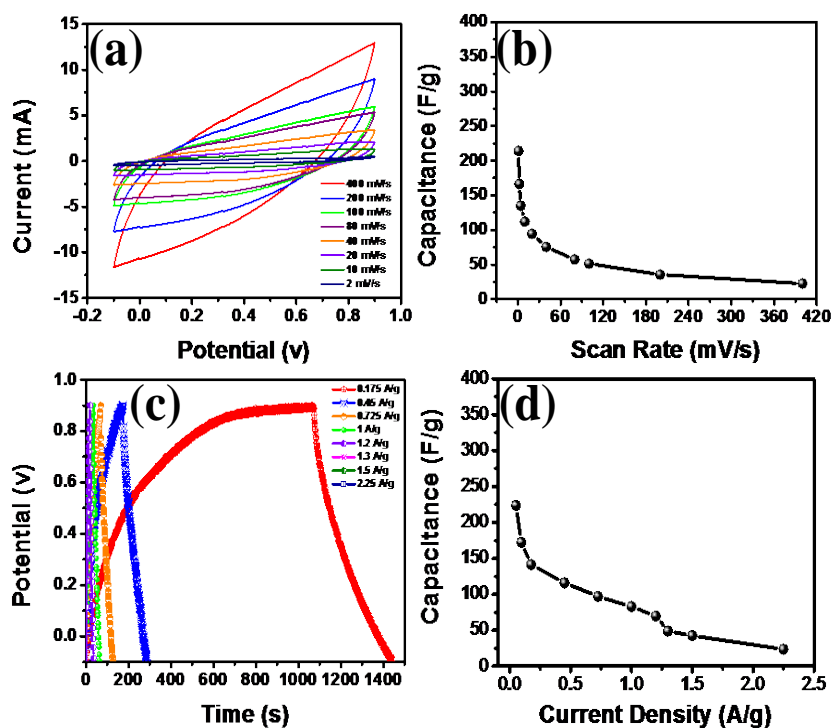


**Figure 2.6.** Supercapacitor data for VS<sub>4</sub>/RGO<sub>0.75</sub>. (a) CV curves at different scan rates (b) plot between specific capacitance and scan rate, (c) CD curves at different current densities, (d) plot between specific capacitance and current density.

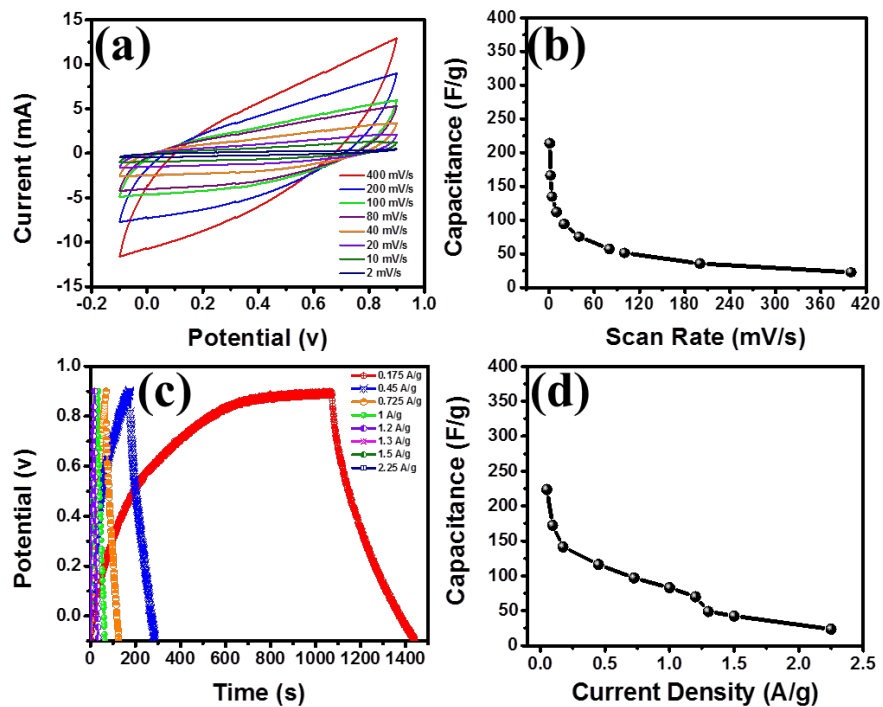


**Figure 2.7.** Supercapacitor data for VS<sub>4</sub>/RGO\_3. (a) CV curves, (b) plot of specific capacitance against scan rate, (c) CD curves at different current densities, (d) specific capacitance vs current density plot.

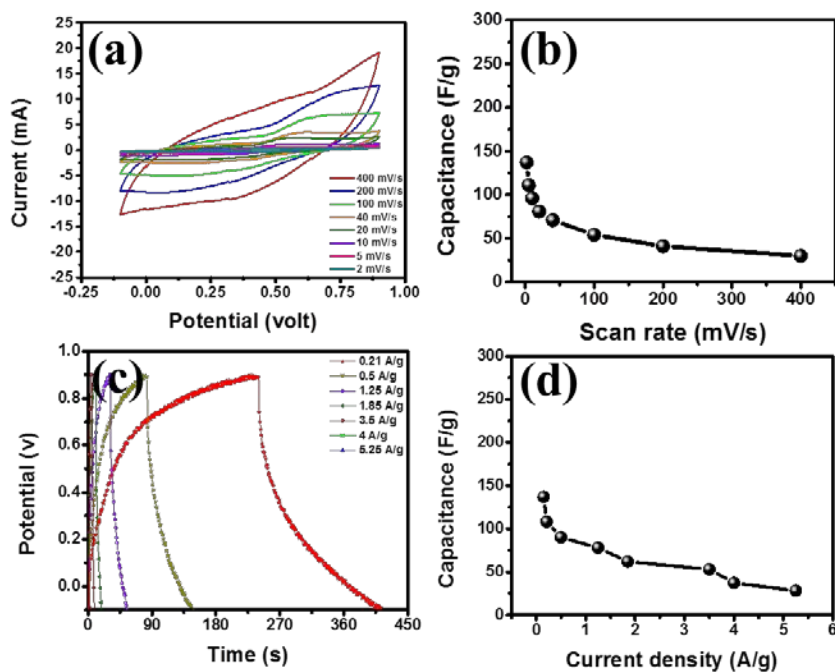


**Figure 2.8.** (a) Supercapacitor data for VS<sub>2</sub> layers. (a) CV curves for VS<sub>2</sub>, (b) variation of specific capacitance with scan rate. (c) CD curves for different current densities. symmetric curves depicting reversible redox (Faradic) reaction. (d) plot between specific capacitance and current density for VS<sub>2</sub>.

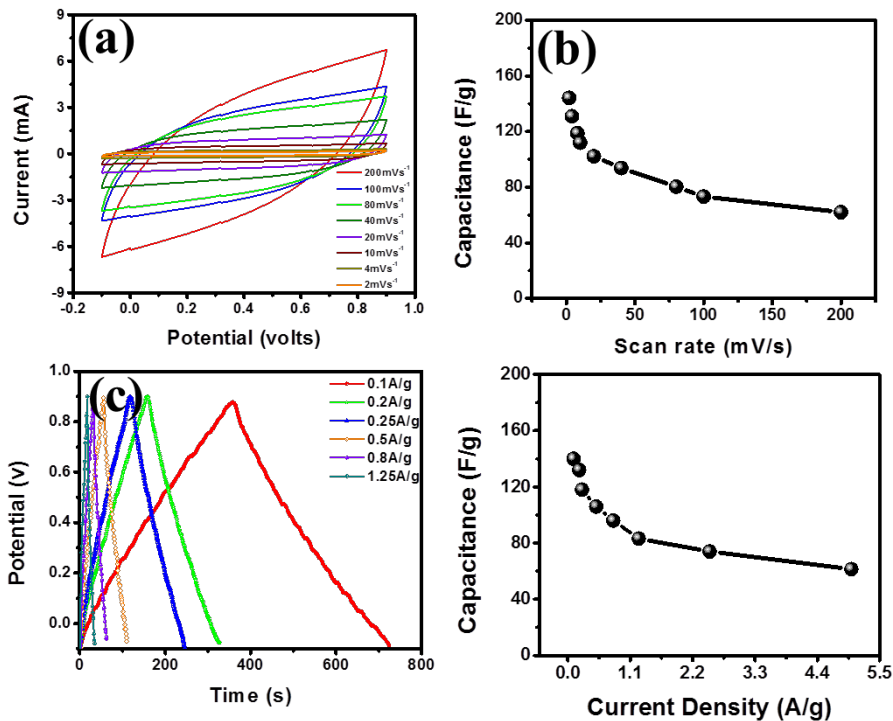


**Figure 2.9.** Supercapacitor data for RGO. (a) CV curves, (b) graph showing variation of specific capacitance with scan rate, (c) CD curves at different current densities, (d) plot between specific capacitance and current density.

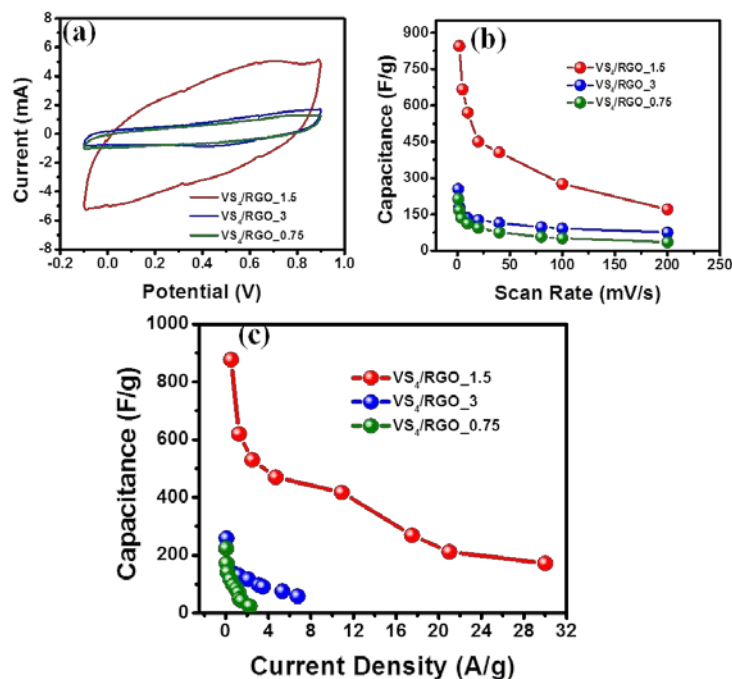


**Figure 2.10.** Supercapacitor performance of VS<sub>4</sub>/RGO<sub>1.5</sub> (red), VS<sub>4</sub>/RGO<sub>3</sub> (blue), and VS<sub>4</sub>/RGO<sub>0.75</sub> (green). (a) CV curves, (b) comparison of capacitance vs scan rate and (c) Capacitance vs current density plot.

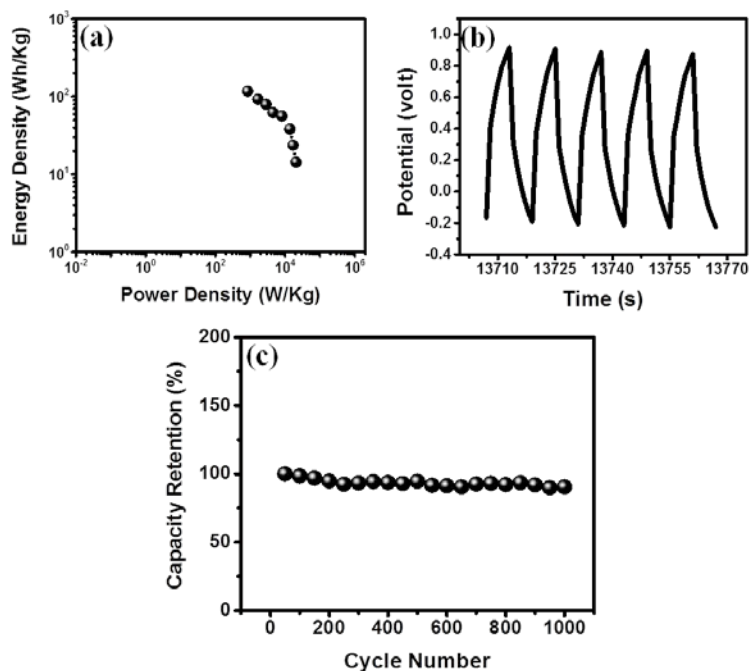


**Figure 2.11.** (a) Ragone plot for VS<sub>4</sub>/RGO\_1.5. (b) Last 5 cycles taken from the long cycle stability test to show no variation of symmetry in the CD pattern even after 1000 cycles. (c) Capacity retention of the hybrid showing much better stability even after 1000 cycles.

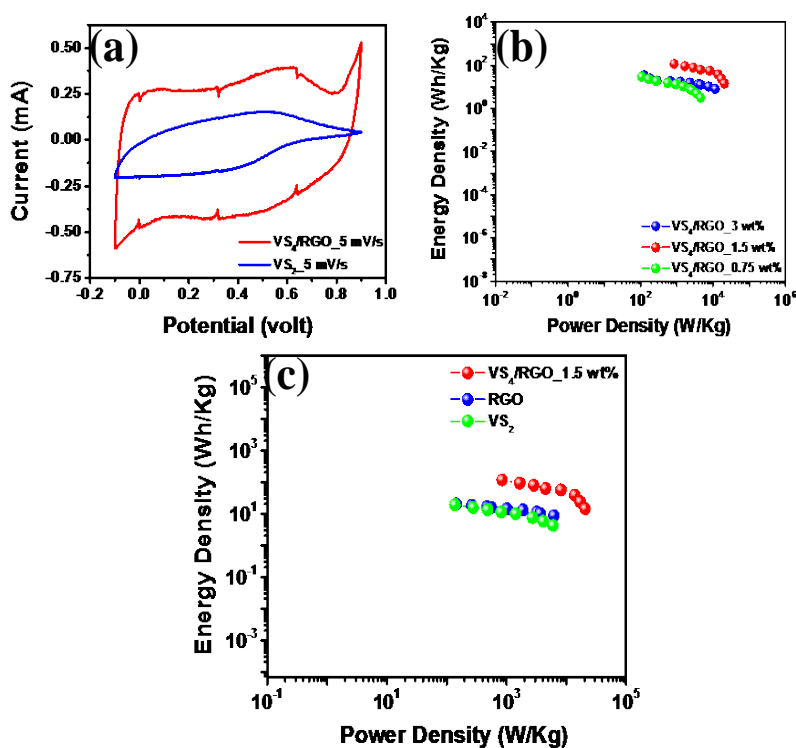


**Figure 2.12.** (a) Three electrode data (CV curves) for VS<sub>4</sub>/RGO\_1.5 (red) and VS<sub>2</sub> (blue), (b) Ragone plot for VS<sub>4</sub>/RGO\_0.75 (green), VS<sub>4</sub>/RGO\_1.5 (red) and VS<sub>4</sub>/RGO\_3 (blue). (c) Ragone plot comparison VS<sub>4</sub>/RGO\_1.5 (red), RGO (blue) and VS<sub>2</sub> (green).

**Table 2.1.** Comparison of supercapacitor performance of VS<sub>4</sub>/RGO\_0.75, VS<sub>4</sub>/RGO\_1.5, VS<sub>4</sub>/RGO\_3, RGO and VS<sub>2</sub>

Sample	Maximum Specific capacitance (A/g)	Maximum Energy Density (Wh/kg)	Maximum Power Density (KW/kg)
VS <sub>4</sub> /RGO_0.75	223 F/g	29.72 Wh/kg	4.53 KW/kg
VS <sub>4</sub> /RGO_1.5	877 F/g	117 Wh/kg	20.65 KW/kg
VS <sub>4</sub> /RGO_3	259 F/g	35.36 Wh/kg	11.57 KW/kg
RGO	144 F/g	20 Wh/kg	6.2 KW/kg
VS <sub>2</sub>	137 F/g	19 Wh/kg	6 W/kg

**Table 2.2.** Comparison of supercapacitor performance of VS<sub>4</sub>/RGO\_1.5 with the reported metal sulfides/graphene hybrids

Hybrid	Maximum Specific capacitance (F/g)	Maximum Energy Density (Wh/kg)	Maximum Power Density (KW/kg)	Reference
NiS/graphene	775 F/g (at 0.5 A/g)	11.2 Wh/kg	~1 KW/kg	61
WS <sub>2</sub> /RGO	350 F/g (at 2 mV/s)	49 Wh/kg	8.2 KW/kg	22
Co <sub>3</sub> S <sub>4</sub> /graphene	675.9 F/g (at 0.5 A/g)	-----	-----	62
CoS <sub>2</sub> /graphene	314 F/g (0.5 A/g)	-----	-----	63
VS <sub>4</sub> /RGO_1.5	877 F/g (at 0.5 A/g)	117 Wh/kg	20.65 W/kg	Present Work

VSe<sub>2</sub>/RGO containing 0.15 wt% of RGO, 0.3 wt% of RGO and 0.75 wt% of RGO has been denoted hereafter as VSe<sub>2</sub>/RGO\_0.15, VSe<sub>2</sub>/RGO\_0.3 and VSe<sub>2</sub>/RGO\_0.75, respectively. FESEM images of the VSe<sub>2</sub>/RGO (0.3 wt%) hybrid confirm uniform distribution of VSe<sub>2</sub> over RGO layer (Figure 2.13a and 2.13b). Figure 2.13d shows the EDAX data of the VSe<sub>2</sub>/RGO\_0.3 hybrid confirming the presence of the components with appropriate proportions. Figure 2.13c shows the PXRD pattern of the hybrid demonstrating a prominent growth along (011) direction with another peak along (102). In the XRD pattern of VSe<sub>2</sub>/RGO, the suppressed carbon peak (at 2θ value of ~26°), characteristic of RGO, is due to the low thickness of the RGO layer and the sharp crystalline peak of VSe<sub>2</sub>/RGO\_0.3. All these diffraction peaks can be assigned to VSe<sub>2</sub> structure with JCPDS file:89-1641. The FESEM studies and XRD analyses for VSe<sub>2</sub> confirms the formation of pure phase without any impurities (JCPDS file: 89-1641) (Figure 2.14).

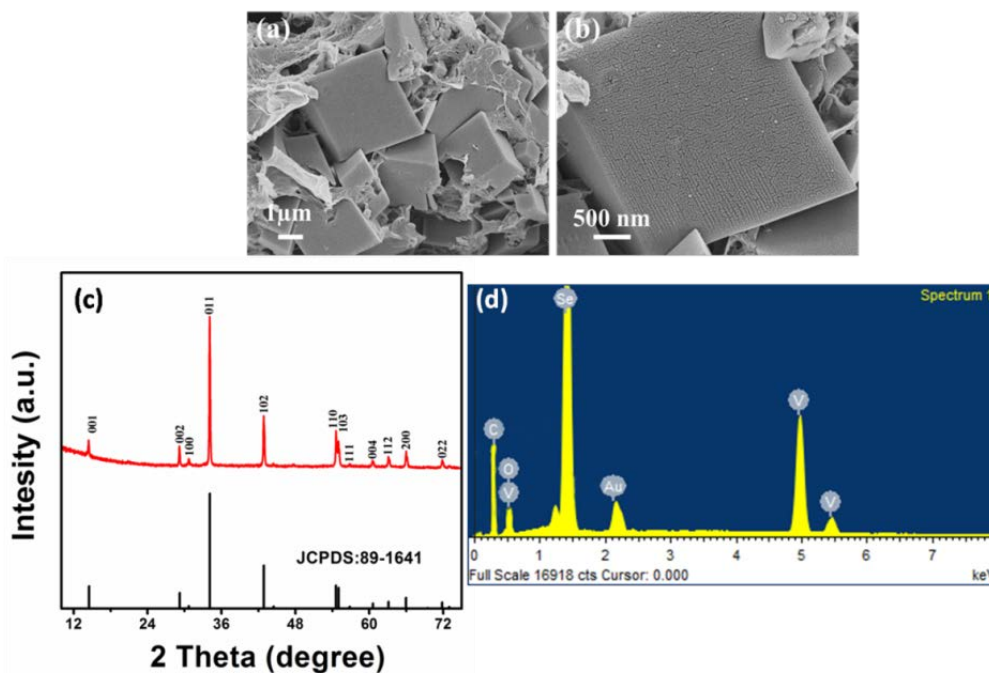


**Figure 2.13.** (a) Low and (b) high magnification FESEM images of VSe<sub>2</sub>/RGO\_0.3 hybrid, (c) PXRD patterns for VSe<sub>2</sub>/RGO\_0.3 hybrid and (d) EDAX spectrum.

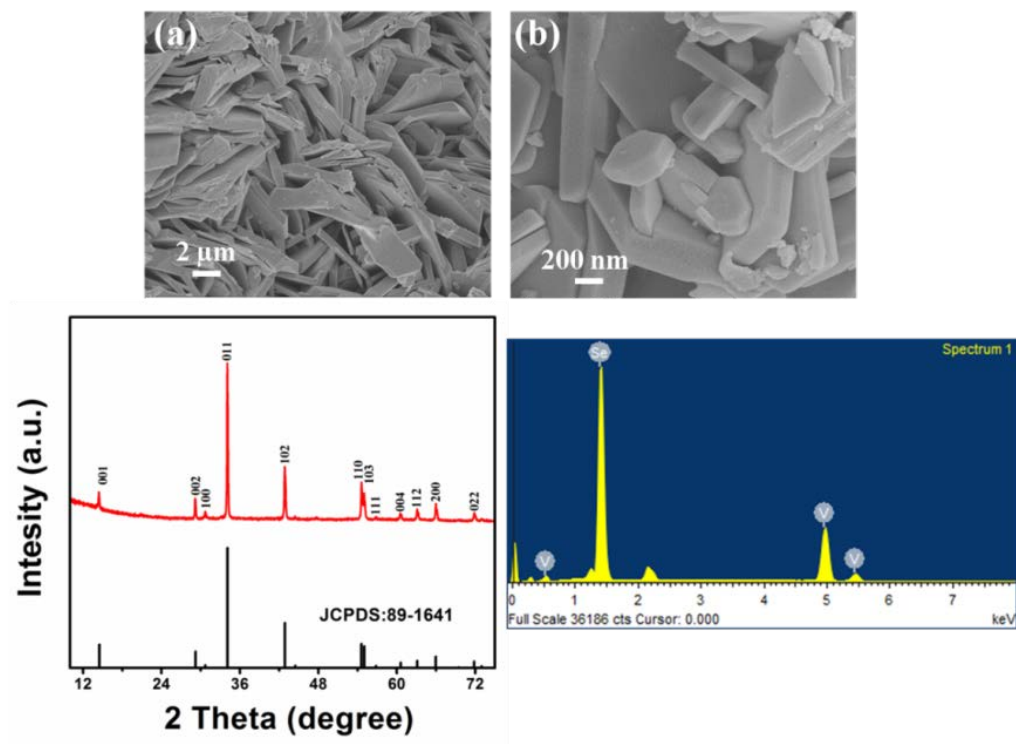


**Figure 2.14.** (a) Low and (b) high magnification FESEM images of VSe<sub>2</sub>. (c) PXRD pattern for VSe<sub>2</sub> and (d) EDAX spectrum.

The electrochemical measurements were performed for VSe<sub>2</sub>, RGO and VSe<sub>2</sub>/RGO at three different concentrations (i.e. 0.15 wt%, 0.3 wt% and 0.75 wt%) of RGO. VSe<sub>2</sub>/RGO\_0.3 shows high specific capacitance as compared to other hybrids, due to the uniform distribution of VSe<sub>2</sub> layers over RGO hybrid and also uniform crystallinity of VSe<sub>2</sub>/RGO\_0.3. Here we have mentioned detailed specific capacitance measurement for VSe<sub>2</sub>/RGO\_0.3 hybrid from CV and CD methods (Figure 2.16). VSe<sub>2</sub>/RGO\_0.3 hybrid shows high specific capacitance in the order of hybrid of 500 F/g at current density of 1 A/g and also from CV showed a capacitance of 400 F/g at scan rate of 5 mV/s. This high value of specific capacitance can be attributed to the EDLC from the RGO layer as well as pseudocapacitive contribution from VSe<sub>2</sub>. Figure 2.18 showed the comparison between capacitance and current density for all the hybrids. Figure 2.17 shows the Ragone plot which depicts the energy density and power density of the hybrid material at

different scan rates. At a scan rate of 5 mV/s, the hybrid material shows a maximum energy density in the order of ~128 Wh/kg and a maximum power density in the order of ~32.81 KW/kg.

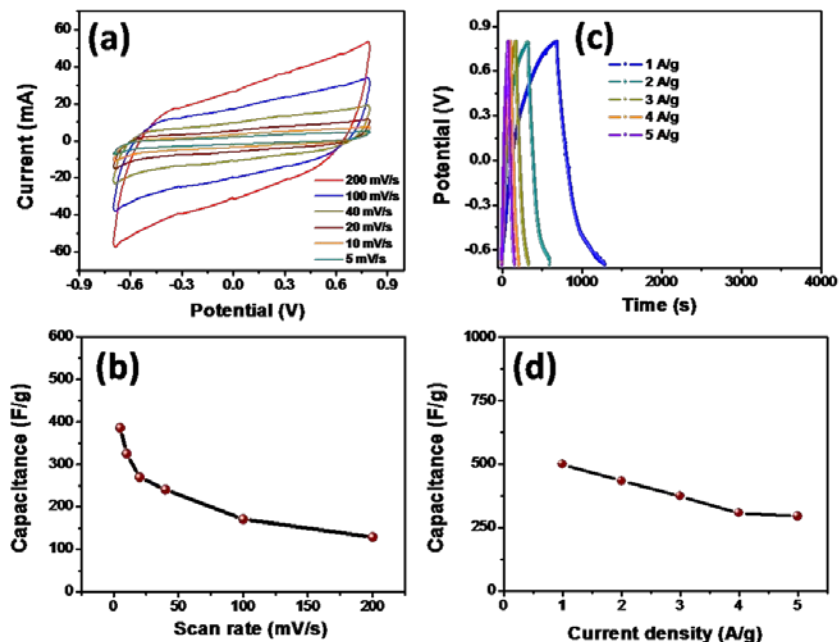


**Figure 2.15.** Supercapacitor performance of VSe<sub>2</sub>/RGO\_0.3. (a) CV curves at different scan rates, (b) plot between specific capacitance and scan rate, (c) CD curves at different current densities and (d) plot between specific capacitance and current density.

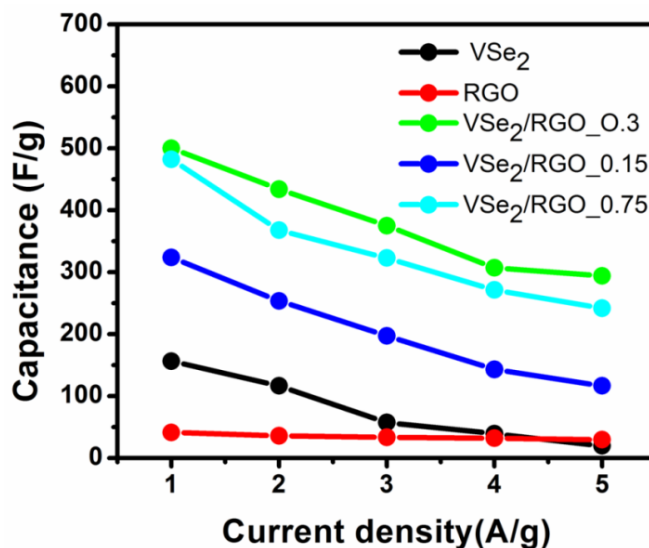


**Figure 2.16** Comparison of capacitance vs. current density.

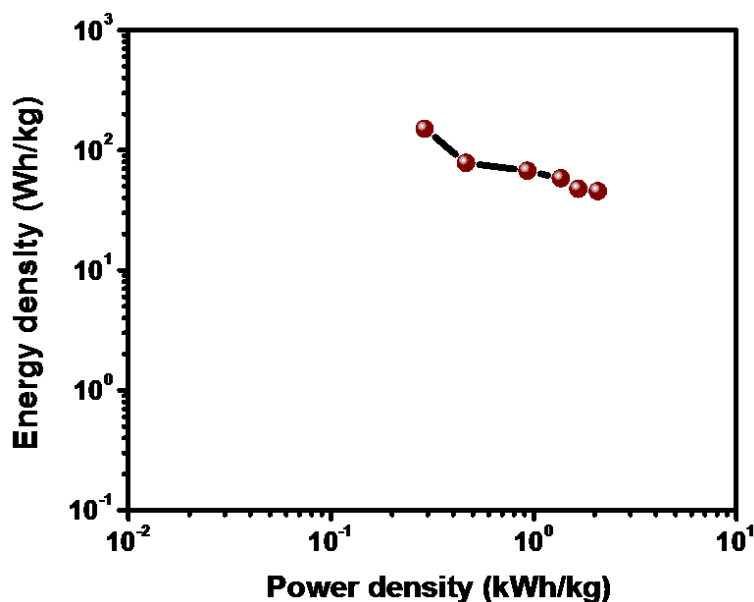


**Figure 2.17** Ragone plot for VSe<sub>2</sub>/RGO<sub>0.3</sub> hybrid.

## 2.8 Conclusions

The synthesis of VSe<sub>2</sub>/RGO and VS<sub>4</sub>/RGO hybrids by facile one-step hydrothermal techniques have been accomplished and its supercapacitor performance is tested. The results obtained so far have shown the great potential of the VSe<sub>2</sub>/RGO and VS<sub>4</sub>/RGO hybrids with the specific capacitance as high as 500 F/g at current density of 1 A/g and 855 F/g at 0.5 A/g respectively. VSe<sub>2</sub>/RGO<sub>0.3</sub> hybrid exhibited enhanced energy density of 128 Wh/kg and power density of 32.81 KW/kg. The second hybrid VS<sub>4</sub>/RGO<sub>3</sub> exhibited enhanced energy density in order of 117 Wh/kg and power density of 20.65 KW/kg which is compared to reported metal sulfides and their graphene based hybrids. From these experimental findings provide these two hybrids useful insights in the design of supercapacitors for potential high performance energy storage application in future.

## 2.9 References

1. Castro Neto, A. H.; Guinea, F.; Peres, N. M. R.; Novoselov, K. S.; Geim, A. K., *Rev. Mod. Phys.* **2009**, *81*, 109.
2. Ferralis, N., *J. Mater. Sci.* **2010**, *45*, 5135.
3. Geim, A. K., *Science* **2009**, *324*, 1530.
4. Li, X.; Cai, W.; An, J.; Kim, S.; Nah, J.; Yang, D.; Piner, R.; Velamakanni, A.; Jung, I.; Tutuc, E.; Banerjee, S. K.; Colombo, L.; Ruoff, R. S., *Science* **2009**, *324*, 1312.
5. Stankovich, S.; Dikin, D. A.; Dommett, G. H. B.; Kohlhaas, K. M.; Zimney, E. J.; Stach, E. A.; Piner, R. D.; Nguyen, S. T.; Ruoff, R. S., *Nature* **2006**, *442*, 282.
6. Geim, A. K.; Novoselov, K. S., *Nat. Mater.* **2007**, *6*, 183.
7. Blake, P.; Brimicombe, P. D.; Nair, R. R.; Booth, T. J.; Jiang, D.; Schedin, F.; Ponomarenko, L. A.; Morozov, S. V.; Gleeson, H. F.; Hill, E. W., *Nano Lett.* **2008**, *8*, 1704.
8. Chatzitheodorou, G.; Fiechter, S.; Kunst, M.; Luck, J.; Tributsch, H., *Mater. Res. Bull.* **1988**, *23*, 1261.
9. Gao, M.-R.; Jiang, J.; Yu, S.-H., *Small* **2012**, *8*, 13.
10. Johari, P.; Shenoy, V. B., *ACS Nano* **2012**, *6*, 5449.
11. Lv, R.; Robinson, J. A.; Schaak, R. E.; Sun, D.; Sun, Y.; Mallouk, T. E.; Terrones, M., *Acc. Chem. Res.* **2014**, *48*, 56.
12. Zhang, X.; Meng, F.; Christianson, J. R.; Arroyo-Torres, C.; Lukowski, M. A.; Liang, D.; Schmidt, J. R.; Jin, S., *Nano Lett.* **2014**, *14*, 3047.
13. Han, J. H.; Lee, S.; Cheon, J., *Chem. Soc. Rev.* **2013**, *42*, 2581.
14. Fang, H.; Battaglia, C.; Carraro, C.; Nemsak, S.; Ozdol, B.; Kang, J. S.; Bechtel, H. A.; Desai, S. B.; Kronast, F.; Unal, A. A.; Conti, G.; Conlon, C.; Palsson, G. K.; Martin, M. C.;

- Minor, A. M.; Fadley, C. S.; Yablonovitch, E.; Maboudian, R.; Javey, A., *Proc. Natl. Acad. Sci. U. S. A.* **2014**, *111*, 6198.
15. Gatensby, R.; McEvoy, N.; Lee, K.; Hallam, T.; Berner, N. C.; Rezvani, E.; Winters, S.; O'Brien, M.; Duesberg, G. S., *Appl. Surf. Sci.* **2014**, *297*, 139.
16. Zhang, Y.; Ye, J.; Matsushashi, Y.; Iwasa, Y., *Nano Lett.* **2012**, *12*, 1136.
17. Yuan, H.; Toh, M.; Morimoto, K.; Tan, W.; Wei, F.; Shimotani, H.; Kloc, C.; Iwasa, Y., *Appl. Phys. Lett.* **2011**, *98*, 012102.
18. Hwang, W. S.; Remskar, M.; Yan, R.; Protasenko, V.; Tahy, K.; Chae, S. D.; Zhao, P.; Konar, A.; Xing, H. G.; Seabaugh, A., *Appl. Phys. Lett.* **2012**, *101*, 013107.
19. Yang, Y.; Fei, H.; Ruan, G.; Xiang, C.; Tour, J. M., *Adv. Mater.* **2014**, *26*, 8163.
20. Zhong, H.; Yang, G.; Song, H.; Liao, Q.; Cui, H.; Shen, P.; Wang, C.-X., *J. Phys. Chem. C* **2012**, *116*, 9319.
21. Bhandavat, R.; David, L.; Singh, G., *J Phys Chem Lett* **2012**, *3*, 1523.
22. Ratha, S.; Rout, C. S., *ACS Appl. Mater. Interfaces* **2013**, *5*, 11427.
23. Wang, T.; Gao, D.; Zhuo, J.; Zhu, Z.; Papakonstantinou, P.; Li, Y.; Li, M., *Chem. Eur. J.* **2013**, *19*, 11939.
24. Bai, Y.; Zong, X.; Yu, H.; Chen, Z. G.; Wang, L., *Chem. Eur. J.* **2014**, *20*, 8670.
25. Ellmer, K., *Phys. Status Solidi B* **2008**, *245*, 1745.
26. Tsai, D.-S.; Liu, K.-K.; Lien, D.-H.; Tsai, M.-L.; Kang, C.-F.; Lin, C.-A.; Li, L.-J.; He, J.-H., *ACS Nano* **2013**, *7*, 3905.
27. Ding, S.; Zhang, D.; Chen, J. S.; Lou, X. W., *Nanoscale* **2012**, *4*, 95.
28. Lei, Y.; Song, S.; Fan, W.; Xing, Y.; Zhang, H., *J. Phys. Chem. C* **2009**, *113*, 1280.
29. David, L.; Bhandavat, R.; Singh, G., *ACS Nano* **2014**, *8*, 1759.

30. Roy, K.; Padmanabhan, M.; Goswami, S.; Sai, T. P.; Ramalingam, G.; Raghavan, S.; Ghosh, A., *Nat. Nanotechnol.* **2013**, *8*, 826.
31. Rout, C. S.; Joshi, P. D.; Kashid, R. V.; Joag, D. S.; More, M. A.; Simbeck, A. J.; Washington, M.; Nayak, S. K.; Late, D. J., *Appl. Phys. Lett.* **2014**, *105*, 043109.
32. Sathish, M.; Mitani, S.; Tomai, T.; Honma, I., *J. Phys. Chem. C* **2012**, *116*, 12475.
33. Wang, D.; Choi, D.; Li, J.; Yang, Z.; Nie, Z.; Kou, R.; Hu, D.; Wang, C.; Saraf, L. V.; Zhang, J.; Aksay, I. A.; Liu, J., *ACS Nano* **2009**, *3*, 907.
34. Xiong, G.; Hembram, K. P. S. S.; Reifengerger, R. G.; Fisher, T. S., *J. Power Sources* **2013**, *227*, 254.
35. Khalid, M.; Tumelero, M. A.; Zoldan, V. C.; Pla Cid, C. C.; Franceschini, D. F.; Timm, R. A.; Kubota, L. T.; Moshkalev, S. A.; Pasa, A. A., *RSC Adv.* **2014**, *4*, 34168.
36. Patil, S.; Harle, A.; Sathaye, S.; Patil, K., *CrystEngComm* **2014**, *16*, 10845.
37. Peng, S.; Li, L.; Tan, H.; Cai, R.; Shi, W.; Li, C.; Mhaisalkar, S. G.; Srinivasan, M.; Ramakrishna, S.; Yan, Q., *Adv. Funct. Mater.* **2014**, *24*, 2155.
38. Amaresh, S.; Karthikeyan, K.; Jang, I. C.; Lee, Y. S., *J. Mater. Chem. A* **2014**, *2*, 11099.
39. Xu, J.; Xue, H.; Yang, X.; Wei, H.; Li, W.; Li, Z.; Zhang, W.; Lee, C.-S., *Small* **2014**, *10*, 4754.
40. Puthussery, J.; Seefeld, S.; Berry, N.; Gibbs, M.; Law, M., *J. Am. Chem. Soc.* **2010**, *133*, 716.
41. Feng, J.; Sun, X.; Wu, C.; Peng, L.; Lin, C.; Hu, S.; Yang, J.; Xie, Y., *J. Am. Chem. Soc.* **2011**, *133*, 17832.
42. Jing, Y.; Zhou, Z.; Cabrera, C. R.; Chen, Z., *J. Phys. Chem. C* **2013**, *117*, 25409.

43. Feng, J.; Peng, L.; Wu, C.; Sun, X.; Hu, S.; Lin, C.; Dai, J.; Yang, J.; Xie, Y., *Adv. Mater.* **2012**, *24*, 1969.
44. Zhang, Y.; Wu, X., *Phys. Lett. A* **2013**, *377*, 3154.
45. Ma, Y.; Dai, Y.; Guo, M.; Niu, C.; Zhu, Y.; Huang, B., *ACS Nano* **2012**, *6*, 1695.
46. Song, C.; Yu, K.; Yin, H.; Fu, H.; Zhang, Z.; Zhang, N.; Zhu, Z., *J. Mater. Chem. C* **2014**, *2*, 4196.
47. Guillard, C.; Lacroix, M.; Vrinat, M.; Breysse, M.; Mocaer, B.; Grimblot, J.; Des Courieres, T.; Faure, D., *Catal. Today* **1990**, *7*, 587.
48. Hillebrand, W. F., *J. Am. Chem. Soc.* **1907**, *29*, 1019.
49. Nakano-Onoda, M.; Yamaoka, S.; Yukino, K.; Kato, K.; Kawada, I., *J. Less-Common Met.* **1976**, *44*, 341.
50. Taniguchi, M.; Wakihara, M.; Shirai, Y., *Z. Anorg. Allg. Chem.* **1980**, *461*, 234.
51. Murugesan, T.; Ramesh, S.; Gopalakrishnan, J.; Rao, C. N. R., *J. Solid State Chem.* **1982**, *44*, 119.
52. Yokoyama, M.; Yoshimura, M.; Wakihara, M.; Somiya, S.; Taniguchi, M., *J. Solid State Chem.* **1985**, *60*, 182.
53. Guo, W.; Wu, D., *Int. J. Hydrogen Energy* **2014**, *39*, 16832.
54. Xu, X.; Jeong, S.; Rout, C. S.; Oh, P.; Ko, M.; Kim, H.; Kim, M. G.; Cao, R.; Shin, H. S.; Cho, J., *J. Mater. Chem. A* **2014**, *2*, 10847.
55. Bayard, M.; Sienko, M. J., *J. Solid State Chem.* **1976**, *19*, 325.
56. Rout, C. S.; Khare, R.; Kashid, R. V.; Joag, D. S.; More, M. A.; Lanzillo, N. A.; Washington, M.; Nayak, S. K.; Late, D. J., *Eur. J. Inorg. Chem.* **2014**, *2014*, 5331.

57. Xu, K.; Chen, P.; Li, X.; Wu, C.; Guo, Y.; Zhao, J.; Wu, X.; Xie, Y., *Angew. Chem. Int. Ed.* **2013**, *52*, 10477.
58. Stankovich, S.; Dikin, D. A.; Piner, R. D.; Kohlhaas, K. A.; Kleinhammes, A.; Jia, Y.; Wu, Y.; Nguyen, S. T.; Ruoff, R. S., *Carbon* **2007**, *45*, 1558.
59. Lee, J. W.; Ahn, T.; Soundararajan, D.; Ko, J. M.; Kim, J.-D., *Chem. Commun.* **2011**, *47*, 6305.
60. Xu, J.; Wang, K.; Zu, S.-Z.; Han, B.-H.; Wei, Z., *ACS Nano* **2010**, *4*, 5019.
61. Li, Y.; Ye, K.; Cheng, K.; Yin, J.; Cao, D.; Wang, G., *J. Power Sources* **2015**, *274*, 943.
62. Wang, Q.; Jiao, L.; Du, H.; Si, Y.; Wang, Y.; Yuan, H., *J. Mater. Chem.* **2012**, *22*, 21387.
63. Wang, B.; Park, J.; Su, D.; Wang, C.; Ahn, H.; Wang, G., *J. Mater. Chem.* **2012**, *22*, 15750.

## CHAPTER-3

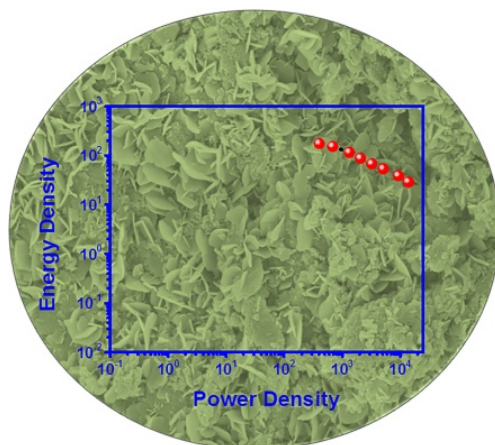
---

### High Energy Density Supercapacitors Based on Patronite/CNTs/RGO Hybrids

---

<b>3.1</b>	Abstract	222
<b>3.2</b>	Introduction	223
<b>3.3</b>	Objective of our work	225
<b>3.4</b>	Experimental section	225
<b>3.4.1</b>	Synthesis of GO, RGO and functionalization of CNTs	225
<b>3.4.2</b>	Synthesis of CNTs/RGO hybrid	226
<b>3.4.3</b>	Synthesis of VS <sub>2</sub> layers	226
<b>3.4.4</b>	Synthesis of VS <sub>4</sub> /RGO hybrids	226
<b>3.4.5</b>	Synthesis of VS <sub>4</sub> /CNTs hybrids	226
<b>3.4.6</b>	Synthesis of VS <sub>4</sub> /CNTs/RGO hybrid	227
<b>3.5</b>	Supercapacitor device fabrication and measurement	227
<b>3.6</b>	Results and discussions	228
<b>3.7</b>	Conclusions	241
<b>3.8</b>	References	242

### 3.1 Abstract



*In this chapter describes the facile hydrothermal synthesis of a patronite hybrid, VS<sub>4</sub>/SWCNTs/RGO is reported. Detailed electrochemical investigations showed an exceptionally high energy density of the hybrid VS<sub>4</sub>/CNTs/RGO which was of the order of ~174 Wh/kg and a moderate power density of ~13.8 KW/kg. The value was compared to other supercapacitor electrodes based on metal sulfides and also some of those having reportedly high energy density values. The comparison reveals the potential of the patronite hybrid to be a fitting candidate for its possible application in energy storage devices.*

## 3.2 Introduction

The electrodes used in supercapacitors are made primarily from carbonaceous materials such as RGO, CNTs, activated carbon etc. which have significant impact on the energy densities of those devices. While the value is much higher than conventional dielectric capacitors, it still lags behind rechargeable batteries due to lower value of energy per unit weight ratio. A thorough research is going on to address this particular issue associated with a typical supercapacitor. There are several ways to enhance the energy density of a supercapacitor. By increasing the amount of charge storage and/or the potential window will surely enhance the energy density of supercapacitors. Controlling the amount of charge storage depends upon the choice of suitable electrode material. One of the important issues is to increase the energy per unit weight ratio in supercapacitor electrodes. Therefore in recent times, much attention has been focused onto pseudocapacitive materials which have the ability to store enormous amount of energy per unit weight in terms of surface redox (faradic) reactions.<sup>1</sup> However, they don't have the advantage of long cyclic stability as in case of carbonaceous materials.<sup>2-3</sup> So, the current research is to bring both the materials together and hybridize them in order to get stable and high performing composite structures.<sup>4-5</sup> In this context, 2D-inorganic analogues of graphene have found special preference over other materials because of their unique physical and chemical properties.<sup>6-8</sup> Such rise of 2D-inorganic analogues of graphene in recent years has earmarked their presence in various areas like valleytronics,<sup>7, 9</sup> biosensors,<sup>10</sup> energy storage and conversion devices etc.<sup>11-12</sup> Prominent among their compounds are TMDCs which have drawn significant attention for the past few years. They have found successful implementations in energy storage devices such as Supercapacitors and lithium ion batteries.<sup>10</sup>

Despite high values of specific capacitances associated with them, energy densities of pseudocapacitive materials (also their hybrid with RGO/or other carbonaceous materials) remain low (in comparison to batteries) due to narrow operational potential windows.<sup>13</sup> Since the working potential window strictly follows the nature of the electrolyte, it is customary to choose a suitable and stable electrolytic material/solution. Aqueous electrolytes, which are normally employed in Supercapacitors, don't have the ability to withstand larger working potential windows as they would eventually get electrolyzed. Though many organic electrolytes reported recently, have wide operational potential window,<sup>14</sup> movement of ions inside the electrolyte is significantly hindered due to the low conductivity associated with them which results in lower values of power densities. Also the high cost associated with such electrolytes would hinder their practical application and scalability. Therefore to form stable supercapacitor architecture with enhanced energy density (without sacrificing the power density significantly); one has to choose, carefully, both an ideal material that is to be used as the electrode and a congenial electrolyte.

TMDCs are easy to synthesize and their properties can be easily modulated for various applications. Some compounds like MoS<sub>2</sub>,<sup>15-17</sup> WS<sub>2</sub>,<sup>18-20</sup> CdSe,<sup>21-22</sup> NiS,<sup>23-24</sup> CoS etc.<sup>25-26</sup> have undergone intense research. Only recently, a novel group of compounds, namely the vanadium sulfides, belonging to this category have come to the fore.<sup>11, 27-30</sup> VS<sub>2</sub> which belongs to this group has showcased promising energy storage activities.<sup>11, 28</sup> Another emerging compound is VS<sub>4</sub>, which contains two S<sub>2</sub><sup>2-</sup> dimers and have an unusual linear chain structure.<sup>29, 31</sup> However, the oxidation state of V remains the same in both VS<sub>2</sub> as well as VS<sub>4</sub>. Few recent reports have suggested that by following a facile hydrothermal method mediated GO/CNTs as active template, VS<sub>4</sub> can be obtained in its pure form.<sup>31-32</sup> Both GO and CNTs provide the required nucleation path in which VS<sub>2</sub> transforms to VS<sub>4</sub>. The template mediated synthesis process

produces a  $VS_4$ /RGO hybrid which is known to show some interesting electrochemical activities towards energy storage applications.<sup>33-34</sup>

### **3.3 Motivation of our work**

As per the above mentioned discussions, Composite materials of TMCs/CNTs/RGO are very good for the storage of high energy and power density in electrochemical super capacitance. However, reports on composite materials of TMCs with CNTs/RGO are very less explored. Vanadium layers ( $VS_2$  and  $VS_4$ ) have emerging applications in electronics and reports are very explored. Hence, we are interesting on  $VS_4$ /SWCNTs/RGO hybrid. In this chapter we discuss the facile synthesis, morphology and their electrochemical supercapacitance of  $VS_2$ ,  $VS_2$ /RGO,  $VS_2$ /CNTs/RGO hybrids by using two electrode measurements. The hybrid  $VS_2$ /CNTs/RGO shows good energy density and moderate power density which was compare with some of the reported composite materials.

### **3.4 Experimental section**

#### **3.4.1 Synthesis of GO, RGO and functionalization of CNTs**

GO was synthesized from graphite powder following a modified Hummer's method as reported in a previous literature.<sup>35</sup> Subsequent reduction of GO to form reduced graphene oxide (RGO) was done by a hydrothermal reaction carried out at 160 °C for 24 h. The as received CNTs (Reinste Nano Ventures Pvt. Ltd., India) were functionalized using a mixture of  $HNO_3$  and  $H_2SO_4$ . The finally obtained precipitate was filtered, dried in vacuum and washed thoroughly prior to use.

### **3.4.2 Synthesis of CNTs/RGO hybrid**

60 mg of GO and 100 mg of functionalised CNTs were separately dispersed in 15 ml of DI water by ultrasonication to get homogeneous mixture solution. Then these two mixture solutions were added under constant stirring condition and DI water is further added to make the final volume, 40 mL. The stirring was continued for about an hour after which the mixture was transferred to a 50 mL Teflon lined stainless steel autoclave. Hydrothermal reaction was carried out at 160 °C for 24 h to get CNTs/RGO hybrid.

### **3.4.3 Synthesis of VS<sub>2</sub>**

Hydrothermal reaction at 160 °C involving sodium orthovanadate (Na<sub>3</sub>VO<sub>4</sub>, Sigma-Aldrich, 99.98%) and thiacetamide (C<sub>2</sub>H<sub>5</sub>NS, Sigma-Aldrich, ≥99%) resulted in the formation of VS<sub>2</sub> layered structures as has been detailed in an earlier report.<sup>31</sup>

### **3.4.4 Synthesis of VS<sub>4</sub>/RGO hybrids**

Under similar hydrothermal conditions (as for VS<sub>2</sub>), the reaction between sodium orthovanadate (Na<sub>3</sub>VO<sub>4</sub>, Sigma-Aldrich, 99.98%) and thioacetamide (C<sub>2</sub>H<sub>5</sub>NS, Sigma-Aldrich, ≥99%) was carried out in GO solution. The reaction resulted in the reduction of GO to form RGO which acted as a template to promote the growth of VS<sub>4</sub>.<sup>31</sup>

### **3.4.5 Synthesis of VS<sub>4</sub>/CNTs hybrids**

100 mg of functionalized CNTs was thoroughly dispersed in DI water by sonication. A mixture containing 0.55 gm of sodium ortho-vanadate and 1.12 gm of thioacetamide was dissolved in 40 mL of DI water. Then the above two mixture solutions were mixed under constant and vigorous stirring condition. The stirring was continued for about 1 h and then the mixture was transferred to a 50 mL Teflon lined stainless steel autoclave and heated at 160 °C for 24 h. After allowing

the final product to cool naturally, it was then filtered and dried in vacuum at 60 °C for 6 h prior to use.

#### **3.4.6 Synthesis of VS<sub>4</sub>/CNTs/RGO hybrid**

First functionalized CNTs (100 mg) and GO (60 mg) were sonicated separately in DI water to give homogeneous mixture solutions. There after a mixture of 0.55 gm sodium orthovanadate and 1.12 gm of thioacetamide was dissolved in 40 mL water. All the three mixture solutions were then thoroughly mixed under vigorous stirring condition. The stirring was further carried for 1-2 h before transferring the final mixture solution to a 50 mL Teflon lined stainless steel autoclave. Hydrothermal treatment was performed at 160 °C for 24 h. The final precipitate was collected by filtration and was dried in vacuum at 60 °C for 6 h prior to use.

#### **3.5 Supercapacitor device fabrication and measurement**

Electrochemical supercapacitive measurements were performed in a two-electrode configuration. For this, a Swagelok type two-electrode setup was used by taking high grade, cylindrical, stainless steel electrodes as current collectors. First the two stainless steel electrodes were polished using alumina slurry on emery paper and then sonicated in DI for about 10-15 min. Then the electrodes were put in a vacuum desiccator to dry. The sample was dispersed in ethanol by sonication to give a near homogeneous mixture solution which was then carefully drop-casted onto the finely polished electrode surface so that each electrode would have 2 mg of the sample on its surface. Then the modified electrodes were further dried in a desiccator for about an hour. A cellulose nitrate membrane having a pore diameter of ~0.22 μm was used as the porous separator. Prior to use, the membrane was thoroughly soaked in 0.5 M aqueous K<sub>2</sub>SO<sub>4</sub> solution. Detailed electrochemical measurement for the fabricated device was carried out with the help of a standard potentiostat/galvanostat (PG 262A, Techno science Ltd., Bangalore, India). For all the

measurements, working potential window was kept at 1.5 V (From highest potential of 0.8 V to lowest potential of -0.7 V).

### 3.6 Results and discussion

Morphology of the VS<sub>4</sub>/CNTs/RGO hybrid was characterized via FESEM along with EDAX, which is shown in Figure 3.1a. From the low magnified image, it can be seen that there is a uniform distribution of VS<sub>4</sub> nanosheet structures on the CNTs/RGO template. The nanosheets consist of rough surfaces with protruding edges (as can be seen in the highly magnified image, Figure 3.1b) which is an ideal condition to facilitate fast charge transportation as well as surface redox reaction. A typical nanosheet has a thickness which would be around ~5-10 nm. These ultrathin, rough and highly edged nanosheets along with RGO and CNTs bring further enhancement in the electrochemical behavior of the reported hybrid. Elemental mapping data is depicted (Figure 3.2) in which the existence of the constituent elements of the hybrid can be observed.

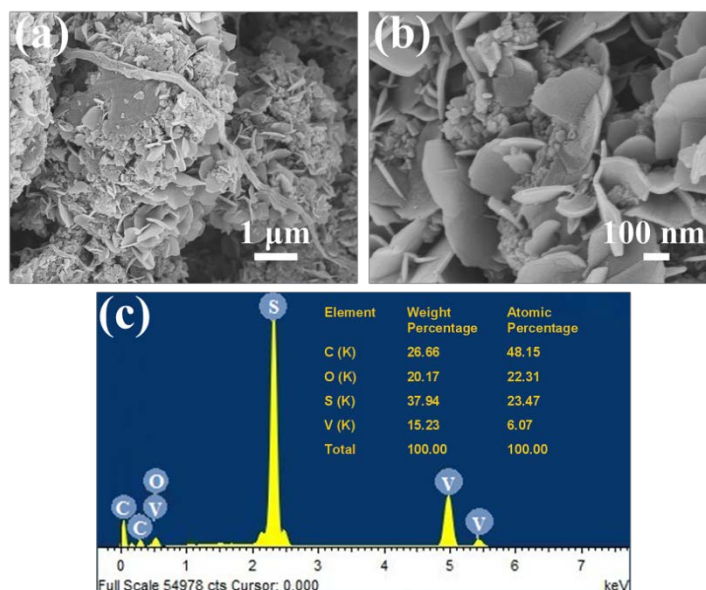


**Figure 3.1.** Low (a) and high (b) magnified FESEM images of VS<sub>4</sub>/CNTs/RGO. (c) EDAX spectroscopy showing the characteristic peaks for constituents of the hybrid with the atomic and weight percentage of the constituent elements.

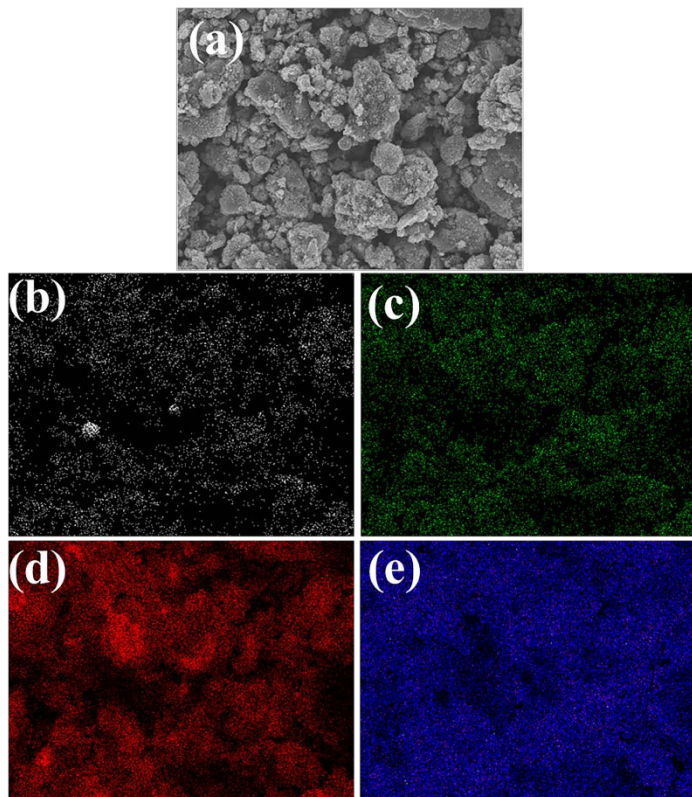


**Figure 3.2.** Elemental mapping data of VS<sub>4</sub>/CNTs/RGO hybrid. (a) Electron image of the region of the sample for which mapping has been done showing the presence of elemental carbon (b), oxygen (c), sulphur (d) and vanadium (e).

Structural characterization of VS<sub>4</sub>/CNTs/RGO hybrid was done by adopting powder X-ray diffraction technique and the subsequent diffraction patterns have been depicted in Figure 3.3. From the diffraction data, two clear sharp peaks were observed at  $\sim 15.8^\circ$  and  $\sim 17^\circ$ , showing the phase growth along (110) and (020) directions, respectively. All these peaks were matched with original crystallographic data (JCPDS file no. 72-1294) which confirmed the formation of body centered V(S<sub>2</sub>)<sub>2</sub> belonging to monoclinic system. The FWHM values for each of those peaks were calculated and by implementing the Scherrer equation it was found that the size of the VS<sub>4</sub> crystallite varies roughly within the range of 22-30 nm. The diffraction patterns of RGO, CNTs and CNTs/RGO have been illustrated in Figure 3.4. The pattern obtained for RGO shows a broad peak at  $2\theta = \sim 25^\circ$  which corresponds to (002) plane and a  $d$ -spacing of  $\sim 3.41 \text{ \AA}$ . The second

peak at  $2\theta = \sim 43^\circ$  shows the growth along (100) direction.<sup>36-38</sup> Figure 3.5 shows the diffraction patterns for  $\text{VS}_2$ . It was found that the phase growth of as prepared  $\text{VS}_2$  is prominent along the (011) direction though growth along (110) and (012) is also clearly observable. These peaks were matched with the stock crystallographic data (JCPDS file: 89-1640) which confirmed the formation of  $\text{VS}_2$  having primitive hexagonal lattice structure. X-ray diffraction patterns for  $\text{VS}_4/\text{CNTs}$ ,  $\text{VS}_4/\text{RGO}$  have also been obtained and compared with that of  $\text{VS}_4/\text{CNTs}/\text{RGO}$  which is shown in Figure 3.6. In all three circumstances (i.e.  $\text{VS}_4/\text{CNTs}$ ,  $\text{VS}_4/\text{RGO}$  and  $\text{VS}_4/\text{CNTs}/\text{RGO}$ ) similar growth phenomena have been observed for  $\text{VS}_4$ , thus indicating its successful nucleation and growth.

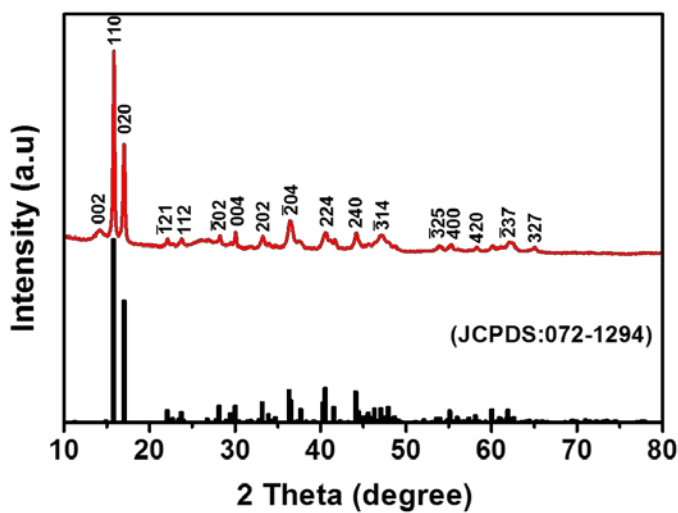


**Figure 3.3.** PXRD patterns for  $\text{VS}_4/\text{CNTs}/\text{RGO}$ .

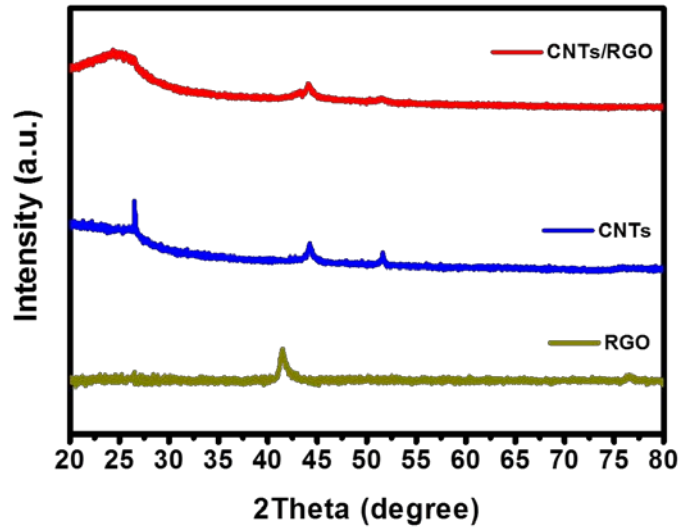


**Figure 3.4.** PXRD patterns for RGO (yellow), CNTs (blue), and CNTs/RGO (red).

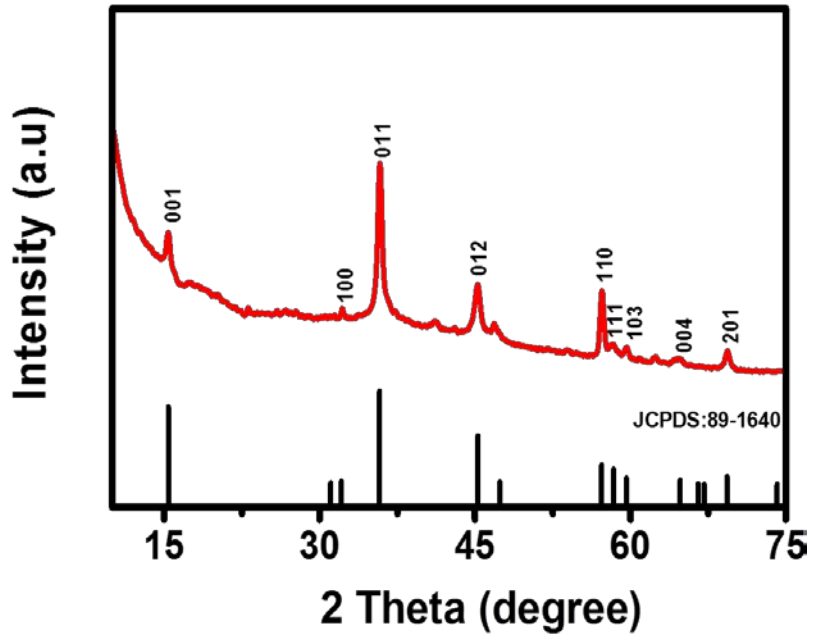


**Figure 3.5.** PXRD patterns for  $VS_2$ .

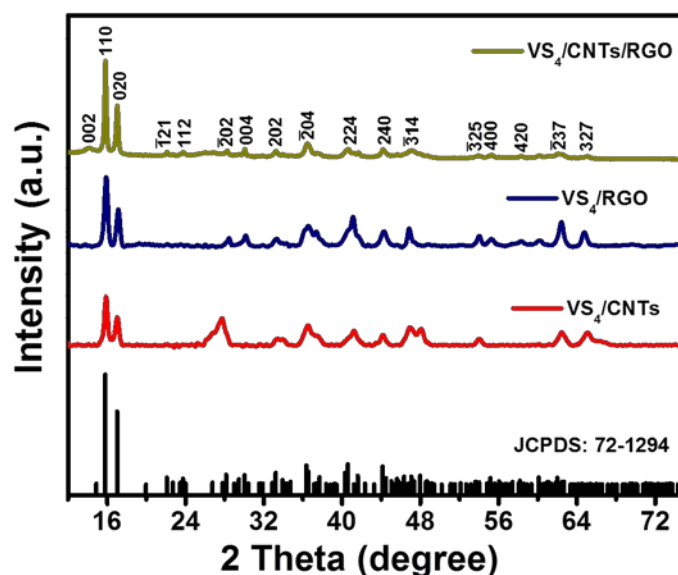


**Figure 3.6.** Comparison of PXRD patterns for  $\text{VS}_4/\text{CNTs}$ ,  $\text{VS}_4/\text{RGO}$  and  $\text{VS}_4/\text{CNTs}/\text{RGO}$ .

The electrochemical supercapacitive investigations were performed in a typical two-electrode configuration. The results are shown in Figure 3.7. The cyclic voltammetry measurements were performed at different scan rates (from 1 mV/s to 200 mV/s) as shown in Figure 3.7a and 3.7b. The working potential window was kept at 1.5 V (-0.7 V to 0.8 V) for all the measurements. Redox peaks due to faradic reaction can be observed at slow scan rates (Figure 3.7a) which is due to the characteristic surface reaction involving  $\text{VS}_4$  and the electrolytic solution.<sup>30</sup> However, at higher scan rates, the redox couples are suppressed (Figure 3.7b) significantly due to kinetically slow surface reactions. In such cases, the electrolytic resistance and slower responsivity of the electrode surface hinders faradic redox reactions and major contribution emerge from the double-layer capacitive effect. Galvanostatic CD measurements were performed at various current densities which are being illustrated in Figure 3.7c. The graph between specific capacitance and scan rate has been depicted in Figure 3.8a.

As can be seen, the value of specific capacitance decreases gradually with increase in the scan rate because at higher scan rates the major contribution is only due to charge trapping by electrostatic double-layer formation whereas at lower scan rates, the significant contribution is

from the pseudocapacitive redox reaction. Similar phenomena have also been observed in the graph between specific capacitance and current density (Figure 3.8b). At lower values of current densities, the hybrid shows high values of specific capacitance, however at higher values of current, there is a significant decline in the capacitance. In addition to the above measurements, cyclic stability test is an essential benchmark to check the feasibility of a supercapacitor electrode for its successful implementation in practical devices. Hence, a long cyclic CD experiment was carried out for 1000 cycles which is shown in Figure 3.8c. A declination of only ~3% (~97% retention) in the initial capacitance value was observed. To showcase the energy density and power density of the hybrid, Ragone plot has been shown in Figure 3.8d. It shows that the hybrid possesses an exceptionally high value of energy density of the order of ~174 Wh/kg, and the maximum value of power density obtained was ~13.8 KW/kg.

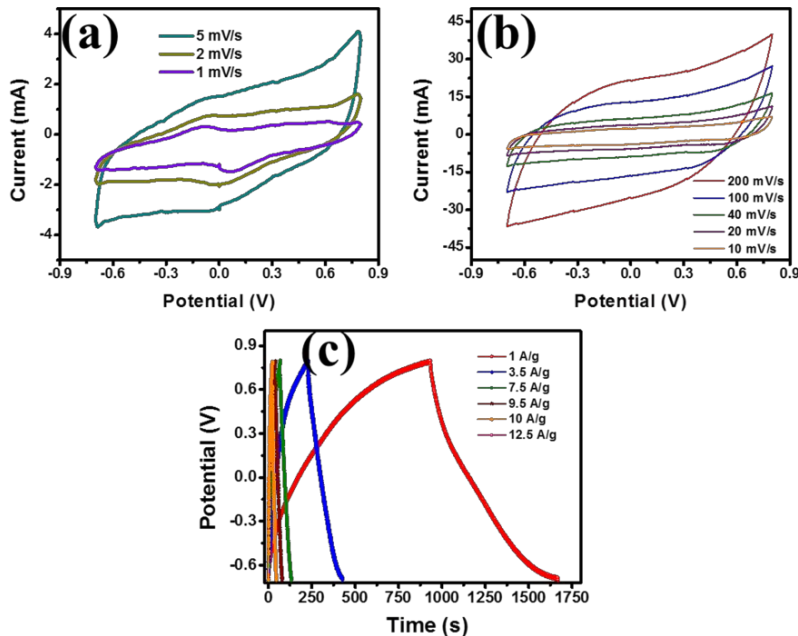


**Figure 3.7.** CV data for the hybrid VS<sub>4</sub>/CNTs/RGO at (a) slower scan rates (i.e. 1 mV/s, 2 mV/s and 5 mV/s) and (b) fast scan rates (i.e. 10, 20, 40, 100 and 200 mV/s). (c) CD curves of the hybrid at different values of current densities.

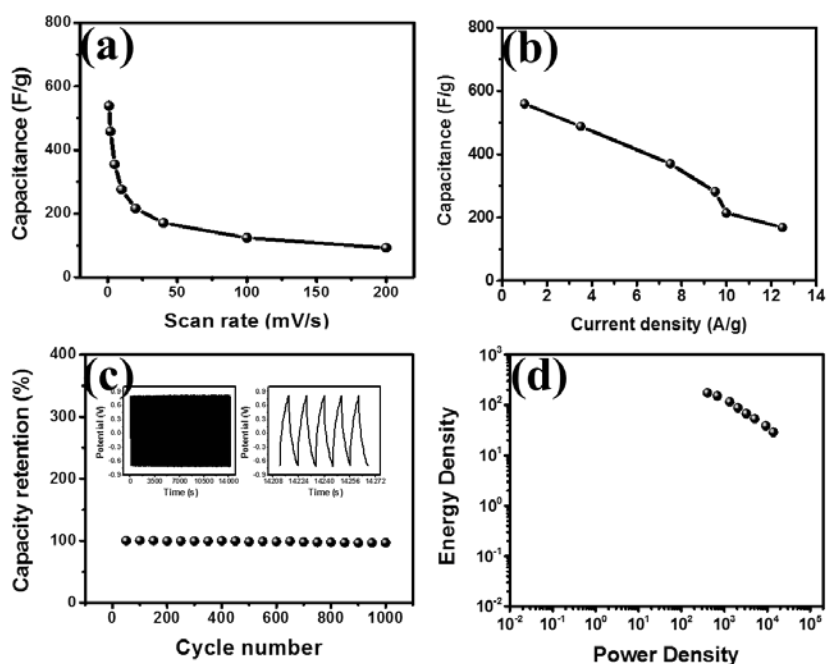


**Figure 3.8.** Variation of specific capacitance with (a) scan rate and (b) current density. (c) Retention capability/ cyclic stability of the hybrid represented by the graph between cycle number and capacity retention in percentage with inset showing the long cycle data. (d) Ragone plot for the hybrid VS<sub>4</sub>/CNTs/RGO.

Similar two-electrode electrochemical measurements were performed for VS<sub>2</sub>, RGO, CNTs, CNTs/RGO, VS<sub>4</sub>/RGO and VS<sub>4</sub>/CNTs in order to investigate the best performing material/hybrid under similar measuring parameters. From Figure 3.9a, the CV curves of VS<sub>2</sub> can be observed. Areas under the curves, obtained at higher scan rates have much lower values, indicating poor faradic activity of VS<sub>2</sub>. Similar observations were made with galvanostatic CD data (Figure 3.9b). Highly unstable faradic reactions were observed with poor coulombic efficiency. Variations of specific capacitance with scan rate and current density for VS<sub>2</sub> have been depicted in Figure 3.9c and Figure 3.9d, respectively. The highest capacitance shown by VS<sub>2</sub> is ~120 F/g (at 1 mV/s) and the value decreases to ~1 F/g at 200 mV/s. Figure 3.10 shows supercapacitor performance of RGO. RGO, being an EDLC material, produced CV curves (Figure 3.10a) which are of quasi-rectangular shape. The CD curves (Figure 3.10b) are almost triangular in shape,

indicating good coulombic efficiency. The capacitance vs. scan rate and capacitance vs. current density plots have been shown in Figure 3.10c and 3.10d, respectively. Results were similar for CNTs, which is also an EDLC material, and shows equivalent electrochemical properties like RGO as shown in Figure 3.11. The highest values of capacitance obtained in case of RGO and CNTs were  $\sim 66$  F/g and  $\sim 60$  F/g, respectively. However, the hybrid mixture of CNTs and RGO, i.e. CNTs/RGO showed exceptional capacitance as compared to its pristine constituents. The highest value of capacitance was measured to be  $\sim 233$  F/g for CNTs/RGO. This shows the synergistic effect of both the constituents towards electrochemical supercapacitive performance. Figure 3.12 shows the detailed electrochemical performance of CNTs/RGO hybrid. Supercapacitive performances of  $\text{VS}_4/\text{CNTs}$  and  $\text{VS}_4/\text{RGO}$  have been represented in Figure 3.13 and 3.14. While  $\text{VS}_4/\text{CNTs}$  showed a capacitance of  $\sim 231$  F/g, the capacitance obtained in case of  $\text{VS}_4/\text{RGO}$  was much better ( $\sim 492$  F/g). It reveals that the incorporation of  $\text{VS}_4$  is better with RGO than CNTs and thus the hybrid,  $\text{VS}_4/\text{RGO}$ , showcased enhanced electrochemical activity. It is to be noted that, there is a significant increase in the energy density and capacitance values of  $\text{VS}_4/\text{CNTs}/\text{RGO}$  than those of  $\text{VS}_4/\text{CNTs}$  and  $\text{VS}_4/\text{RGO}$ . This can be attributed to the synergistic interaction between CNTs and RGO in  $\text{VS}_4/\text{CNTs}/\text{RGO}$ , which resulted in an enhanced supercapacitive performance. Energy densities, power densities and specific capacitances of all the aforementioned samples were compared and have been illustrated in Table 3.1.

Also the comparative supercapacitive performances of all of the above discussed samples have been investigated in terms of capacitance vs. scan rate and capacitance vs. current density graphs, as can be observed from Figure 3.15a and 3.15b, respectively. Furthermore, their energy densities and power densities were compared using Ragone plot technique illustrated in Figure

3.16. The exceptional energy density shown by VS<sub>4</sub>/CNTs/RGO was compared to the energy densities of other earlier reported samples, which has been furnished in Table 3.2.

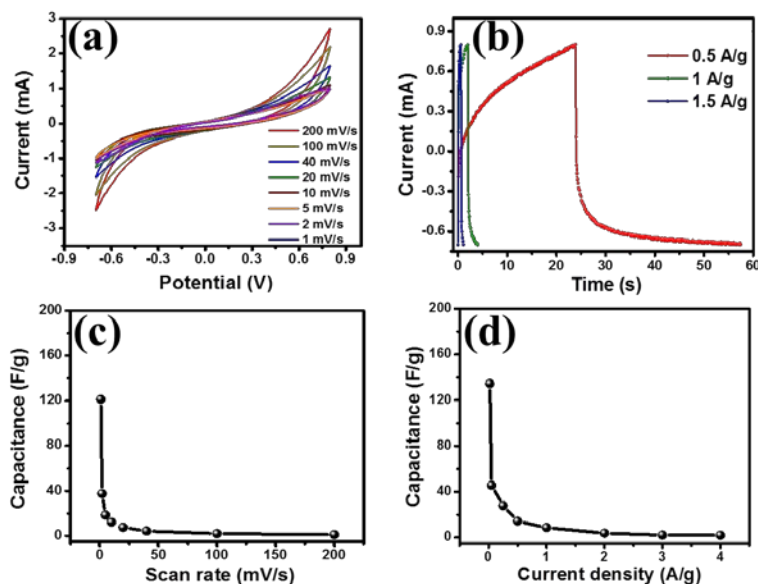


**Figure 3.9.** (a) CV and (b) CD data for VS<sub>2</sub>. Variations of specific capacitance with (c) scan rate and (d) current density.

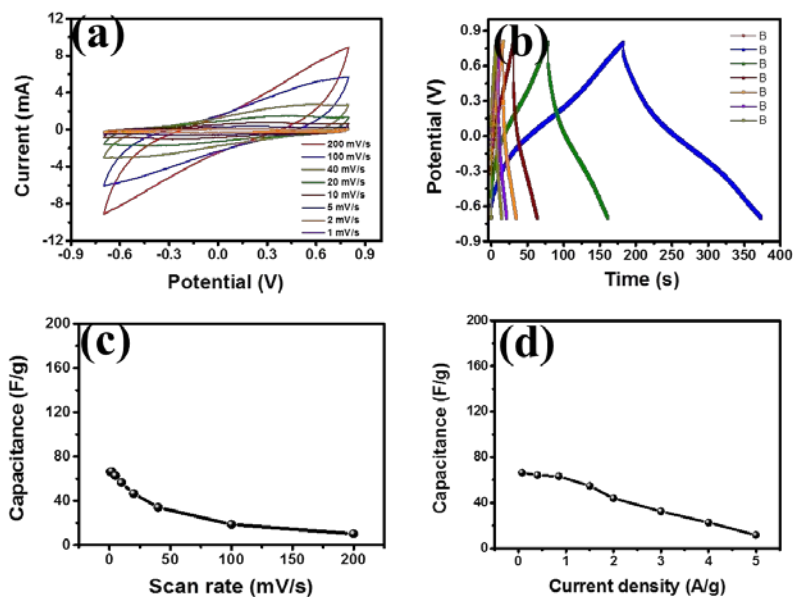


**Figure 3.10.** Two-electrode data for RGO. (a) CV and (b) CD curves along with graphs showing variation in specific capacitance value with (c) scan rate and (d) current density.

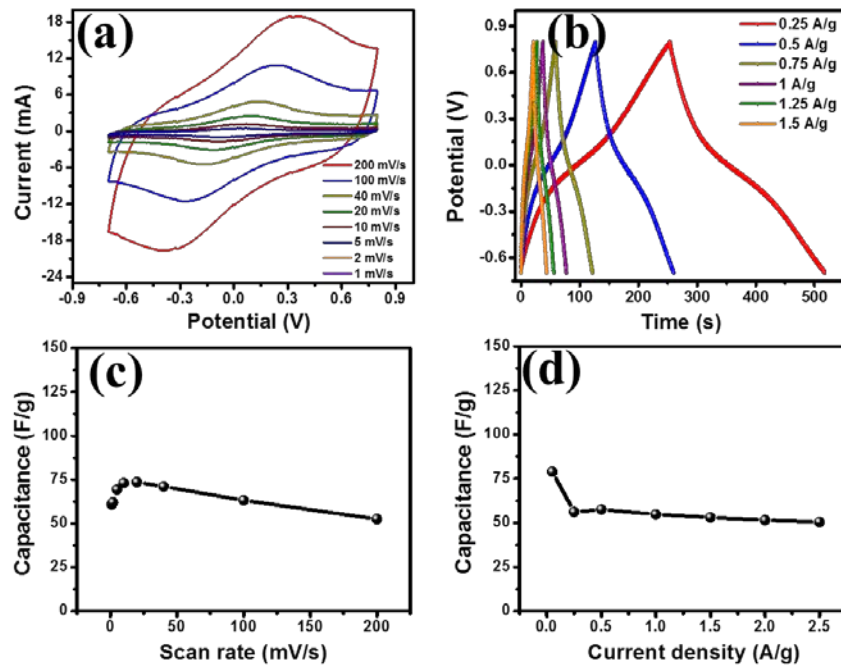


**Figure 3.11.** Two-electrode data for CNTs showing (a) CV and (b) CD curves. (c) and (d) show the variation of specific capacitance with scan rate and current density, respectively.

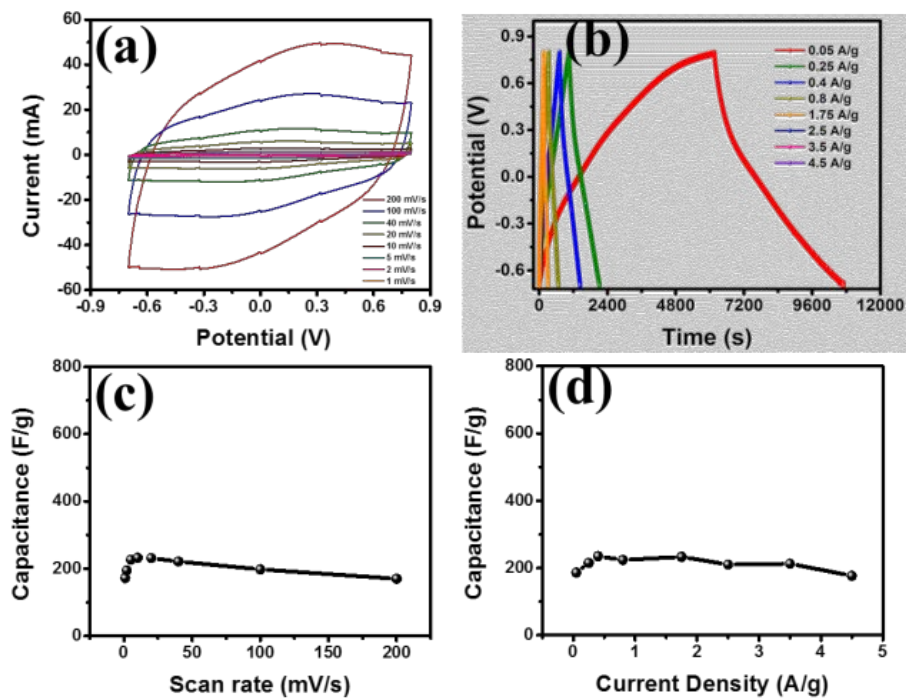


**Figure 3.12.** Two-electrode data for CNTs/RGO. (a) CV and (b) CD curves. (c) and (d) respectively show different values of specific capacitance at different scan rate and current density.

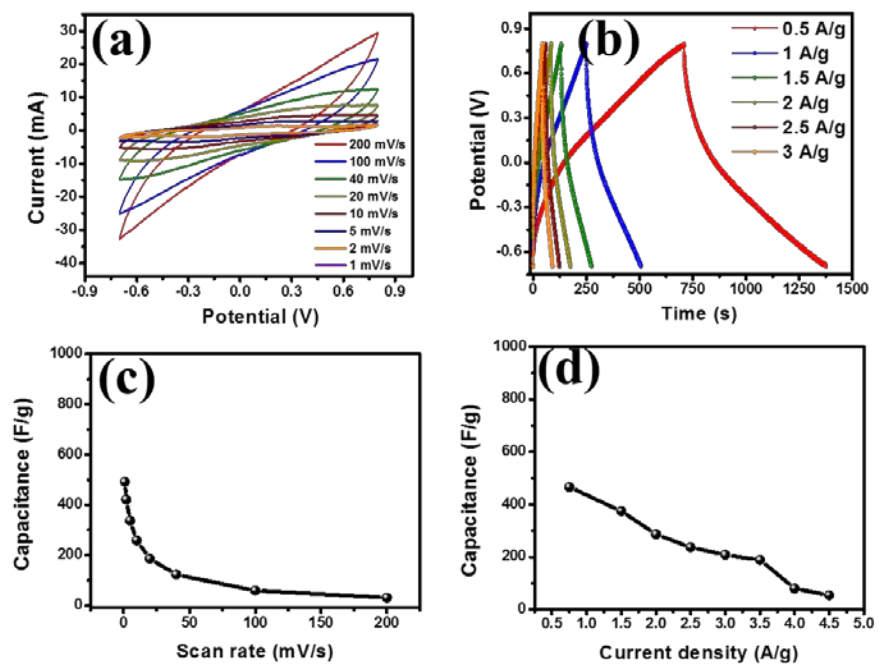


**Figure 3.13.** Two-electrode measurement data for VS<sub>4</sub>/RGO. (a) CV and (b) CD curves. Variations of specific capacitance with (c) scan rate and (d) current density.

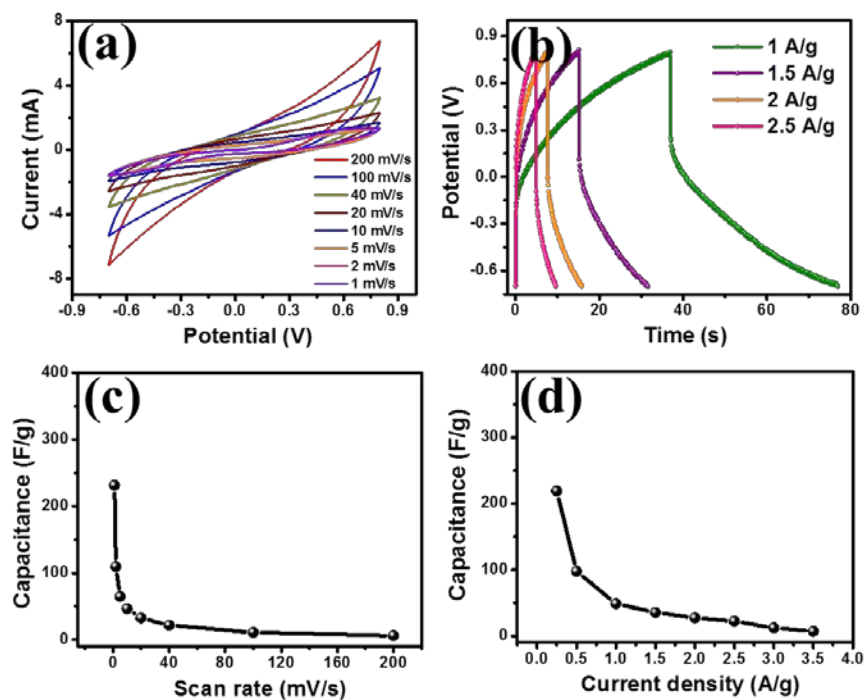


**Figure 3.14.** Two-electrode data for VS<sub>4</sub>/CNTs. (a) CV and (b) CD curves. Variations of specific capacitance with (c) scan rate and (d) current density have been illustrated.

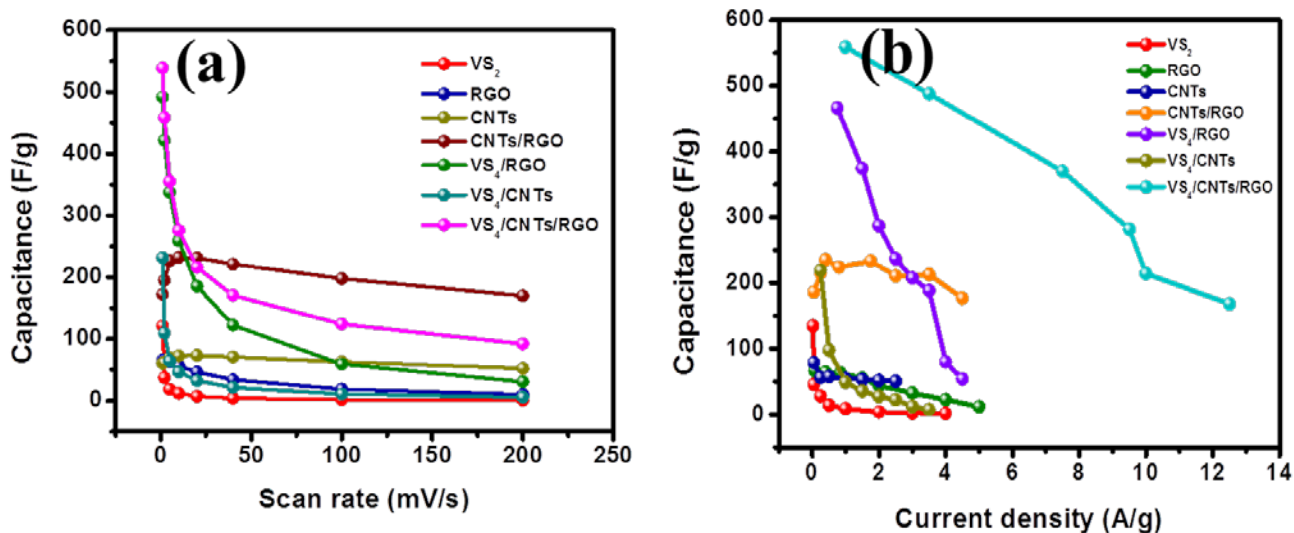


**Figure 3.15.** Graphs showing variation of capacitance with (a) scan rate and (b) current density for  $\text{VS}_2$ , RGO, CNTs, CNTs/RGO,  $\text{VS}_4$ /RGO,  $\text{VS}_4$ /CNTs and  $\text{VS}_4$ /CNTs/RGO.

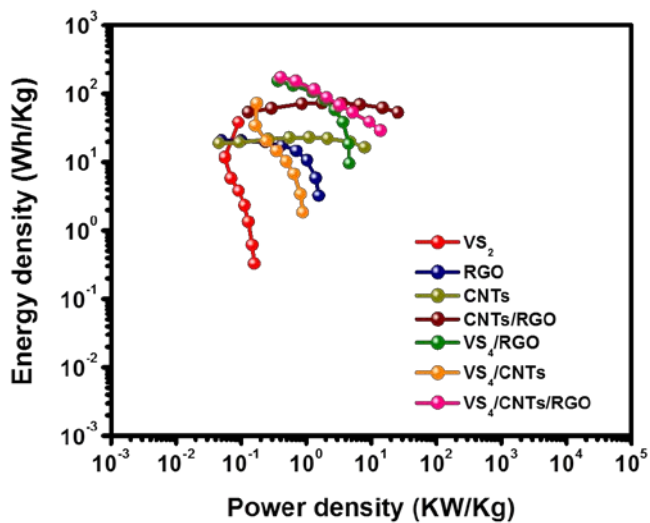


**Figure 3.16.** Comparison of power densities and energy densities of  $\text{VS}_2$ , RGO, CNTs, CNTs/RGO,  $\text{VS}_4$ /RGO,  $\text{VS}_4$ /CNTs and  $\text{VS}_4$ /CNTs/RGO using a typical Ragone plot.

**Table 3.1.** Comparison data of supercapacitive performance of all the samples

Sample	Maximum Specific Capacitance (F/g)	Maximum Energy Density (Wh/kg)	Maximm Power Density (KW/kg)
VS <sub>2</sub>	~121.3 (at 1 mV/s)	~37.9	~0.28
RGO	~66.3 (at 1 mV/s)	~20.7	~1.56
CNTs	~60.7 (at 1 mV/s)	~18.97	~7.88
CNTs/RGO	~233 (at 10 mV/s)	~72.8	~25.5
VS <sub>4</sub> /CNTs	~231 (at 1 mV/s)	~72.2	~0.9
VS <sub>4</sub> /RGO	~492 (at 1 mV/s)	~153.75	~4.59
VS <sub>4</sub> /CNTs/RGO	~558.7 (at 1 A/g)	~174.6	~13.85

**Table 3.2.** Comparison of supercapacitive performance of VS<sub>4</sub>/CNTs/RGO with those reported in other literatures

Sample	Maximum Specific Capacitance (F/g)	Maximum Energy Density (Wh/kg)	Maximum Power Density (KW/kg)	Reference
VS <sub>4</sub> /CNTs/RGO	~558.7 (at 1 A/g)	~174.6	~13.85	Present work
RGO/CNTs/CeO <sub>2</sub>	215 (at 0.1 A/g)	29.86	~0.049	39
RGO/CNTs/NiO	367 (at 1 A/g)	---	---	40
RGO/CNTs/MnO <sub>2</sub>	319 (at 0.5 A/g)	44.3	30.0	41
RGO/CNTs/ $\alpha$ -Ni(OH) <sub>2</sub>	1320 (at 6 A/g)	43.1	5.6	42
VO <sub>x</sub> :Ti-VACNTs	313 (at 2 mV/s)	25	4.5	43
Co <sub>9</sub> S <sub>8</sub> /RGO	1349 (at 2.2 A/g)	68.6	~1.32	44
MnMoO <sub>4</sub>	234 (at 2 A/g)	130	8	45
Gr-MnMoO <sub>4</sub>	364 (at 2 A/g)	202.2	8	45

### 3.7 Conclusions

In summary, a successful template assisted synthesis procedure comprising of a facile hydrothermal reaction was carried out for the obtention of a patronite hybrid, VS<sub>4</sub>/CNTs/RGO. The as prepared hybrid is resulted because of the nucleation of VS<sub>2</sub>, in presence of CNTs/RGO as an active template. Other intermediary samples such as VS<sub>2</sub>, bare CNTs, bare RGO,

CNTs/RGO, VS<sub>4</sub>/CNTs and VS<sub>4</sub>/RGO were also obtained under different controlled experimental procedures. Structural and morphological properties of the hybrid, VS<sub>4</sub>/CNTs/RGO were studied and its electrochemical properties towards supercapacitor application were investigated using a swagelok type two-electrode setup using 0.5 M aqueous solution of K<sub>2</sub>SO<sub>4</sub> as the electrolyte. A thorough comparison was carried out for the supercapacitive properties of all experimentally obtained samples mentioned above, under similar testing conditions. The hybrid, VS<sub>4</sub>/CNTs/RGO showed an impressive energy density of ~174 Wh/kg and a moderate power density of ~13.8 KW/kg. The performance was unambiguously better than those observed in case of remaining samples. Also the performance of the hybrid was compared to some of the best performing hybrids from the literature. The results show that the hybrid reported here has the potential to be implemented as high energy density supercapacitor electrodes.

### 3.8. References

1. Brezesinski, T.; Wang, J.; Tolbert, S. H.; Dunn, B., *Nat. Mater.* **2010**, *9*, 146.
2. Brownson, D. A. C.; Kampouris, D. K.; Banks, C. E., *J. Power Sources* **2011**, *196*, 4873.
3. Yang, M.; Cheng, B.; Song, H.; Chen, X., *Electrochim. Acta* **2010**, *55*, 7021.
4. Ghosh, D.; Giri, S.; Das, C. K., *ACS Sustainable Chem. Eng.* **2013**, *1*, 1135.
5. Yu, X.; Lu, B.; Xu, Z., *Adv. Mater.* **2014**, *26*, 1044.
6. Rao, C. N. R.; Ramakrishna Matte, H. S. S.; Maitra, U., *Angew. Chem., Int. Ed.* **2013**, *52*, 13162.
7. Heine, T., *Acc. Chem. Res.* **2015**, *48*, 65.
8. Chhowalla, M.; Shin, H. S.; Eda, G.; Li, L.-J.; Loh, K. P.; Zhang, H., *Nat. Chem.* **2013**, *5*, 263.

9. Mai, C.; Barrette, A.; Yu, Y.; Semenov, Y. G.; Kim, K. W.; Cao, L.; Gundogdu, K., *Nano Lett.* **2014**, *14*, 202.
10. Pumera, M.; Sofer, Z.; Ambrosi, A., *J. Mater. Chem. A* **2014**, *2*, 8981.
11. Feng, J.; Sun, X.; Wu, C.; Peng, L.; Lin, C.; Hu, S.; Yang, J.; Xie, Y., *J. Am. Chem. Soc.* **2011**, *133*, 17832.
12. Wang, Q. H.; Kalantar-Zadeh, K.; Kis, A.; Coleman, J. N.; Strano, M. S., *Nat. Nanotechnol.* **2012**, *7*, 699.
13. Khomenko, V.; Raymundo-Pinero, E.; Beguin, F., *J. Power Sources* **2008**, *177*, 643.
14. Shin, J.-H.; Henderson, W. A.; Passerini, S., *Electrochem. Commun.* **2003**, *5*, 1016.
15. Jaramillo, T. F.; Jorgensen, K. P.; Bonde, J.; Nielsen, J. H.; Horch, S.; Chorkendorff, I., *Science (Washington, DC, U. S.)* **2007**, *317*, 100.
16. Chen, J.; Kuriyama, N.; Yuan, H.; Takeshita, H. T.; Sakai, T., *J. Am. Chem. Soc.* **2001**, *123*, 11813.
17. Splendiani, A.; Sun, L.; Zhang, Y.; Li, T.; Kim, J.; Chim, C.-Y.; Galli, G.; Wang, F., *Nano Lett.* **2010**, *10*, 1271.
18. Rothschild, A.; Cohen, S. R.; Tenne, R., *Appl. Phys. Lett.* **1999**, *75*, 4025.
19. Voiry, D.; Yamaguchi, H.; Li, J.; Silva, R.; Alves, D. C. B.; Fujita, T.; Chen, M.; Asefa, T.; Shenoy, V. B.; Eda, G.; Chhowalla, M., *Nat. Mater.* **2013**, *12*, 850.
20. Georgiou, T.; Jalil, R.; Belle, B. D.; Britnell, L.; Gorbachev, R. V.; Morozov, S. V.; Kim, Y.-J.; Gholinia, A.; Haigh, S. J.; Makarovskiy, O.; Eaves, L.; Ponomarenko, L. A.; Geim, A. K.; Novoselov, K. S.; Mishchenko, A., *Nat. Nanotechnol.* **2013**, *8*, 100.
21. Mahmoud, W. E.; Yagmour, S. J., *Opt. Mater.* **2013**, *35*, 652.

22. Sharma, H.; Sharma, S. N.; Singh, S.; Kishore, R.; Singh, G.; Shivaprasad, S. M., *Appl. Surf. Sci.* **2007**, *253*, 5325.
23. Kannan, P. K.; Rout, C. S., *Chem. Eur. J.* **2015**, *21*, 9355.
24. Chou, S.-W.; Lin, J.-Y., *J. Electrochem. Soc.* **2013**, *160*, D178.
25. Rakhi, R. B.; Alhebshi, N. A.; Anjum, D. H.; Alshareef, H. N., *J. Mater. Chem. A* **2014**, *2*, 16190.
26. Lin, C.-Y.; Mersch, D.; Jefferson, D. A.; Reisner, E., *Chem. Sci.* **2014**, *5*, 4906.
27. Feng, J.; Peng, L.; Wu, C.; Sun, X.; Hu, S.; Lin, C.; Dai, J.; Yang, J.; Xie, Y., *Adv. Mater.* **2012**, *24*, 1969.
28. Jing, Y.; Zhou, Z.; Cabrera, C. R.; Chen, Z., *J. Phys. Chem. C* **2013**, *117*, 25409.
29. Rout, C. S.; Khare, R.; Kashid, R. V.; Joag, D. S.; More, M. A.; Lanzillo, N. A.; Washington, M.; Nayak, S. K.; Late, D. J., *Eur. J. Inorg. Chem.* **2014**, *2014*, 5331.
30. Ratha, S.; Marri, S. R.; Lanzillo, N. A.; Moshkalev, S.; Nayak, S. K.; Behera, J. N.; Rout, C. S., *J. Mater. Chem. A* **2015**, *3*, 18874.
31. Rout, C. S.; Kim, B.-H.; Xu, X.; Yang, J.; Jeong, H. Y.; Odkhuu, D.; Park, N.; Cho, J.; Shin, H. S., *J. Am. Chem. Soc.* **2013**, *135*, 8720.
32. Mohan, P.; Yang, J.; Jena, A.; Suk Shin, H., *J. Solid State Chem.* **2015**, *224*, 82.
33. Xu, X.; Jeong, S.; Rout, C. S.; Oh, P.; Ko, M.; Kim, H.; Kim, M. G.; Cao, R.; Shin, H. S.; Cho, J., *J. Mater. Chem. A* **2014**, *2*, 10847.
34. Guo, W.; Wu, D., *Int. J. Hydrogen Energy* **2014**, *39*, 16832.
35. Ratha, S.; Rout, C. S., *ACS Appl. Mater. Interfaces* **2013**, *5*, 11427.
36. Gu, Y.; Wu, H.; Xiong, Z.; Al Abdulla, W.; Zhao, X. S., *J. Mater. Chem. A* **2014**, *2*, 451.

37. Xu, J.; Gai, S.; He, F.; Niu, N.; Gao, P.; Chen, Y.; Yang, P., *Dalton Trans.* **2014**, *43*, 11667.
38. Liu, C.-J.; Tai, S.-Y.; Chou, S.-W.; Yu, Y.-C.; Chang, K.-D.; Wang, S.; Chien, F. S.-S.; Lin, J.-Y.; Lin, T.-W., *J. Mater. Chem.* **2012**, *22*, 21057.
39. Rajendran, R.; Shrestha, L. K.; Minami, K.; Subramanian, M.; Jayavel, R.; Ariga, K., *J. Mater. Chem. A* **2014**, *2*, 18480.
40. Rajendran, R.; Shrestha, L. K.; Kumar, R. M.; Jayavel, R.; Hill, J. P.; Ariga, K., *J. Inorg. Organomet. Polym. Mater.* **2015**, *25*, 267.
41. Jiang, H.; Dai, Y.; Hu, Y.; Chen, W.; Li, C., *ACS Sustainable Chem. Eng.* **2014**, *2*, 70.
42. Chen, X.-a.; Chen, X.; Zhang, F.; Yang, Z.; Huang, S., *J. Power Sources* **2013**, *243*, 555.
43. Jampani, P. H.; Velikokhatnyi, O.; Kadakia, K.; Hong, D. H.; Damle, S. S.; Poston, J. A.; Manivannan, A.; Kumta, P. N., *J. Mater. Chem. A* **2015**, *3*, 8413.
44. Jana, M.; Saha, S.; Samanta, P.; Murmu, N. C.; Kim, N. H.; Kuila, T.; Lee, J. H., *J. Mater. Chem. A* **2016**.
45. Ghosh, D.; Giri, S.; Moniruzzaman, M.; Basu, T.; Mandal, M.; Das, C. K., *Dalton Trans.* **2014**, *43*, 11067.

## Summary of Part-2

